Direct Method for Floor Response Spectra Considering Soil-Structure Interaction

by

Yang Zhou

A thesis
presented to the University of Waterloo
in fulfilment of the
thesis requirement for the degree of
Doctor of Philosophy
in
Civil Engineering

Waterloo, Ontario, Canada, 2019

Examining Committee Membership

The following served on the Examining Committee for this thesis. The decision of the Examining Committee is by majority vote.

External Examiner	NAME: Wenxing Zhou Title: Associate Professor
Supervisor(s)	NAME: Wei-Chau Xie Title: Professor
Internal Member	NAME: Mahesh Pandey Title: Professor
Internal Member	NAME: Giovanni Cascante Title: Professor
Internal-external Member	NAME: Xinzhi Liu Title: Professor

Author's Declaration

I hereby declare that I am the sole author of this thesis. This is a true copy of the thesis, including any required final revisions, as accepted by my examiners.

I understand that my thesis may be made electronically available to the public.

Abstract

Soil-Structure Interaction (SSI) analysis is required in structural dynamic analysis under seismic excitations in the current standards, and it significantly influences the Floor Response Spectra (FRS), which are used in the safety assessment for the secondary systems in nuclear power facilities. A direct spectra-to-spectra method is well developed to generate FRS in fixed-base models efficiently and accurately. Thus it is necessary to address SSI effect and integrate it into the free field motion as the seismic input for the fixed-base model. For the fully or partly embedded nuclear power reactors, earthquake excitations come from both bottom foundations and external structures. In this case, the foundations and external structures behave like a foundation system with seismic input at multiple supporting points.

The objective of this study is to develop an approach to address SSI effect considering the foundation flexibility and spatially varying ground motions. A substructure method is analytically derived to convert the three dimensional free field motion, i.e., Foundation Input Response Spectra (FIRS) given by site response analysis, into Foundation Level Input Response Spectra (FLIRS). The latter can be used as the seismic input in the direct spectra-to-spectra method to generate FRS considering SSI. Only FIRS, dynamic soil stiffness, mass matrix, geometry of the structure, and basic modal information, including natural frequencies and modal shapes, are needed. Both flexible and rigid foundations are considered under the excitation of spatially varying ground motions or uniform seismic input. Furthermore, parametric study is performed to examine the influence of the foundation flexibility on SSI analysis and the resultant FRS. It is observed that FLIRS and FRS are amplified significantly due to SSI effect. This amplification is more severe and the associated frequency is smaller with a more flexible foundation.

A semi-analytical method is proposed to generate dynamic soil stiffness of rigid foundations and flexible foundations. Given the soil properties, the Green's influence function is formulated analytically from wave propagation functions. And Boundary Element Method (BEM) is employed to determine the dynamic stiffness of foundations with arbitrary shapes. The resultant $6M \times 6M$ dynamic soil stiffness matrix is then used as the generalized soil springs in the proposed substructure method.

This study presents a fully probabilistic method for addressing the uncertainty resulting from seismic input and soil properties in the generation of FRS. A large number of FLIRS are developed by Monte Carlo simulations, which enables the uncertainty to be propagated from site response analysis to SSI analysis consistently. Then a uniform hazard FLIRS is obtained. Compared to the approach specified in current codes, the uniform hazard FRS lowered the seismic demand significantly to provide a more economical solution for seismic design. Meanwhile, it overcomes the underestimation of FRS by current method in some frequency range. A realistic and continuous distribution is proposed for shear wave velocity (V_S) to replace the current application. Sensitivity study is performed on the correlation coefficient and the standard derivation of V_S. The results show that these two parameters do not influence much in uncertainty analysis.

Based on the proposed method, SSI analysis is performed in a realistic model to develop uniform hazard FLIRS for performance-based seismic design, and the direct spectra-to-spectra method is extended to generate safe and economical FRS considering SSI.

Acknowledgement

I would like to express my deep gratitude to my supervisor, Professor Wei-Chau Xie, for the continuous support and guidance. His advice on both research as well as all aspects of life have been invaluable. I would like to extend my gratitude to my thesis committee members, Professor Wenxing Zhou, Professor Mahesh Pandey, Professor Giovanni Cascante, and Professor Xinzhi Liu for their insightful comments and cares for my research.

Thanks also go to my friends and colleagues, Dr. Shun-Hao Ni, Dr. Bo Li, Dr. Wei Jiang, Dr. Zhen Cai, Lanlan Yang, Rui Wang, Dr. Wenfu Wang, Dr. Sigong Zhang, Dr. Kexue Zhang, Mengcheng Sun and other graduate students in the Department of Civil and Environmental Engineering.

Nobody has been more important to me in the pursuit of this project than the members of my family. This thesis would not be possible without the love, support, and encouragement of my wife, Donghui Lu, and my parents.

The financial support by the Natural Sciences and Engineering Research Council of Canada (NSERC) and the University Network of Excellence in Nuclear Engineering (UNENE) in the form of a Research Assistantship is greatly appreciated.

Contents

List of Figures

Nomenclature

AF	Amplification Factor
ARS	Acceleration Response Spectra
ABC	Absorbing Boundary Condition
BE	Best Estimate
BEM	Boundary Element Method
CENA	Central and Eastern North America
ENA	Eastern North America
EL	Equivalent-Linear
FEM	Finite Element Method
FIRS	Foundation Input Response Spectra
FLIRS	Foundation Level Input Response Spectra
FRS	Floor Response Spectra
FRS-CQC	Complete Quadratic Combination for Floor Response Spectrum
GMPEs	Ground-Motion Prediction Equations
GRS	Ground Response Spectra
IE	Infinite Element
IRVT	Inverse Random Vibration Theory
LB	Lower Bound
NPPs	Nuclear power plants
NEP	Non Exceedance Probability
PEER	Pacific Earthquake Engineering Research
PGA	Peak Ground Acceleration

PSHA	Probabilistic Seismic Hazard Analysis
PSDF	Power Spectral Density Function
PML	Perfectly Matched Layer
PDF	Probability Density Function
SBFEM	Scaled Boundary Finite Element Method
SDOF	Single Degree-of-Freedom
$\mathcal{S}_{\mathrm{A}}$	Spectral acceleration
SSI	Soil-Structure Interaction
SSCs	Structures, Systems and Components
SMRs	Small Modular Rectors
SPRA	Seismic Probability Risk Assessment
tRS	t-response spectrum
RVT	Random Vibration Theory
RP	Return Period
UB	Upper Bound
UHS	Uniform Hazard Spectrum
WNA	Western North America

CHAPTER 1

Introduction

Earthquakes are natural disaster influencing human life and properties significantly. An earthquake can disrupt the structure directly by causing a structure failure or shaking the ground supporting the structure, and damage the secondary system as shown in Figure 1.1. Nuclear power plants (NPPs) design pays more attention to earthquake excitation than other types of structures because of the severe consequence. After the accident of Fukushima Daiichi nuclear power plant in Japan caused by Tohoku Earthquake in 2011, the seismic design of NPPs raised more awareness in North America. Currently, 15 percent of the total electrical power comes from 19 NPPs in Canada, and 19 percent from 104 NPPs in the USA. In order to guarantee their safety, the response of NPPs under earthquake excitation need to be well researched to prevent their damage or failure.

Secondary systems, including electrical systems, mechanical systems, control systems, etc, are structures, systems and components (SSCs) which are attached to or supported by primary systems, such as buildings. During earthquakes, secondary systems are even more vulnerable than primary systems in NPPs. The failure of secondary systems not only causes economic loss, but also threats human lives (Bozorgnia and Bertero, 2004; Villaverde, 2009). The safety assessment of secondary systems in an earthquake relies on the seismic excitations at its supporters which is determined by both the ground motions and the dynamic characteristics of primary structures. Thus it is necessary to develop practical and accurate excitations for the seismic design of secondary systems.

Figure 1.1 Damaged primary structures and secondary system

In the seismic analysis, it is common to assume that the input ground motion at the base is equal to the free-field ground motion without structure. For structures founded on rigid rock, this assumption is justified since the high stiffness of the base can constrain the structure motion to be close to the free-field one as the left structure in Figure 1.2. For structures supported on soft soil or with large mass, however, the ground motion is different from the free-field one due to the change in geometry and properties of the wave propagation medium caused by the structure. In this case, the structure suffers both translational and rotational ground motions as the right structure in Figure 1.2. This effect is called Soil-Structure Interaction (SSI) defined as the interdependence between a structure and its foundation soil (Villaverde, 2009). That is, the dependence of the dynamic response of a structure on the dynamic response of its supporting foundation soil and

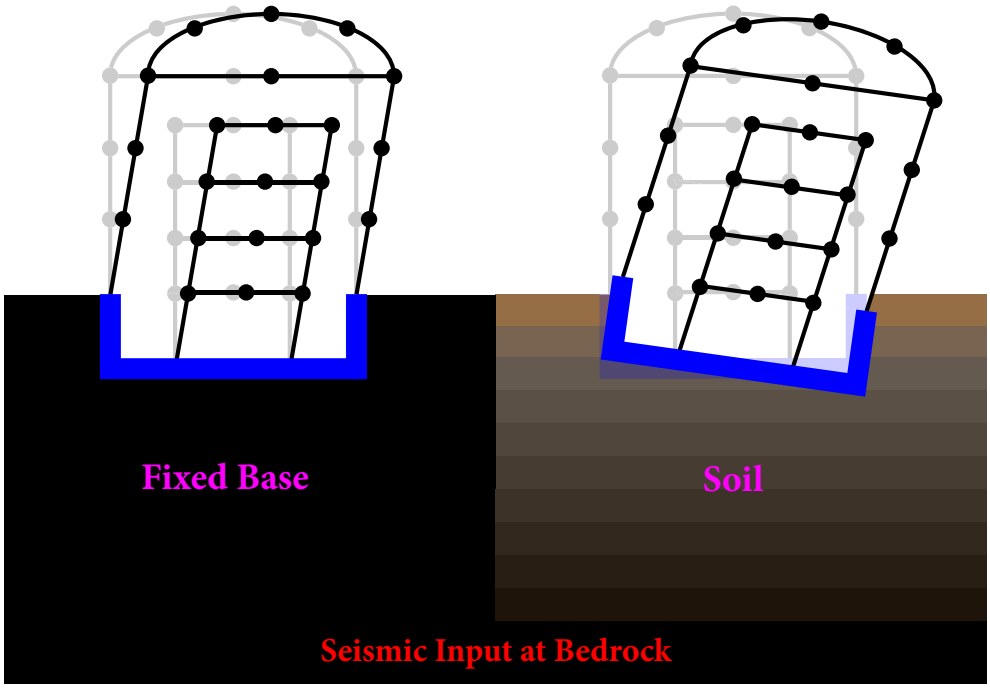

Figure 1.2 Illustration of soil-structure interaction

the dependence of the dynamic response of a soil deposit on the dynamic response of the structure supported by it.

The SSI effect could be important for stiff and massive structures such as NPPs. SSI analysis is mandatory for safety-related secondary systems in nuclear structures by ASCE (2000). Based on SSI analysis, the resultant ground motion integrated with local site effect and SSI effect will be obtained as a basis for the structural analysis and to analyze secondary design. It can also be used in Seismic Probability Risk Assessment (SPRA) for seismic safety evaluation of existing power stations, and seismic design of new-built plants. Besides, the current research mainly focus on the SSI analysis with a rigid foundation. For Small Modular Rectors (SMRs) fully or partly embedded in the site, the earthquake excitation comes from both the bottom foundation and the external structure of SMRs. In this case, the external structure and the foundation perform like a structure-foundation system undergoing seismic input at multiple points. Therefore, it is necessary to develop a reliable and efficient approach to provide the seismic input considering SSI effect with flexible foundation systems for seismic design of secondary systems.

1.1 Generation of Floor Response Spectra

In secondary systems, there are a large number of SSCs, and their stiffness and mass are relatively smaller than the primary structure. It is computationally expensive to model the primary structure and secondary system together, and some problems, such as ill-conditioning of the stiffness matrix, may arise in the mathematical model of entire structure systems. Since the interaction between secondary systems and their supporting structures are negligible due to the relatively small mass of SSCs, a decoupled approach, floor response spectrum approach, is usually used in seismic response analysis: secondary systems and primary structures are analyzed separately (ASCE, 1978).

In floor response spectrum approach, the dynamic analysis is firstly performed for the primary structure without considering the secondary system under seismic excitation. The response of the supporting structure, such as floors and walls where secondary systems are attached, as Floor Response Spectra (FRS). Then FRS is utilized as the seismic input for SSCs analysis. In this decoupled approach, the change of SSCs only leads to reanalyze secondary systems, and dose not influence the primary structure, which improves the efficiency of engineering design.

Two methods are proposed to generate FRS: time history analyses and a direct spectra-to-spectra method as shown in Figure 1.3 (ASCE, 2000).

- In the time history method, the spectrum-compatible time history with a target Ground Response Spectra (GRS) is taken as the seismic input for the primary structure. Then the time histories at the desired location is obtained for the seismic design of secondary systems. Since the real ground motion is unavailable, and the input time history is artificial, there are significant variabilities in the generation of FRS by this method (Chen and Soong, 1988; Singh, 1988; Villaverde, 1997). In order to provide reliable FRS, a large number of spectrum-compatible time histories are needed, which means the variability of FRS is involved and it is time-consuming.
- For direct spectra-to-spectra method, GRS is considered as the seismic input directly. FRS is obtained analytically based on the input GRS and the modal information of the

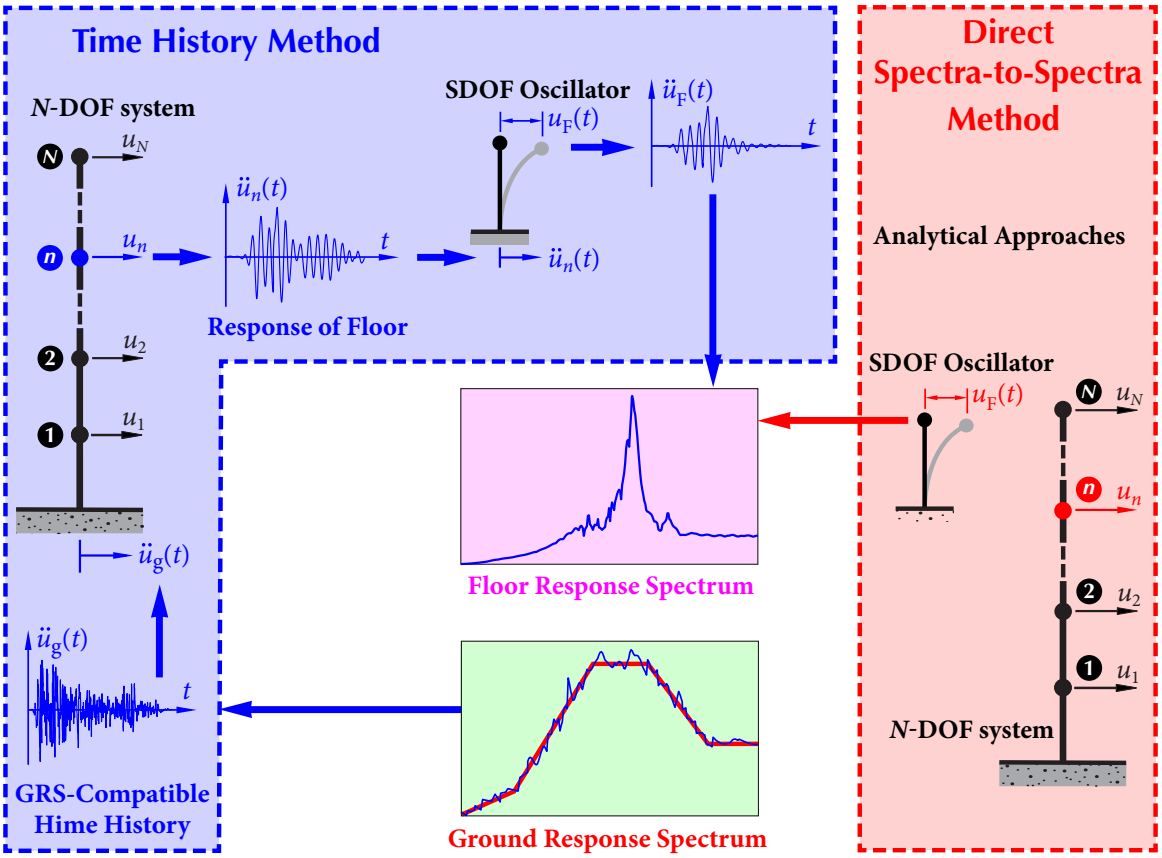

Figure 1.3 Time history method and direct method to generate FRS

primary structure, e.g., natural frequencies, mode shapes, and modal participation factors. Therefore, the variability is avoided and the efficiency is high.

In the traditional direct spectra-to-spectra method, FRS can not be determined accurately under the tuning cases, i.e., the frequency and damping ratio of a single degree-of-freedom (SDOF) oscillator is equal to those of a SDOF supporting structure, which accounts for the uncertainty of FRS resulting from ground motions (Li, 2015). In order to generate probabilistic FRS, t-Response Spectrum (tRS) is proposed to illustrate how tuning cases influence the uncertainty of FRS by Li (2015). The tRS represents equipment-structure resonance or tuning corresponding to a specified GRS. Based on numerical simulations with a wide variety of selected two dimensional ground motions at different sites, it is demonstrated that tRS is almost independent on site conditions in the horizontal direction, while the influence

of site conditions can not be neglected in the vertical direction. Therefore, a statistical relationship between tRS and GRS is established in horizontal direction for all sites, and vertical relationships are obtained at hard sites and soft sites, respectively. The resultant tRS are effective for any GRS in the valid coverage, including design spectra in USNRC R.G. 1.60 and NUREG/CR-0098, UHS in Western North America (WNA). Besides, amplification ratio method is developed to calculate tRS under seismic input with high frequency spectral accelerations, e.g., UHS in Central and Eastern North America (CENA). With the proposed method to generate tRS, exact FRS considering uncertainty from GRS can be obtained by the direct spectra-to-spectra method.

A new direct spectra-to-spectra method for generating FRS in three-dimensional structures is developed by Jiang *et al.* (2015). In this method, seismic response of a SDOF oscillator supported by a SDOF primary structure is derived at first, and tRS is employed for the tuning case. Based on Random Vibration Theory (RVT), a new modal combination

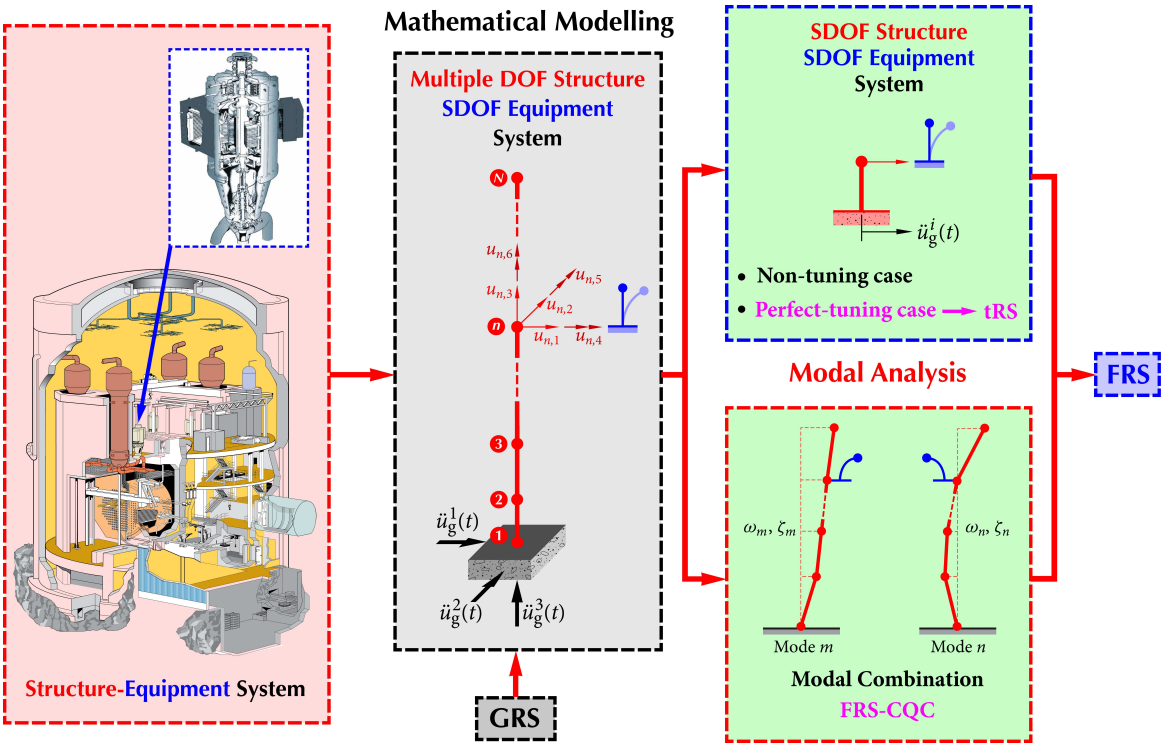

Figure 1.4 Direct method for generating FRS

method for generating FRS, i.e., FRS-CQC, is then proposed to represent the correlation of responses between SSCs and the associated primary structure with closely-spaced modes, by which a SDOF oscillator supported by a multiple DOF primary structure is considered. As a result, FRS can be obtained from input GRS and the modal information of primary structures which is calculated by a typical modal analysis. The general procedure of this direct spectra-to-spectra method is illustrated in Figure 1.4. In this direct spectra-to-spectra method, accurate FRS in the perfect-tuning and near-tuning cases can be generated for conventional Newmark-type GRS and UHS with high frequency spectral accelerations by tRS. Through FRS-CQC combination, FRS in complex three-dimensional structures under tri-directional seismic input can be developed with closely-spaced modes.

In this direct method, the mathematical model of structures is a fixed model which can not deal with SSI effect. Hence, SSI analysis should be conducted to integrate the SSI effect into GRS, which extends the direct spectra-to-spectra method to generate FRS considering SSI.

1.2 Soil-Structure Interaction

Modern SSI analysis can be traced to 1970s (Veletsos and Wei, 1971; Luco and Westmann, 1972) starting from an equivalent single-degree-of freedom system method (Kausel, 1984). Currently, SSI analysis are usually performed by two kinds of methods: complete method and substructure method.

1.2.1 Complete Method

In the complete method, a part of the surrounding soil deposit called near field soil and the structure are modeled as a single system, soil-structure system, and analyzed in one step based on the seismic input as shown in Figure 1.5 (Wolf, 1985; Bielak and Christiano, 1984). This model is always based on the Finite Element Method (FEM), and the system is discretized into finite elements. Since the soil deposit is actually an unbounded continuous solid and cannot be modeled by finite elements, an artificial boundary is needed to get

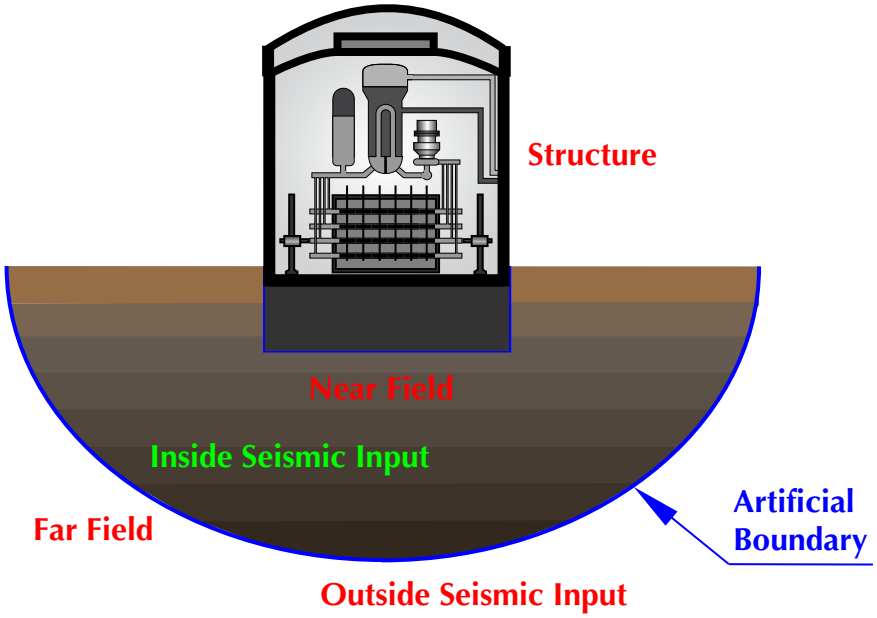

Figure 1.5 Finite element model for SSI complete method

the near field soil separated in SSI analysis. The response of each node can be solved by performing the finite element analysis.

The analysis of the soil-structure system can be performed in frequency domain or time domain. For analysis in frequency domain, the input ground motion is first transformed to frequency domain by Fourier transform. Then the response of system is obtained by multiplying the transfer function. Based on the same transfer function, the response for different input ground motions can be easily obtained. The frequency domain method assumes the systems are linear and an iterative analysis is needed for nonlinear system to get stain-compatible properties. In time domain, the response is solved by a step-by-step integration and the nonlinear properties are considered. Since some input parameters, e.g., artificial boundaries, are frequency dependent, an iterative procedure is required.

When establishing the artificial boundary to make the system bounded, one needs to deal with the reflected waves by the boundary which do not exist in actual unbounded soil. One method to treat the reflected waves is to make them absorbed at the boundary. This kind of boundaries is called Absorbing Boundary Condition (ABC).

The first ABC is viscous boundary. In the viscous boundary, the viscous dampers are added to absorb the waves without any reflection. It behaves as simple dashpots and was em-

ployed by Lysmer and Kuhlemeyer (1969). Then a model based on paraxial approximations was developed by Clayton and Engquist (1977) for elastic wave propagation problems. Some other models (Higdon, 1978; Higdon, 1991) relying on the same approach were proposed for different problems. These techniques can be combined with the approach based on layers of damping materials to eliminate the reflection on the artificial boundary. Since the viscous boundary only deals with waves coming from a certain direction. A new boundary was proposed to absorb reflected waves in up to 2 directions by Higdon (1990). Then Collino (1993) developed the first high order ABC which increased the accuracy of ABC and was able to be used in numerical simulations (Givoli, 2004). The high order ABC usually led to long-time instability issues which was overcame by a new ABC proposed by Baffet *et al.* (2012). The Perfectly Matched Layer (PML), which can absorb all incoming waves without any reflection, was developed by Berenger (1994), and was applied in dynamic problems by Basu and Chopra (2003). Compared to high order ABC, PML is more convenient to implement in engineering domain (Rabinovich *et al.*, 2010).

Another choice of the artificial boundary is Infinite Elements (IE). The IE was presented by Ungless (1973) to account for radiation condition at infinite far field. This approach combines the shape functions of the FEM framework with oscillatory decay functions which can simulate the asymptotic behaviour. Bettess (1977) and Astley (1983) developed different decay functions for different wave propagation problems. The main drawbacks of this approach is that some parameters, e.g., the decay function, have to be evaluated by analytical solutions or empirical results (Mesquita and Pavanello, 2005; Shah *et al.*, 2011).

In the complete method, the procedures are simple, and much computational effort and time are needed to work on the system with a large amount of degrees-of-freedom.

1.2.2 Substructure Method

In the substructure method (Gutierrez and Chopra, 1978), the structure and the soil deposit are considered separately at first so that these two substructures can be analyzed by suitable methods.

The coupled soil-structure model is shown in Figure 1.6. Let $\mathbf{U}_s$ be the absolute displacement vector of the superstructure while let $\mathbf{U}_b$ be that of the foundation. The subscripts

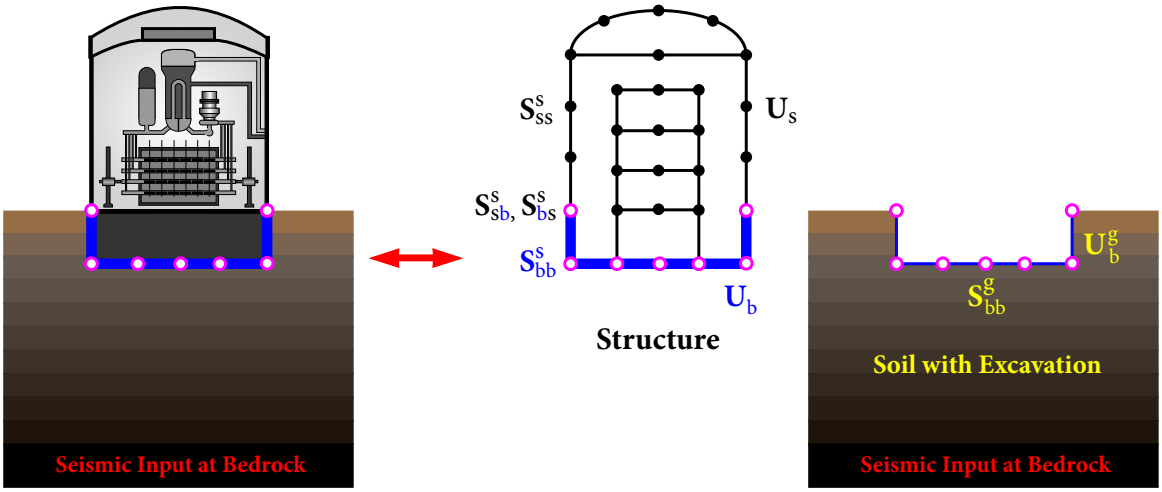

Figure 1.6 Coupled soil-structure model

"s" and "b" stand for the degrees-of-freedom of "structure"and "base", respectively. The equation of of motion for the structure is expressed by

$$\begin{bmatrix} \mathbf{S}^s_{ss} & \mathbf{S}^s_{sb} \\ \mathbf{S}^s_{bs} & \mathbf{S}^s_{bb} \end{bmatrix} \begin{Bmatrix} \mathbf{U}_s \\ \mathbf{U}_b \end{Bmatrix} = \begin{Bmatrix} \mathbf{P}_s \\ \mathbf{P}_b \end{Bmatrix}, \tag{1.1}$$

where $\mathbf{P}_s$ is the load vector applied on the structure while $\mathbf{P}_b$ is the interaction force vector between the structure and soil. During earthquake ground motion, the structure, except the part contacting with the soil, are not loaded, which leads to

$$\mathbf{P}_b = \mathbf{S}^s_{ss}\,\mathbf{U}_s + \mathbf{S}^s_{sb}\,\mathbf{U}_b = \mathbf{0}. \tag{1.2}$$

For the soil with excavation, let $\mathbf{S}^G_{bb}$ and $\mathbf{U}^G_b$ be the dynamic stiffness matrix and the absolute displacement vector under earthquake ground motion, respectively, where the subscript "g" stands for the soil with excavation. $\mathbf{P}_b$ is determined by the relative displacement between the foundation and the soil as

$$\mathbf{P}_b = \mathbf{S}^G_{bb}\,(\mathbf{U}_b - \mathbf{U}^G_b). \tag{1.3}$$

Then equation (1.5) becomes

$$\begin{bmatrix} \mathbf{S}^s_{ss} & \mathbf{S}^s_{sb} \\ \mathbf{S}^s_{bs} & \mathbf{S}^s_{bb} + \mathbf{S}^G_{bb} \end{bmatrix} \begin{Bmatrix} \mathbf{U}_s \\ \mathbf{U}_b \end{Bmatrix} = \begin{Bmatrix} \mathbf{0} \\ \mathbf{S}^G_{bb}\,\mathbf{U}^G_b \end{Bmatrix}. \tag{1.4}$$

In equation (1.4), the soil-structure system is characterized by the dynamic stiffness of the structure and soil, and the ground motion on the soil-structure interface. Thus the system is analyzed by the structure and the soil separately.

In substructure method, the analysis of structure can be conducted by FEM, which is adequate based on the current technique. It is necessary to generate the dynamic stiffness of soil deposit, also called soil impedance, which varies with the excitation frequency and consists of complex values. The dynamic soil stiffness represents the constitutive relationship between interaction forces and the relevant displacements in three translational directions and three rotational directions at the soil-foundation interface. Then the results of two parts are combined to get the response of the structure with input ground motions. Starting as early as 1960s, numerous research focused on the generation of dynamic soil stiffness (Kausel, 1984).

An integral equation approach was firstly proposed to develop the analytical solutions of the vibration of rigid circular foundations supported by elastic half-space (Luco, 1971; Veletsos and Wei, 1971; Veletsos and Verbic, 1973). Then this method was extended to half-space with multiple horizontal layers by Luco (1974; 1976). And the performance of strip foundations were considered under dynamic loads by Gazetas and Rosset (1976). After that, the dynamic stiffness of embedment foundation with arbitrary shapes was generated for horizontally layered half-space by a semi-analytical method (Luco and Apsel, 1983; Apsel and Luco, 1983; Veletsos and Verbic, 1987). For this kind of method, it is computationally expensive.

Rizzo (1967) developed the Boundary Element Method (BEM) for boundary value problems of elastostatics. In this approach, only the domain boundaries are discretized and the number of mesh is reduced. The BEM is well-adapted to simulate unbounded domains, and the coupling of BEM and FEM is an interesting choice to account for SSI analysis for many researchers. The dynamic stiffness of a strip foundation, two dimensional foundation, resting on viscoelastic half-space was derived by Abascal and Dominguez (1986). Based on BEM, the dynamic response of three dimensional foundation–soil–foundation interaction on layered soil site was studied by Karabalis and Mohammadi (1991). Estorff and Kausel (1989) presented a time domain formulation of BEM. Despite much research (Estorff and

Prabucki, 1990; Elleithy and Tanaka, 2003) focused on transient BEM-FEM formulations to solve nonlinear problems, this approach can be formulated in the frequency domain as well (Wolf and Darbre, 1984) especially for layered medium (Pak and Guzina, 1999). The main shortcoming of BEM is that it has to consider fully populated (and possibly non-symmetric) matrices, which leads to much computational effort for large models.

A new kind of semi-analytical method, the Scaled Boundary Finite Element Method (SBFEM), proposed by Wolf and Song (1995A; 1995B; 1996A; 1996B; 1997), is another alternative to model the unbounded domain. This approach is based on a similarity technique (Dasgupta, 1982), and the dynamic soil stiffness is obtained by formulating the similarity relationships between the dynamic stiffness of the original and scaled SSI-interface. Recently, Birk and Behnke (2012) applied the modified SBFEM to perform SSI analysis. In this approach, only the boundaries have to be discretized and no fundamental solution is required. It can be applied for both rigid and flexible foundations supported by layered soil site.

The dynamic stiffness can also be obtained by numerical methods, e.g., FEM with artificial boundaries as introduced in 1.2.1. Besides the aforementioned boundaries to isolate the near field, the consistent boundary is developed based on the Thin Layer Method (TLM) (Waas, 1972; Lysmer and Waas, 1972; Kausel *et al.*, 1975;). At this kind of boundary, the interaction forces on the boundary are the same as the ones imposed by the far field, which yields the effect as the waves are transmitted to far field. The weakness of consistent boundary is that it can only focus on plane strain and symmetric cases.

In the substructure method, the different techniques, i.e., numerical or analytical method, are allowable for the structure and soil, and it requires less computational effort and time to perform the SSI analysis. Once the analysis of each substructure are finished, further modification only leads to repeated computation of the modified part.

1.3 Local Site Response on Seismic Analysis

The topography and soil properties can significantly affect characteristics of the earthquake ground motions propagating in the soil deposit. When earthquake ground motions propa-

gate in a soil deposit, the flexibility of the site makes it vibrate and the motions can be greatly amplified due to resonant effects. The extent of this influence depends on the inherent stiffness, density, and damping characteristics of the site. On the other hand, the soil dynamic properties are changed due to the soil strain caused by earthquake. The local site response determines the free field motion and strain-compatible soil properties. The former is the seismic input for SSI analysis, and the latter is the essential information for the calculation of dynamic soil stiffness. Therefore, site response analysis is a precursor to SSI analysis.

To evaluate the effect of local site on earthquake waves, two types of methods to describe the soil site effect are used: Equivalent-Linear (EL) site response analysis and nonlinear (NL) site response analysis.

1.3.1 Equivalent Linear Site Response Analysis

In EL method (Seed and Idress, 1969), site response analysis is performed with one dimensional vertically propagating shear waves in horizontally layered halfspace. The model shows that shear modulus (G) and the damping ratio (ζ) of soil deposit are shear strain-dependent, and an iterative procedure is established to obtain the equivalent soil properties.

The EL method analyzes the earthquake wave propagation through the soil deposit in frequency domain, and assumes that the G and ζ have constant values during the ground motion. This method starts with initial G and ζ for each soil layer. Linear-elastic analysis is performed and the effective shear strains for soil layers are obtained. Based on the shear strain-dependent normalized modulus ($G/G_{\max}$) reduction curves and damping curves, the new G and ζ are evaluated. This process is repeated until the stain-compatible properties are consistent with the input properties.

This method requires a few input parameters and small computational effort. Several equivalent-linear computer codes are available, such as SHAKE (Schnabel *et al.*, 1972), SHAKE91 (Idriss and Sun, 1992), and Deepsoil (Hashash and Park, 2002).

1.3.2 Nonlinear Site Response Analysis

In NL analysis, the nonlinear behavior of soil during cyclic ground motions and the effect of pwp generation on soil properties can be represented. These two factors influence the

soil site significantly when high seismicity and soft soils are present. NL analysis solves the ground motion propagating the soil deposit in time domain. Two types of NL analysis are used including nonlinear total stress analysis and nonlinear analysis with pwp change.

In total stress analysis, the soil deposit is discretized into lumped mass or finite element. The equation of motion is written as

$$\mathbf{M}\ddot{\mathbf{u}} + \mathbf{C}\dot{\mathbf{u}} + \mathbf{K}\mathbf{u} = -\mathbf{M}\ddot{\mathbf{u}}_g, \tag{1.5}$$

where **M**, **C**, and **K** are the mass matrix, damping matrix, and stiffness matrix, respectively. $\ddot{\mathbf{u}}$, $\dot{\mathbf{u}}$, and **u** are the displacements, velocities, and accelerations of the mass relative to the bedrock, respectively. $\ddot{\mathbf{u}}_g$ is the earthquake ground acceleration. The ground motion after propagating in the soil deposit can be obtained by solving equation (1.5). The influence of pwp is neglected in this analysis.

For the nonlinear analysis with pwp change, the influence of pwp is taken into consideration in two ways: semi-empirical pwp generation models and advanced effective-stress-based models. In the former models, pwp generation is calculated by semi-empirical models, in which the most widely used one is Modified Konder and Zelasko (MKZ) model by Matasovic and Vucetic (1993; 1995). In the advanced effective-stress-based models, the pwp is computed as the difference between effective-stresses and total stresses. Then the effect of pwp generation is included when calculating **K** in equation (1.5), and the required ground motion is obtained by performing the total stress analysis.

1.4 Objectives of Proposed Research

The objective of this study is to develop an approach accounting for SSI effect accurately and efficiently. The specific objectives of this study include:

- The frequency-dependent dynamic soil stiffness is generated for flexible foundations, which bridges the site response analysis and SSI analysis.
- The uncertainty in earthquake excitations and soil properties are considered consistently in site response analysis and SSI analysis to provide site-structure specific amplification factors for performance-based seismic design.

- A substructure method is developed to conduct SSI analysis considering flexible foundations under spatially varying ground motions, which combines the SSI effect with the fixed-base model in the generation of FRS by the direct spectra-to-spectra method.

1.5 Organization of This Study

In Chapter 2, the RVT-based one dimensional EL site response analysis is reviewed. Based on random vibration theory, the fourier response spectrum is obtained from acceleration response spectrum to enable site response analysis to be performed in frequency domain. In order to address the local site effect, the transfer function from bedrock motion to the ground motion at any level is derived, which provides the free field motion for SSI analysis. Meanwhile, the strain compatible soil properties is generated to be further used in the calculation of dynamic soil stiffness.

In Chapter 3, the substructure method to address SSI effect with rigid foundations is reviewed. Based on the soil stiffness and structural modal information, a transfer function is derived to convert the three dimensional free-field motion into FLIRS, which is then used as the seismic input to the fixed-base model to generate FRS using the direct spectra-to-spectra method. The frequency dependant complex soil stiffness is utilized in the application of this substructure method.

In Chapter 4, a semi-analytical method is proposed to generate dynamic soil stiffness. In the horizontally layered soil model, the three dimensional wave propagation function is derived based on the boundary conditions. The flexibility functions are then developed representing the relationship between point loads and the associated displacements in k domain. According to Fourier series and Bessel transform pair, the frequency dependent stiffness matrix under a unit load is obtained in frequency domain, which is then utilized to develop the dynamic soil stiffness under rigid foundations or flexible foundations by BEM. The effect of dynamic soil stiffness on the resultant FLIRS and FRS is studied illustrating its significance in seismic design.

In Chapter 5, a fully probabilistic method is proposed to perform site response analysis and SSI analysis addressing the uncertainty resulting from earthquake excitations and soil properties. Based on the proposed substructure method, the uncertainty of seismic input at bedrock, the variability of soil parameters, and the nonlinear behavior of soil properties are comprehensively integrated into SSI analysis to develop amplification factors which is employed to generate uniform hazard FLIRS with a specific annual exceedance probability. According to the current treatment of epistemic and aleatory uncertainty in shear wave velocity profiles, a continuous and realistic distribution of shear wave velocities is proposed. The correlation coefficient in adjacent soil layers and standard derivation of the distribution is studied. The resultant uniform hazard FLIRS is utilized to develop FRS which leads to a safe and economical demand in seismic design.

In Chapter 6, a methodology is developed to account for the effect of soil-structure interaction with flexible foundations under spatially varying ground motions. The structural response of a three-dimensional structure under multi-point excitations, three translational and three rotational directions at each point, is derived, and is expressed by the modal information of the structure and coupled stiffness matrix between structures and foundations. Then the transfer matrix, which is determined by modal information of the structure-foundation system and the generalized soil springs, is developed to modify FIRS by SSI effect. The modified seismic input, FLIRS, are then considered as the input at multiple points of the fixed-base structure to generate FRS through the direct spectra-to-spectra method. The parametric study is performed to demonstrate the influence of foundation flexibility on FLIRS and FRS.

In Chapter 7, some conclusions from this study are presented, and directions for further research are proposed.

CHAPTER 2

Seismic Site Response Analysis

Seismic site response analysis has to be performed to obtain the dynamic properties of the site and develop the modified ground motions due to the propagation of shear waves in the soil deposit. Therefore, seismic site response plays a significant role in seismic design and provides strain-compatible soil properties and ground motions at a specific elevation level to conduct Soil-Structure Interaction (SSI) analysis.

The site response analysis is generally conducted based on one-dimensional elastic wave propagation in the soil column, incorporating the nonlinear effects of the soil deposit. The procedure includes two steps:

- Development of the input ground motions at reference hard rock.
- Calculation of transfer functions and strain-compatible soil properties in the geotechnical model.

2.1 Developing Input Ground Motions

2.1.1 Stochastic Ground Motion Model

A theoretical-empirical modelling method is employed to estimate ground motion amplitudes in Eastern North America (ENA) (EPRI TR-102293-V1, EPRI, 1993a). This approach uses a stochastic ground motion model, which has been validated using data largely from California, where instrumental records are available over a wide range of magnitudes and

distances (McGuire *et al.*, 1984), to estimate ground motion amplitudes in the frequency band of interest to engineering analysis and design.

For sites in the ENA, a point-source stochastic model is used to determine the total Fourier Amplitude Spectrum (FAS) $\mathcal{F}_{\mathrm{D}}(M_0, R, f)$ of ground motion displacement due to earthquake sources

$$\mathcal{F}_{\mathrm{D}}(M_0, R, f) = E(M_0, f) \cdot P(R, f) \cdot G(f), \tag{2.1}$$

where $E(M_0, f)$ is the Brune point-source spectrum, $P(R, f)$ represents the propagation path effects, and $G(f)$ is the modification due to site effects. M_0 is seismic moment

$$M_0 = 10^{1.5\,(\mathcal{M}+10.7)}, \tag{2.2}$$

where $\mathcal{M}$ is the moment magnitude. R is hypocenter distance determined by

$$R = \sqrt{R_{\mathrm{epi}}^2 + d^2}, \tag{2.3}$$

where R_{epi} is the epicenter distance, and d is the source depth (the perpendicular distance between the source and generic hard rock surface).

$E(M_0, f)$ can be expressed as (Boore, 2003)

$$E(M_0, f) = C\, M_0\, S(f), \quad C = \frac{R_{\theta\phi}\, V F}{4\pi \rho_{\mathrm{s}} \beta_{\mathrm{s}}^3 R_0}, \tag{2.4}$$

where $R_{\theta\phi} = 0.55$ is the shear-wave radiation pattern average over the focal sphere, $V = 1/\sqrt{2}$ is the partition of total shear-wave energy into two horizontal components, $F = 2$ is the effect of the free surface, ρ_{s} and β_{s} are the density and shear-wave velocity in the vicinity of the earthquake source, and $R_0 = 1$ km is the reference distance. For sites in ENA, Mid-Continent Crustal Model with $\rho_{\mathrm{s}} = 2.71$ g/cm^3 and $\beta_{\mathrm{s}} = 3.52$ km/s in Table B-5 of EPRI-1025287 is used.

$S(f)$ is the source spectrum, which can be obtained from a single-corner frequency source model as

$$S(f) = \frac{1}{1 + (f/f_{\mathrm{c}})^2}, \qquad f_{\mathrm{c}} = 4.9 \times 10^6\, \beta_{\mathrm{s}} \left(\Delta\sigma / M_0\right)^{1/3}, \tag{2.5}$$

or a empirical double-corner frequency source model

$$S(f) = S_{\mathrm{a}}(f) \times S_{\mathrm{b}}(f), \tag{2.6}$$

where f is frequency in Hz, f_c is the corner frequency, and $\Delta\sigma$ is the stress drop, which is taken as 110 bars in Table B-4 of EPRI-1025287. $S_a(f)$ and $S_b(f)$ are given by Boore (2003).

Propagation path effects $P(R, f)$ is given by

$$P(R, f) = Z(R) \cdot \exp\left\{-\frac{\pi f R}{Q(f)\beta_s}\right\}, \tag{2.7}$$

where $Z(R)$ is geometric spreading function, given in Boore (2003),

$$Z(R) = \begin{cases} \dfrac{R_0}{R}, & R \leqslant R_1, \\ Z(R_i)\left(\dfrac{R_i}{R}\right)^{p_i}, & R_i \leqslant R \leqslant R_{i+1}, \quad i = 1, 2, \ldots, n. \end{cases} \tag{2.8}$$

Three-segment geometric spreading operator is usually used in GMPEs in ENA. For example, in Atkinson and Boore (1995), $R_0 = 1$ km, $R_1 = 70$ km, $p_1 = 0$, $R_2 = 130$ km, and $p_2 = 0.5$ are used. Seismic quality factor $Q(f)$ is given by

$$Q(f) = Q_0 \cdot f^{\eta}. \tag{2.9}$$

For sites in ENA, $Q_0 = 670$ and $\eta = 1/3$ in Tables B-4 and B-7 of EPRI-1025287 are usually used.

Site effects $G(f)$ is given by

$$G(f) = A(f) \cdot D(f), \tag{2.10}$$

where $A(f)$ is amplification factor relative to source depth velocity conditions; in practice, amplification factors given in Table 2.1 are usually used (Table 4, Campbell, 2003). $D(f)$ accounts for the path-independent loss of high-frequency energy in ground motions and can be obtained by (EPRI-1025287)

$$D(f) = \mathrm{e}^{-\pi\kappa_0 f}, \tag{2.11}$$

where the diminution parameter $\kappa_0 = 0.006$ is used for sites in ENA. An alternative f_{max} filter (Boore, 2003),

$$D(f) = \left[1 + (f/f_{max})^8\right]^{-1/2}, \tag{2.12}$$

can be combined with (2.11), and $f_{max} = 50$ Hz may be used for sites in ENA.

Table 2.1 Site amplification factors from the ENA stochastic model.

Frequency f (Hz)	0.1	0.2	0.3	0.5	0.9	1.25	1.8	3.0	5.0	8.0	14.0	100
Amplification $A(f)$	1.02	1.03	1.05	1.07	1.09	1.11	1.12	1.13	1.14	1.15	1.15	1.15

Bazzurro and Cornell (2004) demonstrate that soil amplification is virtually independent of earthquake magnitude $\mathcal{M}$ except when frequencies f are less than initial resonant frequency f_{SC} of soil column. A sufficient depth is required to be taken so that $f_{\text{SC}} \leqslant 0.5$ Hz to ensure that site response has no influence on frequencies greater than 0.5 Hz (EPRI-1025287). Furthermore, sensitivity analysis also shows that the difference in the derived amplification functions for different earthquake magnitudes is minor. Hence, in practice, a representative earthquake magnitude is obtained from seismic hazard deaggregation (SHD) with a mean AEP of 1×10^{-4}. If the representative earthquake magnitude is very close to $\mathcal{M}6.5$, then $\mathcal{M}6.5$ is used; otherwise, the actual representative earthquake magnitude is used.

Given a pair of earthquake magnitude $\mathcal{M}$ and hypocenter distance R, and seismological parameters, FAS at reference hard rock can be obtained from equation (2.1).

2.1.2 Developing Acceleration Response Spectra

Having obtained FAS, Random Vibration Theory (RVT) is often employed to obtain Acceleration Response Spectra (ARS) (Kottke *et al.*, 2013).

Consider a single degree-of-freedom (SDOF) oscillator (with circular frequency ω_0 and damping ratio ζ_0) that is mounted on the reference hard rock and under the excitation of reference hard rock motion in terms of FAS $\mathcal{F}_{\text{A}}(M_0, R, \omega)$. The FAS of the absolute acceleration $\ddot{u}(t) = \ddot{x}(t) + \ddot{u}_{\text{HR}}(t)$ is

$$\left| \ddot{\mathcal{U}}(\omega) \right| = \omega_0^2 \left| \text{H}(\omega) \right| \mathcal{F}_{\text{A}}(M_0, R, \omega). \tag{2.13}$$

$\text{H}(\omega)$ is complex frequency response function with respect to base excitation of the SDOF oscillator given by

$$\text{H}(\omega) = \frac{1}{(\omega_0^2 - \omega^2) + \text{i}2\zeta_0\omega_0\omega}.$$

Applying the Parseval's theorem, the mean-square response of the absolute acceleration is

$$\begin{aligned}\ddot{u}_{\mathrm{RMS}}^2 &= \frac{1}{T_{\mathrm{RMS}}}\int_0^{T_{\mathrm{RMS}}} \ddot{u}^2(t)\,\mathrm{d}t = \frac{1}{T_{\mathrm{RMS}}}\cdot\frac{1}{2\pi}\int_0^{\infty} \omega_0^4 \left|\mathrm{H}(\omega)\right|^2 \mathcal{F}_{\mathrm{A}}^2(M_0,R,\omega)\,\mathrm{d}\omega \\ &= \frac{1}{T_{\mathrm{RMS}}}\int_0^{\infty} f_0^4 \left|\mathrm{H}(f)\right|^2 \mathcal{F}_{\mathrm{A}}^2(M_0,R,f)\,\mathrm{d}f, \end{aligned} \tag{2.14}$$

in which

$$\mathrm{H}(f) = \frac{1}{(f_0^2 - f^2) + \mathrm{i}2\zeta_0 f_0 f}.$$

By considering the responses of the oscillator and using results from time-domain numerical simulations, Boore and Joyner (1984) proposed to determine the root-mean-square duration T_{RMS} as

$$T_{\mathrm{RMS}} = T_{\mathrm{GM}} + T_{\mathrm{O}}\left(\frac{\kappa^n}{\kappa^n + \alpha}\right), \quad \kappa = \frac{T_{\mathrm{GM}}}{T_{\mathrm{O}}}, \tag{2.15}$$

where $T_{\mathrm{O}} = 1/(\omega_0\zeta_0)$ is the duration of the SDOF oscillator, and $T_{\mathrm{GM}} = T_{\mathrm{S}} + T_{\mathrm{P}}$ is the duration of ground motion. T_{RMS} approaches T_{GM} and $T_{\mathrm{GM}} + T_{\mathrm{O}}$, respectively, for small and large earthquakes. $T_{\mathrm{S}} = 1/f_{\mathrm{c}}$ is the source duration with f_{c} being the corner frequency obtained from equation (2.5). T_{P} is path duration given by, for sites in ENA (Atkinson and Boore, 2006),

$$T_{\mathrm{P}} = \begin{cases} 0, & R \leqslant 10, \\ 0.16\,(R-10), & 10 < R \leqslant 70, \\ 9.6 - 0.03\,(R-70), & 70 < R \leqslant 130, \\ 7.8 + 0.04\,(R-130), & R > 130. \end{cases} \tag{2.16}$$

In equation (2.15), the constants $n = 3$ and $\alpha = 1/3$ are used by Boore (2003). Liu and Pezeshk (1999) suggest that $n = 2$ and α is taken as

$$\alpha = \left[2\pi\left(1 - \frac{\lambda_1^2}{\lambda_0\lambda_2}\right)\right]^{1/2}, \tag{2.17}$$

where

$$\lambda_k = \int_0^{\infty} (2\pi f)^k f_0^4 \left|\mathrm{H}(f)\right|^2 \mathcal{F}_{\mathrm{A}}^2(M_0,R,f)\,\mathrm{d}f, \quad k = 0, 1, \ldots. \tag{2.18}$$

Having obtained the root-mean-square response $\ddot{u}_{\text{RMS}}$ from equation (2.14), peak acceleration response $|\ddot{u}|_{\max}$ or ARS can be determined through the peak factor $\mathcal{PF}$

$$\mathcal{S}_{\text{A}}(f_0) = |\ddot{u}|_{\max} \approx \mathcal{PF} \cdot \ddot{u}_{\text{RMS}}. \tag{2.19}$$

In Cartwright and Longuet-Higgins (1956) peak factor model, the expected $\mathcal{PF}$ is calculated by

$$\mathcal{PF} = \sqrt{2}\int_0^{+\infty} \left\{1 - \left[1 - \mathcal{A}\,\mathrm{e}^{-z^2}\right]^{N_{\text{E}}}\right\} \mathrm{d}z, \tag{2.20}$$

in which N_{E} is the number of extrema given as (Boore, 1983)

$$N_{\text{E}} = \frac{T_{\text{GM}}}{\pi}\sqrt{\frac{\lambda_4}{\lambda_2}}. \tag{2.21}$$

To cover the range of loading levels, a minimum of eleven expected (median) peak acceleration values at reference hard rock (usually taken at $f_0 = 100$ Hz) are needed to span from $0.01g$ to $1.50g$ (i.e., $0.01g$, $0.05g$, $0.10g$, $0.20g$, $0.30g$, $0.40g$, $0.50g$, $0.75g$, $1.00g$, $1.25g$, $1.50g$). Given the earthquake magnitude $\mathcal{M}$ and seismological parameters, changing the hypocenter distance R can result in the ARS with these eleven peak acceleration values.

2.1.3 Developing Input Ground Motions in Frequency Domain

When ARS is given in Section 2.1.2, input ground motions at reference hard rock can be determined in frequency-domain (Kottke *et al.*, 2013).

An Inverse Random Vibration Theory (IRVT) method is applied to convert ARS to FAS, which are used as the input ground motions at reference hard rock. The IRVT technique proposed by Gasparini and Vanmarcke (1976) and further developed by Rathje and Kottke (2008) gives the square of FAS at f_0 of an SDOF oscillator (with frequency f_0 and damping ratio ζ_0) as

$$\mathcal{F}_{\text{A}}^2(f_0) \approx \frac{1}{\displaystyle\int_0^{\infty} f_0^4 \left|\mathrm{H}(f)\right|^2 \mathrm{d}f - f_0}\left[\frac{T_{\text{RMS}}}{2}\cdot\frac{\mathcal{S}_{\text{A}}^2(f_0)}{\mathcal{PF}^2} - \int_0^{f_0}\left|\mathcal{F}_{\text{A}}(f)\right|^2 \mathrm{d}f\right], \tag{2.22}$$

in which $\mathcal{S}_{\text{A}}(f_0)$ is the target ARS obtained from equation (2.19). It can be shown that

$$\int_0^{\infty} f_0^4 \left|\mathrm{H}(f)\right|^2 \mathrm{d}f = f_0^4 \cdot \frac{\pi}{4\zeta_0 f_0^3} = \frac{\pi f_0}{4\zeta_0}. \tag{2.23}$$

Hence, equation (2.22) can be simplified as

$$\mathcal{F}_{\mathrm{A}}^2(f_0) \approx \frac{1}{f_0\left(\frac{\pi}{4\zeta_0}-1\right)}\left[\frac{T_{\mathrm{RMS}}}{2}\cdot\frac{\mathcal{S}_{\mathrm{A}}^2(f_0)}{\mathcal{PF}^2}-\int_0^{f_0}\mathcal{F}_{\mathrm{A}}^2(f)\,\mathrm{d}f\right]. \tag{2.24}$$

To solve for FAS, equation (2.24) is applied first to determine $\mathcal{F}(f_0)$ at a sufficient low frequency, e.g., $f_0=0.01$ Hz. At this low frequency, the integral in equation (2.24) is assumed to be zero. The peak factor $\mathcal{PF}$ is assumed to be a preset value, e.g., $\mathcal{PF}=2.5$. Having obtained $\mathcal{F}(f_0)$ at 0.01 Hz, FAS values at frequency $f_0^{(i)}$, $i\geqslant 1$, can be determined by

$$\mathcal{F}_{\mathrm{A}}^2\big(f_0^{(i)}\big) \approx \frac{1}{f_0^{(i)}\left(\frac{\pi}{4\zeta_0}-1\right)}\left\{\frac{T_{\mathrm{RMS}}}{2}\cdot\frac{\mathcal{S}_{\mathrm{A}}^2(f_0^{(i)})}{\mathcal{PF}^2}-\sum_{k=1}^{i}\mathcal{F}_{\mathrm{A}}^2\big(f_0^{(k-1)}\big)\cdot\big[f_0^{(k)}-f_0^{(k-1)}\big]\right\}. \tag{2.25}$$

The accuracy of the estimated FAS $\mathcal{F}_{\mathrm{A}}(f_0)$ is improved iteratively by comparing the ARS $\mathcal{S}_{\mathrm{A}}^{\mathrm{RVT}}(f_0)$ determined from the estimated FAS $\mathcal{F}_{\mathrm{A}}(f_0)$ using the IRVT technique and the target ARS $\mathcal{S}_{\mathrm{A}}(f_0)$:

1. Initial FAS $\mathcal{F}_{\mathrm{A}}\big(f_0^{(i)}\big)$, $i\geqslant 0$, is determined by equations (2.24) and (2.25).
2. Calculate the ARS $\mathcal{S}_{\mathrm{A}}^{\mathrm{RVT}}(f_0)$ associated with the initial FAS using the RVT presented in Section 2.1.2, i.e., equations (2.13) and (2.18).
3. Determine the correction factor by

$$\mathcal{C}(f_0)=\frac{\mathcal{S}_{\mathrm{A}}(f_0)}{\mathcal{S}_{\mathrm{A}}^{\mathrm{RVT}}(f_0)}. \tag{2.26}$$

   Multiplying the FAS by $\mathcal{C}(f_0)$ results in a new FAS.
4. Based on the new FAS, new peak factor $\mathcal{PF}$ can be obtained from equations (2.17) and (2.20); the new ARS $\mathcal{S}_{\mathrm{A}}^{\mathrm{RVT}}(f_0)$ is then determined using equations (2.13) and (2.18).
5. Steps 3 and 4 are repeated until one of following conditions is met:
   - a preset maximum number of iterations (e.g., 30) is reached;
   - the absolute error of root-mean-square response between $|\ddot{u}|_{\max}^{\mathrm{RVT}}$ corresponding to $\mathcal{S}_{\mathrm{A}}^{\mathrm{RVT}}(f_0)$, determined using equations (2.13), and $|\ddot{u}|_{\max}$ corresponding to $\mathcal{S}_{\mathrm{A}}(f_0)$ is less than a prespecified tolerance (e.g., 0.005);

- change in the error of root-mean-square response is less than a prespecified value (e.g., 0.001).

2.2 Addressing Local Site Effect

Given the input ground motion at bedrock, site response analysis is performed in frequency domain to evaluate the local site effect based on the equivalent-linear method given by Schnabel *et al*. (1972). The FAS at bedrock is multiplied by the transfer function to generate FAS at each layer. Then ARS can be obtained by 2.1.2. In site response analysis, the soil deposit is considered as a one-dimensional continuous model characterized by the layer thickness (H), density (ρ), shear wave velocity (V_s), shear modulus (G), and damping ratio (ζ). The nonlinear effect of shear modulus and damping ratio is taken into consideration by an equivalent linearization technique, i.e., an iteration process.

2.2.1 Transfer Function in Site Response Analysis

The displacement u in a single layer caused by bedrock motion with frequency ω can be expressed as

$$u(z,t) = [A\exp(\mathrm{i}kz) + B\exp(-\mathrm{i}kz)]\exp(\mathrm{i}\omega t), \tag{2.27}$$

where A and B represent the amplitudes of waves traveling upward and downward, respectively, z is the depth in the layer ranging from 0 to H, k is the wave number defined as

$$k = \frac{\omega}{{V_s}^*},$$

and ${V_s}^*$ is the complex shear wave velocity as

$${V_s}^* = V_s\sqrt{(1+2\zeta\,\mathrm{i})}.$$

According to equation (2.27), the shear stress can be obtained as

$$\tau(z,t) = G^*\frac{\partial u}{\partial z} = \mathrm{i}kG^*[A\exp(\mathrm{i}kz) - B\exp(-\mathrm{i}kz)]\exp(\mathrm{i}\omega t), \tag{2.28}$$

where G^* is the complex shear modulus calculated by

$$G^* = G(1+2\zeta\,\mathrm{i}).$$

Since the displacement and the shear stress are the same in two layers at their interface, one obtains

$$u_{i+1}(0,t) = u_i(H_i,t), \tag{2.29}$$

$$\tau_{i+1}(0,t) = \tau_i(H_i,t), \tag{2.30}$$

in which i represents the number of soil layers ranging from 1 to n, and n is total number of soil layers.

Based on equations (2.27) and (2.28), equations (2.29) and (2.30) can be rewritten as

$$A_{i+1} + B_{i+1} = A_i \exp(\mathrm{i}kH_i) + B_i \exp(-\mathrm{i}kH_i), \tag{2.31}$$

$$k_{i+1}G^*_{i+1}(A_{i+1} - B_{i+1}) = k_iG^*_i[A_i \exp(\mathrm{i}kH_i) - B_i \exp(-\mathrm{i}kH_i)]. \tag{2.32}$$

Solving equations (2.31) and (2.32) yields

$$A_{i+1} = \frac{A_i}{2}(1+\alpha_i)\exp(\mathrm{i}kH_i) + \frac{B_i}{2}(1-\alpha_i)\exp(-\mathrm{i}kH_i), \tag{2.33}$$

$$B_{i+1} = \frac{A_i}{2}(1-\alpha_i)\exp(\mathrm{i}kH_i) + \frac{B_i}{2}(1+\alpha_i)\exp(-\mathrm{i}kH_i), \tag{2.34}$$

where α is equal to

$$\alpha = \frac{k_iG^*_i}{k_{i+1}G^*_{i+1}}.$$

At the free surface, i.e., $i = 1$ and $z = 0$, the shear stress should be vanished. This leads to

$$\tau_1(0,t) = \mathrm{i}k_1G^*_1[A_1 - B_1]\exp(\mathrm{i}\omega t) = 0, \tag{2.35}$$

which results in $A_1 = B_1$.

By performing a recursive process on equations (2.33) and (2.34) and introducing $A_1 = B_1$, the amplitudes in the ith layer can be expressed as

$$A_i = a_i(\omega)A_1, \tag{2.36}$$

$$B_i = b_i(\omega)A_1. \tag{2.37}$$

Then transfer function from the top of jth layer to the top of ith layer is

$$H_{ij}(\omega) = \frac{u_i(0,t)}{u_j(0,t)} = \frac{(A_i + B_i)\exp(\mathrm{i}\omega t)}{(A_j + B_j)\exp(\mathrm{i}\omega t)} = \frac{a_i + b_i}{a_j + b_j}. \tag{2.38}$$

Particularly, the transfer function from the bedrock motion to the free surface is

$$H_{1n}(\omega) = \frac{u_1(0,t)}{u_n(0,t)} = \frac{(A_1 + B_1)\exp(\mathrm{i}\omega t)}{(A_n + B_n)\exp(\mathrm{i}\omega t)} = \frac{2}{a_n + b_n}. \tag{2.39}$$

If the bedrock is considered as a outcrop, i.e., bedrock is not influenced by the soil deposit, the amplitudes of the upward and downward waver are the same, which means $A_n = B_n$. The transfer function (2.39) becomes

$$H_{1n}(\omega) = \frac{1}{a_n}. \tag{2.40}$$

Finally, based on the input FAS and soil parameters, the FAS at any depth can be calculated by equations (2.36) to (2.40).

2.2.2 Treatment of Soil Nonlinearity

Under severe ground motions, the shear strain of soil is high, which leads to a nonlinear stress-strain behavior in soils. In this case, G and ζ vary with the shear strain of soil. For example, the curves showing nonlinear soil properties in EPRI TR-102293-V2 (EPRI, 1993B) are shown in Figure 2.1.

The soil nonlinearity is considered by an equivalent linear method in frequency domain. In this technique, G and ζ are assumed to be constant in the analysis. Initially, G and ζ are taken as low-strain values. Then the shear strain can be obtained as

$$\gamma(z,t) = \frac{\partial u}{\partial z} = \mathrm{i}k[A\exp(\mathrm{i}kz) - B\exp(-\mathrm{i}kz)]\exp(\mathrm{i}\omega t). \tag{2.41}$$

Based on the resultant strain, new G and ζ are obtained from the shear modulus and hysteretic damping curves. This process is performed repeatedly until G and ζ become stable, i.e., the difference of them in successive iterations is smaller than 1%.

As a result, the ground motion at free field and strain-compatible soil properties are determined.

2.3 Summary

In this chapter, the methodology of seismic site response analysis, including generation of input motions, the transfer function, and the treatment of nonlinearity in soil is presented. Some conclusions are obtained:

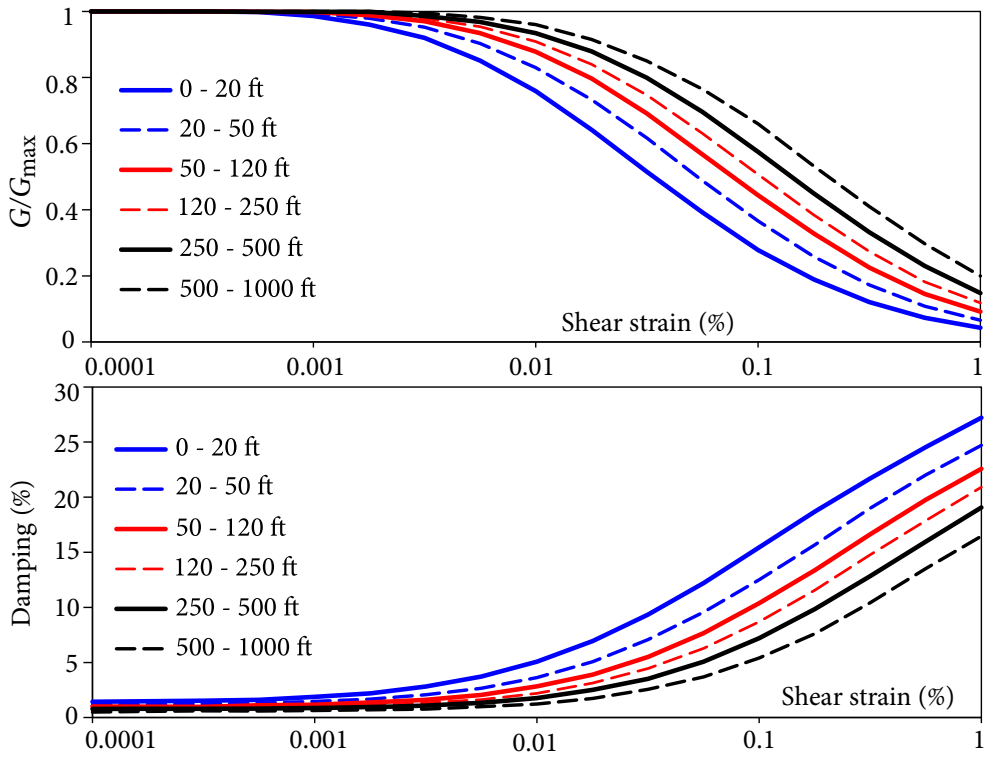

Figure 2.1 Shear modulus and hysteretic damping curves for cohesionless soil

- The ground motion is modified during the propagation from bedrock to free field.
- Due to the ground motion, the soil properties vary with the resultant soil strains.

Strain-compatible soil properties and the site-specific free filed motion are obtained, which are essential for the calculation of dynamic soil stiffness and the conduction SSI analysis.

CHAPTER 3

Soil-Structure Interaction Analysis with Rigid Foundation

Since the presence of structure in a soil deposit and the interaction between soil and structure, the dynamic response of a soil deposit is different from the free field and response of structure is different from that with fixed-base. The Floor Response Spectra (FRS) vary significantly compared to the fixed-base model (Jiang, 2016). A direct spectra-to-spectra method have recently developed by Jiang *et al*. (2015) for fixed-base structures. The effect of Soil-Structure Interaction (SSI) cannot be neglected for soil site. In this Chapter, the substructure method for Soil-Structure Interaction (SSI) analysis in Jiang *et al*. (2015) is reviewed, and extended to perform with frequency dependent soil stiffness. Foundation Level Input Response Spectra (FLIRS) is generated by combining SSI effect into free field motion, so that the direct spectra-to-spectra method for generating FRS can be applied for structures founded on soil.

Based on the modal information of structures, the structural response is obtained under the seismic input at the foundation for the fixed-base model. Then the equilibrium equations are established for structure nodes and the entire structure-foundation system, which makes it possible to get the structural response from the free field motion. By eliminating the structural response, a transfer function bridging the free field motion and fixed-base motion is determined. Finally, the modification factor from Foundation Input Response Spectra (FIRS) to FLIRS is calculated by random vibration theory.

3.1 Substructure Method

3.1.1 Substructure Model for Rigid Foundation

In many engineering applications, such as in nuclear power plants, the foundations can be assumed to be rigid. In this case, the free-field earthquake excitation is applied at only one node O on the foundation. The coupled soil-structure model is shown in Figure 3.1. Let $\mathbf{U}_s$ and $\mathbf{U}_O$ be amplitudes of the absolute displacement vectors of the superstructure and foundation, respectively, where the subscripts "s" and "O" stand for the degrees-of-freedom of "structure" and "base" (or boundary of soil-structure interface), respectively. The equation of of motion for the structure is expressed by

$$\begin{bmatrix} \mathbf{S}_{ss}^{s} & \mathbf{S}_{sO}^{s} \\ \mathbf{S}_{Os}^{s} & \mathbf{S}_{OO}^{s} \end{bmatrix} \begin{Bmatrix} \mathbf{U}_s \\ \mathbf{U}_O \end{Bmatrix} = \begin{Bmatrix} \mathbf{P}_s \\ \mathbf{P}_O \end{Bmatrix}, \tag{3.1}$$

where $\mathbf{P}_s$ is the amplitude vector of the load applied on the nodes of the structure, and $\mathbf{P}_O$ is the amplitude vector of the interaction forces between the structure and soil. For earthquake excitation, the nodes of the structure not in contact with the soil are not loaded, i.e., $\mathbf{P}_s = \mathbf{0}$, and hence

$$\mathbf{S}_{ss}^{s}\,\mathbf{U}_s + \mathbf{S}_{sO}^{s}\,\mathbf{U}_O = \mathbf{0}. \tag{3.2}$$

For the soil with excavation, let $\mathbf{S}_{OO}^{G}$ and $\mathbf{U}_O^{G}$ be the dynamic stiffness matrix and the amplitudes of absolute displacement vector under earthquake ground motion, respectively, where the subscript "g" stands for the soil with excavation. The interaction forces of the soil depend on the relative displacement between the foundation (base) and the soil at the interface, i.e.,

$$\mathbf{P}_O = \mathbf{S}_{OO}^{G}\,(\mathbf{U}_O - \mathbf{U}_O^{G}). \tag{3.3}$$

Then equation (3.1) becomes

$$\begin{bmatrix} \mathbf{S}_{ss}^{s} & \mathbf{S}_{sO}^{s} \\ \mathbf{S}_{Os}^{s} & \mathbf{S}_{OO}^{s} + \mathbf{S}_{OO}^{G} \end{bmatrix} \begin{Bmatrix} \mathbf{U}_s \\ \mathbf{U}_O \end{Bmatrix} = \begin{Bmatrix} \mathbf{0} \\ \mathbf{S}_{OO}^{G}\,\mathbf{U}_O^{G} \end{Bmatrix}. \tag{3.4}$$

In equation (3.4), the earthquake excitation is characterized by $\mathbf{U}_O^{G}$, which is the motion of the node on the soil-structure interface of the soil with excavation. It is desirable to replace $\mathbf{U}_O^{G}$ by the free-field motion $\mathbf{U}_O^{F}$ that does not depend on the excavation.

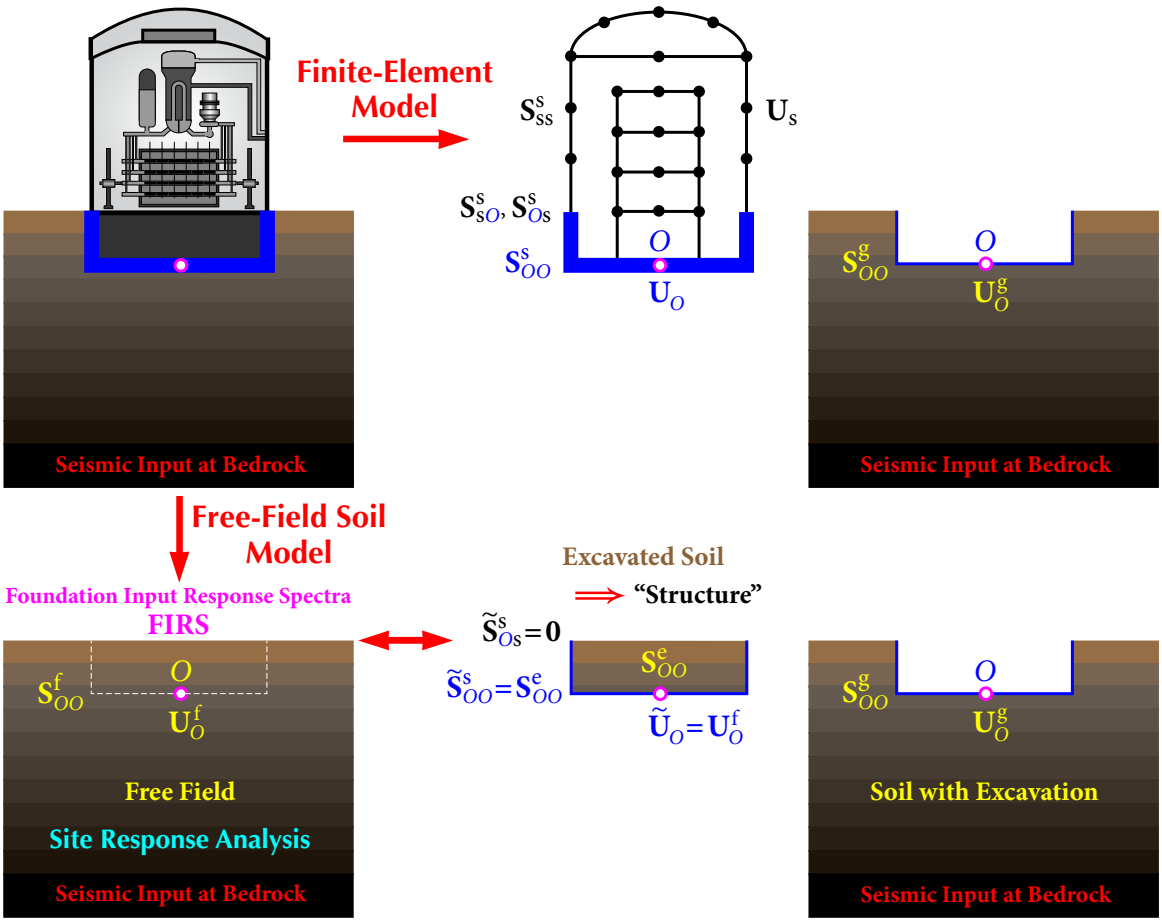

Figure 3.1 Coupled soil-structure model with rigid foundation

3.1.2 Free-Field Soil Model

The free-field soil can be divided into the excavated soil and the soil without excavation as shown in Figure 3.1. Regarding the excavated soil as a "structure", referring to the coupled soil-structure model and equation (3.4), one has $\tilde{\mathbf{U}}_O = \mathbf{U}^{\mathrm{F}}_O$, $\tilde{\mathbf{S}}_{\delta_s} = \mathbf{0}$, and hence $\tilde{\mathbf{S}}^s_{sO} = \mathbf{S}^{\mathrm{E}}_{OO}$, which is the dynamic stiffness matrix of the excavated soil; the subscript "e" stands for excavated soil. Hence, the second block-row of equation (3.4) gives

$$\begin{bmatrix} \tilde{\mathbf{S}}^{\delta}_{Os} & \tilde{\mathbf{S}}^s_{sO} + \mathbf{S}^{\mathrm{G}}_{OO} \end{bmatrix} \begin{Bmatrix} \times \\ \mathbf{U}^{\mathrm{F}}_O \end{Bmatrix} = \begin{Bmatrix} \mathbf{S}^{\mathrm{G}}_{OO} \mathbf{U}^{\mathrm{G}}_O \end{Bmatrix} \Longrightarrow (\mathbf{S}^{\mathrm{E}}_{OO} + \mathbf{S}^{\mathrm{G}}_{OO}) \mathbf{U}^{\mathrm{F}}_O = \mathbf{S}^{\mathrm{G}}_{OO} \mathbf{U}^{\mathrm{G}}_O . \tag{3.5}$$

Note that adding the excavated soil to the soil with excavation leads to the free-field system, i.e.,

$$\mathbf{S}^{\mathrm{G}}_{OO} + \mathbf{S}^{\mathrm{E}}_{OO} = \mathbf{S}^{\mathrm{F}}_{OO}, \quad \text{or} \quad \mathbf{S}^{\mathrm{G}}_{OO} = \mathbf{S}^{\mathrm{F}}_{OO} - \mathbf{S}^{\mathrm{E}}_{OO}. \tag{3.6}$$

Hence, equation (3.5) can be written as

$$\mathbf{S}^{\mathrm{F}}_{OO}\mathbf{U}^{\mathrm{F}}_{O} = \mathbf{S}^{\mathrm{G}}_{OO}\mathbf{U}^{\mathrm{G}}_{O}, \tag{3.7}$$

where $\mathbf{S}^{\mathrm{F}}_{OO}$ is the dynamic stiffness matrix of the free-field that is discretized at the nodes at which the structure is inserted, and $\mathbf{U}^{\mathrm{F}}_{O}$ is the free-field motion at the nodes of the soil-structure interface. Hence, $\mathbf{U}^{\mathrm{F}}_{O}$ is the free-field response of the soil at the foundation level; the acceleration response spectra of $\ddot{\mathbf{u}}^{\mathrm{F}}_{O}$ are the Foundation Input Response Spectra (FIRS), which can be obtain from a site response analysis of the free-field.

Using equation (3.7), equation (3.4) becomes

$$\begin{bmatrix} \mathbf{S}^{\mathrm{S}}_{\mathrm{ss}} & \mathbf{S}^{\mathrm{S}}_{\mathrm{s}O} \\ \mathbf{S}^{\mathrm{S}}_{O\mathrm{s}} & \mathbf{S}^{\mathrm{S}}_{OO} + \mathbf{S}^{\mathrm{G}}_{OO} \end{bmatrix} \begin{Bmatrix} \mathbf{U}_{\mathrm{s}} \\ \mathbf{U}_{O} \end{Bmatrix} = \begin{Bmatrix} \mathbf{0} \\ \mathbf{S}^{\mathrm{F}}_{OO}\mathbf{U}^{\mathrm{F}}_{O} \end{Bmatrix}. \tag{3.8}$$

Equation (3.8) is the equation of motion of the structure supported on a generalized spring characterized by the dynamic stiffness matrix $\mathbf{S}^{\mathrm{G}}_{OO}$, and the other end of the spring is subjected to earthquake excitation $\mathbf{U}^{\mathrm{F}}_{O}$, which is free-field response at the foundation level (node O as shown in Figure 3.2).

Using equation (3.6), equation (3.8) can also be written as

$$\begin{bmatrix} \mathbf{S}^{\mathrm{S}}_{\mathrm{ss}} & \mathbf{S}^{\mathrm{S}}_{\mathrm{s}O} \\ \mathbf{S}^{\mathrm{S}}_{O\mathrm{s}} & (\mathbf{S}^{\mathrm{S}}_{OO} - \mathbf{S}^{\mathrm{E}}_{OO}) + \mathbf{S}^{\mathrm{F}}_{OO} \end{bmatrix} \begin{Bmatrix} \mathbf{U}_{\mathrm{s}} \\ \mathbf{U}_{O} \end{Bmatrix} = \begin{Bmatrix} \mathbf{0} \\ \mathbf{S}^{\mathrm{F}}_{OO}\mathbf{U}^{\mathrm{F}}_{O} \end{Bmatrix}. \tag{3.9}$$

For a structure with N nodes (not including the rigid foundation), each node has 6 DOF (three translational and three rotational). The rigid foundation has one node O with 6 DOF. The dimensions of the vectors $\mathbf{U}_{\mathrm{s}}$, $\mathbf{U}_{O}$, and $\mathbf{U}^{\mathrm{F}}_{O}$ are $6N$, 6, and 6, respectively. The dimensions of the dynamic stiffness sub-matrices of the structure $\mathbf{S}^{\mathrm{S}}_{\mathrm{ss}}$, $\mathbf{S}^{\mathrm{S}}_{\mathrm{s}O}$, $\mathbf{S}^{\mathrm{S}}_{O\mathrm{s}}$, $\mathbf{S}^{\mathrm{S}}_{OO}$ are $6N\times6N$, $6N\times6$, $6\times6N$, and 6×6, respectively. The dimensions of the dynamic stiffness sub-matrices of the soil $\mathbf{S}^{\mathrm{F}}_{OO}$, $\mathbf{S}^{\mathrm{G}}_{OO}$, and $\mathbf{S}^{\mathrm{E}}_{OO}$ are all 6×6.

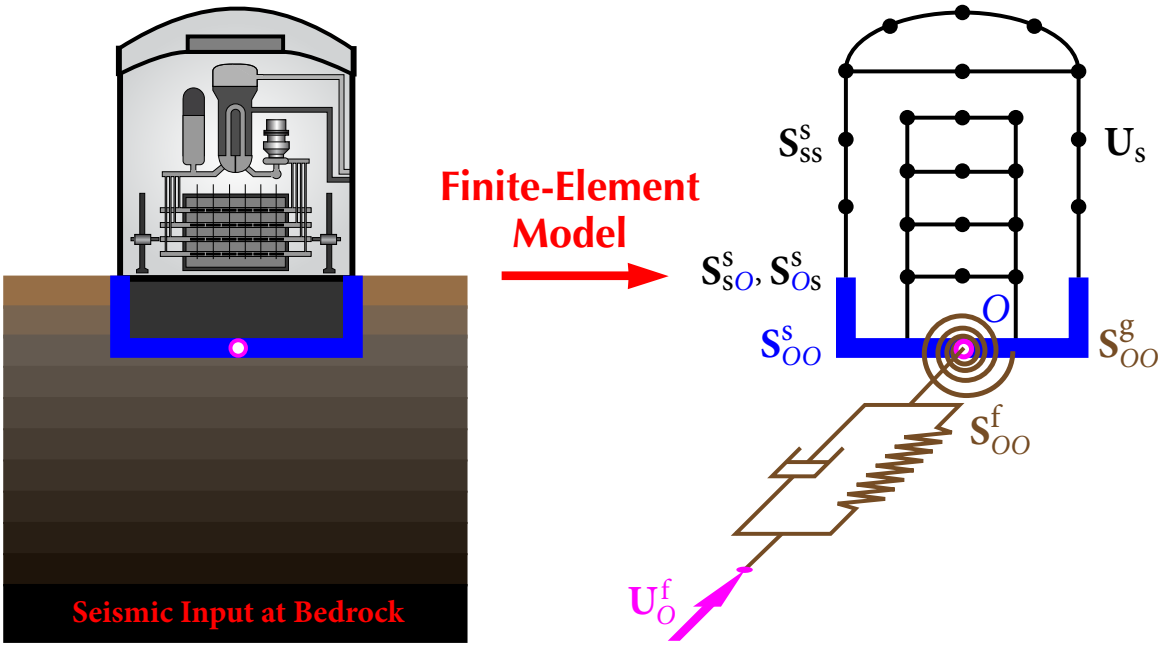

Figure 3.2 Soil-spring model of SSI with rigid foundation

3.1.3 Fixed-Base Model for Rigid Foundation

If the soil is firm enough so that the structure can be considered as fixed-base as shown in Figure 3.3, the motion of point O of the basemat is the earthquake input to the structure. From the first block-row of equation (3.8), one has

$$\mathbf{S}^{s}_{ss}\,\mathbf{U}_s + \mathbf{S}^{s}_{sO}\,\mathbf{U}_O = \mathbf{0} \quad \Longrightarrow \quad \mathbf{U}_s = \mathbf{S}^{FB}\,\mathbf{U}_O, \quad \mathbf{S}^{FB} = -\left(\mathbf{S}^{s}_{ss}\right)^{-1}\mathbf{S}^{s}_{sO}, \tag{3.10}$$

where $\mathbf{S}^{FB}$ is the dynamic stiffness matrix for fixed-base analysis, the superscript "FB" stands for fixed-base.

In seismic analysis, rotational ground motions are not considered and only translational ground motions are considered. Re-organize vector $\mathbf{U}_s$ and rewrite $\mathbf{U}_O$ as

$$\mathbf{U}_s = \begin{Bmatrix} \mathbf{U}_{s,T} \\ \mathbf{U}_{s,R} \end{Bmatrix}_{6N\times 1}, \qquad \mathbf{U}_O = \begin{Bmatrix} \mathbf{U}^{FB}_O \\ \mathbf{0} \end{Bmatrix}_{6\times 1}, \tag{3.11}$$

in which the subscripts "T" and "R" stand for translational and rotational degrees-of-

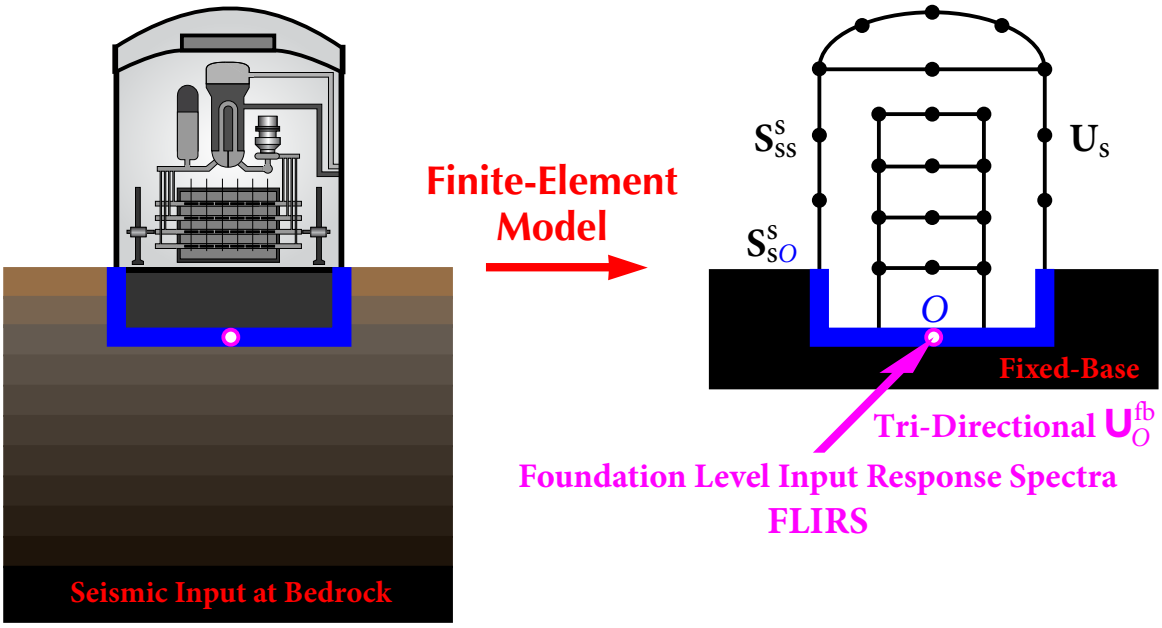

Figure 3.3 Fixed-base model with rigid foundation

freedom, respectively. Re-arrange and partition $\mathbf{S}^{\text{FB}}$ accordingly, one has

$$\mathbf{S}^{\text{FB}} = \begin{bmatrix} \mathbf{S}^{\text{FB}}_{\text{TT}} & \mathbf{S}^{\text{FB}}_{\text{TR}} \\ \mathbf{S}^{\text{FB}}_{\text{RT}} & \mathbf{S}^{\text{FB}}_{\text{RR}} \end{bmatrix}_{6N\times 6}, \tag{3.12}$$

in which each submatrix is of dimension $3N\times 3$. Equation (3.10) can be written as

$$\begin{Bmatrix} \mathbf{U}_{\text{s,T}} \\ \mathbf{U}_{\text{s,R}} \end{Bmatrix} = \begin{bmatrix} \mathbf{S}^{\text{FB}}_{\text{TT}} & \mathbf{S}^{\text{FB}}_{\text{TR}} \\ \mathbf{S}^{\text{FB}}_{\text{RT}} & \mathbf{S}^{\text{FB}}_{\text{RR}} \end{bmatrix} \begin{Bmatrix} \mathbf{U}^{\text{FB}}_O \\ \mathbf{0} \end{Bmatrix} = \begin{Bmatrix} \mathbf{S}^{\text{FB}}_{\text{TT}}\,\mathbf{U}^{\text{FB}}_O \\ \mathbf{S}^{\text{FB}}_{\text{RT}}\,\mathbf{U}^{\text{FB}}_O \end{Bmatrix}. \tag{3.13}$$

Multiplying the first block-row of equation (3.13) by $\left(\mathbf{S}^{\text{FB}}_{\text{TT}}\right)^T$ yields

$$\left(\mathbf{S}^{\text{FB}}_{\text{TT}}\right)^T \mathbf{U}_{\text{s,T}} = \left[\left(\mathbf{S}^{\text{FB}}_{\text{TT}}\right)^T \mathbf{S}^{\text{FB}}_{\text{TT}}\right] \mathbf{U}^{\text{FB}}_O. \tag{3.14}$$

The reason for performing this manipulation is to make $\left[\left(\mathbf{S}^{\text{FB}}_{\text{TT}}\right)^T \mathbf{S}^{\text{FB}}_{\text{TT}}\right]$ a square matrix of dimension 3×3, the purpose of which will be clear in Section 3.1.4.

The tri-directional (translational) acceleration response spectra $\mathbf{U}^{\text{FB}}_O$ applied at the foundation of a *fixed-base* structure are called Foundation Level Input Response Spectra (FLIRS), as shown in Figure 3.3. It is important to note that FLIRS are different from

Foundation Input Response Spectra (FIRS), which are the acceleration response spectra at the elevation of the foundation of the free-field, as illustrated in Figure 3.2.

The concept of FLIRS, which are the seismic input to fixed-base structures, is important in seismic design and assessment of nuclear power plants. Generic design of a nuclear power plant is based on fixed-base analysis under the tri-directional seismic excitations represented by standard GRS, such as those in CSA N289.3 or USNRC R.G. 1.60, anchored at a specific Peak Ground Acceleration (PGA). By comparing the site-specific FLIRS with the standard GRS, based on which the generic nuclear power plant is designed, initial feasibility of the generic design at the desired site can be assessed and Systems, Structures, and Components (SSCs) that may be vulnerable can be identified.

Since the dimension of the dynamic stiffness sub-matrix $\mathbf{S}_{ss}^{s}$ is $6N\times 6N$, the evaluation of its inverse in equation (3.10) could be numerically challenging when N is large. To take advantage of the modal properties of the structure, a modal analysis is conducted.

For a three-dimensional model of a structure with N nodes (not including rigid foundation), a typical node n has six DOF: three translational DOF $u_{n,1}$, $u_{n,2}$, $u_{n,3}$, and three rotational DOF $u_{n,4}$, $u_{n,5}$, $u_{n,6}$. The structure is subjected to tri-directional seismic excitations at the foundation. In nuclear industry, the structures are required to stay linear under any exactions. So the relative displacement vector x of dimension $6N$ is governed by (see, e.g., Jiang *et al.*, 2015)

$$\mathbf{M}\ddot{\mathbf{x}}(t) + \mathbf{C}\dot{\mathbf{x}}(t) + \mathbf{K}\mathbf{x}(t) = -\mathbf{M}\sum_{i=1}^{3} \boldsymbol{\mathcal{T}}^{i}\ddot{u}_{g}^{i}(t), \tag{3.15}$$

where

$$\mathbf{x} = \begin{Bmatrix} \mathbf{x}_1 \\ \mathbf{x}_2 \\ \vdots \\ \mathbf{x}_N \end{Bmatrix}, \quad \mathbf{x}_n = \begin{Bmatrix} x_{n,1} \\ x_{n,2} \\ \vdots \\ x_{n,6} \end{Bmatrix}, \quad \boldsymbol{\mathcal{T}}^{i} = \begin{Bmatrix} \mathbf{1}^{i} \\ \mathbf{1}^{i} \\ \vdots \\ \mathbf{1}^{i} \end{Bmatrix}, \quad \mathbf{1}^{i} = \begin{Bmatrix} \delta_{i1} \\ \delta_{i2} \\ \vdots \\ \delta_{i6} \end{Bmatrix}, \tag{3.16}$$

$\mathbf{M}$, $\mathbf{C}$, $\mathbf{K}$ are, respectively, the mass, damping, and stiffness matrices of dimension $6N\times 6N$, $\mathbf{x}_n$ is the relative displacement vector of node n, $\boldsymbol{\mathcal{T}}^{i}$ is the influence vector of the seismic excitation in direction i, and δ_{ij} denotes the Kronecker delta function.

When considering the rotational components of the excitations, equation (3.15) can be written as

$$\mathbf{M}\ddot{\mathbf{x}}(t) + \mathbf{C}\dot{\mathbf{x}}(t) + \mathbf{K}\mathbf{x}(t) = -\mathbf{M}\boldsymbol{\mathcal{I}}\ddot{\mathbf{u}}_O(t), \tag{3.17}$$

where node O is at the rigid foundation, and

$$\boldsymbol{\mathcal{I}} = \left[\, \boldsymbol{\mathcal{I}}^1 \;\; \boldsymbol{\mathcal{I}}^2 \;\; \boldsymbol{\mathcal{I}}^3 \;\; \boldsymbol{\mathcal{I}}^4 \;\; \boldsymbol{\mathcal{I}}^5 \;\; \boldsymbol{\mathcal{I}}^6 \,\right], \qquad \ddot{\mathbf{u}}_O(t) = \left\{ \ddot{u}_O^1(t),\, \ddot{u}_O^2(t),\, \ddot{u}_O^3(t),\, \ddot{\theta}_O^1(t),\, \ddot{\theta}_O^2(t),\, \ddot{\theta}_O^3(t) \right\}^T.$$

Here $\boldsymbol{\mathcal{I}}^i$ is defined in equation (3.16) for $i = 1, 2, 3$, and

$$\boldsymbol{\mathcal{I}}^4 = \begin{Bmatrix} \mathbf{r}_1^1 \\ \mathbf{r}_1^2 \\ \vdots \\ \mathbf{r}_1^N \end{Bmatrix}, \quad \boldsymbol{\mathcal{I}}^5 = \begin{Bmatrix} \mathbf{r}_2^1 \\ \mathbf{r}_2^2 \\ \vdots \\ \mathbf{r}_2^N \end{Bmatrix}, \quad \boldsymbol{\mathcal{I}}^6 = \begin{Bmatrix} \mathbf{r}_3^1 \\ \mathbf{r}_3^2 \\ \vdots \\ \mathbf{r}_3^N \end{Bmatrix},$$

$$\mathbf{r}_1^n = \begin{Bmatrix} 0 \\ -(\bar{z}_n - \bar{z}_O) \\ \bar{y}_n - \bar{y}_O \\ 1 \\ 0 \\ 0 \end{Bmatrix}, \quad \mathbf{r}_2^n = \begin{Bmatrix} \bar{z}_n - \bar{z}_O \\ 0 \\ -(\bar{x}_n - \bar{x}_O) \\ 0 \\ 1 \\ 0 \end{Bmatrix}, \quad \mathbf{r}_3^n = \begin{Bmatrix} -(\bar{y}_n - \bar{y}_O) \\ \bar{x}_n - \bar{x}_O \\ 0 \\ 0 \\ 0 \\ 1 \end{Bmatrix},$$

where $\bar{x}_n$, $\bar{y}_n$, and $\bar{z}_n$ are the coordinates of the nth node while $\bar{x}_O$, $\bar{y}_O$, and $\bar{z}_O$ represent the coordinates of Node O in a Cartesian coordinate system.

Letting $\mathbf{x}(t) = \mathbf{X}\mathrm{e}^{\mathrm{i}\omega t}$ and $\mathbf{u}_O(t) = \mathbf{U}_O\,\mathrm{e}^{\mathrm{i}\omega t}$, equations (3.17) becomes

$$(-\omega^2\mathbf{M} + \mathrm{i}\omega\mathbf{C} + \mathbf{K})\mathbf{X} = \omega^2\mathbf{M}\boldsymbol{\mathcal{I}}\,\mathbf{U}_O. \tag{3.18}$$

Substituting $\mathbf{X} = \boldsymbol{\Phi}\mathbf{Q}$ and multiplying $\boldsymbol{\Phi}^T$ from the left, where $\boldsymbol{\Phi}$ is the modal matrix, lead to

$$(-\omega^2\boldsymbol{\Phi}^T\mathbf{M}\boldsymbol{\Phi} + \mathrm{i}\omega\,\boldsymbol{\Phi}^T\mathbf{C}\boldsymbol{\Phi} + \boldsymbol{\Phi}^T\mathbf{K}\boldsymbol{\Phi})\,\mathbf{Q} = \omega^2\boldsymbol{\Phi}^T\mathbf{M}\boldsymbol{\mathcal{I}}\,\mathbf{U}_O. \tag{3.19}$$

If the modal shapes are normalized such that $\boldsymbol{\Phi}^T\mathbf{M}\boldsymbol{\Phi} = \mathbf{I}$, applying the orthogonality yields

$$\mathrm{diag}\left\{-\omega^2 + \mathrm{i}2\zeta_n\omega_n\omega + \omega_n^2\right\}\mathbf{Q} = \omega^2\boldsymbol{\Gamma}\,\mathbf{U}_O, \tag{3.20}$$

where $\mathbf{\Gamma} = \mathbf{\Phi}^T \mathbf{M} \boldsymbol{\mathcal{I}}$ is a $6N \times 6$ matrix of the modal contribution factors. Hence,

$$\mathbf{X} = \omega^2 \mathbf{\Phi} \mathbf{H} \mathbf{\Gamma} \mathbf{U}_O, \tag{3.21}$$

where $\mathbf{H}$ is a a diagonal matrix of the complex frequency response functions, i.e.,

$$\mathbf{H} = \text{diag} \left\{ \frac{1}{\omega_n^2 - \omega^2 + \text{i} 2\zeta_n \omega_n \omega} \right\}.$$

Since the relative displacement $\mathbf{x} = \mathbf{u} - \boldsymbol{\mathcal{I}} \mathbf{u}_O$, substituting into equation (3.21) gives

$$\mathbf{U} = (\omega^2 \mathbf{\Phi} \mathbf{H} \mathbf{\Gamma} + \boldsymbol{\mathcal{I}}) \mathbf{U}_O. \tag{3.22}$$

Comparing equation (3.22) with equations (3.10), one obtains

$$\mathbf{S}^{\text{FB}} = \omega^2 \mathbf{\Phi} \mathbf{H} \mathbf{\Gamma} + \boldsymbol{\mathcal{I}}. \tag{3.23}$$

Based on Newton's second law, the dynamic force equilibrium of the structure-foundation system in Direction 1, as illustrated in Figure 3.3, is given by

$$-\omega^2 \left[(\boldsymbol{\mathcal{I}}^1)^T \mathbf{M} \mathbf{U} + m_{O,1} U_{O,1} \right] = F_{O,1}, \tag{3.24}$$

and the the dynamic moment equilibrium of the structure-foundation system in Direction 5 is given by

$$-\omega^2 \left[(\boldsymbol{\mathcal{I}}^5)^T \mathbf{M} \mathbf{U} + m_{O,5} U_{O,5} \right] = M_{O,5}. \tag{3.25}$$

The dynamic equilibrium in other directions can be derived similarly. Therefore, the dynamic equilibrium of the entire system is

$$-\omega^2 (\boldsymbol{\mathcal{I}}^T \mathbf{M} \mathbf{U} + \mathbf{M}_O \mathbf{U}_O) = \mathbf{F}_O, \tag{3.26}$$

where $\mathbf{M}_O$ is a 6×6 mass matrix of the foundation, and $\mathbf{F}_O$ denotes the vector of SSI forces acting on the foundation, which is equal to $\mathbf{S}_{OO}^{\text{F}} (\mathbf{U}_O^{\text{F}} - \mathbf{U}_O)$ according to equation (3.7).

Hence, equation (3.26) can be rewritten as

$$-\omega^2 \boldsymbol{\mathcal{I}}^T \mathbf{M} \mathbf{U} + \left(-\omega^2 \mathbf{M}_O + \mathbf{S}_{OO}^{\text{F}} \right) \mathbf{U}_O = \mathbf{S}_{OO}^{\text{F}} \mathbf{U}_O^{\text{F}}. \tag{3.27}$$

Comparing with the second block-row of equation (3.9), a structure founded on the ground surface implies $\mathbf{S}_{OO}^{\text{E}} = \mathbf{0}$; hence

$$\mathbf{S}_{\text{Os}}^{\text{S}} = -\omega^2 \boldsymbol{\mathcal{I}}^T \mathbf{M}, \qquad \mathbf{S}_{OO}^{\text{S}} = -\omega^2 \mathbf{M}_O. \tag{3.28}$$

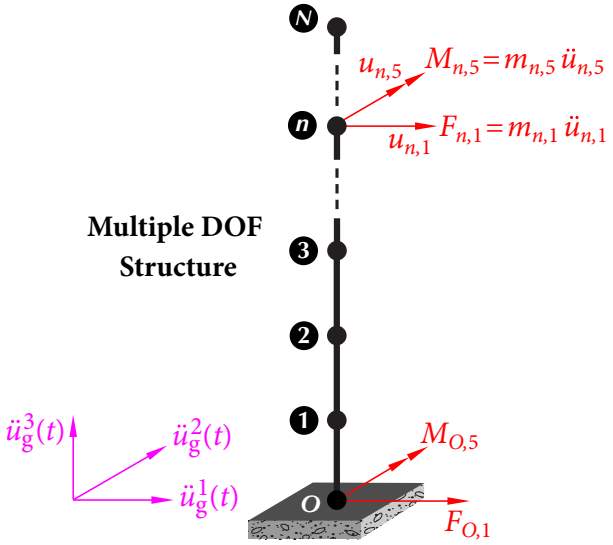

Figure 3.4 Dynamic equilibrium of structure-foundation system

3.1.4 Foundation Level Input Response Spectra (FLIRS)

As discussed in Section 3.1.3, it is desirable to determine the equivalent FLIRS for the structure with rigid foundation in seismic design and assessment. In SSI analysis, a fixed-base analysis can be performed using the equivalent FLIRS as the seismic input, instead of a coupled soil-structure analysis using FIRS as the seismic input.

From the first block-row of equation (3.9), one obtains

$$\mathbf{U}_s = -\left(\mathbf{S}_{ss}^{S}\right)^{-1}\mathbf{S}_{sO}^{S}\mathbf{U}_O = \mathbf{S}^{FB}\mathbf{U}_O. \tag{3.29}$$

From the second block-row of equation (3.9), one has

$$\mathbf{S}_{Os}^{S}\mathbf{U}_s + \left[\left(\mathbf{S}_{OO}^{S} - \mathbf{S}_{OO}^{E}\right) + \mathbf{S}_{OO}^{F}\right]\mathbf{U}_O = \mathbf{S}_{OO}^{F}\mathbf{U}_O^{F}. \tag{3.30}$$

Substituting equation (3.29) into (3.30) yields

$$\mathbf{S}_{Os}^{S}\mathbf{S}^{FB}\mathbf{U}_O + \left[\left(\mathbf{S}_{OO}^{S} - \mathbf{S}_{OO}^{E}\right) + \mathbf{S}_{OO}^{F}\right]\mathbf{U}_O = \mathbf{S}_{OO}^{F}\mathbf{U}_O^{F},$$

which gives

$$\underbrace{\mathbf{U}_O}_{6\times1} = \underbrace{\mathbf{S}^{-1}}_{6\times6}\,\underbrace{\mathbf{S}_{OO}^{F}}_{6\times6}\,\underbrace{\mathbf{U}_O^{F}}_{6\times1}, \tag{3.31}$$

$$\mathbf{S} = \underbrace{\mathbf{S}_{Os}^{S}}_{6\times6N}\,\underbrace{\mathbf{S}^{FB}}_{6N\times6} + \underbrace{\left(\mathbf{S}_{OO}^{S} - \mathbf{S}_{OO}^{E}\right) + \mathbf{S}_{OO}^{F}}_{6\times6}. \tag{3.32}$$

Note that $\mathbf{S}^{-1}\mathbf{S}^{\mathrm{F}}_{OO}$ is a square matrix of dimension 6×6; partition it as follows:

$$\mathbf{S}^{-1}\mathbf{S}^{\mathrm{F}}_{OO} = \mathbf{T} = \begin{bmatrix} \mathbf{T}_{\mathrm{TT}} & \mathbf{T}_{\mathrm{TR}} \\ \mathbf{T}_{\mathrm{RT}} & \mathbf{T}_{\mathrm{RR}} \end{bmatrix}_{6\times 6}, \tag{3.33}$$

in which each submatrix is of dimension 3×3.

Substituting equation (3.28) into equation (3.33)

$$\mathbf{S} = -\omega^2\left(\boldsymbol{\mathcal{I}}^T\mathbf{M}\mathbf{S}^{\mathrm{FB}} + \mathbf{M}_O\right) + \mathbf{S}^{\mathrm{F}}_{OO}. \tag{3.34}$$

Since the earthquake influence matrix $\boldsymbol{\mathcal{I}}$ and the fixed-base model structural response transfer matrix $\mathbf{S}^{\mathrm{FB}}$ are dimensionless, and $\mathbf{S}^{\mathrm{F}}_{OO}$ denotes the dynamic stiffness of the soil springs, equation (3.34) can be expressed in terms of a standard dynamic stiffness matrix as

$$\mathbf{S} = -\omega^2\tilde{\mathbf{M}} + \mathrm{i}\omega\mathbf{C}^{\mathrm{f}} + \mathbf{K}^{\mathrm{f}}, \tag{3.35}$$

where $\tilde{\mathbf{M}} = \boldsymbol{\mathcal{I}}^T\mathbf{M}\mathbf{S}^{\mathrm{FB}} + \mathbf{M}_O$ is a 6×6 mass matrix which is determined by the structure and foundation mass matrices, influence matrix, and the fixed-base structure transfer matrix $\mathbf{S}^{\mathrm{FB}}$; $\mathbf{K}^{\mathrm{f}}$ and $\mathbf{C}^{\mathrm{f}}$ are the stiffness and damping matrices of soil springs, respectively. Therefore, the problem can be interpreted as a synthesized 6-DOF mass, which is frequency-dependent, supported by generalized soil springs.

In a site response analysis, the soil medium is modelled as a half-space, and the rational responses of free-field should be very small under the translational excitation at bedrock. Hence, the rotational input at foundation level is negligible compared to the translational input; the rotational input is usually not given by a site response analysis and is taken as 0.

From equations (3.29) and (3.32), one has $\mathbf{U}_{\mathrm{s}} = \mathbf{S}^{\mathrm{FB}}\mathbf{T}\mathbf{U}^{\mathrm{F}}_{O}$, i.e.,

$$\begin{aligned} \begin{Bmatrix} \mathbf{U}_{\mathrm{s,T}} \\ \mathbf{U}_{\mathrm{s,R}} \end{Bmatrix}_{6N\times 1} &= \begin{bmatrix} \mathbf{S}^{\mathrm{FB}}_{\mathrm{TT}} & \mathbf{S}^{\mathrm{FB}}_{\mathrm{TR}} \\ \mathbf{S}^{\mathrm{FB}}_{\mathrm{RT}} & \mathbf{S}^{\mathrm{FB}}_{\mathrm{RR}} \end{bmatrix}_{6N\times 6} \begin{bmatrix} \mathbf{T}_{\mathrm{TT}} & \mathbf{T}_{\mathrm{TR}} \\ \mathbf{T}_{\mathrm{RT}} & \mathbf{T}_{\mathrm{RR}} \end{bmatrix}_{6\times 6} \begin{Bmatrix} \mathbf{U}^{\mathrm{F}}_{O,\mathrm{T}} \\ \mathbf{0} \end{Bmatrix}_{6\times 1} \\ &= \begin{bmatrix} \mathbf{S}^{\mathrm{FB}}_{\mathrm{TT}} & \mathbf{S}^{\mathrm{FB}}_{\mathrm{TR}} \\ \mathbf{S}^{\mathrm{FB}}_{\mathrm{RT}} & \mathbf{S}^{\mathrm{FB}}_{\mathrm{RR}} \end{bmatrix} \begin{bmatrix} \mathbf{T}_{\mathrm{TT}}\mathbf{U}^{\mathrm{F}}_{O,\mathrm{T}} \\ \mathbf{T}_{\mathrm{RT}}\mathbf{U}^{\mathrm{F}}_{O,\mathrm{T}} \end{bmatrix} = \begin{Bmatrix} \mathbf{S}^{\mathrm{FB}}_{\mathrm{TT}}\mathbf{T}_{\mathrm{TT}}\mathbf{U}^{\mathrm{F}}_{O,\mathrm{T}} + \mathbf{S}^{\mathrm{FB}}_{\mathrm{TR}}\mathbf{T}_{\mathrm{RT}}\mathbf{U}^{\mathrm{F}}_{O,\mathrm{T}} \\ \mathbf{S}^{\mathrm{FB}}_{\mathrm{RT}}\mathbf{T}_{\mathrm{TT}}\mathbf{U}^{\mathrm{F}}_{O,\mathrm{T}} + \mathbf{S}^{\mathrm{FB}}_{\mathrm{RR}}\mathbf{T}_{\mathrm{RT}}\mathbf{U}^{\mathrm{F}}_{O,\mathrm{T}} \end{Bmatrix}. \end{aligned} \tag{3.36}$$

Note that it is not possible to have a single set of tri-directional translational FLIRS in a fixed base analysis to give both correct translational responses $\mathbf{U}_{\mathrm{s,T}}$ and rotational responses

$\mathbf{U}_{s,R}$. In the generation of floor response spectra (FRS), only translational responses are needed. Hence, from the first block-row of equation (3.36), one has

$$\mathbf{U}_{s,T} = \mathbf{S}_{TT}^{FB}\,\mathbf{T}_{TT}\,\mathbf{U}_{O,T}^{F} + \mathbf{S}_{TR}^{FB}\,\mathbf{T}_{RT}\,\mathbf{U}_{O,T}^{F}. \tag{3.37}$$

Multiplying $\left(\mathbf{S}_{TT}^{FB}\right)^T$ from the left yields

$$\begin{aligned}\left(\mathbf{S}_{TT}^{FB}\right)^T\mathbf{U}_{s,T} &= \left\{\left(\mathbf{S}_{TT}^{FB}\right)^T\mathbf{S}_{TT}^{FB}\,\mathbf{T}_{TT} + \left(\mathbf{S}_{TT}^{FB}\right)^T\mathbf{S}_{TR}^{FB}\,\mathbf{T}_{RT}\right\}\mathbf{U}_{O,T}^{F}\\ &= \left[\left(\mathbf{S}_{TT}^{FB}\right)^T\mathbf{S}_{TT}^{FB}\right]\left\{\mathbf{T}_{TT} + \left[\left(\mathbf{S}_{TT}^{FB}\right)^T\mathbf{S}_{TT}^{FB}\right]^{-1}\left(\mathbf{S}_{TT}^{FB}\right)^T\mathbf{S}_{TR}^{FB}\,\mathbf{T}_{RT}\right\}\mathbf{U}_{O,T}^{F}.\end{aligned} \tag{3.38}$$

Since $\left[\left(\mathbf{S}_{TT}^{FB}\right)^T\mathbf{S}_{TT}^{FB}\right]$ is a square matrix of dimension 3×3, it is straightforward to determine its inverse. Comparing equation (3.38) with equation (3.14), one obtains the equivalent FLIRS as

$$\mathbf{U}_{O}^{FB} = \boldsymbol{\mathcal{T}}\,\mathbf{U}_{O,T}^{F}, \tag{3.39}$$

where $\boldsymbol{\mathcal{T}}$ is a complex transfer matrix from FIRS (generated by $\mathbf{U}_{O,T}^{F}$) to FLIRS (generated by $\mathbf{U}_{O}^{FB}$), given as

$$\underbrace{\boldsymbol{\mathcal{T}}}_{3\times3} = \underbrace{\mathbf{T}_{TT}}_{3\times3} + \underbrace{\left[\left(\mathbf{S}_{TT}^{FB}\right)^T\mathbf{S}_{TT}^{FB}\right]^{-1}}_{3\times3}\underbrace{\left(\mathbf{S}_{TT}^{FB}\right)^T}_{3\times3N}\underbrace{\mathbf{S}_{TR}^{FB}}_{3N\times3}\underbrace{\mathbf{T}_{RT}}_{3\times3}. \tag{3.40}$$

The first and second terms of $\boldsymbol{\mathcal{T}}$ denote the contributions from the translational and rotational motions of the foundation in the soil-structure system, respectively.

It is important to emphasize that, although the FLIRS given by equation (3.39) would not give correct rotational responses $\mathbf{U}_{s,R}$ of a structure, it gives exact translation responses FRS because only translational responses are required to generate FRS. Therefore, the fixed-base analysis of the structure under the excitation of FLIRS $\mathbf{U}_{O}^{FB}$ given by equation (3.39) gives exactly the same FRS as a full coupled soil-structure analysis under the excitation of FIRS $\mathbf{U}_{O,T}^{F}$.

Based on the theory of random vibration, the relation between the power spectral density functions of $\mathbf{U}_{O}^{FB}$ and $\mathbf{U}_{O,T}^{F}$ can be determined by

$$\boldsymbol{S}_{\ddot{U}\ddot{U}}^{fb}(\omega) = \left[\left|\boldsymbol{\mathcal{T}}(\omega)\right|^2\right]\boldsymbol{S}_{\ddot{U}\ddot{U}}^{f}(\omega), \tag{3.41}$$

where $\boldsymbol{S}^{\mathrm{fb}}_{\ddot{U}\ddot{U}}(\omega)$ and $\boldsymbol{S}^{\mathrm{f}}_{\ddot{U}\ddot{U}}(\omega)$ are the 3×1 vectors of the power spectral density functions of $\mathbf{U}^{\mathrm{FB}}_{O}$ and $\mathbf{U}^{\mathrm{F}}_{O,\mathrm{T}}$, respectively. In equation (3.41), $\left[\left|\boldsymbol{\mathcal{T}}(\omega)\right|^2\right]$ denotes a matrix in which each element is equal to the squared modulus of the corresponding element in $\boldsymbol{\mathcal{T}}$. For a complex number $a+\mathrm{i}b$, its modulus is defined as $\left|a+\mathrm{i}b\right|=\sqrt{a^2+b^2}$. It is found that, for structures in nuclear power plants, the off-diagonal terms of $\boldsymbol{\mathcal{T}}$ are relatively small compared to the diagonal terms, and thus may be neglected. It means that the motion of the foundation in one direction is only induced by the excitations in the same direction.

It is known that the mean square response of a SDOF oscillator under a base excitation $\mathbf{U}^{\mathrm{F}}_{O,\mathrm{T}}$ can be obtained by

$$\mathrm{E}\left[\ddot{\mathrm{X}}^2_0(t)\right]=\int_{-\infty}^{\infty}\left|\omega_0^2 H_0(\omega)\right|^2\boldsymbol{S}^{\mathrm{f}}_{\ddot{U}\ddot{U}}(\omega)\,\mathrm{d}\omega\,, \tag{3.42}$$

in which $H_0(\omega)$ is the complex frequency response function characterized by the circular frequency ω_0 and damping ratio ζ_0 of the SDOF oscillator. For excitations with wide-band power spectral densities, $\boldsymbol{S}^{\mathrm{f}}_{\ddot{U}\ddot{U}}(\omega)$ can be approximated by constant $\boldsymbol{S}^{\mathrm{f}}_{\ddot{U}\ddot{U}}$. From equations (3.41) and (3.42), the ratios between the mean square responses of a SDOF oscillator under base excitation $\mathbf{U}^{\mathrm{FB}}_{O}$ and those under base excitation $\mathbf{U}^{\mathrm{F}}_{O,\mathrm{T}}$ can be calculated by

$$\boldsymbol{\mathcal{R}}^2(\omega_0,\zeta_0)=\frac{\displaystyle\int_{-\infty}^{\infty}\left|\omega_0^2 H_0(\omega)\right|^2\left[\left|\boldsymbol{\mathcal{T}}(\omega)\right|^2\right]\boldsymbol{S}^{\mathrm{f}}_{\ddot{U}\ddot{U}}(\omega)\,\mathrm{d}\omega}{\displaystyle\int_{-\infty}^{\infty}\left|\omega_0^2 H_0(\omega)\right|^2\boldsymbol{S}^{\mathrm{f}}_{\ddot{U}\ddot{U}}(\omega)\,\mathrm{d}\omega}=\frac{\displaystyle\int_{-\infty}^{\infty}\left|H_0(\omega)\right|^2\left[\left|\boldsymbol{\mathcal{T}}(\omega)\right|^2\right]\mathbf{1}\,\mathrm{d}\omega}{\displaystyle\int_{-\infty}^{\infty}\left|H_0(\omega)\right|^2\,\mathrm{d}\omega}, \tag{3.43}$$

The maximum response of a SDOF oscillator, which is by definition the response spectrum, is usually related to its root mean square response through a peak factor as

$$\mathcal{S}_{\mathrm{A}}(\omega_0,\zeta_0)=\left|X_0(t)\right|_{\max}=\mathcal{P}\cdot\sqrt{\mathrm{E}\left[X_0^2(t)\right]}. \tag{3.44}$$

Combining equations (3.43) and (3.44) yields the tri-directional fixed-base FLIRS

$$\boldsymbol{\mathcal{S}}^{\mathrm{fb}}_{\mathrm{A}}(\omega_0,\zeta_0)=\frac{\mathcal{P}^{\mathrm{fb}}}{\mathcal{P}^{\mathrm{f}}}\cdot\boldsymbol{\mathcal{R}}(\omega_0,\zeta_0)\,\boldsymbol{\mathcal{S}}^{\mathrm{f}}_{\mathrm{A}}(\omega_0,\zeta_0). \tag{3.45}$$

For responses in earthquake engineering, the values of peak factors $\mathcal{P}^{\mathrm{fb}}$ and $\mathcal{P}^{\mathrm{f}}$ are not different significantly; they are often assigned the numerical value 3. Hence

$$\boldsymbol{\mathcal{S}}^{\mathrm{fb}}_{\mathrm{A}}(\omega_0,\zeta_0)=\boldsymbol{\mathcal{R}}(\omega_0,\zeta_0)\,\boldsymbol{\mathcal{S}}^{\mathrm{f}}_{\mathrm{A}}(\omega_0,\zeta_0), \tag{3.46}$$

in which $\mathcal{R}(\omega_0, \zeta_0)$ can be interpreted as response spectrum modification factors from FIRS to FLIRS.

3.1.5 Generating FRS Considering SSI

For a structure in a nuclear power plant with its rigid foundation embedded in layered soil, a procedure for generating FRS considering SSI is illustrated in Figure 3.5 and is summarized as follows:

1. Consider the layered soil as a free-field. With seismic input applied at the bedrock, a site response analysis is performed to obtain the Foundation Input Response Spectra (FIRS) $\mathbf{U}_O^{\mathrm{F}}$ or $\mathbf{U}_{O,\mathrm{T}}^{\mathrm{F}}$ at the elevation of the foundation.
2. Establish a model of the layered soil. Determined the dynamic stiffness matrices of the excavated soil $\mathbf{S}_{OO}^{\mathrm{E}}$ and the soil with excavation $\mathbf{S}_{OO}^{\mathrm{G}}$. The dynamic stiffness matrix of the free-field is $\mathbf{S}_{OO}^{\mathrm{F}} = \mathbf{S}_{OO}^{\mathrm{G}} + \mathbf{S}_{OO}^{\mathrm{E}}$.
3. Set up a finite element model of the structure. Determine the dynamic stiffness matrices $\mathbf{S}_{\mathrm{ss}}^{\mathrm{s}}$, $\mathbf{S}_{\mathrm{ss}}^{\mathrm{s}}$, $\mathbf{S}_{\mathrm{s}O}^{\mathrm{s}}$, $\mathbf{S}_{O\mathrm{s}}^{\mathrm{s}}$, and $\mathbf{S}_{OO}^{\mathrm{s}}$. Perform a modal analysis to obtain the modal frequencies ω_n, modal damping coefficients ζ_n, modal matrix $\mathbf{\Phi}$, and matrix of modal contribution factors $\mathbf{\Gamma}$.
4. Determine the Foundation Level Input Response Spectra (FLIRS):

   - $\mathbf{S}^{\mathrm{FB}} = \omega^2 \mathbf{\Phi} \mathbf{H} \mathbf{\Gamma} + \mathcal{I} = \begin{bmatrix} \mathbf{S}_{\mathrm{TT}}^{\mathrm{FB}} & \mathbf{S}_{\mathrm{TR}}^{\mathrm{FB}} \\ \mathbf{S}_{\mathrm{RT}}^{\mathrm{FB}} & \mathbf{S}_{\mathrm{RR}}^{\mathrm{FB}} \end{bmatrix}_{6N \times 6}$

     $\mathbf{H} = \mathrm{diag}\left\{ \dfrac{1}{\omega_n^2 - \omega^2 + \mathrm{i}2\zeta_n \omega_n \omega} \right\}_{6N \times 6N}$

     $\mathbf{\Gamma} = \mathbf{\Phi}^T \mathbf{M} \mathcal{I}$ is a $6N \times 6$ matrix of the modal contribution factors.

     $\mathcal{I} = \left[\mathcal{I}^1 \;\; \mathcal{I}^2 \;\; \mathcal{I}^3 \;\; \mathcal{I}^4 \;\; \mathcal{I}^5 \;\; \mathcal{I}^6 \right]_{6N \times 6}$

   - $\mathbf{S} = \mathbf{S}_{O\mathrm{s}}^{\mathrm{s}} \mathbf{S}^{\mathrm{FB}} + \left(\mathbf{S}_{OO}^{\mathrm{s}} - \mathbf{S}_{OO}^{\mathrm{E}} \right) + \mathbf{S}_{OO}^{\mathrm{F}}$

     Determine the inverse $\mathbf{S}^{-1}$. The dimension is 6×6.

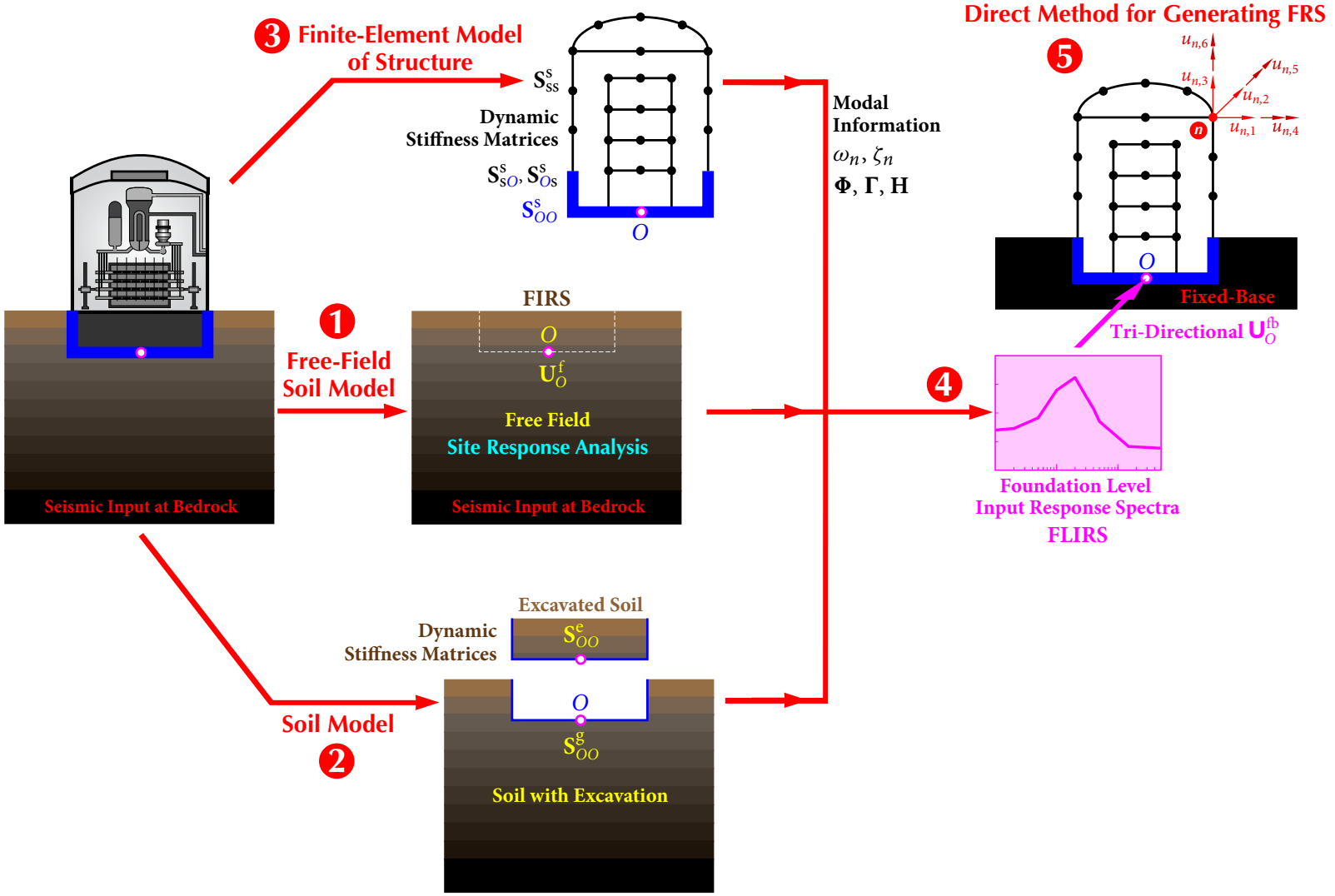

Figure 3.5 Procedure for generating FRS considering SSI

- $\begin{bmatrix} \mathbf{T}_{TT} & \mathbf{T}_{TR} \\ \mathbf{T}_{RT} & \mathbf{T}_{RR} \end{bmatrix}_{6\times 6} = \mathbf{S}^{-1}\mathbf{S}^{\mathrm{F}}_{OO}$
- Transfer matrix: $\boldsymbol{\mathcal{T}} = \mathbf{T}_{TT} + \left[\left(\mathbf{S}^{\mathrm{FB}}_{TT}\right)^T \mathbf{S}^{\mathrm{FB}}_{TT}\right]^{-1}\left(\mathbf{S}^{\mathrm{FB}}_{TT}\right)^T \mathbf{S}^{\mathrm{FB}}_{TR}\,\mathbf{T}_{RT}$
- FLIRS modification factor: $\boldsymbol{\mathcal{R}}^2(\omega_0,\zeta_0) = \dfrac{\displaystyle\int_{-\infty}^{\infty} \left|H_0(\omega)\right|^2 \left[\left|\boldsymbol{\mathcal{T}}(\omega)\right|^2\right] \mathbf{1}\,\mathrm{d}\omega}{\displaystyle\int_{-\infty}^{\infty} \left|H_0(\omega)\right|^2 \,\mathrm{d}\omega}$
- FLIRS: $\boldsymbol{S}^{\mathrm{fb}}_{\mathrm{A}}(\omega_0,\zeta_0) = \boldsymbol{\mathcal{R}}(\omega_0,\zeta_0)\,\boldsymbol{S}^{\mathrm{f}}_{\mathrm{A}}(\omega_0,\zeta_0)$

5. The FLIRS $\boldsymbol{S}^{\mathrm{fb}}_{\mathrm{A}}(\omega_0,\zeta_0)$ are input to the fixed-base finite-element model of the structure to generate the required FRS, which are exactly the same as the FRS obtained from a full coupled soil-structure analysis under the excitation of FIRS.

   Hence, when the direct spectra-to-spectra method developed by Jiang *et al.* (2015) is applied to the fixed-base structure under the excitation of FLIRS $\boldsymbol{S}^{\mathrm{fb}}_{\mathrm{A}}(\omega_0,\zeta_0)$, FRS with complete probabilistic descriptions of FRS peaks, i.e., FRS with any desired level of NEP p can be obtained. If the method of time history is applied, such a result could only be obtained from a large number of coupled soil-structure analyses using a commercial finite-element software, such as ACS SASSI, with a large number of generated time histories compatible with the FIRS.

3.2 Numerical Example

To verify the accuracy and efficiency of the proposed method, FRS of a typical reactor building and a service building in nuclear power plants founded on the surface of a homogeneous half-space are generated following the procedure summarized in Section 3.1. The resultant FRS are then compared with the FRS obtained from a commercial software ACS SASSI, which generates FRS based on time history method. The transfer function, modification factor, which affect the resultant FRS when considering SSI effect, are investigated.

Model information

The selected reactor building consists of a containment and an internal structure that are supported by a circular disk foundation with a radius of 19.8m, as shown in Figure 3.6. Using the commercial finite element software ANSYS, the building is modelled as a lumped-parameter system with a foundation at the bottom, which can characterize the most

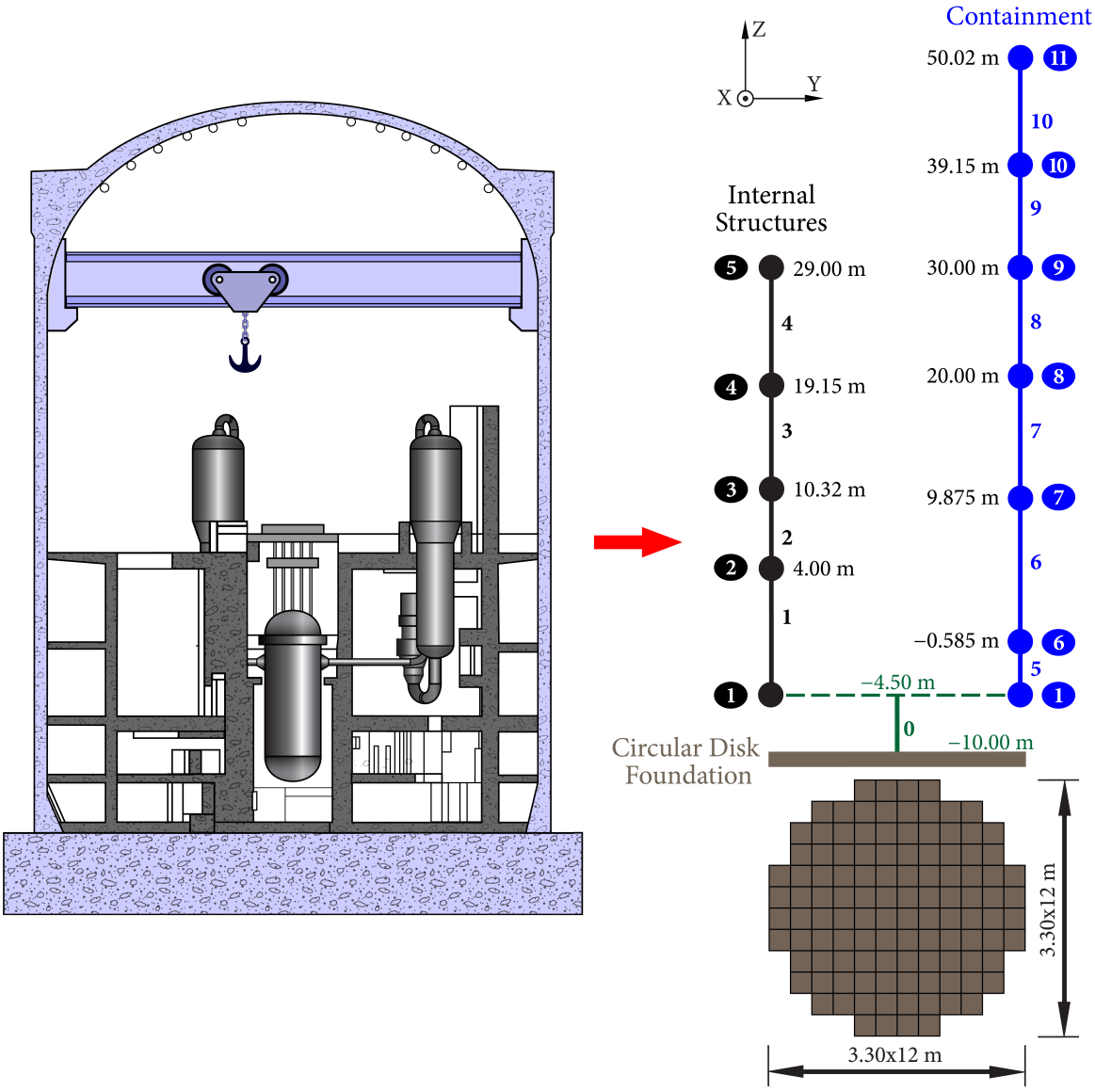

Figure 3.6 Primary and secondary systems in a nuclear power plant

significant dynamic properties of the structure. There are 11 nodes for the superstructure and 112 plate elements for the rigid foundation. For a fixed-base model, the DOF of all the nodes at the foundation elevation, are constrained. The model is symmetric about X- and Y-axes, and the information of the finite element model is described in Tables 3.1 and 3.2 (Li *et al.*, 2005). The plates are 2 meters thick.

Service Building

A three dimensional finite element model of a typical service building of a nuclear power plant, as shown in Figure 3.7, is established using ANSYS and ACS SASSI. The superstructure of the building consists of steel frames and concrete floor slabs, and the basement is constructed using concrete. The finite element model information is given in detail in Jiang *et al.* (2015).

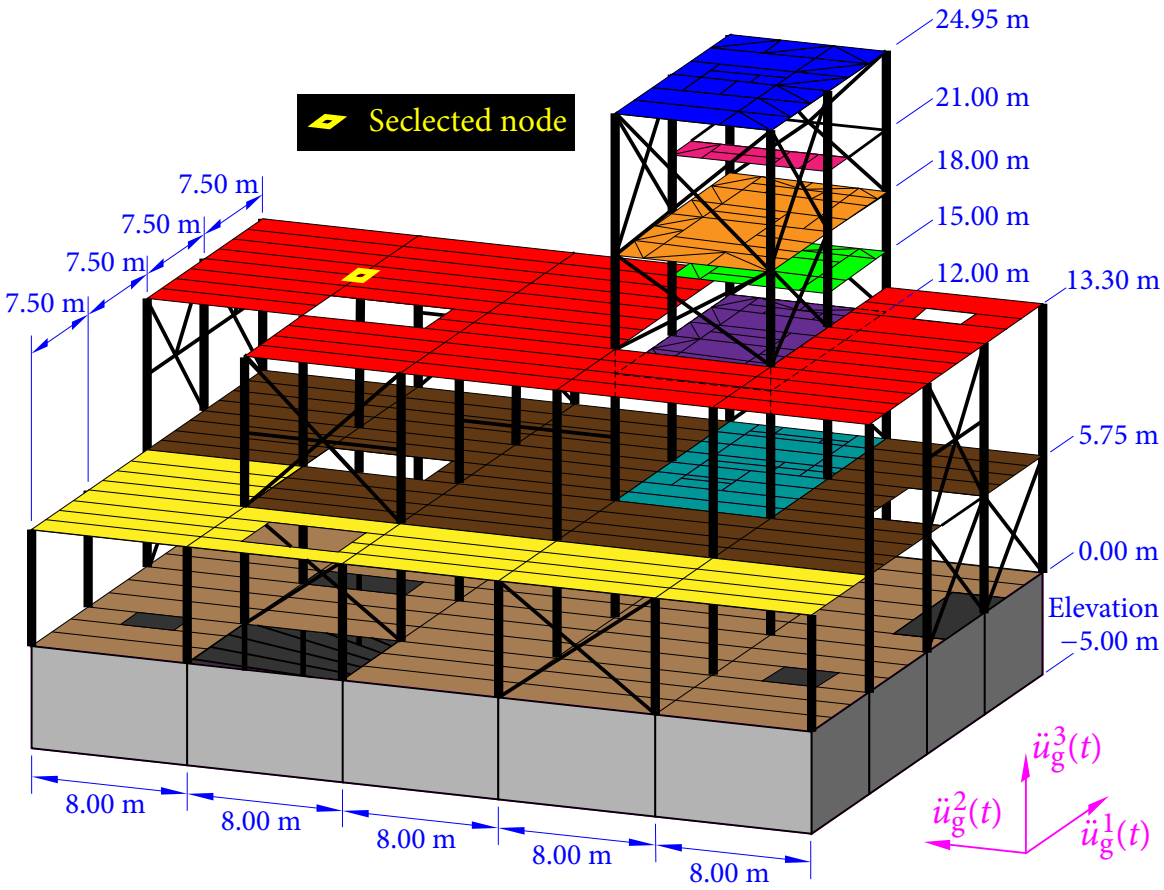

Figure 3.7 Finite element model of service building

Table 3.1 Nodal information of reactor building model

Node	Elevation (m)	Mass ($\times 10^6$ kg)	Moment of inertia ($\times 10^6$ kg $\cdot$ m^2)	
			$I_{xx} = I_{yy}$	I_{zz}
1	-4.5	13420	1260	1931
2	4	5710	370	0
3	10.32	5970	394	0
4	19.15	6750	500	0
5	29	1270	110	0
6	-0.585	2288	424	824
7	9.875	3033	568	1087
8	20	2960	554	1063
9	30	2960	554	1063
10	39.15	3068	562	1081
11	50.02	6271	910	1727

Table 3.2 Beam Element Properties of reactor building model

Section	Beam	Area (m^2)	Shear area (m^2)	Second area moment (m^4)
1	0	1204	1084.7	115436
2	1	50	19	5720
3	2	110	70	8160
4	3	140	70	8160
5	4	60	30	325
6	5	176	88	30570
7	6-10	107	53.5	19241

Soil Property

The underlying site consists of 3 infinite soil layers resting on a homogeneous half-space. The unit weight γ, Poisson's ratio ν, damping ratio ζ, thickness of the top layers H, and V_s are shown in Figure 3.8.

Foundation input response spectra

The R.G. 1.60 response spectra (USNRC, 1973) are assumed as the foundation input response spectra (FIRS) obtained from a site response analysis. The peak ground accelerations are anchored to $0.3g$ and $0.2g$ for the horizontal and vertical directions, respectively. 30 sets of tri-directional time histories, which are compatible with the target FIRS, are generated by the Hilbert-Huang Transform method (Ni *et al.*, 2013, 2011), and are used to

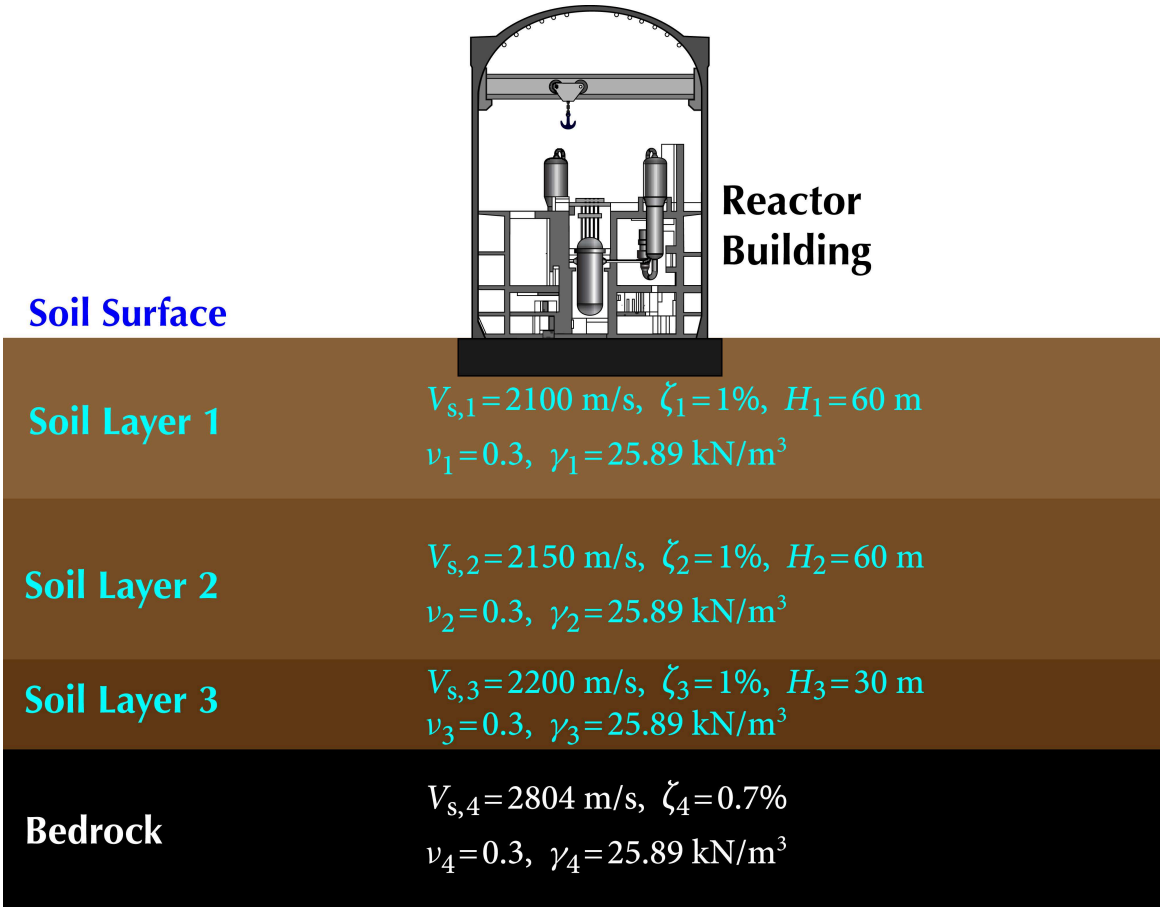

Figure 3.8 The soil layers and properties

perform SSI analysis by ACS SASSI for comparison. The response spectra of 30 sets of time histories in horizontal direction are shown in Figure 3.9.

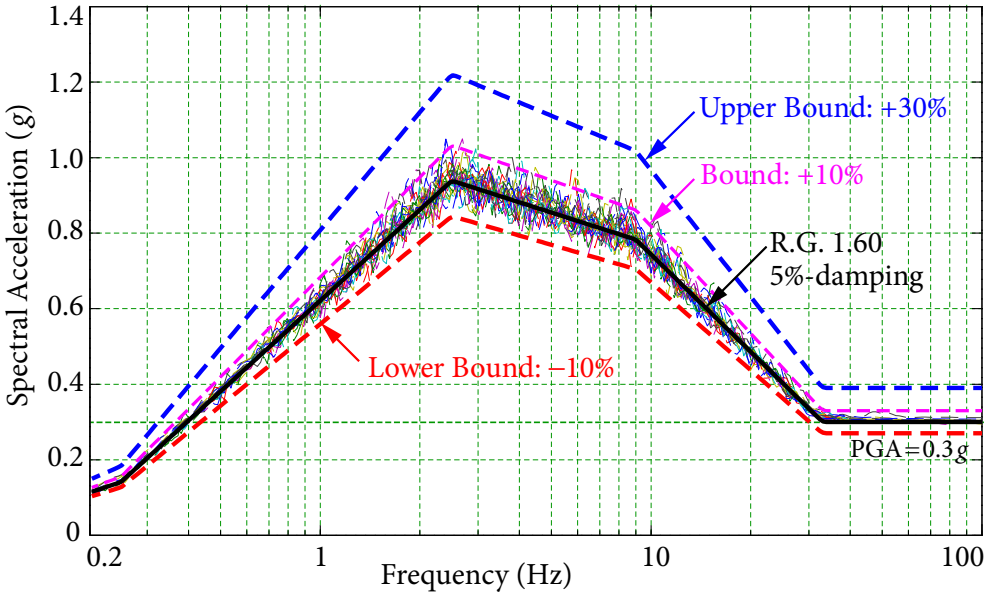

Figure 3.9 Foundation input response spectrum

Development of foundation level input response spectra (FLIRS)

The soil impedance matrix used to conduct SSI analysis is extracted from the analysis of ACS SASSI, which provides the same basis for this study and ACS SASSI. The dynamic soil stiffness is frequency dependent as shown in Figure 3.10.

According to Step 4 in Section 6.2.1, a modal analysis is performed for the fixed-base model by ANSYS, which provides the structure information, including natural frequencies, mode shapes of all the modes, mass matrix, influence matrix, and modal contribution factors. The damping ratio of the structure is taken as 5%. The dimensionless transfer matrix, regarded as fixed-base transfer function, of the fixed-base model $\mathbf{S}^{\mathrm{FB}}$ is calculated for different values of ω, varying from 0.4π to 200π. The modulus of the elements corresponding to the translational DOF at Nodes 2 to 5 are shown in Figure 3.11. It can be seen that the modulus of the transfer functions peak at the structural frequencies, i.e., 5.45 Hz and 12.72 Hz, of the significant modes.

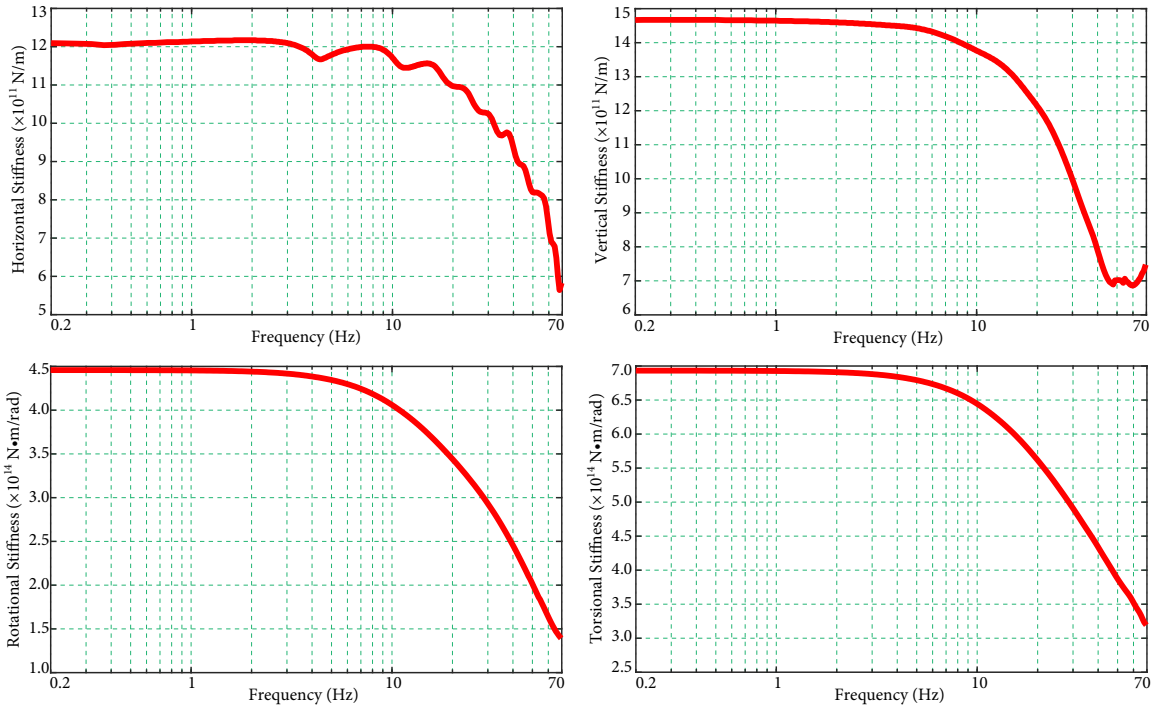

Figure 3.10 Dynamic soil stiffness of reactor building in SASSI

The transfer matrix $\mathcal{T}$ is defined by equation (3.40), in which the first term $\mathbf{T}_{\mathrm{TT},11}$ indicates the translational component and the second term accounts for the rotational component. The modulus of entire transfer function $\mathcal{T}_{11}$ and the translational component are shown in Figure 3.12. It shows that their difference is pronounced in the frequency range of 2 Hz to 10 Hz, which covers the frequencies of the dominant structural modes. Therefore, the rotational movement of foundation during the ground motion cannot be neglected.

Analogous to the modulus of the transfer matrix of the fixed-base structure shown in Figure 3.11, where peaks emerge at the frequencies of the significant structural modes, the frequencies corresponding to the peaks in Figure 3.12 can be interpreted as the natural frequencies of the entire soil-structure system (or the equivalent synthesized mass-spring-damper system). For instance, the first two peaks of the soil-structure system, located at 4.1 Hz and 5.2 Hz, can be explained as a result of the frequency shifting of the fixed-base model from 4.4 Hz and 5.4 Hz due to the SSI effect. Meanwhile, the significant modal frequencies

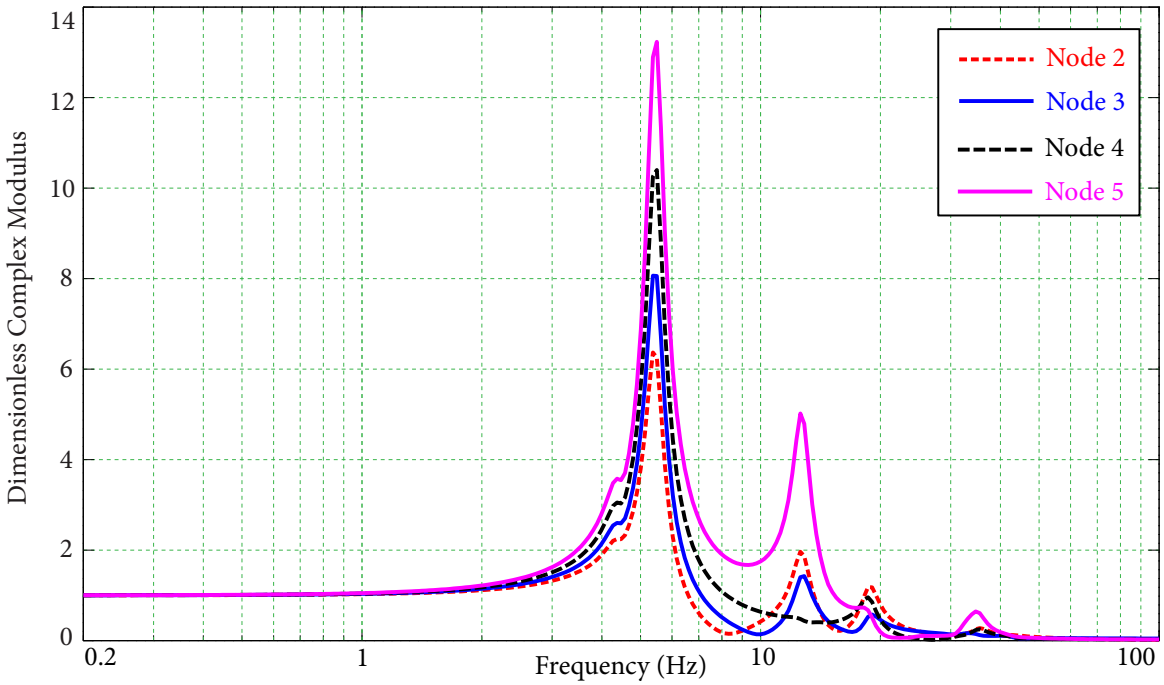

Figure 3.11 Modulus of fixed-base model transfer function for Nodes 2 to 5 in *X*-direction

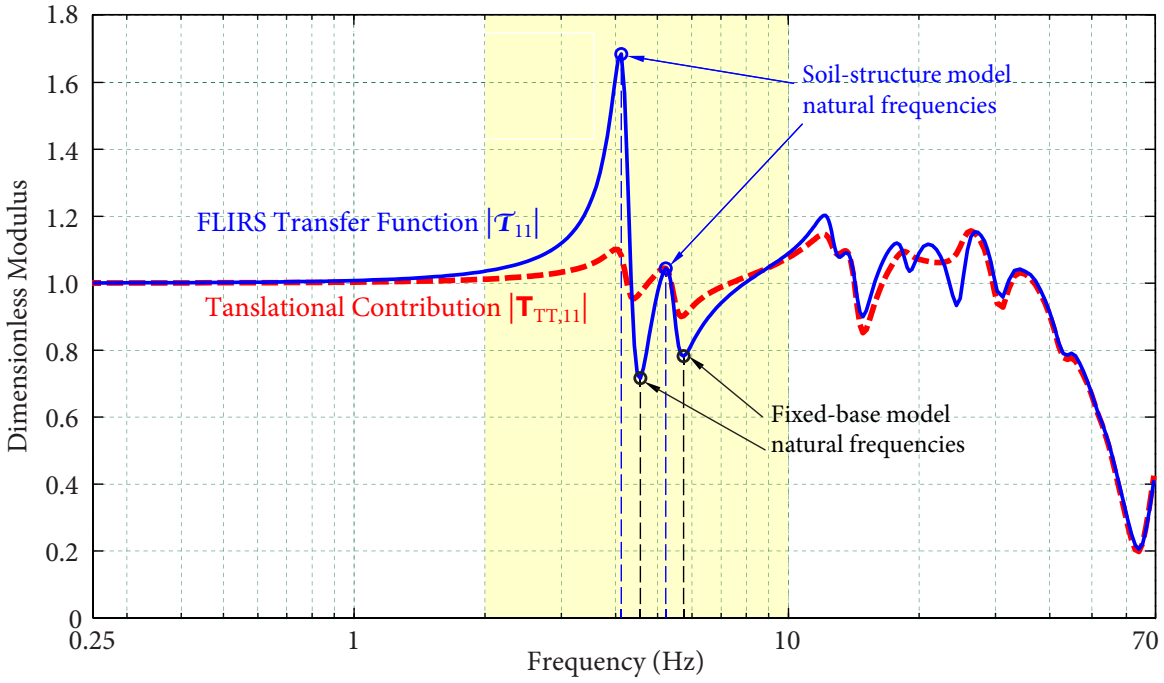

Figure 3.12 Modulus of horizontal component in FLIRS transfer matrix

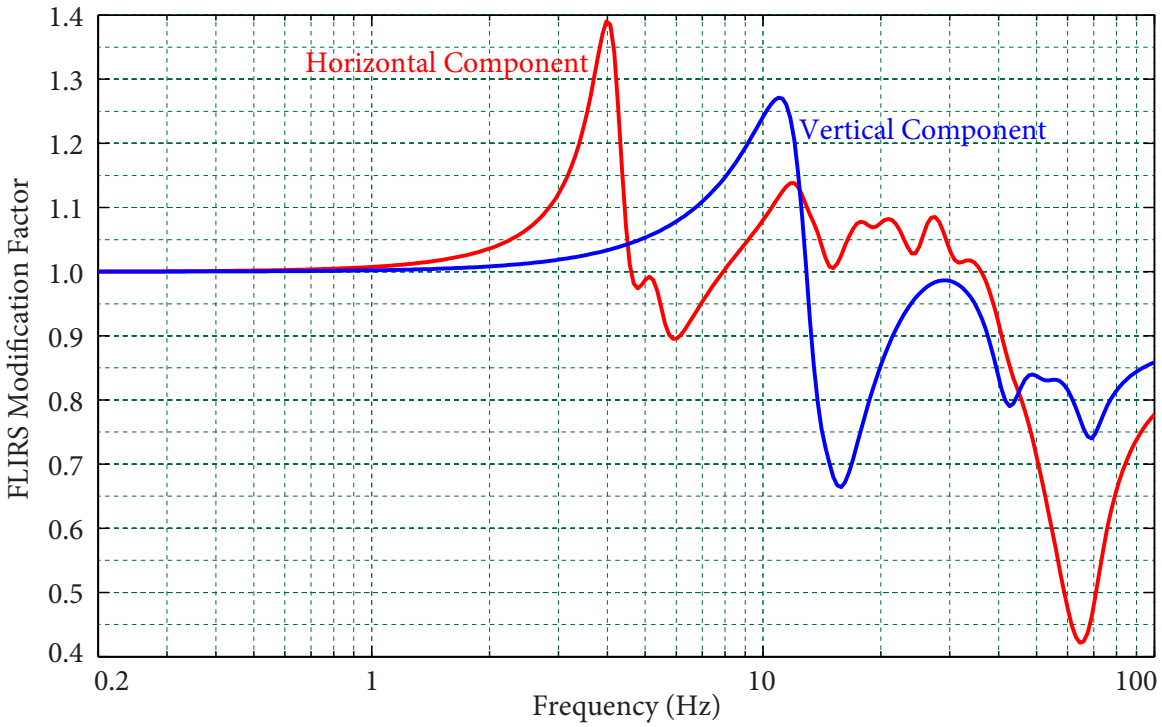

Figure 3.13 Modification factor from FIRS to FLIRS

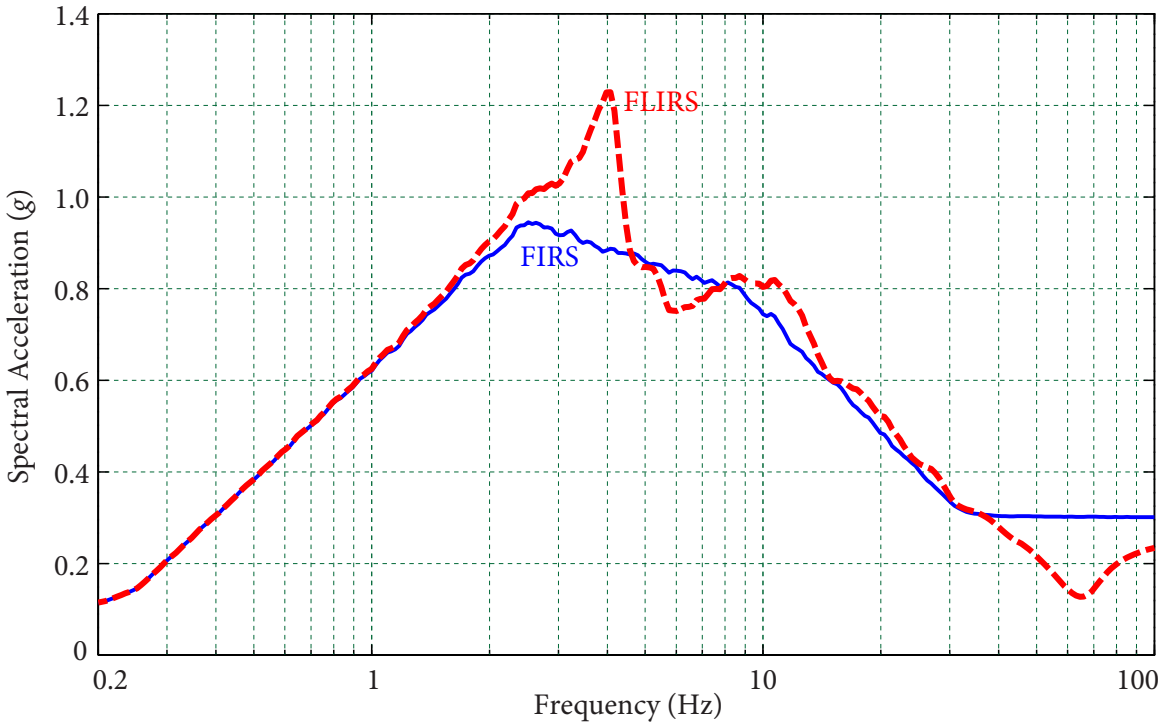

Figure 3.14 Horizontal FLIRS

of the fixed-base model correspond to the bottom of the valley between the peaks, implying considerable reductions of the responses of the structure.

The FLIRS modification factors $\mathcal{R}(\omega_0, \zeta_0)$ are then used to generate FLIRS from FIRS; FLIRS are used in the direct method for generating FRS from the fixed-base model. Figure 3.13 shows the horizontal and vertical components of the FLIRS modification factors. The resultant horizontal FLIRS are shown in Figure 3.14. The modification factor shows that the FLIRS change significantly around the natural frequency of the entire system and are scaled by up to 1.4 compared to FIRS, which may lead to increase of FRS at certain frequencies.

Development of floor response spectra (FRS)

In ACS SASSI, 30 sets of spectra-compatible time histories are used to generate 30 sets of FRS. The general procedure to generate FRS at node 5 is shown in Figure 3.15. For each input time history, a different FRS is developed by time history method. Since the input

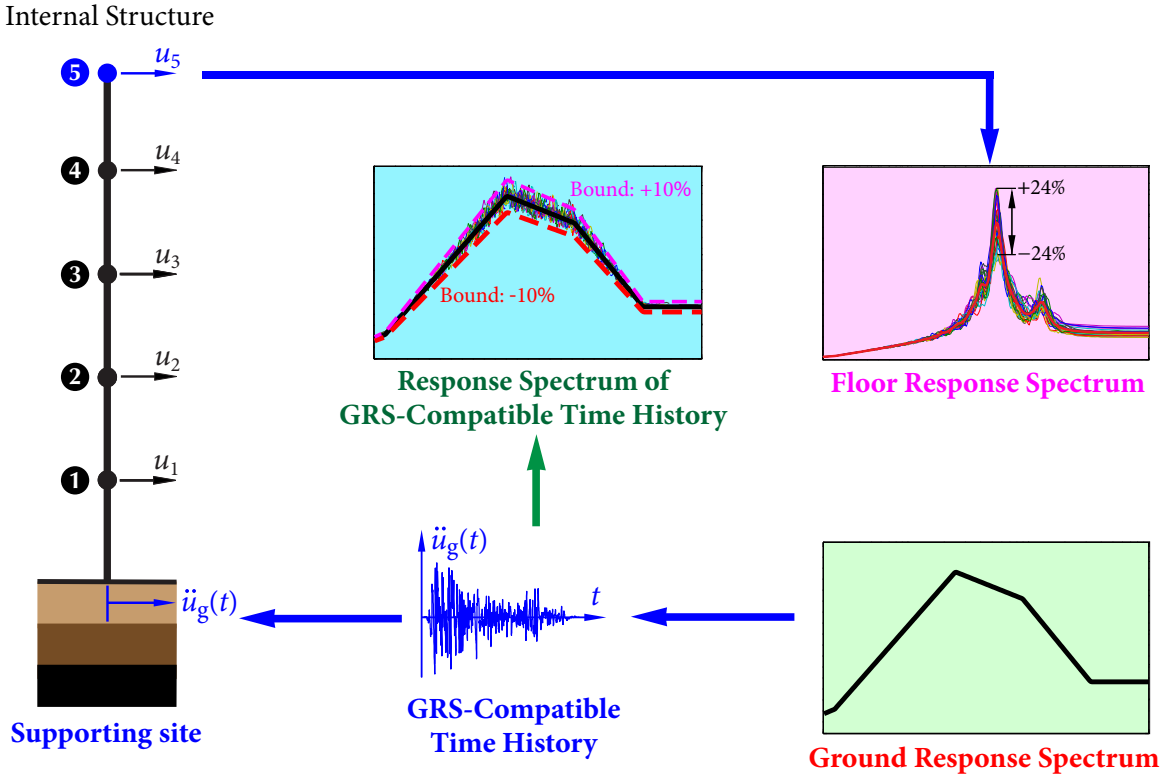

Figure 3.15 Generation of FRS in ACS SASSI

time history is artificial and not perfectly compatible with target GRS, the variability of the resultant FRS is very large. Comparing to the mean values of 30 results at node 5, the peak of FRS varies between -24% and +24%.

The direct spectra-to-spectra method (Jiang *et al.*, 2015; Li *et al.*, 2015) is applied to generate FRS at Nodes 4 and 5 in the internal structure. The mean values of resultant FLIRS are used as the input response spectra to the fixed-base model. FRS are calculated at 200 frequencies including the natural frequencies of the structure. The resultant FRS with 50% Non Exceedance Probability (NEP) at Node 4 and Node 5 are plotted along with FRS generated by time history analyses by ACS SASSI based on 30 sets of time history in Figures 3.16 and 3.17, respectively. FRS obtained by the direct method and the mean FRS of the time history analyses, which are regarded as the benchmark FRS, are shown in black solid lines and red dash lines, respectively. It is seen that the FRS obtained by the direct method generally agree very well with the benchmark FRS over the entire frequency range, whereas individual FRS from time history analyses exhibit large variability. Particularly, FRS peak values, which are of main interest of engineers, can be overestimated by more than 24% or underestimated by more than 23%. However, the differences at the FRS peaks between the direct method and the benchmark FRS are generally less than 5%, which are well within the range of acceptable errors. Figures 3.18 and 3.19 present the FRS with 84.1% NEP by the two approaches, which demonstrates the accuracy of the proposed method.

FRS at the selected node of the three-dimensional service building are also generated following the same procedure. Figure 3.20 shows that the proposed method also produces excellent results for a complex 3D model. The relative errors at FRS peaks are less than 5%, while the results of time history method exhibit large variations from $+226\%$ to -30%, even though the time histories are well compatible with the target input response spectra.

3.3 Summary

In this chapter, the substructure method to conduct the SSI analysis with rigid foundation is reviewed. The frequency dependant soil stiffness is utilized in the application. Based on the free-field ground motion (FIRS), soil properties, and structural modal information,

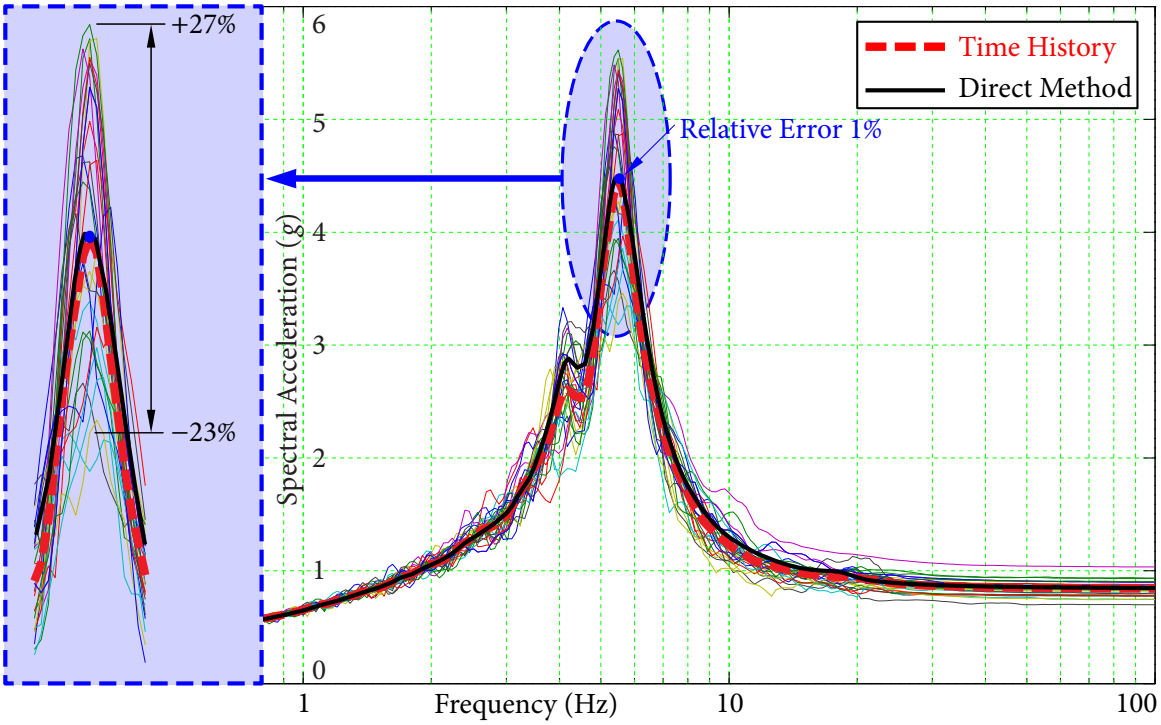

Figure 3.16 Comparison of FRS with 50% NEP at Node 4 in reactor building

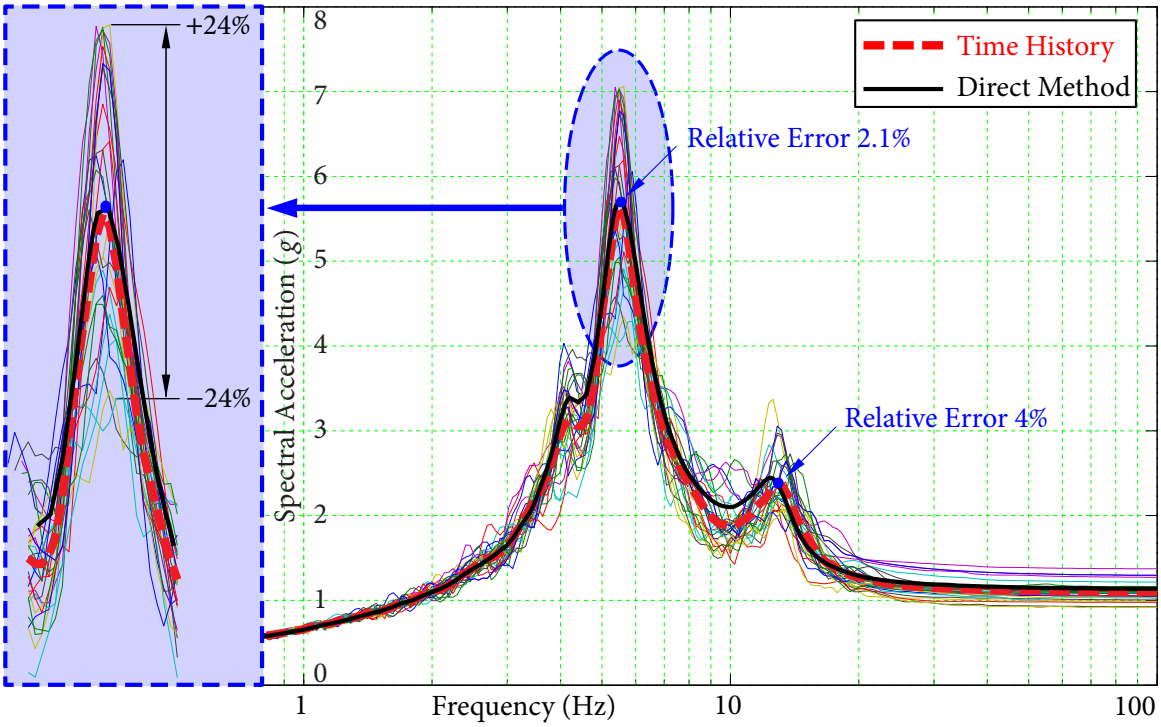

Figure 3.17 Comparison of FRS with 50% NEP at Node 5 in reactor building

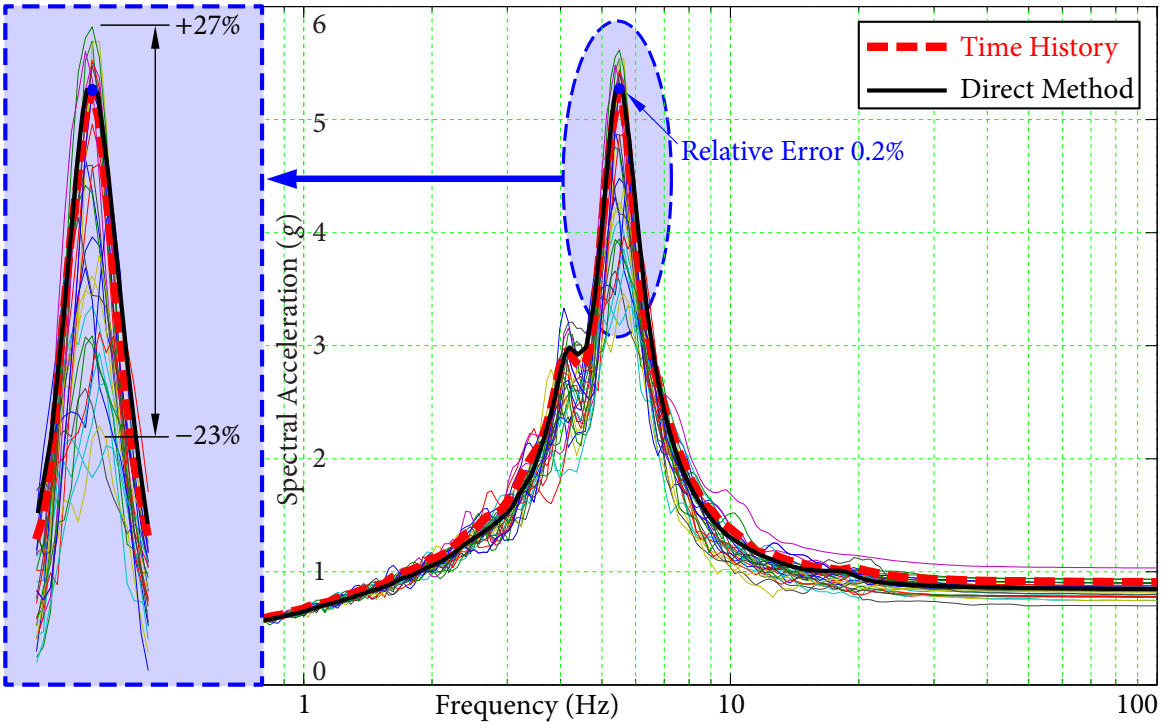

Figure 3.18 Comparison of FRS with 84% NEP at Node 4 in reactor building

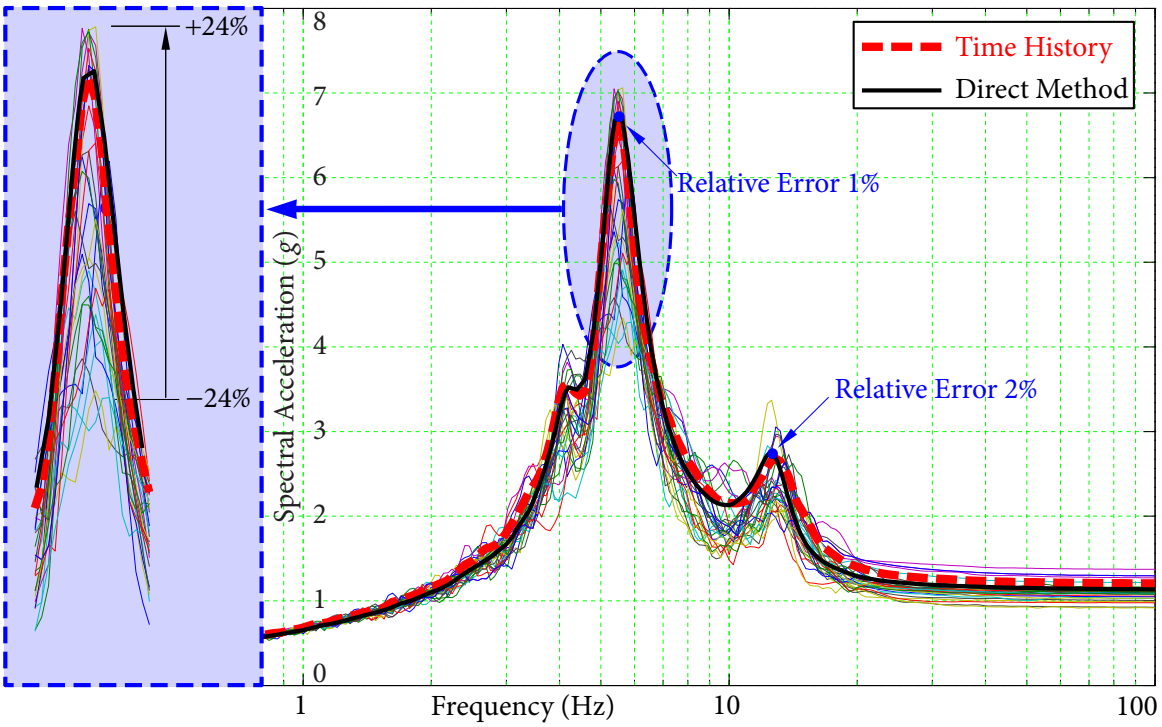

Figure 3.19 Comparison of FRS with 84% NEP at Node 5 in reactor building

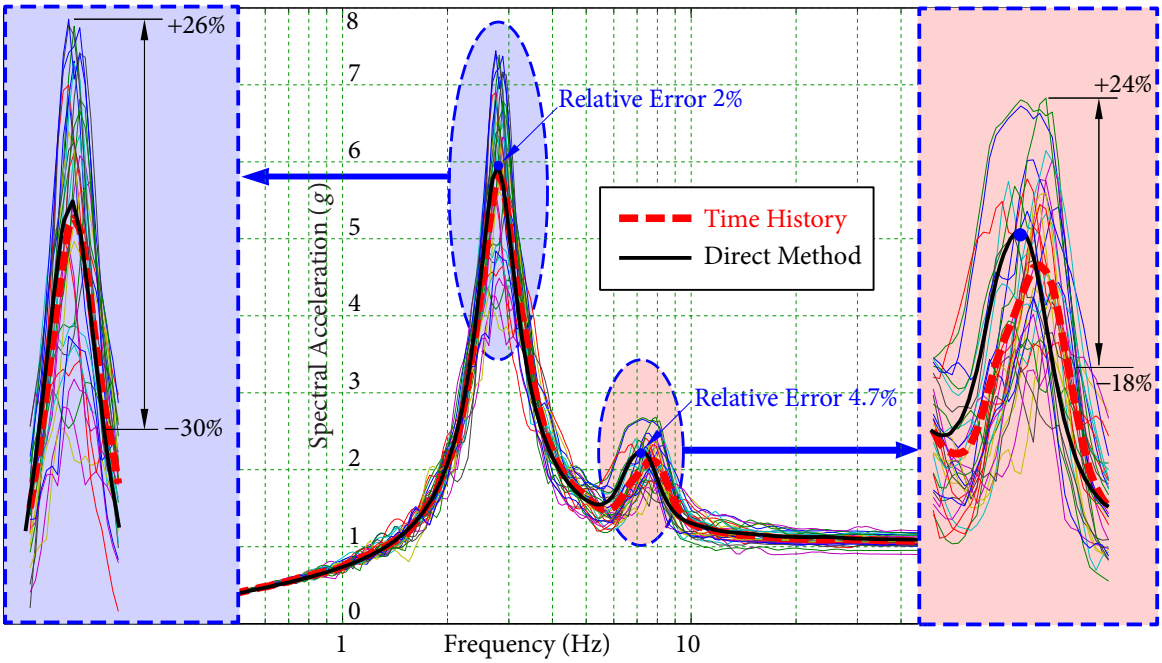

Figure 3.20 Comparison of FRS with 50% NEP in service building

the tri-directional response spectra are determined considering SSI effect. The modified response spectra, called foundation level input response spectra (FLIRS), are then used as the input to the fixed-base structure to generate FRS using the direct spectra-to-spectra method (Jiang *et al.*, 2015; Li *et al.*, 2015).

Numerical examples are performed to verify the proposed method. FRS of a reactor building and a service building are generated considering SSI by 30 sets of time history analyses and the proposed method. It is observed that the FRS obtained by the proposed method agree well with the resultant FRS from a large number of time history analyses, which are regarded as the benchmark FRS; whereas FRS obtained from time history analyses exhibit large variability at the FRS peaks. It is also demonstrated that the effect of SSI may increase FRS at certain frequencies, which leads to higher seismic demands for SSCs mounted on the supporting structure.

Some conclusions are obtained:

- The difference between the FLIRS and FIRS is significant. The numerical example shows the spectral acceleration is scaled up to 1.4 at certain frequencies and the natural frequency of the soil-structure system is different from the fixed-base structure.
- From the numerical example, the FRS based on FLIRS and direct method agrees well with the result of SASSI in most frequency domain. Large variability is observed in time time history analyses by ACS SASSI, which is overcame by the proposed method.
- The frequency dependent soil stiffness varies dramatically over the frequency range, especially in high frequency domain (more than 10 Hz). It is necessary to generate frequency dependent soil stiffness in SSI analysis.

In summary, the concept of FLIRS is proposed to represent the seismic input considering SSI effect. It can be obtained conveniently based on the modal information of structure and dynamic soil stiffness. FRS can be generated by the proposed substructure method and direct method accurately and efficiently without any variability.

CHAPTER 4

Formulation of Dynamic Soil Stiffness

In Soil-Structure Interaction (SSI) analysis, the frequency-dependent dynamic soil stiffness determines the response of soil base under foundation. It is a necessary element in SSI analysis. In this chapter, it is aimed to generate dynamic soil stiffness by a semi-analytical method based on the Green's function by Wolf (1985).

A flexible foundation can be represented by m nodes. If the foundation is rigid, m is equal to 1. For each node, there are 3 translational and 3 rotational degrees of freedom. Hence, the soil stiffness is a $6m \times 6m$ matrix. The element S_{ij} in dynamic stiffness matrix is the amplitude of the reaction force at node i when the displacement at node j is forced to be equal to $e^{i\omega t}$ as shown in Figure 4.1. ω is the excitation frequency, and t is the time. Thus dynamic soil stiffness is frequency dependent $6m \times 6m$ matrices.

In this study, the soil is modeled as a layered half-space characterized by the soil properties, including layer thickness, density, shear wave velocity, Poisson's ratio, and damping ratio. The soil properties are assumed to be linear in the generation of soil stiffness. Starting from the wave propagation function, the relevant displacements under three dimensional point loads are derived in wave number domain rigorously. The constitutive relation is then established in frequency domain according to Fourier series and Bessel transform pair. Finally, the Boundary Element Method (BEM) is employed to calculate the total stiffness matrix for rigid or flexible foundations with arbitrary shapes.

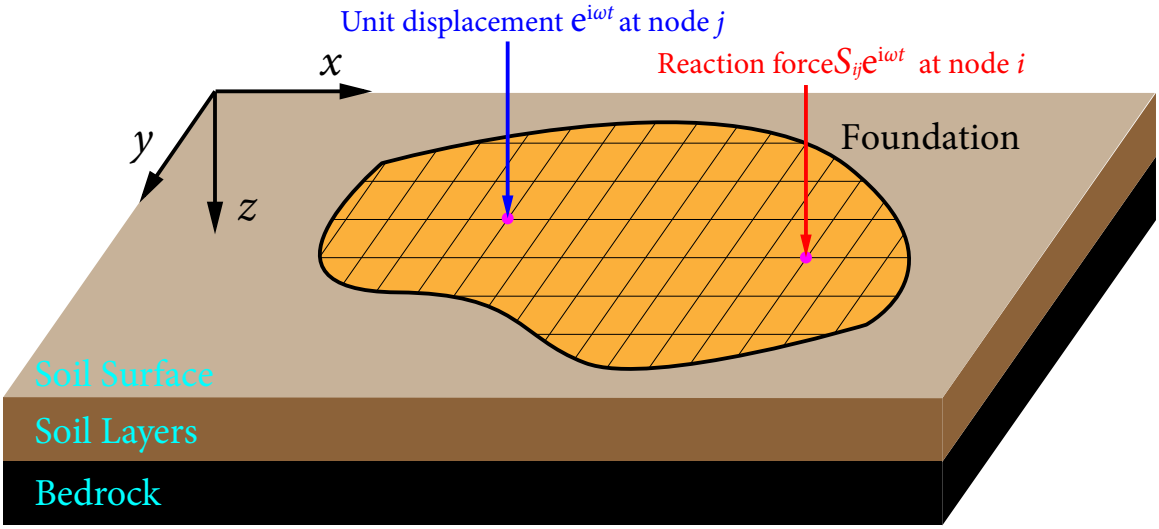

Figure 4.1 Definition of dynamic soil stiffness

4.1 Generation of Dynamic Soil Stiffness

4.1.1 Wave Propagation Function

For harmonic excitation with frequency ω, the three dimensional equilibrium equations in Cartesian coordinates x, y, and z directions are

$$\begin{aligned} \sigma_{x,x} + \tau_{xy,y} + \tau_{xz,z} &= -\rho\omega^2 u, \\ \tau_{yx,x} + \sigma_{y,y} + \tau_{yz,z} &= -\rho\omega^2 v, \\ \tau_{zx,x} + \tau_{zy,y} + \sigma_{z,z} &= -\rho\omega^2 w, \end{aligned} \tag{4.1}$$

where σ and τ are normal stress and shear stress, respectively. ρ is the density. u, v, and w are displacements in x, y, and z directions. The comma denotes a partial derivative.

The strain-displacement relationship are expressed as

$$\begin{aligned} \epsilon_x = u_{,x}\,, \quad \epsilon_y = v_{,y}\,, \quad \epsilon_z = w_{,z}\,, \\ \gamma_{xy} = u_{,y} + v_{,x}\,, \quad \gamma_{xz} = u_{,z} + w_{,x}\,, \quad \gamma_{yz} = v_{,z} + w_{,y}\,, \end{aligned} \tag{4.2}$$

in which ϵ is normal strain, and γ is shear strain.

Based on Hooke's law, the constitutive equations are

$$\begin{aligned}
\sigma_x &= \lambda(\epsilon_x + \epsilon_y + \epsilon_z) + 2G\epsilon_x, \\
\sigma_y &= \lambda(\epsilon_x + \epsilon_y + \epsilon_z) + 2G\epsilon_y, \\
\sigma_z &= \lambda(\epsilon_x + \epsilon_y + \epsilon_z) + 2G\epsilon_z, \\
\tau_{xy} = G\gamma_{xy}, &\quad \tau_{xz} = G\gamma_{xz}, \quad \tau_{yz} = G\gamma_{yz},
\end{aligned} \tag{4.3}$$

where G is the shear modulus, and λ is given by

$$\lambda = \frac{\nu E}{(1+\nu)(1-2\nu)}. \tag{4.4}$$

E is the elasticity modulus, and ν is Poisson's ratio. G can be expressed by E and ν as

$$G = \frac{E}{2(1+\nu)}. \tag{4.5}$$

Substituting equations (4.2) and (4.3) into equations (4.1) leads to

$$\begin{aligned}
(\lambda + 2G)(u_{,xx} + v_{,yx} + w_{,zx}) + 2G(u_{,yy} + u_{,zz}) &= -\rho\omega^2 u, \\
(\lambda + 2G)(u_{,xy} + v_{,yy} + w_{,zy}) + 2G(v_{,xx} + v_{,zz}) &= -\rho\omega^2 v, \\
(\lambda + 2G)(u_{,xz} + v_{,yz} + w_{,zz}) + 2G(w_{,xx} + w_{,yy}) &= -\rho\omega^2 w.
\end{aligned} \tag{4.6}$$

In order to solve the displacements and identify the different types of waves, new variables are introduced as

$$e = u_{,x} + v_{,y} + w_{,z}, \tag{4.7}$$

and

$$\Omega_x = \tfrac{1}{2}(w_{,y} - v_{,z}), \qquad \Omega_y = \tfrac{1}{2}(u_{,z} - w_{,x}), \qquad \Omega_z = \tfrac{1}{2}(v_{,x} - u_{,z}), \tag{4.8}$$

where e represents the volumetric strain, while Ω is the rotation-strain vector. So e can be considered as the strain causing by primary waves (P-wave), and Ω results from shear waves (S-wave).

Substituting equations (4.7) and (4.8) into equations (4.6) gives

$$(\lambda + 2G)e_{,x} + 2G(\Omega_{y,z} - \Omega_{z,y}) = -\rho\omega^2 u, \tag{4.9}$$

$$(\lambda + 2G)e_{,y} + 2G(\Omega_{z,x} - \Omega_{x,z}) = -\rho\omega^2 v, \tag{4.10}$$

$$(\lambda + 2G)e_{,z} + 2G(\Omega_{x,y} - \Omega_{y,x}) = -\rho\omega^2 w. \tag{4.11}$$

Differentiating equation (4.9) with respect to x, equation (4.10) with respect to y, equation (4.11) with respect to z, and taking the summation of these three equations result in

$$(\lambda + 2G)(e_{,xx} + e_{,yy} + e_{,xx}) = -\rho\omega^2 e. \tag{4.12}$$

By introducing the primary wave velocity

$$c_p^2 = \frac{\lambda + 2G}{\rho}, \tag{4.13}$$

equation (4.12) is rewritten as

$$\nabla e = -\frac{\omega^2}{c_p^2} e. \tag{4.14}$$

Differentiating equation (4.11) with respect to y, equation (4.10) with respect to z, and letting the former equation subtract the latter yield

$$G(\Omega_{x,xx} + \Omega_{x,yy} + \Omega_{x,zz}) = -\rho\omega^2\Omega_x, \tag{4.15}$$

Similarly,

$$G(\Omega_{y,xx} + \Omega_{y,yy} + \Omega_{y,zz}) = -\rho\omega^2\Omega_y, \tag{4.16}$$

$$G(\Omega_{z,xx} + \Omega_{z,yy} + \Omega_{z,zz}) = -\rho\omega^2\Omega_z. \tag{4.17}$$

By introducing the shear wave velocity

$$c_s^2 = \frac{G}{\rho}, \tag{4.18}$$

equations (4.15)-(4.17) are rewritten as

$$\nabla\Omega = -\frac{\omega^2}{c_s^2}\Omega. \tag{4.19}$$

Under harmonic excitation, the equations of motion are specified in equation (4.14) with the amplitude of volumetric strain e and (4.19) with the amplitude of rotation strain vector Ω.

Propagation Function of P-wave

The displacements resulting from P-waves are shown in Figure 4.2.

The solution of equation (4.14) is

$$e = -\frac{\mathrm{i}\omega}{c_p} A_{\mathrm{P}} \exp\left[\frac{\mathrm{i}\omega}{c_p}(-l_x x - l_y y - l_z z)\right], \tag{4.20}$$

where A_{P} is the amplitude of P-wave. l_x, l_y, and l_z can be considered as the cosines of the angles between the direction of P-wave and x, y, and z axis. They meet

$$l_x^2 + l_y^2 + l_z^2 = 1. \tag{4.21}$$

The corresponding displacements caused by P-wave are governed by

$$\begin{aligned} u_p &= l_x A_{\mathrm{P}} \exp\left[\frac{\mathrm{i}\omega}{c_p}(-l_x x - l_y y - l_z z)\right], \\ v_p &= l_y A_{\mathrm{P}} \exp\left[\frac{\mathrm{i}\omega}{c_p}(-l_x x - l_y y - l_z z)\right], \\ w_p &= l_z A_{\mathrm{P}} \exp\left[\frac{\mathrm{i}\omega}{c_p}(-l_x x - l_y y - l_z z)\right]. \end{aligned} \tag{4.22}$$

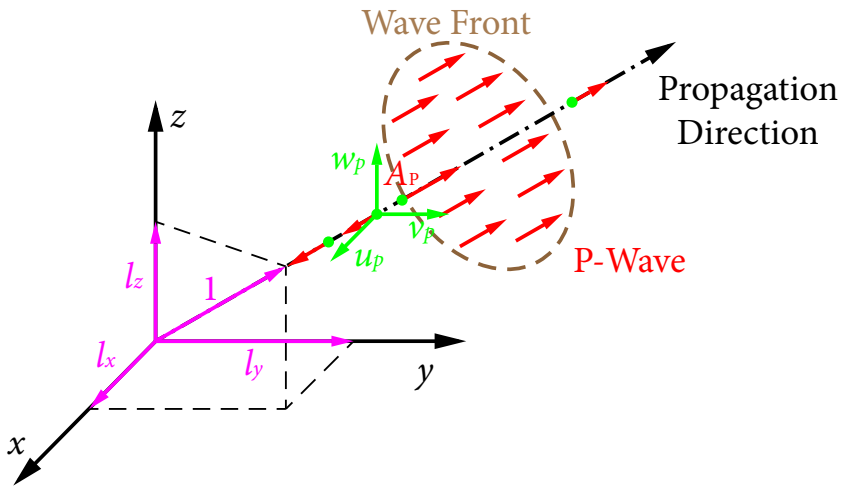

Figure 4.2 Displacements associated with P-waves

Propagation Function of S-wave

The displacements resulting from S-waves are shown in Figure 4.3.

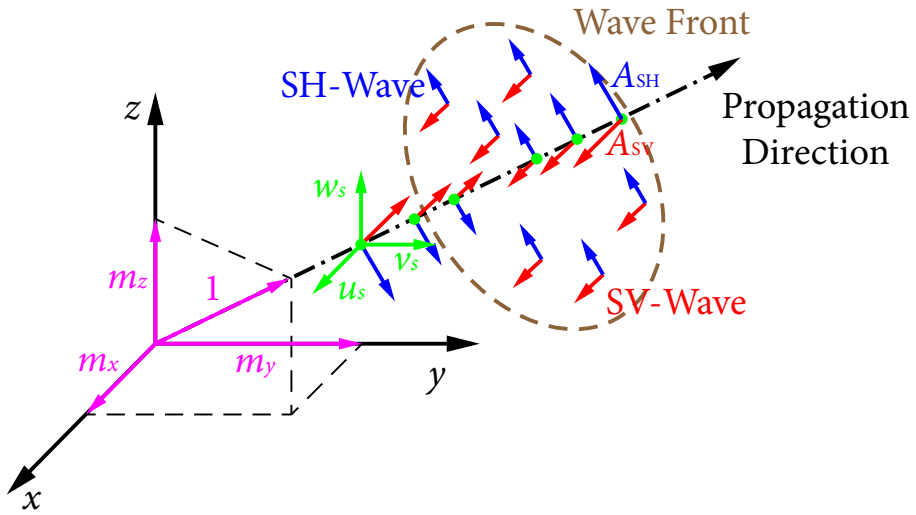

Figure 4.3 Displacements associated with S-waves

The solution of equation (4.19) is

$$\Omega = -\frac{i\omega}{2c_p} C \exp\left[\frac{i\omega}{c_p}(-m_x x - m_y y - m_z z)\right], \tag{4.23}$$

where vector C represents the amplitude of S-wave. m_x, m_y, and m_z can be considered as the cosines of the angles between the direction of S-wave and x, y, and z axis. They meet

$$m_x^2 + m_y^2 + m_z^2 = 1. \tag{4.24}$$

The corresponding displacements caused by S-wave are

$$\begin{aligned} u_s &= (m_x C_y - m_y C_z)\exp\left[\frac{i\omega}{c_s}(-m_x x - m_y y - m_z z)\right], \\ v_s &= (m_x C_z - m_z C_x)\exp\left[\frac{i\omega}{c_s}(-m_x x - m_y y - m_z z)\right], \\ w_s &= (m_y C_x - m_x C_y)\exp\left[\frac{i\omega}{c_s}(-m_x x - m_y y - m_z z)\right]. \end{aligned} \tag{4.25}$$

S-wave is usually decomposed into two components as SH-wave, containing the displacement in x-y plane, and SV-wave, containing the displacement in z axis and propagation direction plane. Hence, the corresponding displacement amplitude A_{SH} and A_{SV} are ex-

pressed as

$$A_{\mathrm{SH}} = \frac{C_x}{\sqrt{m_x^2 + m_y^2}},$$
$$A_{\mathrm{SV}} = \frac{m_x C_y - m_y C_x}{\sqrt{m_x^2 + m_y^2}}.$$

Then the displacements become

$$u_s = \frac{m_x m_z A_{\mathrm{SV}} - m_y A_{\mathrm{SH}}}{\sqrt{m_x^2 + m_y^2}} \exp\Big[\frac{\mathrm{i}\omega}{c_s}(-m_x x - m_y y - m_z z)\Big],$$
$$v_s = \frac{m_y m_z A_{\mathrm{SV}} + m_x A_{\mathrm{SH}}}{\sqrt{m_x^2 + m_y^2}} \exp\Big[\frac{\mathrm{i}\omega}{c_s}(-m_x x - m_y y - m_z z)\Big], \tag{4.26}$$
$$w_s = -\sqrt{m_x^2 + m_y^2} A_{\mathrm{SV}} \exp\Big[\frac{\mathrm{i}\omega}{c_s}(-m_x x - m_y y - m_z z)\Big].$$

Propagation Function of Total Earthquake Wave

Since the directions of propagation are always assumed to be in a vertical plane, e.g., x-z plane or y-z plane, this means, when x-z plane is considered,

$$l_y = m_y = 0.$$

In this case, taking both P-wave and S-wave into consideration gives

$$u = l_x A_{\mathrm{P}} \exp\Big[\frac{\mathrm{i}\omega}{c_p}(-l_x x - l_z z)\Big] + m_z A_{\mathrm{SV}} \exp\Big[\frac{\mathrm{i}\omega}{c_s}(-m_x x - m_z z)\Big], \tag{4.27}$$
$$v = A_{\mathrm{SH}} \exp\Big[\frac{\mathrm{i}\omega}{c_s}(-m_x x - m_z z)\Big], \tag{4.28}$$
$$w = l_z A_{\mathrm{P}} \exp\Big[\frac{\mathrm{i}\omega}{c_p}(-l_x x - l_z z)\Big] + m_x A_{\mathrm{SV}} \exp\Big[\frac{\mathrm{i}\omega}{c_s}(-m_x x - m_z z)\Big]. \tag{4.29}$$

The total displacement equations show that the displacements u and w depend on P-wave and SV-wave in x-z plane, while v is determined by SH-wave out of x-z plane.

4.1.2 Addressing Material Damping

The material damping of soil is introduced by replacing the elastic constants by the complex values as

$$\lambda^* + 2G^* = (\lambda + 2G)(1 + 2\zeta_p \mathrm{i}),$$

$$c_s^* = c_s\sqrt{(1 + 2\zeta_s \mathrm{i})},$$

where ζ_p and ζ_s are damping ratios for P-wave and S-wave, respectively. The superscript symbol $*$ represents the corresponding complex values.

4.1.3 Dynamic Stiffness Matrix under Point Loads

The analytical solution of dynamic stiffness matrix in a single layer, which is derived by Wolf (1985), is used in this research.

A horizontal layer with depth d, P-damping ζ_p, S-damping as ζ_s, complex shear wave velocity c_s^*, complex primary wave velocity c_p^*, complex shear modulus G^*, and density ρ is studied.

The dynamic stiffness of this layer under three dimensional point loads with frequency ω is addressed. The origin is located at the top of the layer and z axis is pointing downward.

Dynamic Stiffness Matrix of Out-of-Plane Motion under Point Load

The displacements v, strains τ_{yz}, and external forces Q associated with out-of-plane motion in a horizontal layer are shown in Figure 4.4. The half-space can be considered as a layer with infinite thickness, i.e., d approaches infinity.

In order to meet the boundary condition and address the waves propagating in both positive and negative z directions, a second wave in x direction is introduced. Then the out-of-plane motion, equation (4.28) becomes

$$v(x,z) = A_{SH}\exp\Big[\frac{\mathrm{i}\omega}{c_s}(-m_x x - m_z z)\Big] + B_{SH}\exp\Big[\frac{\mathrm{i}\omega}{c_s}(-m_x x + m_z z)\Big], \tag{4.30}$$

where B_{SH} is the amplitude of wave propagating in the negative direction.

Since

$$m_x^2 + m_z^2 = 1,$$

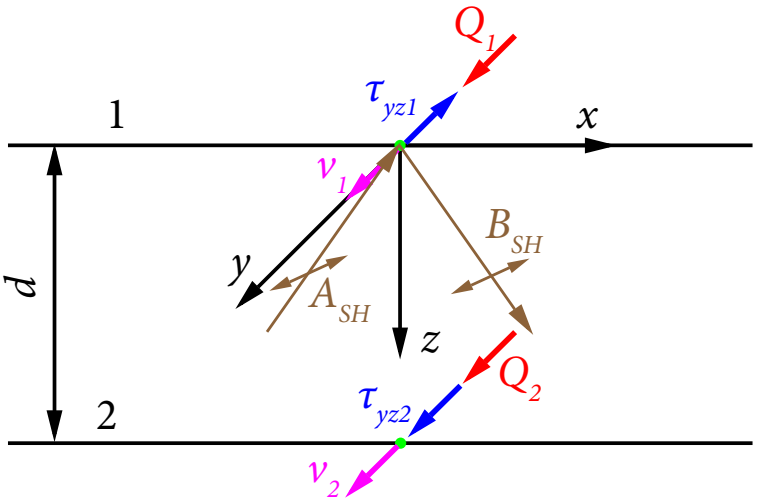

Figure 4.4 Out-of-plane motion model for a horizontal layer

letting

$$m_z = -\sqrt{1 - m_x^2}, \tag{4.31}$$

and introducing

$$k = \frac{\omega m_x}{c_s^*}, \tag{4.32}$$

$$t = \sqrt{\frac{1}{m_x^2} - 1}, \tag{4.33}$$

lead to

$$v(x,z) = v(z)\exp(-\mathrm{i}kx), \tag{4.34}$$

in which

$$v(z) = A_{\mathrm{SH}}\exp(\mathrm{i}ktz) + B_{\mathrm{SH}}\exp(-\mathrm{i}ktz). \tag{4.35}$$

The variable k can be considered as the wave number.

Since the out-of-plane motion and in-plane motion are uncoupled, $w_{,y}$ is equal to 0. Based on equations (4.2) and (4.3), it is derived in

$$\tau_{yz}(x,z) = G^* v_{,z} = \mathrm{i}ktG^*\left[A_{\mathrm{SH}}\exp(\mathrm{i}ktz) + B_{\mathrm{SH}}\exp(-\mathrm{i}ktz)\right]\exp(-\mathrm{i}kx). \tag{4.36}$$

Then the displacement and stress at the top surface of layer with $z = 0$ (subscript 1) are governed by

$$\begin{Bmatrix} v_1 \\ \tau_{yz1} \end{Bmatrix} = \begin{bmatrix} 1 & 1 \\ \mathrm{i}ktG^* & -\mathrm{i}ktG^* \end{bmatrix} \begin{Bmatrix} A_{\mathrm{SH}} \exp(-\mathrm{i}kx) \\ B_{\mathrm{SH}} \exp(-\mathrm{i}kx) \end{Bmatrix}. \tag{4.37}$$

The displacement and stress at the bottom surface of layer with $z = d$ (subscript 2) are governed by

$$\begin{Bmatrix} v_2 \\ \tau_{yz2} \end{Bmatrix} = \begin{bmatrix} \exp(\mathrm{i}ktd) & \exp(-\mathrm{i}ktd) \\ \mathrm{i}ktG^* \exp(\mathrm{i}ktd) & -\mathrm{i}ktG^* \exp(-\mathrm{i}ktd) \end{bmatrix} \begin{Bmatrix} A_{\mathrm{SH}} \exp(-\mathrm{i}kx) \\ B_{\mathrm{SH}} \exp(-\mathrm{i}kx) \end{Bmatrix}. \tag{4.38}$$

Due to Euler's formula, substituting (4.37) into (4.38) to eliminate A_{SH}, B_{SH}, and $(-\mathrm{i}kx)$ gives

$$\begin{Bmatrix} v_2 \\ \tau_{yz2} \end{Bmatrix} = \begin{bmatrix} \cos ktd & (ktG^*)^{-1} \sin ktd \\ -ktG^* \sin ktd & \cos ktd \end{bmatrix} \begin{Bmatrix} v_1 \\ \tau_{yz1} \end{Bmatrix}. \tag{4.39}$$

For the surface, the external load is

$$Q_1 = -\tau_{yz1},$$

denoting the load at the bottom as

$$Q_2 = \tau_{yz2},$$

and performing a transformation of equation (4.39) lead to

$$\begin{Bmatrix} Q_1 \\ Q_2 \end{Bmatrix} = \mathbf{K}_{\mathrm{out}} \begin{Bmatrix} v_1 \\ v_2 \end{Bmatrix}, \tag{4.40}$$

in which $\mathbf{K}_{\mathrm{out}}$ is the dynamic stiffness matrix of out-of-plane motion in a single layer as

$$\mathbf{K}_{\mathrm{out}} = \frac{ktG^*}{\sin ktd} \begin{bmatrix} \cos ktd & -1 \\ -1 & \cos ktd \end{bmatrix}. \tag{4.41}$$

For half-space, which means d approaches to infinity, both Q_2 and v_2 are equal to 0. $\mathbf{K}_{\mathrm{out}}$ becomes

$$\mathbf{K}_{\mathrm{out}} = \left[\mathrm{i}ktG^*\right]. \tag{4.42}$$

Dynamic Stiffness Matrix of In-Plane Motion under Point Load

The displacements u and w, strains τ_{xz} and σ, and external forces R and P associated with in-plane motion in a horizontal layer are shown in Figure 4.5.

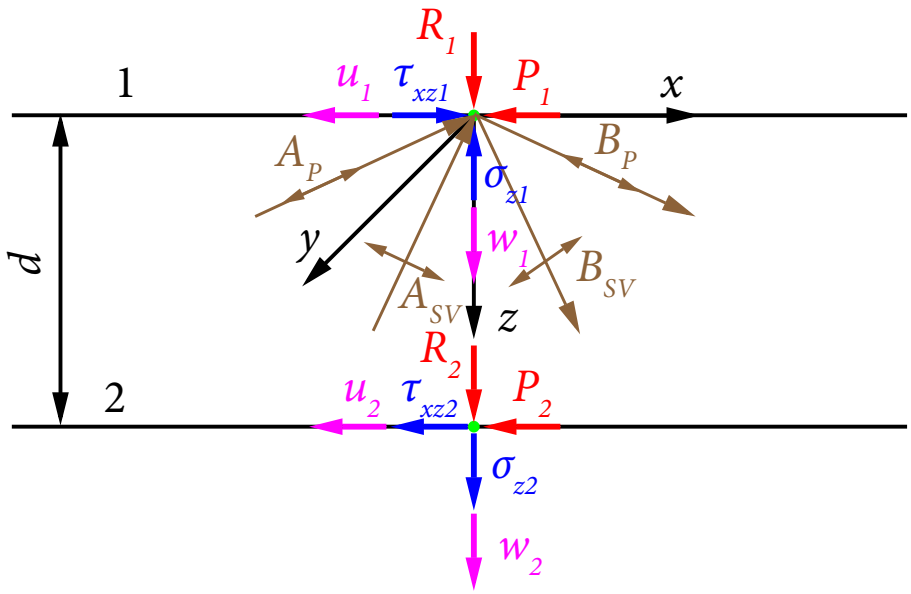

Figure 4.5 In-plane motion model for a horizontal layer

The in-plane motions are caused by P-wave and SH-wave. The displacements in x and z direction are given by equations (4.27) and (4.29). The boundary conditions of these two motions will vary with x due to the terms $\exp(-\mathrm{i}\omega l_x x/c_p^*)$ and $\exp(-\mathrm{i}\omega m_x x/c_s^*)$. In this case, letting

$$\frac{l_x}{c_p^*} = \frac{m_x}{c_s^*},$$

allows the analysis to concentrate on the variation with z.

Similar to out-of-plane case, a second wave with the same amplitude in x direction is introduced. Then the in-plane motions, equations (4.27) and (4.29), become

$$\begin{aligned} u(x,z) = {} & l_x A_{\mathrm{P}} \exp\left[\frac{\mathrm{i}\omega}{c_p^*}(-l_x x - l_z z)\right] + l_x B_{\mathrm{P}} \exp\left[\frac{\mathrm{i}\omega}{c_p^*}(-l_x x + l_z z)\right] \\ & + m_z A_{\mathrm{SV}} \exp\left[\frac{\mathrm{i}\omega}{c_s^*}(-m_x x - m_z z)\right] + m_z B_{\mathrm{SV}} \exp\left[\frac{\mathrm{i}\omega}{c_s^*}(-m_x x + m_z z)\right], \end{aligned} \tag{4.43}$$

$$w(x,z) = l_z A_{\mathrm{P}} \exp\Big[\frac{\mathrm{i}\omega}{c_p^*}(-l_x x - l_z z)\Big] + l_z B_{\mathrm{P}} \exp\Big[\frac{\mathrm{i}\omega}{c_p^*}(-l_x x + l_z z)\Big]$$
$$+ m_x A_{\mathrm{SV}} \exp\Big[\frac{\mathrm{i}\omega}{c_s^*}(-m_x x - m_z z)\Big] + m_x B_{\mathrm{SV}} \exp\Big[\frac{\mathrm{i}\omega}{c_s^*}(-m_x x + m_z z)\Big], \quad (4.44)$$

where B_{P} and B_{SH} are the amplitudes of waves propagating in the negative direction.

Since

$$l_x^2 + l_z^2 = 1,$$

letting

$$l_z = -\sqrt{1 - l_x^2}, \quad (4.45)$$

introducing

$$s = \sqrt{\frac{1}{m_l^2} - 1}, \quad (4.46)$$

and substituting (4.32) and (4.33) lead to

$$u(x,z) = u(z)\exp(-\mathrm{i}kx), \quad (4.47)$$

$$w(x,z) = w(z)\exp(-\mathrm{i}kx), \quad (4.48)$$

in which

$$u(z) = l_x\big[A_{\mathrm{P}}\exp(\mathrm{i}ksz) + B_{\mathrm{P}}\exp(-\mathrm{i}ksz)\big] - m_x t\big[A_{\mathrm{SV}}\exp(\mathrm{i}ktz) - B_{\mathrm{SV}}\exp(-\mathrm{i}ktz)\big], \quad (4.49)$$

$$w(z) = -l_x s\big[A_{\mathrm{P}}\exp(\mathrm{i}ksz) - B_{\mathrm{P}}\exp(-\mathrm{i}ksz)\big] - m_x\big[A_{\mathrm{SV}}\exp(\mathrm{i}ktz) + B_{\mathrm{SV}}\exp(-\mathrm{i}ktz)\big]. \quad (4.50)$$

Based on equations (4.2) and (4.3), it gives

$$\sigma_z(x,z) = \lambda^*(u_{,x} + w_{,z}) + 2G^* w_{,z}$$
$$= \mathrm{i}kl_x(1 - t^2)G^*\big[A_{\mathrm{P}}\exp(\mathrm{i}ksz) + B_{\mathrm{P}}\exp(-\mathrm{i}ksz)\big]\exp(-\mathrm{i}kx)$$
$$- 2\mathrm{i}km_x tG^*\big[A_{\mathrm{SV}}\exp(\mathrm{i}ktz) - B_{\mathrm{SV}}\exp(-\mathrm{i}ktz)\big]\exp(-\mathrm{i}kx), \quad (4.51)$$

$$\tau_{xz}(x,z) = G^*(u_{,z} + w_{,x})$$
$$= \mathrm{i}2kl_x sG^*\big[A_{\mathrm{P}}\exp(\mathrm{i}ksz) - B_{\mathrm{P}}\exp(-\mathrm{i}ksz)\big]\exp(-\mathrm{i}kx)$$
$$+ \mathrm{i}km_x(1 - t^2)G^*\big[A_{\mathrm{SV}}\exp(\mathrm{i}ktz) + B_{\mathrm{SV}}\exp(-\mathrm{i}ktz)\big]\exp(-\mathrm{i}kx). \quad (4.52)$$

Then the displacements and stresses at the top surface of layer with $z = 0$ (subscript 1) are governed by

$$\begin{Bmatrix} u_1 \\ w_1 \\ \sigma_{z1} \\ \tau_{xz1} \end{Bmatrix} = \begin{bmatrix} l_x & l_x & -m_x t & m_x t \\ -l_x s & l_x s & -m_x & -m_x \\ \mathrm{i}kl_x(1-t^2)G^* & \mathrm{i}kl_x(1-t^2)G^* & -2\mathrm{i}km_x tG^* & 2\mathrm{i}km_x tG^* \\ \mathrm{i}2kl_x sG^* & -\mathrm{i}2kl_x sG^* & \mathrm{i}km_x(1-t^2)G^* & \mathrm{i}km_x(1-t^2)G^* \end{bmatrix} \begin{Bmatrix} A_\mathrm{P}\exp(-\mathrm{i}kx) \\ B_\mathrm{P}\exp(-\mathrm{i}kx) \\ A_\mathrm{SV}\exp(-\mathrm{i}kx) \\ B_\mathrm{SV}\exp(-\mathrm{i}kx) \end{Bmatrix}. \tag{4.53}$$

The displacements and stresses at the bottom surface of layer with $z = d$ (subscript 2) are governed by

$$\begin{Bmatrix} u_2 \\ w_2 \\ \sigma_{z2} \\ \tau_{xz2} \end{Bmatrix} = \begin{bmatrix} l_x\exp(\mathrm{i}ksd) & l_x\exp(-\mathrm{i}ksd) & -m_x t\exp(\mathrm{i}ktd) & m_x t\exp(-\mathrm{i}ktd) \\ -l_x s\exp(\mathrm{i}ksd) & l_x s\exp(textiksd) & -m_x\exp(\mathrm{i}ktd) & -m_x\exp(-\mathrm{i}ktd) \\ \mathrm{i}kl_x(1-t^2)G^*\exp(\mathrm{i}ksd) & \mathrm{i}kl_x(1-t^2)G^*\exp(-\mathrm{i}ksd) & -2\mathrm{i}km_x tG^*\exp(\mathrm{i}ktd) & 2\mathrm{i}km_x tG^*\exp(-\mathrm{i}ktd) \\ \mathrm{i}2kl_x sG^*\exp(\mathrm{i}ksd) & -\mathrm{i}2kl_x sG^*\exp(-\mathrm{i}ksd) & \mathrm{i}km_x(1-t^2)G^*\exp(\mathrm{i}ktd) & \mathrm{i}km_x(1-t^2)G^*\exp(-\mathrm{i}ktd) \end{bmatrix}$$

$$\begin{Bmatrix} A_\mathrm{P}\exp(-\mathrm{i}kx) \\ B_\mathrm{P}\exp(-\mathrm{i}kx) \\ A_\mathrm{SV}\exp(-\mathrm{i}kx) \\ B_\mathrm{SV}\exp(-\mathrm{i}kx) \end{Bmatrix}. \tag{4.54}$$

Based on Euler's formula, substituting (4.53) into (4.54) to eliminate A_{P}, B_{P}, A_{SV}, B_{SV}, and $-\mathrm{i}kx$ leads to

$$\begin{Bmatrix} u_2 \\ w_2 \\ \sigma_{z2} \\ \tau_{xz2} \end{Bmatrix} = \frac{1}{1+t^2} \left[\begin{array}{cccc} 2\cos ksd+ & \mathrm{i}\frac{1-t^2}{s}\sin ksd+ & \frac{1}{ksG^*}\sin ksd+ & \frac{\mathrm{i}}{kG^*}\cos ksd- \\ (t^2-1)\cos ktd & \mathrm{i}2t\sin ktd & \frac{t}{kG^*}\sin ktd & \frac{\mathrm{i}}{kG^*}\cos ktd \\ \hline -\mathrm{i}2s\sin ksd- & (t^2-1)\cos ksd+ & \frac{\mathrm{i}}{kG^*}\cos ksd- & \frac{s}{kG^*}\sin ksd+ \\ \mathrm{i}\frac{1-t^2}{t}\sin ktd & 2\cos ktd & \frac{\mathrm{i}}{kG^*}\cos ktd & \frac{1}{ktG^*}\sin ktd \\ \hline -4kG^*s\sin ksd- & \mathrm{i}2kG^*(1-t^2)\cos ksd- & 2\cos ksd+ & -\mathrm{i}2s\sin ksd- \\ kG^*\frac{(1-t^2)^2}{t}\sin ktd & \mathrm{i}2kG^*(1-t^2)\cos ktd & (t^2-1)\cos ktd & \mathrm{i}\frac{1-t^2}{t}\sin ktd \\ \hline \mathrm{i}2kG^*(1-t^2)\cos ksd- & -kG^*\frac{(1-t^2)^2}{s}\sin ksd- & \mathrm{i}\frac{1-t^2}{s}\sin ksd+ & (t^2-1)\cos ksd+ \\ \mathrm{i}2kG^*(1-t^2)\cos ktd & 4kG^*t\sin ktd & \mathrm{i}2t\sin ktd & 2\cos ktd \end{array}\right] \begin{Bmatrix} u_1 \\ w_1 \\ \sigma_{z1} \\ \tau_{xz1} \end{Bmatrix}. \tag{4.55}$$

At the surface, the external loads are

$$P_1 = -\tau_{xz1}, \quad R_1 = -\sigma_{z1},$$

denoting the loads at the bottom as

$$P_2 = \tau_{xz2}, \quad R_2 = \sigma_{z2},$$

and performing a transformation of equation (4.55) result in

$$\begin{Bmatrix} P_1 \\ \mathrm{i}R_1 \\ P_2 \\ \mathrm{i}R_2 \end{Bmatrix} = \mathbf{K}_{\mathrm{in}} \begin{Bmatrix} u_1 \\ \mathrm{i}w_1 \\ u_2 \\ \mathrm{i}w_2 \end{Bmatrix}, \tag{4.56}$$

in which i is added before R_1, R_2, w_1, and w_2 to keep $\mathbf{K}_{\text{in}}$ symmetric.

$\mathbf{K}_{\text{in}}$ is the dynamic stiffness matrix of in-plane motion in a single layer expressed as

$$\mathbf{K}_{\text{in}} = \frac{(1+t^2kG^*)}{D}\times$$

$$\left[\begin{array}{c|c|c|c}
\begin{array}{c}\frac{1}{t}\cos ksd\sin ktd+\\ s\sin ksd\cos ktd\end{array} & \begin{array}{c}\mathrm{i}\frac{3-t^2}{1+t^2}(1-\cos ksd\cos ktd)+\\ \mathrm{i}\frac{1+2s^2t^2-t^2}{st(1+t^2)}\sin ksd\sin ktd\end{array} & \begin{array}{c}-s\sin ksd-\\ \frac{1}{t}\sin ktd\end{array} & \begin{array}{c}\mathrm{i}\cos ksd-\\ \mathrm{i}\cos ktd\end{array} \\ \hline
\begin{array}{c}-\mathrm{i}\frac{3-t^2}{1+t^2}(1-\cos ksd\cos ktd)-\\ \mathrm{i}\frac{1+2s^2t^2-t^2}{st(1+t^2)}\sin ksd\sin ktd\end{array} & \begin{array}{c}\frac{1}{s}\sin ksd\cos ktd+\\ t\cos ksd\sin ktd\end{array} & \begin{array}{c}\mathrm{i}\cos ksd-\\ \mathrm{i}\cos ktd\end{array} & \begin{array}{c}-\frac{1}{s}\sin ksd-\\ t\sin ktd\end{array} \\ \hline
\begin{array}{c}-s\sin ksd-\\ \frac{1}{t}\sin ktd\end{array} & \begin{array}{c}-\mathrm{i}\cos ksd+\\ \mathrm{i}\cos ktd\end{array} & \begin{array}{c}\frac{1}{t}\cos ksd\sin ktd+\\ s\sin ksd\cos ktd\end{array} & \begin{array}{c}-\frac{3-t^2}{1+t^2}(1-\cos ksd\cos ktd)-\\ \mathrm{i}\frac{1+2s^2t^2-\mathrm{i}t^2}{st(1+t^2)}\sin ksd\sin ktd\end{array} \\ \hline
\begin{array}{c}-\mathrm{i}\cos ksd+\\ \mathrm{i}\cos ktd\end{array} & \begin{array}{c}-\frac{1}{s}\sin ksd-\\ t\sin ktd\end{array} & \begin{array}{c}\mathrm{i}\frac{3-t^2}{1+t^2}(1-\cos ksd\cos ktd)+\\ \mathrm{i}\frac{1+2s^2t^2-t^2}{st(1+t^2)}\sin ksd\sin ktd\end{array} & \begin{array}{c}\frac{1}{s}\sin ksd\cos ktd+\\ +t\cos ksd\sin ktd\end{array}
\end{array}\right], \tag{4.57}$$

where

$$D = 2(1-\cos ksd\cos ktd) + (st + \frac{1}{st}\sin ksd\sin ktd).$$

For half-space, which means d approaches infinity, P_2, R_2, u_2 and w_2 are equal to 0. $\mathbf{K}_{\text{in}}$ becomes

$$\mathbf{K}_{\text{in}} = \frac{kG^*}{1+st}\begin{bmatrix} \mathrm{i}s(1+t^2) & 1+2st-t^2 \\ 1+2st-t^2 & \mathrm{i}t(1+t^2)\end{bmatrix}. \tag{4.58}$$

4.1.4 Formulation of Flexibility Function

A site with n horizontal layers on a half-space is considered. Three dimensional forces with frequency ω are applied at the origin as shown in Figure 4.6.

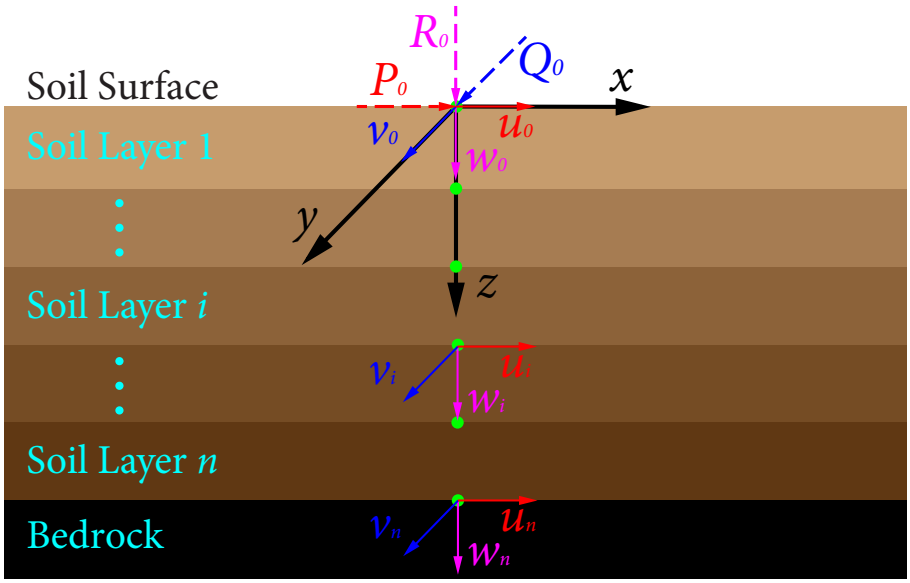

Figure 4.6 Layered half-space under three-dimensional forces

Flexibility Function of Out-of-Plane Motion

According to equation (4.40), the equilibrium equations are expressed as

$$\begin{Bmatrix} Q_1^i \\ Q_2^i \end{Bmatrix} = \mathbf{K}_{\text{out}}^i \begin{Bmatrix} v_1^i \\ v_2^i \end{Bmatrix}, \tag{4.59}$$

where i is the number of layer, and varies from 1 to $n-1$. The subscripts 1 and 2 are denoted the top and bottom of the layer, respectively. When i is equal to n, i.e., the bottom half-space, the equilibrium equation is

$$Q_1^n = \mathbf{K}_{\text{out}}^n v_1^n. \tag{4.60}$$

Since all the forces, excluding the external forces applied at the surface, are internal forces, it means the forces at any interface follow

$$Q_2^i + Q_1^{i+1} = 0.$$

Then the total equilibrium equations for out-of-plane motion is obtained by assembling the equilibrium equations of each layer as

$$\mathbf{L}_{\text{out}} = \mathbf{S}_{\text{out}}\boldsymbol{\Delta}_{\text{out}}, \tag{4.61}$$

where $\mathbf{L}_{\text{out}}$ and $\boldsymbol{\Delta}_{\text{out}}$ are the $n\times 1$ vectors of external loads and displacements in y direction, respectively, given as

$$\mathbf{L}_{\text{out}} = \{Q_1,\, Q_2,\, \cdots,\, Q_n\}^T = \{Q_1,\, 0,\, \cdots,\, 0\}^T$$

$$\boldsymbol{\Delta}_{\text{out}} = \{v_1,\, v_2,\, \cdots,\, v_n\}^T.$$

$\mathbf{S}_{\text{out}}$ is a $n\times n$ matrix and assembled by $\mathbf{K}^i_{\text{out}}$ and $\mathbf{K}^n_{\text{out}}$. For two adjacent layers, $\mathbf{K}^i_{\text{out}}$ are partly overlapped.

Rewriting equation (4.61) as

$$\begin{Bmatrix} \mathbf{Q}_1 \\ \mathbf{Q}_{2\sim n} \end{Bmatrix} = \begin{bmatrix} \mathbf{S}_{\text{out},1,1} & \mathbf{S}_{\text{out},1,2\sim n} \\ \mathbf{S}_{\text{out},2\sim n,1} & \mathbf{S}_{\text{out},2\sim n,2\sim n} \end{bmatrix} \begin{Bmatrix} \mathbf{v}_1 \\ \mathbf{v}_{2\sim n} \end{Bmatrix}$$

to eliminate $\mathbf{v}_{2\sim n}$ gives

$$\begin{aligned} \mathbf{Q}_1 &= \mathbf{S}_{\text{out},1,1}\cdot\mathbf{v}_1 + \mathbf{S}_{\text{out},1,2\sim n}\cdot\mathbf{S}^{-1}_{\text{out},2\sim n,2\sim n}\cdot\left(\mathbf{Q}_{2\sim n} - \mathbf{S}_{\text{out},2\sim n,1}\cdot\mathbf{v}_1\right) \\ &= \left(\mathbf{S}_{\text{out},1,1} - \mathbf{S}_{\text{out},1,2\sim n}\cdot\mathbf{S}^{-1}_{\text{out},2\sim n,2\sim n}\cdot\mathbf{S}_{\text{out},2\sim n,1}\right)\cdot\mathbf{v}_1. \end{aligned} \tag{4.62}$$

Based on equation (4.62), one obtains

$$\mathbf{v}_1 = \mathbf{F}_{\text{out}}\mathbf{Q}_1, \tag{4.63}$$

in which $\mathbf{F}_{\text{out}}$ is the flexibility function of out-of-plane motion and it is equal to

$$\mathbf{F}_{\text{out}} = \mathbf{F}_{vv} = \left(\mathbf{S}_{\text{out},1,1} - \mathbf{S}_{\text{out},1,2\sim n}\mathbf{S}^{-1}_{\text{out},2\sim n,2\sim n}\mathbf{S}_{\text{out},2\sim n,1}\right)^{-1}. \tag{4.64}$$

Flexibility Function of In-Plane Motion

According to equation (4.56), the equilibrium equations fir in-plane motion are expressed as

$$\begin{Bmatrix} P_1^i \\ R_1^i \\ P_2^i \\ R_2^i \end{Bmatrix} = \mathbf{K}_{\text{in}}^i \begin{Bmatrix} u_1^i \\ w_1^i \\ u_2^i \\ w_2^i \end{Bmatrix}. \tag{4.65}$$

When i is equal to n, i.e., the half-space case, the equilibrium equations become

$$\begin{Bmatrix} P_1^n \\ R_1^n \end{Bmatrix} = \mathbf{K}_{\text{in}}^n \begin{Bmatrix} u_1^n \\ w_1^n \end{Bmatrix}. \tag{4.66}$$

Since all the forces, except the external forces applied at the surface, are internal forces, it means the forces at any interface follow

$$P_2^i + P_1^{i+1} = 0,$$

$$R_2^i + R_1^{i+1} = 0.$$

Then the total equilibrium equations for in-plane case is obtained by assembling the equilibrium equations of each layer as

$$\mathbf{L}_{\text{in}} = \mathbf{S}_{\text{in}} \boldsymbol{\Delta}_{\text{in}}, \tag{4.67}$$

where $\mathbf{L}_{\text{in}}$ and $\boldsymbol{\Delta}_{\text{in}}$ are the $2n \times 1$ vectors of external loads and displacements in x and z directions, respectively, as

$$\mathbf{L}_{\text{in}} = \left\{P_1,\, R_1,\, P_2,\, R_2,\, \cdots,\, P_n,\, R_n\right\}^T = \left\{P_1,\, R_1,\, 0,\, 0,\, \cdots,\, 0,\, 0\right\}^T,$$

$$\boldsymbol{\Delta}_{\text{in}} = \left\{u_1,\, w_1,\, u_2,\, w_2,\, \cdots,\, u_n,\, w_n\right\}^T.$$

$\mathbf{S}_{\text{in}}$ is a $2n \times 2n$ matrix and assembled by $\mathbf{K}_{\text{in}}^i$ and $\mathbf{K}_{\text{in}}^n$. For two adjacent layers, $\mathbf{K}_{\text{in}}^i$ are partly overlapped.

Rewriting equation (4.67) as

$$\begin{Bmatrix} \mathbf{L}_{\text{in},1\sim2} \\ \mathbf{L}_{\text{in},3\sim2n} \end{Bmatrix} = \begin{bmatrix} \mathbf{S}_{\text{in}1\sim2,1\sim2} & \mathbf{S}_{\text{in},1\sim2,3\sim2n} \\ \mathbf{S}_{\text{in},3\sim2n,1\sim2} & \mathbf{S}_{\text{in},3\sim2n,3\sim2n} \end{bmatrix} \begin{Bmatrix} \boldsymbol{\Delta}_{\text{in},1\sim2} \\ \boldsymbol{\Delta}_{\text{in},3\sim2n} \end{Bmatrix}$$

to eliminate $\mathbf{\Delta}_{\text{in},3\sim 2n}$ gives

$$\begin{aligned}\mathbf{L}_{\text{in},1\sim 2} &= \mathbf{S}_{\text{in},1\sim 2,1\sim 2}\cdot\mathbf{\Delta}_{\text{in},1\sim 2}\\ &\quad+\mathbf{S}_{\text{in},1\sim 2,3\sim 2n}\cdot\mathbf{S}^{-1}_{\text{in},3\sim 2n,3\sim 2n}\cdot\left(\mathbf{L}_{\text{in},3\sim 2n}-\mathbf{S}_{\text{in},3\sim 2n,1\sim 2}\cdot\mathbf{\Delta}_{\text{in},1\sim 2}\right)\\ &=\left(\mathbf{S}_{\text{in},1\sim 2,1\sim 2}-\mathbf{S}_{\text{in},1\sim 2,3\sim 2n}\cdot\mathbf{S}^{-1}_{\text{in},3\sim 2n,3\sim 2n}\cdot\mathbf{S}_{\text{in},3\sim 2n,1\sim 2}\right)\cdot\mathbf{\Delta}_{\text{in},1\sim 2}.\end{aligned}\tag{4.68}$$

Based on equation (4.68), it is derived in

$$\begin{Bmatrix}u_1\\ w_1\end{Bmatrix}=\mathbf{F}_{\text{in}}\begin{Bmatrix}P_1\\ R_1\end{Bmatrix},\tag{4.69}$$

in which $\mathbf{F}_{\text{in}}$ is the flexibility function of in-plane motion and it is equal to

$$\mathbf{F}_{\text{in}}=\begin{bmatrix}F_{uu} & F_{uw}\\ F_{wu} & F_{ww}\end{bmatrix}=\left(\mathbf{S}_{\text{in},1\sim 2,1\sim 2}-\mathbf{S}_{\text{in},1\sim 2,3\sim 2n}\mathbf{S}^{-1}_{\text{in},3\sim 2n,3\sim 2n}\mathbf{S}_{\text{in},3\sim 2n,1\sim 2}\right)^{-1}.\tag{4.70}$$

4.1.5 Formulation of Green's Influence Function

Based on the flexibility function, Green's influence function is formulated to get the displacement of any points when a small circular disk is loaded (Wolf, 1985). A circular disk with radius of a under uniformly distributed horizontal loads, p_0 and q_0, and vertical load r_0 is studied as shown in Figure 4.7.

In cylindrical coordinates, the load can be expressed as Fourier series as

$$p(r,\theta,z,n)=\sum_n p_s(r,\theta,z)\cos\theta+\sum_n p_a(r,\theta,z)\sin\theta,\tag{4.71}$$

where r, θ, and z are radial distance, azimuth, and height. n is the Fourier series number. p_s and p_a are the symmetric and anti-symmetric amplitude in Fourier series.

The load and displacement can also be expanded in frequency domain with wave number k by Bessel transform pair

$$\left\{f(k,n)\right\}=a_n\int_{r=0}^{\infty}r\mathbf{C}_n(kr)\int_{\theta=0}^{\pi}\mathbf{D}_{n\theta}\left\{f(r,\theta)\right\}\mathrm{d}\theta\,\mathrm{d}r,\tag{4.72}$$

$$\left\{f(r,\theta)\right\}=\sum_{r=0}^{\infty}\mathbf{D}_{n\theta}\int_{k=0}^{\infty}k\mathbf{C}_n(kr)\left\{f(k,n)\right\}\mathrm{d}k,\tag{4.73}$$

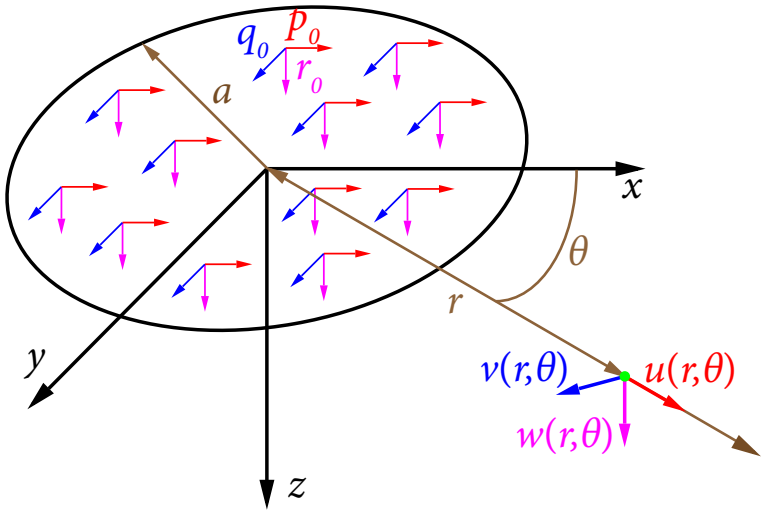

Figure 4.7 Disk under three-dimensional uniform load

where a_n is equal to $1/2\pi$ $(n = 0)$, or $1/\pi$ $(n \neq 0)$.

$\mathbf{C}_n(kr)$ is given by

$$\mathbf{C}_n(kr) = \begin{bmatrix} \frac{1}{k}J_n(kr)_{,r} & \frac{n}{kr}J_n(kr) & 0 \\ \frac{n}{kr}J_n(kr) & \frac{1}{k}J_n(kr)_{,r} & 0 \\ 0 & 0 & -J_n(kr) \end{bmatrix}, \tag{4.74}$$

in which $J_n(kr)$ is the Bessel function of order n of the first kind. The Bessel function holds the following features:

$$\left[x^n J_n(x)\right]_{,x} = x^n J_{n-1}(x) \quad \text{or} \quad \int x^n J_{n-1}(x)\mathrm{d}x = x^n J_n(x) + \text{constant}, \tag{4.75}$$

$$\left[x^{-n} J_n(x)\right]_{,x} = -x^{-n} J_{n+1}(x), \tag{4.76}$$

$$\left[J_n(x)\right]_{,x} = J_{n-1}(x) - \frac{n}{x}J_n(x) = \frac{n}{x}J_n(x) - J_{n+1}(x). \tag{4.77}$$

$\mathbf{D}_{n\theta}$, for symmetric case, is equal to

$$\mathbf{D}_{n\theta} = \begin{bmatrix} \cos n\theta & 0 & 0 \\ 0 & -\sin n\theta & 0 \\ 0 & 0 & \cos n\theta \end{bmatrix}, \tag{4.78}$$

while, for anti-symmetric case, it is

$$\mathbf{D}_{n\theta} = \begin{bmatrix} \sin n\theta & 0 & 0 \\ 0 & \cos n\theta & 0 \\ 0 & 0 & \sin n\theta \end{bmatrix}. \tag{4.79}$$

Green's Influence Function Under Vertical Load

The vertical uniform load r_0 is considered at first as shown in Figure 4.8.

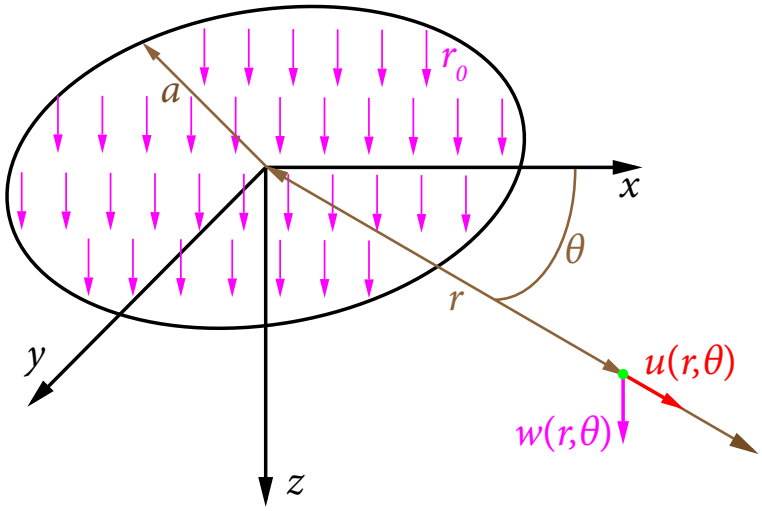

Figure 4.8 Disk under vertical uniform load

Based on equation (4.71), p_z can be considered as symmetric load with Fourier index of 0 as

$$p_z(r,\theta) = r_0.$$

According to equation (4.72), p_z can be transformed in k domain as

$$p_z(k) = \frac{1}{2\pi}\int_{r=0}^{a} r\big[-J_0(kr)\big]\int_0^{2\pi}\cos\theta\, r_0 \mathrm{d}\theta \mathrm{d}r = -r_0\int_{r=0}^{a} rJ_0(kr)\mathrm{d}r. \tag{4.80}$$

Given the identity of Bessel function as shown in equation (4.75), equation (4.80) can be rewritten as

$$p_z(k) = -\frac{a}{k}J_1(ka)r_0. \tag{4.81}$$

Then the displacements in racial, u, and vertical directions, w, in frequency domain are given based on equation (4.73) as

$$\begin{Bmatrix} u(r,\theta) \\ w(r,\theta) \end{Bmatrix} = \begin{bmatrix} \cos\theta & 0 \\ 0 & \cos\theta \end{bmatrix} \int_{k=0}^{\infty} k \begin{bmatrix} \frac{J_0(kr),_r}{r} & 0 \\ 0 & -J_0(kr) \end{bmatrix} \begin{Bmatrix} u(k) \\ w(k) \end{Bmatrix} \mathrm{d}k. \tag{4.82}$$

Based on equations (4.63) and (4.69), one obtains

$$\begin{Bmatrix} u(k) \\ w(k) \end{Bmatrix} = \begin{Bmatrix} F_{uw}(k) \\ F_{ww}(k) \end{Bmatrix} p_z(k). \tag{4.83}$$

Substituting equations (4.83) and (4.81) into equation (4.82), and applying the identity of Bessel function as shown in equation (4.76), lead to

$$\begin{Bmatrix} u(r,\theta) \\ w(r,\theta) \end{Bmatrix} = \begin{Bmatrix} G_{uw} \\ G_{ww} \end{Bmatrix} r_0, \tag{4.84}$$

where G_{uw} and G_{ww} are Green's function in radial and vertical directions under the vertical load as

$$\begin{Bmatrix} G_{uw} \\ G_{ww} \end{Bmatrix} = a \int_{k=0}^{\infty} J_1(ka) \begin{Bmatrix} F_{uw}(k) J_1(kr) \\ F_{ww}(k) J_0(kr) \end{Bmatrix} \mathrm{d}k, \tag{4.85}$$

Green's Influence Function Under Horizontal Load

Then the horizontal uniform load p_0 is studied as shown in Figure 4.9.

Based on equation (4.71), p_x and p_y can be considered as anti-symmetric load with Fourier index of 1 as

$$p_x(r,\theta) = p_0 \cos\theta, \qquad p_y(r,\theta) = -p_0 \sin\theta.$$

According to equation (4.72), it is derived in k domain as

$$\begin{Bmatrix} p_x(k) \\ p_y(k) \end{Bmatrix} = \frac{1}{\pi} \int_{r=0}^{a} r \begin{bmatrix} \frac{1}{k} J_1(kr),_r & \frac{1}{kr} J_1(kr) \\ \frac{1}{kr} J_1(kr) & \frac{1}{k} J_1(kr),_r \end{bmatrix} \mathrm{d}r \int_0^{2\pi} \begin{bmatrix} \cos\theta & 0 \\ 0 & -\sin\theta \end{bmatrix} \begin{Bmatrix} p_0 \cos\theta \\ -p_0 \sin\theta \end{Bmatrix} \mathrm{d}\theta$$

$$= \frac{p_0}{k} \int_{r=0}^{a} \begin{bmatrix} rJ_1(kr),_r + J_1(kr) \\ rJ_1(kr),_r + J_1(kr) \end{bmatrix} \mathrm{d}r. \tag{4.86}$$

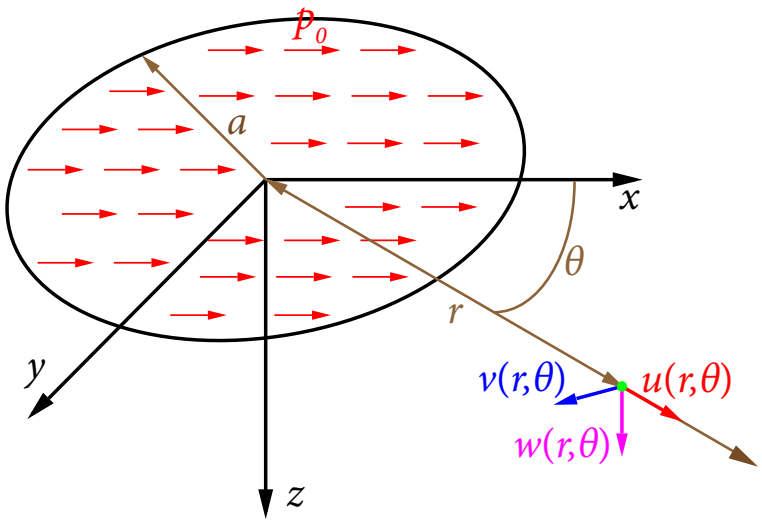

Figure 4.9 Disk under horizontal uniform load

Based on identities of Bessel functions as shown in equation (4.75), equation (4.86) can be rewritten as

$$\begin{aligned} p_x(k) = p_y(k) &= \frac{p_0}{k}\int_{r=0}^{a}\left(rJ_1(kr)_{,r} + J_1(kr)\right)\mathrm{d}r \\ &= \frac{p_0}{k}\left(\int_{r=0}^{a} krJ_0(kr)\mathrm{d}r + \int_{r=0}^{a} J_1(kr)\mathrm{d}r\right) = \frac{p_0 a}{k}J_1(ka). \end{aligned} \tag{4.87}$$

Then the displacements in racial, u, and vertical directions, w, are given in frequency domain by equation (4.73) as

$$\begin{Bmatrix} u(r,\theta) \\ v(r,\theta) \\ w(r,\theta) \end{Bmatrix} = \begin{bmatrix} \cos\theta & 0 & 0 \\ 0 & -\sin\theta & 0 \\ 0 & 0 & \cos\theta \end{bmatrix} \int_{k=0}^{\infty} k \begin{bmatrix} \frac{1}{k}J_1(kr)_{,r} & \frac{1}{kr}J_1(kr) & 0 \\ \frac{n}{kr}J_1(kr) & \frac{1}{k}J_1(kr)_{,r} & 0 \\ 0 & 0 & -J_1(kr) \end{bmatrix} \begin{Bmatrix} u(k) \\ v(k) \\ w(k) \end{Bmatrix} \mathrm{d}k. \tag{4.88}$$

Through equations (4.63) and (4.69), one obtains

$$\begin{Bmatrix} u(k) \\ v(k) \\ w(k) \end{Bmatrix} = \begin{bmatrix} F_{uu}(k) & 0 \\ 0 & F_{vv}(k) \\ F_{wu}(k) & 0 \end{bmatrix} \begin{Bmatrix} p_x(k) \\ p_y(k) \end{Bmatrix}. \tag{4.89}$$

Substituting equations (4.87) and (4.89) into equation (4.88), and applying the identities of Bessel functions as equations (4.76) and (4.77) result in

$$\begin{Bmatrix} u(r,\theta) \\ v(r,\theta) \\ w(r,\theta) \end{Bmatrix} = \begin{Bmatrix} G_{uu} \\ G_{vu} \\ G_{wu} \end{Bmatrix} p_0, \tag{4.90}$$

where G_{uu}, G_{vu}, and G_{wu} are Green's function in radial, angular, and vertical directions under horizontal load in x direction as

$$\begin{Bmatrix} G_{uu} \\ G_{vu} \\ G_{wu} \end{Bmatrix} = a \begin{bmatrix} \cos\theta & 0 & 0 \\ 0 & -\sin\theta & 0 \\ 0 & 0 & \cos\theta \end{bmatrix} \int_{k=0}^{\infty} J_1(ka) \begin{bmatrix} \frac{1}{2}J_0(kr) - \frac{1}{2}J_2(kr) & 0\frac{1}{2}J_0(kr) + \frac{1}{2}J_2(kr) & 0 \\ \frac{1}{2}J_0(kr) + \frac{1}{2}J_2(kr) & 0\frac{1}{2}J_0(kr) - \frac{1}{2}J_2(kr) & 0 \\ 0 & 0 & -J_1(kr) \end{bmatrix} \begin{Bmatrix} F_{uu}(k) \\ F_{vv}(k) \\ F_{wu}(k) \end{Bmatrix} \mathrm{d}k. \tag{4.91}$$

For the horizontal load in y direction q_0, it can be considered as an anti-symmetric load in cylindric coordinate. $\mathbf{D}_{n\theta}$ is applied as (4.79) rather than (4.78). So the Green's influence function is expressed as

$$\begin{Bmatrix} G_{uv} \\ G_{vv} \\ G_{wv} \end{Bmatrix} = a \begin{bmatrix} \sin\theta & 0 & 0 \\ 0 & \cos\theta & 0 \\ 0 & 0 & \sin\theta \end{bmatrix} \int_{k=0}^{\infty} J_1(ka) \begin{bmatrix} \frac{1}{2}J_0(kr) - \frac{1}{2}J_2(kr) & \frac{1}{2}J_0(kr) + \frac{1}{2}J_2(kr) & 0 \\ \frac{1}{2}J_0(kr) + \frac{1}{2}J_2(kr) & \frac{1}{2}J_0(kr) - \frac{1}{2}J_2(kr) & 0 \\ 0 & 0 & -J_1(kr) \end{bmatrix} \begin{Bmatrix} F_{uu}(k) \\ F_{vv}(k) \\ F_{wu}(k) \end{Bmatrix} \mathrm{d}k, \tag{4.92}$$

Green's Influence Function Under Three Dimensional Loads

When three dimensional loads, i.e., p_0, q_0, and r_0, are considered simultaneously, the displacements at point i in cylindrical coordinate are

$$\begin{Bmatrix} u_i(r,\theta) \\ v_i(r,\theta) \\ w_i(r,\theta) \end{Bmatrix} = \mathbf{G}_i^c \begin{Bmatrix} p_i \\ q_i \\ r_i \end{Bmatrix}, \tag{4.93}$$

where

$$\mathbf{G}_i^c = \begin{bmatrix} G_{uu,i} & G_{uv,i} & G_{uw,i} \\ G_{vu,i} & G_{uv,i} & 0 \\ G_{wu,i} & G_{wv,i} & G_{ww,i} \end{bmatrix}. \tag{4.94}$$

Then the displacements in cartesian coordinate, $\delta_{x,i}$, $\delta_{y,i}$, and $\delta_{x,i}$, can be expressed as

$$\begin{Bmatrix} \delta_{x,i}(x,y) \\ \delta_{y,i}(x,y) \\ \delta_{z,i}(x,y) \end{Bmatrix} = \mathbf{T}_i \begin{Bmatrix} u_i(r,\theta) \\ v_i(r,\theta) \\ w_i(r,\theta) \end{Bmatrix} = \mathbf{T}_i \mathbf{G}_i^c \begin{Bmatrix} p_i \\ q_i \\ r_i \end{Bmatrix}, \tag{4.95}$$

where

$$\mathbf{T}_i = \begin{bmatrix} \cos\theta_i & -\sin\theta_i & 0 \\ \sin\theta_i & \cos\theta_i & 0 \\ 0 & 0 & 1 \end{bmatrix}, \tag{4.96}$$

in which θ^i is the coordinate of point i in cylindric coordinate with the origin of the disk center.

So the Green's influence function in cartesian coordinate is given by

$$\mathbf{G}_i = \mathbf{T}_i \mathbf{G}_i^c. \tag{4.97}$$

4.1.6 Total Dynamic Soil Stiffness by Boundary Element Method

Dynamic Stiffness for Rigid Foundation

A rigid foundation can be simplified as one node with 6 degrees of freedom, i.e., three translational components and three rotational components. A rigid foundation with arbitrary

shape supported by a horizontally layered half-space are shown in Figure 4.10. The foundation is discretized into n uniformly distributed subdisks with the radius a. The total area of subdisks is the same as the original foundation. a is small enough that the displacement within each subdisk can be considered the same. Since 6 points in a wavelength are needed to address each wave (Wolf, 1985), a should be no more than $c_s/6f_{\max}$, in which $f_{\max}$ is the maximum frequency under consideration.

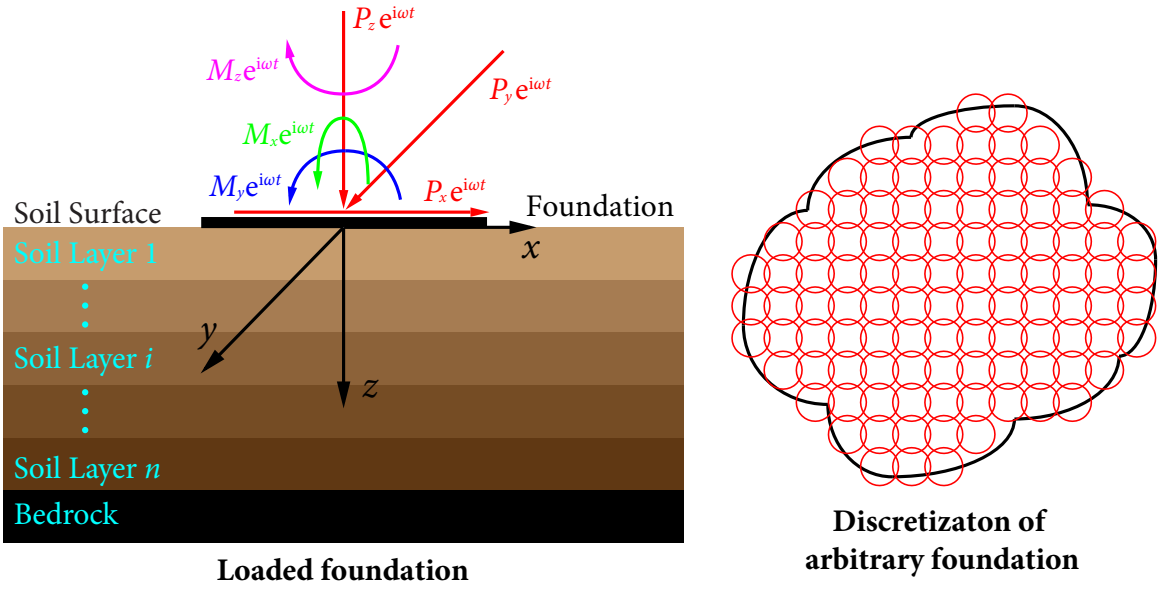

Figure 4.10 Foundation-site model and discretization of foundation

The six dimensional external loads $\mathbf{P}_r$ applied on the foundation and the displacements $\mathbf{\Delta}_r$ caused by the load vector are

$$\mathbf{P}_r = \left\{F_x,\, F_y,\, F_z,\, M_x,\, M_y,\, M_z\right\}^T,$$

$$\mathbf{\Delta}_r = \left\{\Delta_x,\, \Delta_y,\, \Delta_z,\, \theta_x,\, \theta_y,\, \theta_z\right\}^T,$$

where F_x, F_y, and F_z are translational loads in x, y, and z directions, respectively, while M_x, M_y, and M_z are moments in three directions. Δ_x, Δ_y, and Δ_z are translational displacements in x, y, and z directions, respectively, and θ_x, θ_y, and θ_z are rotations in three directions.

Then the ith subdisk is considered, where i ranges from 1 to n. When the three dimensional loads $p_{x,i}$, $p_{y,i}$, and $p_{z,i}$ are applied on this disk, the displacements of the jth disk are

$$\begin{Bmatrix} \delta_{x,ji} \\ \delta_{y,ji} \\ \delta_{z,ji} \end{Bmatrix} = \mathbf{G}_{ji} \begin{Bmatrix} p_{x,i} \\ p_{y,i} \\ p_{z,i} \end{Bmatrix}, \tag{4.98}$$

where is $\mathbf{G}_{ji}$ a 3×3 matrix given by equation (4.97).

By loading the disks one by one, the total displacements of each disk can be obtained as

$$\boldsymbol{\delta} = \mathbf{G}\mathbf{p}, \tag{4.99}$$

where $\boldsymbol{\delta}$ and $\mathbf{p}$ are the $3n\times1$ displacement vector and the $3n\times1$ load vector of all nodes, respectively, as

$$\boldsymbol{\delta} = \left\{\delta_{x,1}, \delta_{y,1}, \delta_{z,1}, \cdots, \delta_{x,n}, \delta_{y,n}, \delta_{z,n}\right\}^T,$$
$$\mathbf{p} = \left\{p_{x,1}, p_{y,1}, p_{z,1}, \cdots, p_{x,n}, p_{y,n}, p_{z,n}\right\}^T,$$

and $\mathbf{G}$ are the $3n\times3n$ total Green's function matrix as

$$\mathbf{G} = \begin{bmatrix} \mathbf{G}_{11} & \mathbf{G}_{12} & \cdots & \mathbf{G}_{1n} \\ \mathbf{G}_{21} & \mathbf{G}_{22} & \cdots & \mathbf{G}_{2n} \\ \vdots & \vdots & \ddots & \vdots \\ \mathbf{G}_{n1} & \mathbf{G}_{n2} & \cdots & \mathbf{G}_{nn} \end{bmatrix}.$$

The relationship of $\boldsymbol{\Delta}_r$ and δ is

$$\boldsymbol{\delta} = \mathbf{N}_r\boldsymbol{\Delta}_r, \tag{4.100}$$

where $\mathbf{N}_r$ is a $3n\times6$ matrix given by

$$\mathbf{N}_r = \left\{\mathbf{N}_1, \mathbf{N}_2, \cdots, \mathbf{N}_n\right\}^T,$$

in which

$$\mathbf{N}_i = \begin{bmatrix} 1 & 0 & 0 & 0 & 0 & -y_i \\ 0 & 1 & 0 & 0 & 0 & x_i \\ 0 & 0 & 1 & y_i & x_i & 0 \end{bmatrix},$$

x_i and y_i are the coordinates of ith disk center.

For the external loads, one obtains

$$\mathbf{P}_r = \mathbf{N}_r^T \mathbf{p}. \tag{4.101}$$

Substituting equations (4.99) and (4.100) into equation (4.101) leads to

$$\mathbf{P}_r = \mathbf{N}_r^T \mathbf{G}^{-1} \boldsymbol{\delta}_{3n\times 1} = \mathbf{N}_r^T \mathbf{G}^{-1} \mathbf{N}_r \boldsymbol{\Delta}_r,$$

which can be written as

$$\mathbf{P}_r = \mathbf{K}_r \boldsymbol{\Delta}_r, \tag{4.102}$$

where $\mathbf{K}_r$ is the 6×6 stiffness matrix of the soil base as

$$\mathbf{K}_r = \mathbf{N}_r^T \mathbf{G}^{-1} \mathbf{N}_r. \tag{4.103}$$

$\mathbf{K}_r$ is determined by the frequency of excitation forces, the geometry of the foundation, soil properties, and thickness of each layer.

Dynamic Stiffness for Flexible Foundation

A flexible foundation, e.g., a group of independent foundations or a foundation consisting of more than one member, can be simplified as m nodes with $6m$ degrees of freedom. Each node represents a rigid part or member. The whole flexible foundation is then discretized into n uniformly distributed subdisks with the radius a. The total area of subdisks is the same as the original foundation.

The $6m\times 1$ external loads vector $\mathbf{P}_f$ applied on the foundation and the $6m\times 1$ displacements vector $\boldsymbol{\Delta}_f$ caused by the load vector are

$$\mathbf{P}_f = \left\{\mathbf{P}^1,\ \mathbf{P}^2,\ \cdots,\ \mathbf{P}^m\right\}^T,$$

$$\boldsymbol{\Delta}_f = \left\{\boldsymbol{\Delta}^1,\ \boldsymbol{\Delta}^2,\ \cdots,\ \boldsymbol{\Delta}^m\right\}^T,$$

where

$$\mathbf{P}^j = \left\{F_x^j,\ F_y^j,\ F_z^j,\ M_x^j,\ M_y^j,\ M_z^j\right\}^T,$$

$$\boldsymbol{\Delta}^j = \left\{\Delta_x^j,\ \Delta_y^j,\ \Delta_z^j,\ \theta_x^j,\ \theta_y^j,\ \theta_z^j\right\}^T,$$

the superscript j is the foundation node number, F_x^j, F_y^j, and F_z^j are translational loads in x, y, and z directions on jth foundation member, respectively, while M_x^j, M_y^j, and M_z^j are moments in three directions. Δ_x^j, Δ_y^j, and Δ_z^j are translational displacements in x, y, and z directions on jth foundation member, respectively, and θ_x^j, θ_y^j, and θ_z^j are rotations in three directions.

Similar to the rigid foundation, the relationship of $\boldsymbol{\Delta}_f$ and $\boldsymbol{\delta}$ is

$$\boldsymbol{\delta} = \mathbf{N}_f \boldsymbol{\Delta}_f, \tag{4.104}$$

where $\mathbf{N}_f$ is a $3n \times 6m$ matrix.

When the foundation is considered as flexible and represented by m foundation nodes, $\mathbf{N}_f$ can be obtained from the stiffness and damping matrices of foundations. If external loads $\mathbf{P}\mathrm{e}^{\mathrm{i}\omega t}$ are applied on m foundation nodes, the displacement are governed by

$$\begin{bmatrix} \mathbf{M}_{\mathrm{m}} & \mathbf{0} \\ \mathbf{0} & \mathbf{0} \end{bmatrix} \begin{Bmatrix} \ddot{\mathbf{u}}_{\mathrm{m}}(t) \\ \ddot{\mathbf{u}}_{\mathrm{n}}(t) \end{Bmatrix} + \begin{bmatrix} \mathbf{C}_{\mathrm{mm}} & \mathbf{C}_{\mathrm{mn}} \\ \mathbf{C}_{\mathrm{nm}} & \mathbf{C}_{\mathrm{nn}} \end{bmatrix} \begin{Bmatrix} \dot{\mathbf{u}}_{\mathrm{m}}(t) \\ \dot{\mathbf{u}}_{\mathrm{n}}(t) \end{Bmatrix} + \begin{bmatrix} \mathbf{K}_{\mathrm{mm}} & \mathbf{K}_{\mathrm{mn}} \\ \mathbf{K}_{\mathrm{nm}} & \mathbf{K}_{\mathrm{nn}} \end{bmatrix} \begin{Bmatrix} \mathbf{u}_{\mathrm{m}}(t) \\ \mathbf{u}_{\mathrm{n}}(t) \end{Bmatrix} = \begin{bmatrix} \mathbf{P}\mathrm{e}^{\mathrm{i}\omega t} \\ 0 \end{bmatrix}, \tag{4.105}$$

where $\mathbf{M}$, $\mathbf{C}$, $\mathbf{K}$ are, respectively, the mass, damping, and stiffness matrices. They can be extracted from finite element model. The subscripts m and n represent foundation nodes and subdisks nodes, respectively.

Introducing $\mathbf{u}_{\mathrm{m}}(t) = \boldsymbol{\Delta}\,\mathrm{e}^{\mathrm{i}\omega t}$ and $\mathbf{u}_{\mathrm{n}}(t) = \boldsymbol{\delta}\,\mathrm{e}^{\mathrm{i}\omega t}$ leads the second block row of Equation (4.105) to

$$(-\mathrm{i}\omega\mathbf{C}_{\mathrm{nm}} + \mathbf{K}_{\mathrm{nm}})\boldsymbol{\Delta} + (-\mathrm{i}\omega\mathbf{C}_{\mathrm{nn}} + \mathbf{K}_{\mathrm{nn}})\boldsymbol{\delta} = 0, \tag{4.106}$$

which can be rewritten as

$$\boldsymbol{\delta} = \mathbf{N}_f \boldsymbol{\Delta}, \tag{4.107}$$

where

$$\mathbf{N}_f = -(-\mathrm{i}\omega\mathbf{C}_{\mathrm{nn}} + \mathbf{K}_{\mathrm{nn}})^{-1}(-\mathrm{i}\omega\mathbf{C}_{\mathrm{nm}} + \mathbf{K}_{\mathrm{nm}}). \tag{4.108}$$

When the foundation consists of m rigid components, e.g., a discrete foundation system, $\mathbf{N}_f$ is given by

$$\mathbf{N}_f = \begin{Bmatrix} \mathbf{N}_{11} & \mathbf{N}_{12} & \cdots & \mathbf{N}_{1m} \\ \mathbf{N}_{21} & \mathbf{N}_{22} & \cdots & \mathbf{N}_{2m} \\ \vdots & \vdots & \ddots & \vdots \\ \mathbf{N}_{n1} & \mathbf{N}_{2n} & \cdots & \mathbf{N}_{nm} \end{Bmatrix},$$

in which, when the ith subdisk is within the jth foundation member,

$$\mathbf{N}_{ij} = \begin{bmatrix} 1 & 0 & 0 & 0 & 0 & -(y_i - y_j) \\ 0 & 1 & 0 & 0 & 0 & x_i - x_j \\ 0 & 0 & 1 & y_i - y_j & x_i - x_j & 0 \end{bmatrix}.$$

Otherwise $\mathbf{N}_{ij}$ is a zero matrix if the ith subdisk is not under the jth foundation component. x_j and y_j are the coordinates of jth foundation component center.

Considering the external loads, one obtains

$$\mathbf{P}_f = \mathbf{N}_f^T \mathbf{p}. \tag{4.109}$$

Substituting equations (4.99) and (4.104) into equation (4.109) leads to

$$\mathbf{P}_f = \mathbf{N}_f^T \mathbf{G}^{-1} \boldsymbol{\delta}_{3n\times 1} = \mathbf{N}_f^T \mathbf{G}^{-1} \mathbf{N}_f \boldsymbol{\Delta}_f,$$

which can be written as

$$\mathbf{P}_f = \mathbf{K}_f \boldsymbol{\Delta}_f, \tag{4.110}$$

where $\mathbf{K}_r$ is the frequency-dependent $6m\times 6m$ stiffness matrix of the soil base under the flexible foundation as

$$\mathbf{K}_f = \mathbf{N}_f^T \mathbf{G}^{-1} \mathbf{N}_f. \tag{4.111}$$

4.1.7 Procedures of Generating Frequency-Dependant Complex Soil Stiffness

The derivation of frequency-dependent dynamic soil stiffness is illustrated in Figure 4.11.

For a horizontally layered soil site, a procedure for generating frequency-dependant dynamic soil stiffness is summarized as follows:

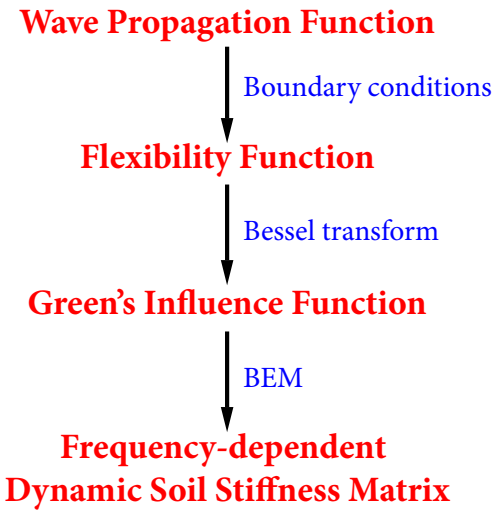

Figure 4.11 Procedures to generate frequency-dependent soil stiffness

1. Given the soil properties of each layer, the dynamic stiffness matrix is established for each layer under point loads.
2. The dynamic stiffness matrix is assembled to calculate the flexibility function.
3. The foundation is discretized into small subdisks, i.e., circular elements. Through considering the loaded subdisk one by one, the Green's Function is obtained based on the flexibility function.
4. Boundary element method is applied to generate frequency-dependent dynamic soil stiffness.

4.2 Numerical Examples of the Generation of Dynamic Soil Stiffness

In order to verify the proposed method, four numerical examples are performed. The resultant dynamic soil stiffness are compared.

4.2.1 A Rigid Square Foundation Supported by a Layer on Half-space

The dynamic soil stiffness of a rigid square foundation with side length of L is considered on a layer with the thickness of L resting on a half-space. The Poisson's ratio for the both layers is 0.33, and the damping ratios are equal to 0.05 for the top layer and 0.03 for the half-space. The ratios of the shear-wave velocities and densities are $c_{s,2}/c_{s,1} = 1.25$ and $\rho_2/\rho_1 = 1.13$, in which the subscripts 1 and 2 denote the top layer and half-space, respectively. In this example, the square foundation is divided into 256 subdisks with the diameter of $L/16$. The foundation-soil model, and the discretization of foundation are shown in Figure 4.12.

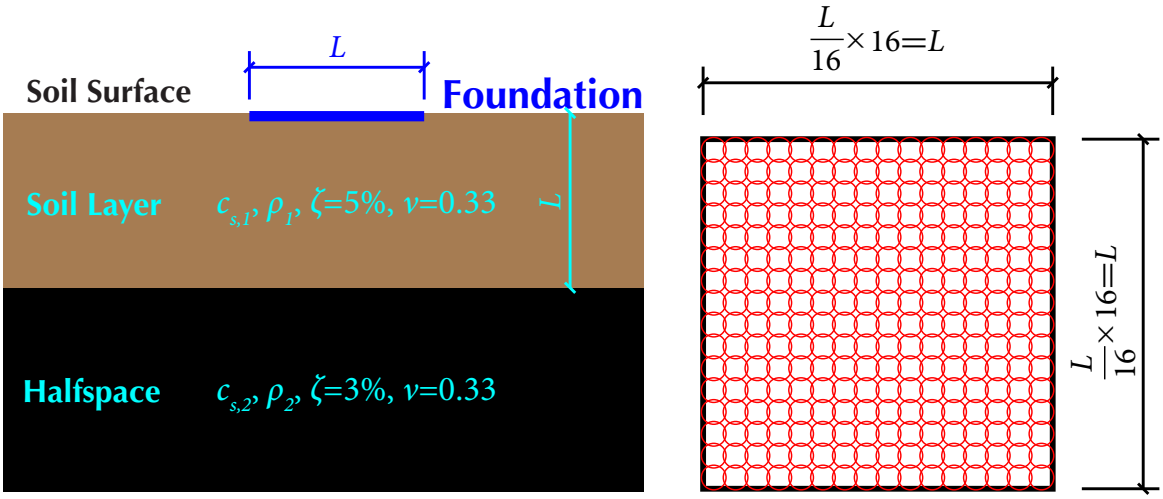

Foundation and soil site **Discretizaton of foundation**

Figure 4.12 Square foundation-site model and discretization of foundation

The results are compared to those calculated by Wong and Luco (1985). A dimensionless frequency a_o is introduced as

$$a_o = \frac{\omega R}{c_s}, \tag{4.112}$$

where R is the radius or equivalent radius of foundations, and the dynamic stiffness can be expressed as

$$K = K_s + \mathrm{i}a_o C_s,$$

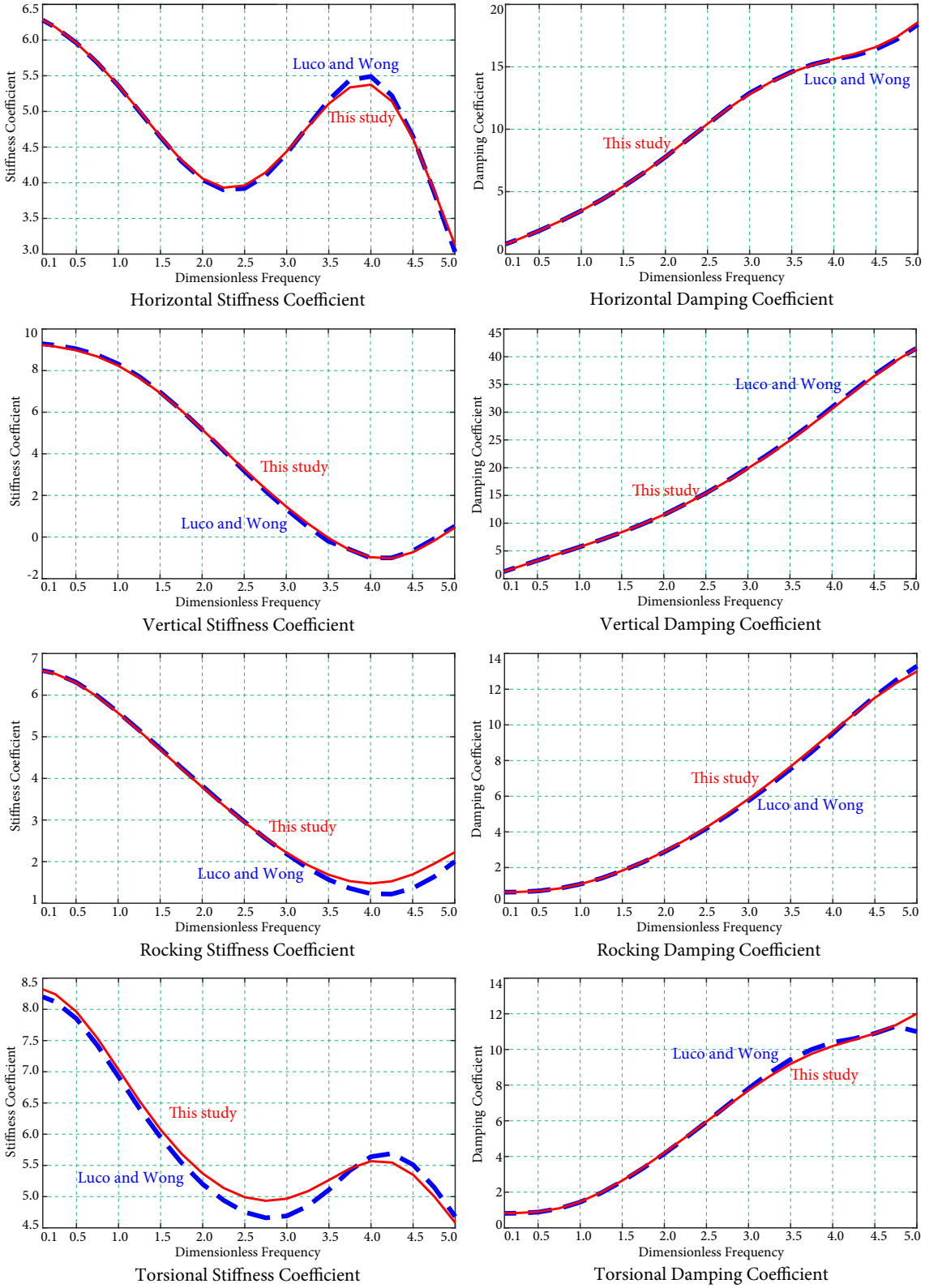

Figure 4.13 Dynamic soil stiffness of square foundation on a layer and halfspace

where K_s is the stiffness coefficient, i.e., real part, and C_s is damping coefficient, i.e., imaginary part.

In Wong's case, the layer and half-space are assumed to be elastic, homogeneous, and isotropic.

The dynamic soil stiffness are shown in Figures 4.13. The comparison of results show that the dynamic soil stiffness by proposed method agrees perfectly with Wong's results.

4.2.2 A Rigid Circular Foundation Supported by a Layer on Half-space

The dynamic stiffness of a rigid circular foundation with radius of R is considered on a layer with the thickness of R resting on a half-space. For the both layers, the Poisson's ratio is 0.25, and the damping ratio are equal to 0.001. The ratios of the shear-wave velocities and densities are $c_{s,1}/c_{s,2} = 0.8$ and $\rho_1/\rho_2 = 0.85$, in which the subscripts 1 and 2 denote the top layer and half-space, respectively. In this example, the circular foundation is divided into 200 subdisks with the radius of $R/8$. The foundation-soil model, and the discretization of foundation are shown in Figure 4.14.

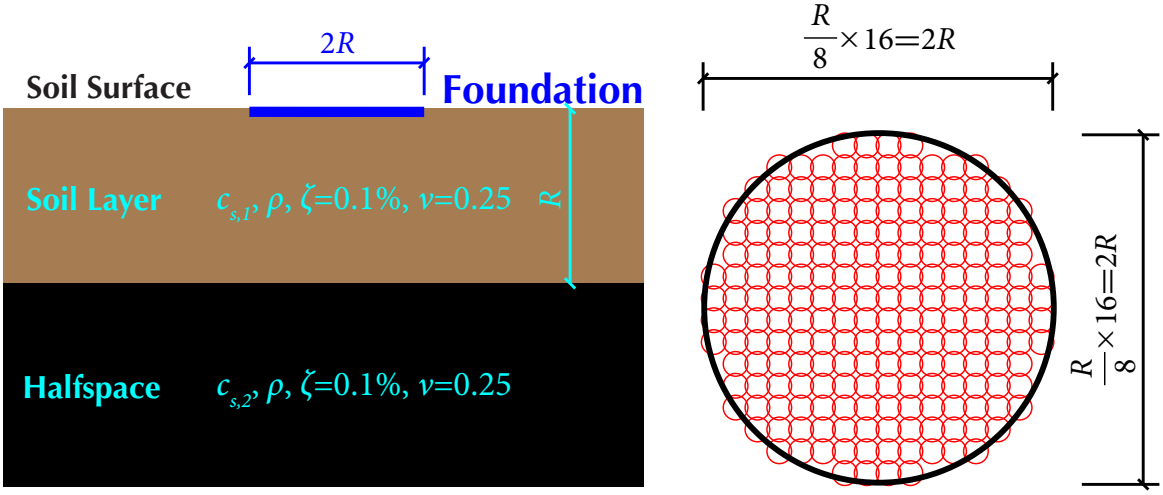

Foundation and soil site **Discretizaton of foundation**

Figure 4.14 Circular foundation-site model and discretization of foundation

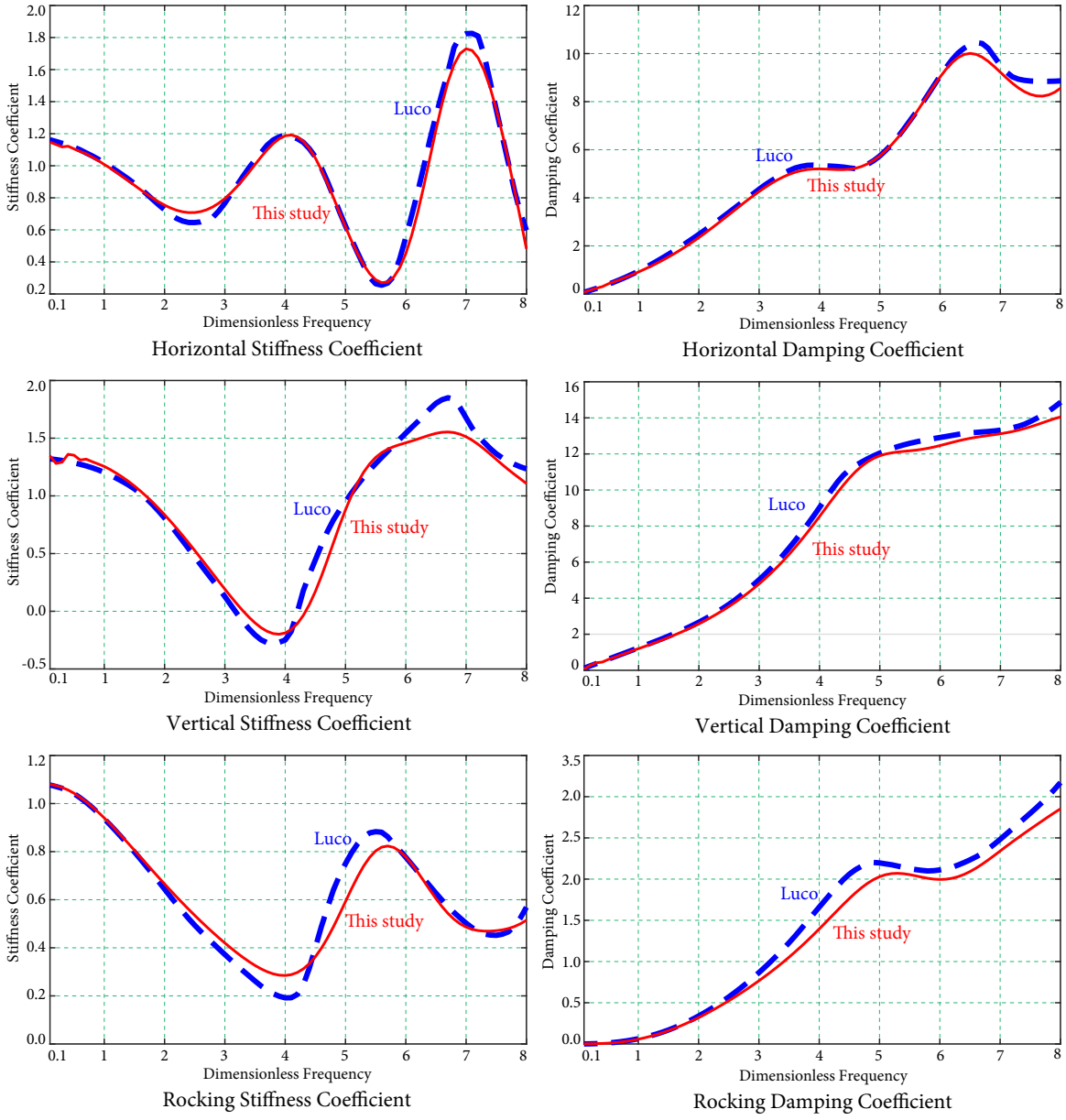

Figure 4.15 Dynamic soil stiffness of circular foundation on a layer and halfspace

The decomposed dynamic stiffness based on the dimensionless frequency a_o are introduced to illustrate the result as

$$K = K_o(k + \mathrm{i}a_o c), \tag{4.113}$$

where k and c are the dimensionless stiffness and damping coefficients, respectively. K_o is equal to a coefficient β multiplies the static-stiffness, and the static-stiffness (Wolf, 1985)

given as

$$K_h = \frac{8GR}{2-\nu}, \quad K_v = \frac{4GR}{1-\nu}, \quad K_{\phi h} = \frac{8GR^3}{3(1-\nu)}, \quad K_{\phi v} = \frac{16GR^3}{3},$$

where K_h, K_v, $K_{\phi h}$, and $K_{\phi v}$ are horizontal, vertical, rocking, and torsional stiffness, respectively.

The results are compared to those calculated by Luco (1974). In Luco's calculation, the layer and half-space are assumed to be elastic, homogeneous, and isotropic. The contact between the foundation and the underlying site is considered to be relaxed, i.e., no friction exits between the foundation and the soil for vertical and rocking vibrations, while for horizontal vibrations the normal component of stress at the contact is assumed to be zero. Based on the boundary conditions, the dynamic stiffness is obtained by a set of Fredholm integral equations.

The resultant soil stiffness associated with Luco's are shown in Figures 4.2.2. Excellent agreement with Luco's results shows the good accuracy of the proposed method.

4.2.3 A Rigid Circular Foundation Supported by Half-space and a Layer on Half-space

The dynamic stiffness of a rigid circular foundation with radius of R is considered in two sites. In the first case, the foundation is supported by a homogeneous half-space. The Poisson's ratio is $\nu = 0.33$. For the second case, a layer with the thickness of R rests on a half-space. For the both layers, the Poisson's ratio is 0.33, the damping ratio is equal to 0.05, and the densities are the same. The ratio of the shear-wave velocities is $c_{s,2}/c_{s,1} = 2$, in which the subscripts 1 and 2 denote the top layer and half-space, respectively.

In this example, the circular foundation is divided into 200 subdisks, which is the same as the previous circular foundation as shown in Figure 4.14.

The results are compared to those calculated by Wolf (1985) shown in Figures 4.16 and 4.17. The coefficient β_h, β_v, $\beta_{\phi h}$, and $\beta_{\phi v}$ are 1.01, 1.02, 1.03, and 1.00 for half-space case, respectively, while they are 1.32, 1.82, 1.19, and 1.04 for a layer on the half-space. The comparison of results show that the dynamic stiffness agrees well with Wolf's results.

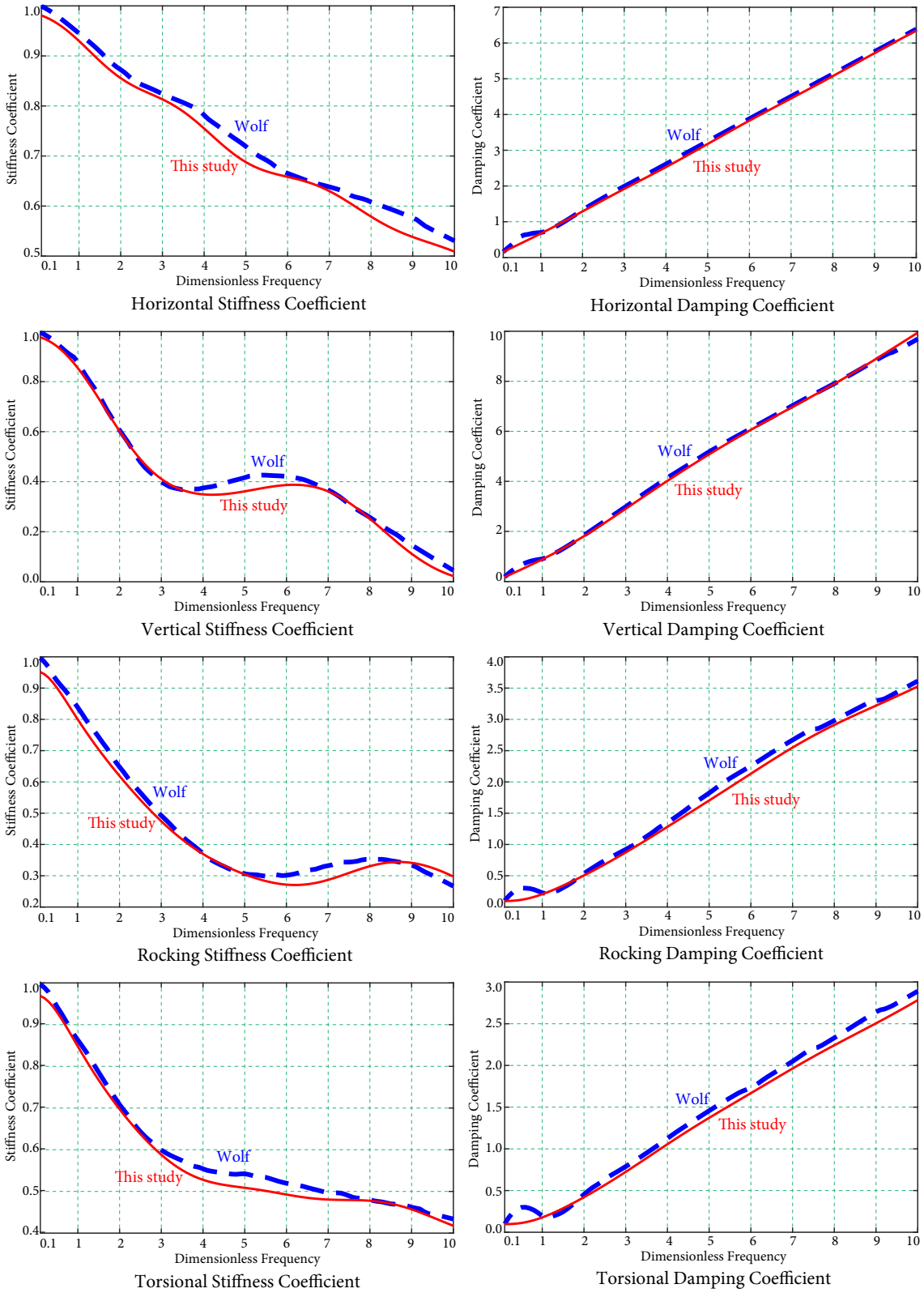

Figure 4.16 Dynamic soil stiffness of circular foundation on halfspace

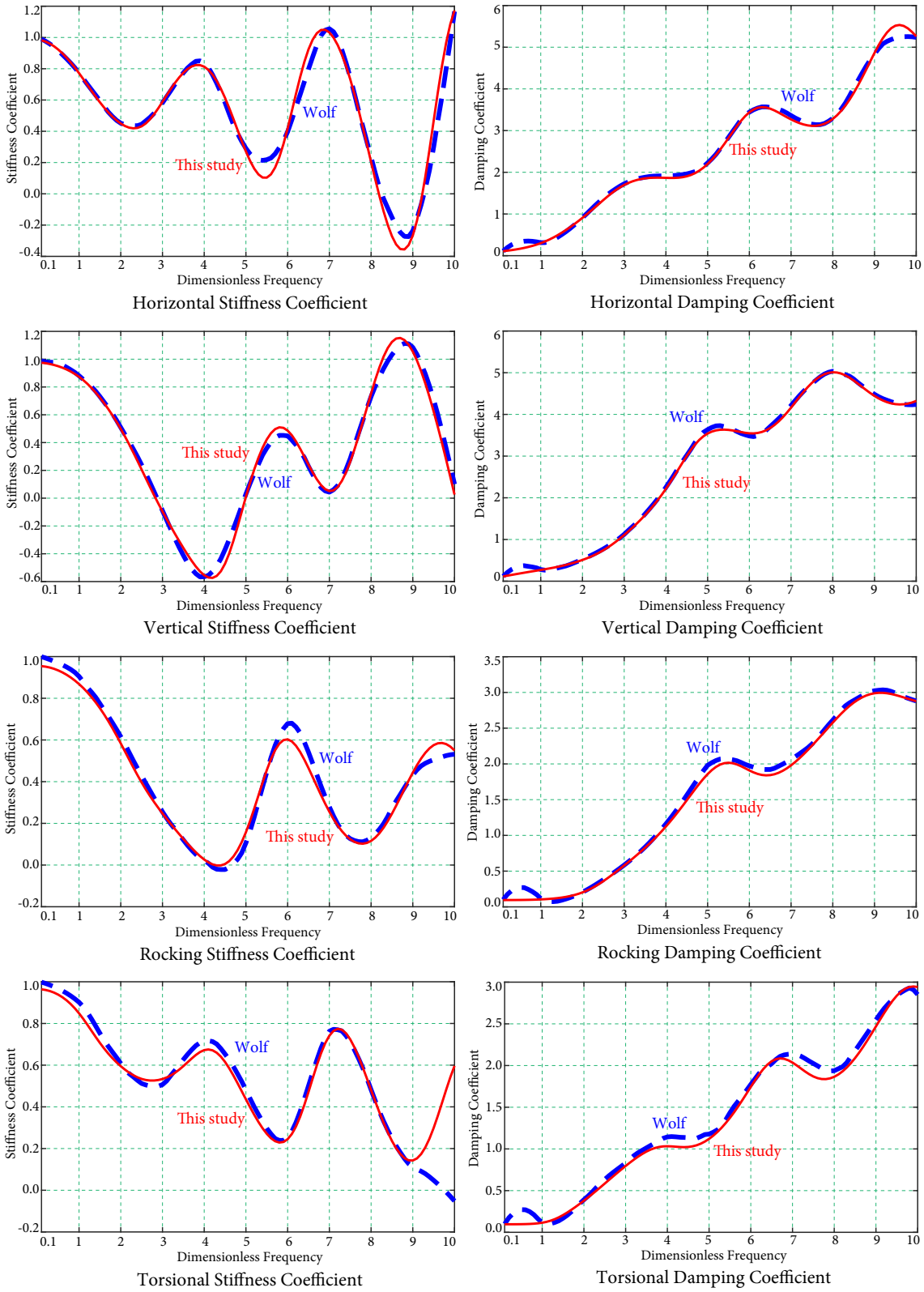

Figure 4.17 Dynamic soil stiffness of circular foundation on a layer and halfspace

4.3 Numerical Examples of the Generation of FRS

Floor response spectra (FRS) of a typical reactor building in nuclear power plants is generated based on the dynamic soil stiffness given by the proposed method and ACS SASSI, respectively, to examine the proposed method in the application.

At first, one set of soil stiffness is calculated by the proposed method, and the other set of soil stiffness is obtained from ACS SASSI. Then foundation level input response spectra (FLIRS) are developed based on the two sets of soil stiffness. Finally, FRS are generated by the direct method. The two sets of soil stiffness, FLIRS, and FRS are compared and discussed.

The model information of the selected reactor building, foundation input response spectra, and the soil properties are given in 3.2.

Computing Soil Stiffness

According to the proposed method, the soil stiffness is calculated and shown in Figure 4.18, along with the ACS SASSI soil stiffness. It can be observed that the difference of horizontal and vertical soil stiffness is small, while the difference of rocking and torsional soil stiffness is significant.

For a half-space case, the soil stiffness at low frequency domain is approximately equal to the static frequency-independent soil stiffness (Wolf, 1985; Luco, 1974). If vertical static uniform load q_s is applied at the foundation placed on the soil surface, the additional stress at the bottoms of the top 3 layers are $0.14q_s$, $0.039q_s$, and $0.026q_s$, respectively, which indicates that the top 3 layers play the dominant role in the determination of static soil stiffness. Since the V_s of top 3 layers are 2100 m/s, 2150 m/s, and 2200 m/s, respectively, the soil stiffness in low frequency domain is reasonable to be larger than half-space with V_s of 2100 m/s, and smaller than half-space with V_s of 2200 m/s.

The static stiffness of halfspace is calculated by equations in ASCE (2000). The rocking and torsional soil stiffness at 0.2 Hz and static values are given in Table 4.1. It can be seen that the rocking and torsional soil stiffness by the proposed method at 0.2 Hz are between the values of two half-space cases, while ACS SASSI results are noticeably larger than half-

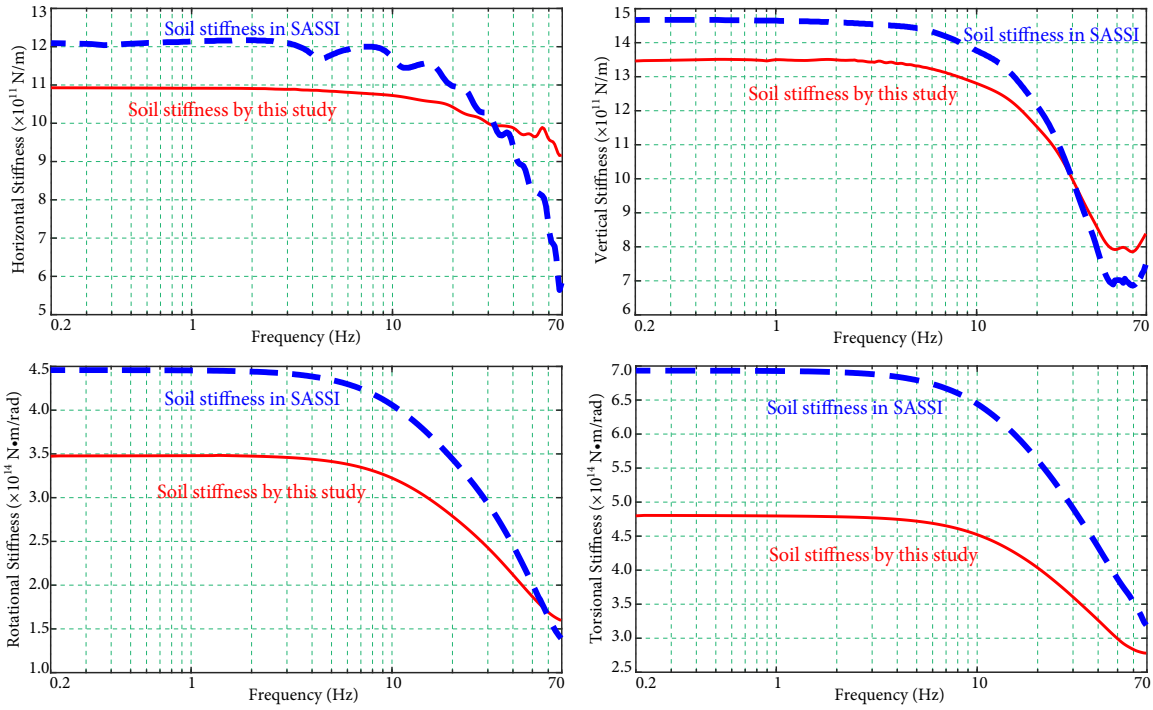

Figure 4.18 Dynamic soil stiffness of reactor building

space case with V_s of 2200 m/s. It means the rocking and torsional soil stiffness are too large in ACS SASSI, which will influence the analysis of SSI effect.

Table 4.1 Rocking and torsional stiffness in reactor building case

Item	Rocking Stiffness ($\times 10^{14}$ N·m/rad)	Torsional Stiffness ($\times 10^{14}$ N·m/rad)
Half-space (V_s = 2100m/s)	3.39	4.75
Half-space (V_s = 2200m/s)	3.72	5.21
This study (at 0.2 Hz)	3.50	4.80
SASSI (at 0.2 Hz)	4.46	6.93

Developing Foundation Level Input Response Spectra

The translational component of horizontal transfer matrix are shown in Figure 4.19. It represents the contribution of translational motions in the determination of FLIRS. The main difference of two sets ranges from 10 Hz to 40 Hz.

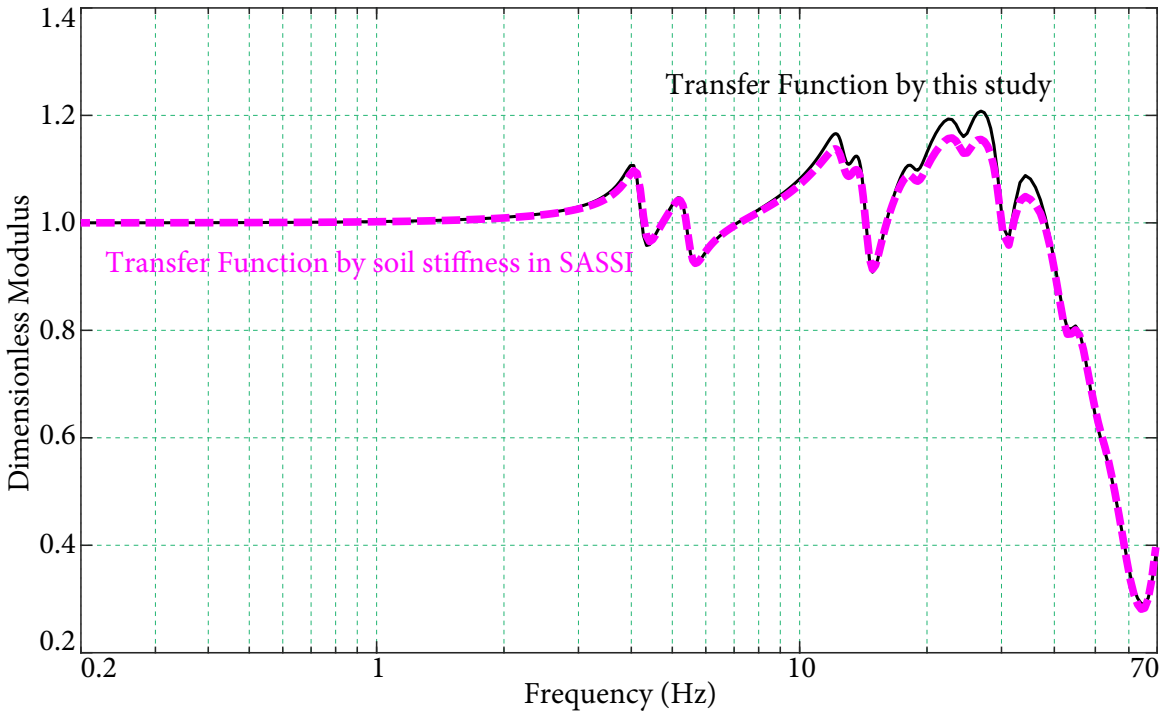

Figure 4.19 Translational component of horizontal transfer matrix of reactor building

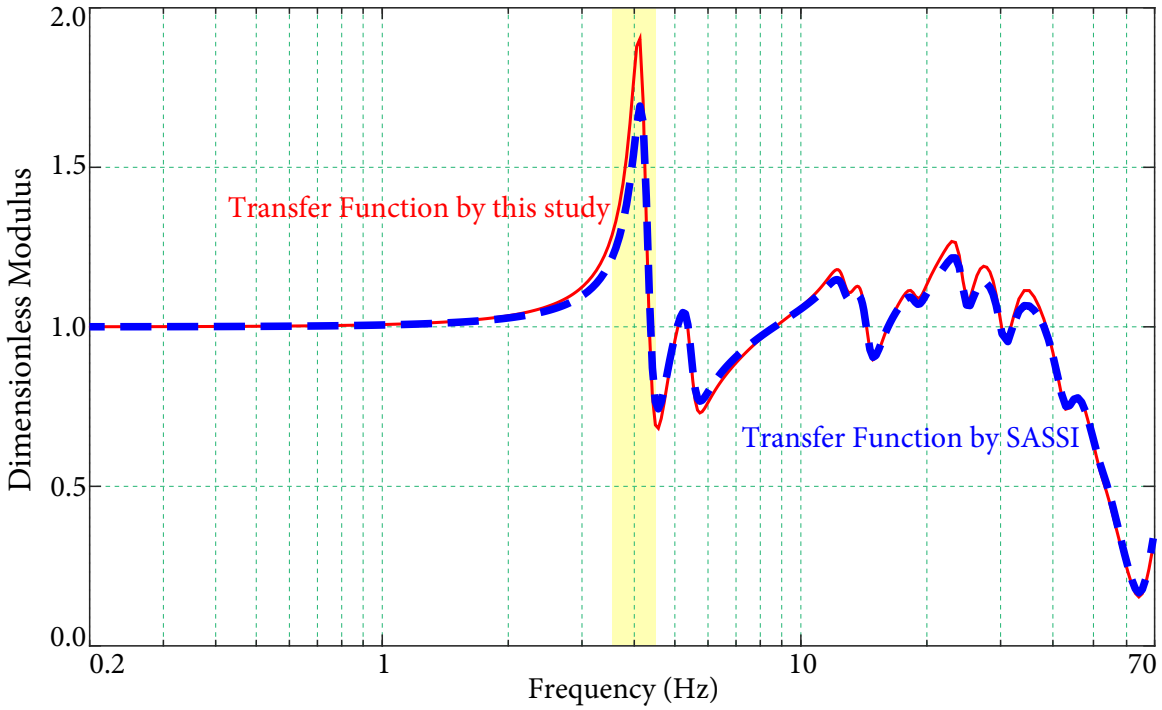

Figure 4.20 Horizontal transfer matrix of reactor building

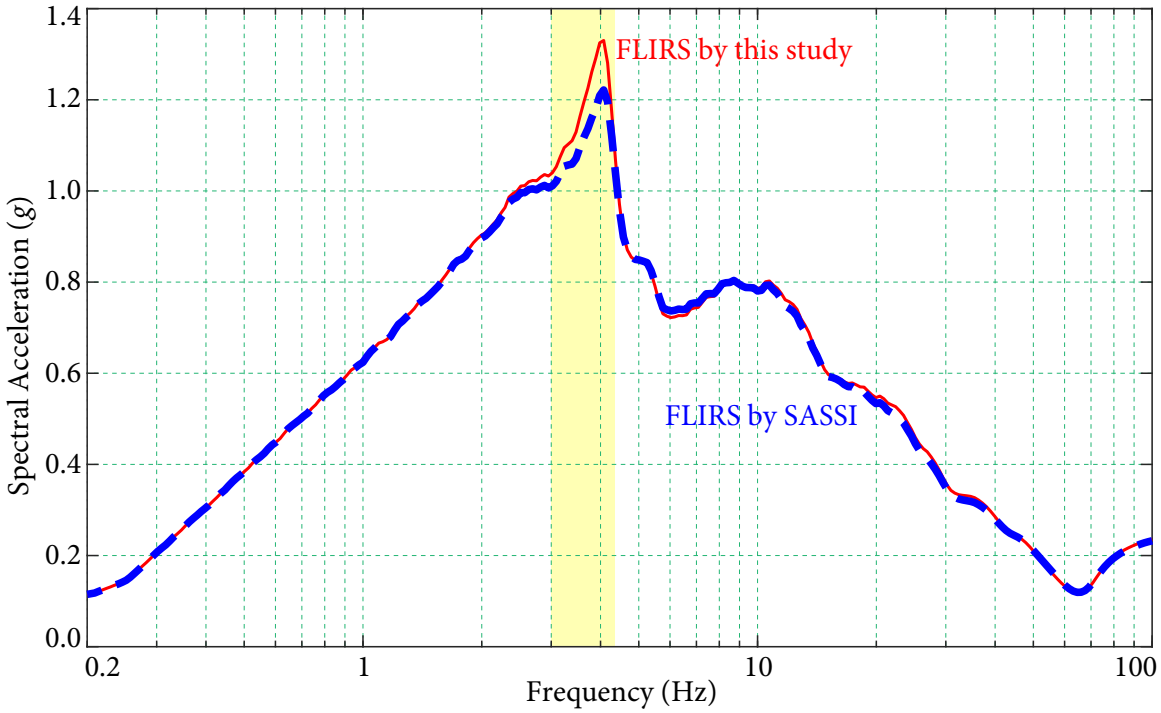

Figure 4.21 Horizontal FLIRS of reactor building

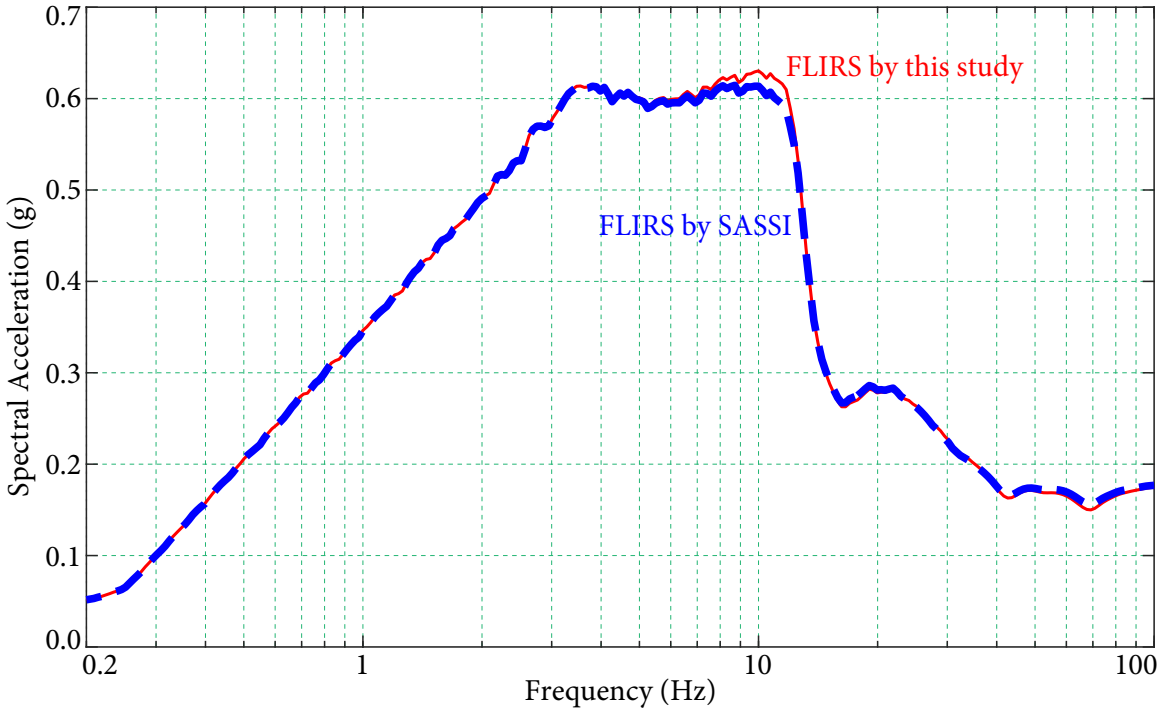

Figure 4.22 Vertical FLIRS of reactor building

The horizontal transfer function $\mathcal{T}$ are shown in Figure 4.20. This transfer function represents the relationship from FIRS to FLIRS. The shape and values of two sets transfer matrix are almost the same. It consists of translational components and rotational components. Compared to the noticeable difference of peak values at 4.1 Hz, the difference resulting from the translation component between 10 Hz and 40 Hz are not significant. Hence, this means the main difference is caused by the rotational components influenced by the rotational and torsional stiffness.

FLIRS are then developed as shown in Figures 4.21 and 4.22. It shows that the difference of horizontal FLIRS at around 4 Hz and vertical FLIRS at around 12 Hz can not be neglected, which is consistent with the trend of transfer function. Due to the accurate rocking and torsional soil stiffness, the SSI effect is addressed reasonably in this study. Apart from that, the two sets of FLIRS match each other well.

Generating Floor Response Spectra

FRS at nodes 4 and 5 are generated by the direct method as shown in Figures 4.23 and 4.24. The two sets of FRS agree well with each other except the first peak at around 4 Hz. It results from the difference of FLIRS, which represents the importance of accurate dynamic soil stiffness. For FLIRS in the other frequency domain, the relative error does not exceed 1.2%.

4.4 Summary

In this chapter, a semi-analytical method is developed for accurate and efficient generation of dynamic soil stiffness. Depending on the soil properties, the flexibility function on the ground surface is derived analytically from wave propagation function. Then the Green's influence function is formulated under a three-dimensional loads according to Fourier series and Bessel transform pair. Based on the discretized foundation, the dynamic stiffness matrix of the whole soil base is established accurately and efficiently.

Numerical examples are presented to validate the proposed method. The dynamic soil stiffness is calculated for foundations with different shapes, i.e., circular foundation and square foundation, supported by layered halfspace. The results agree well with the former

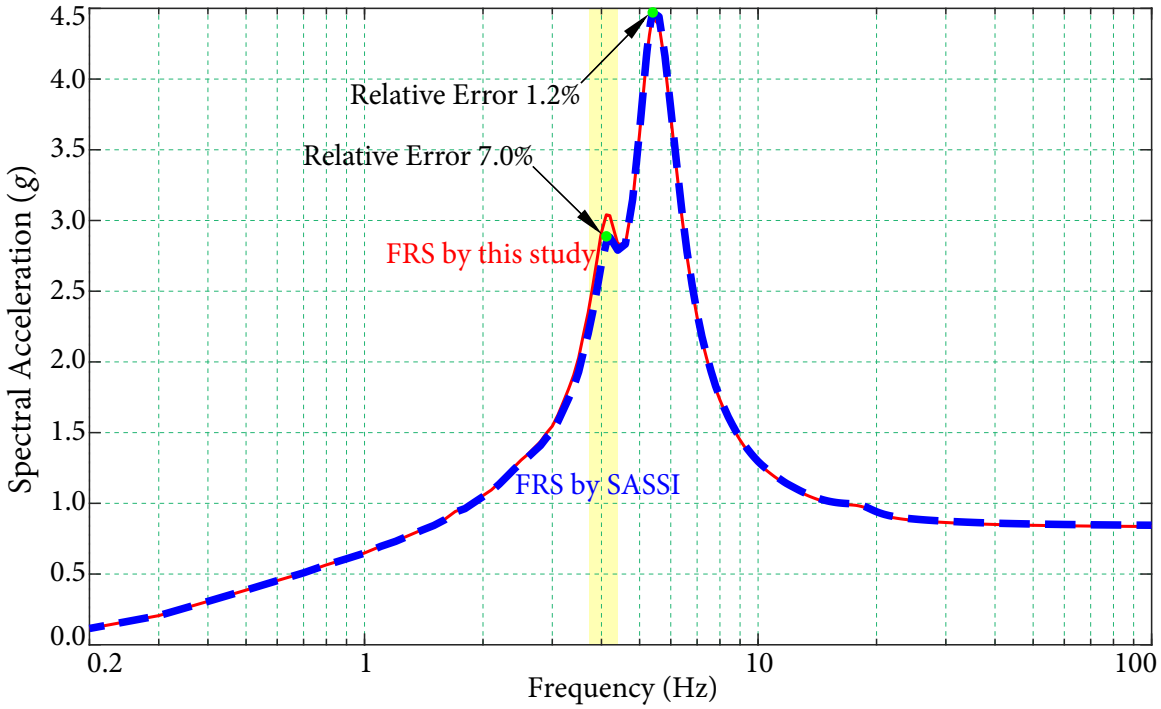

Figure 4.23 Comparison of FRS at Node 4 at reactor building

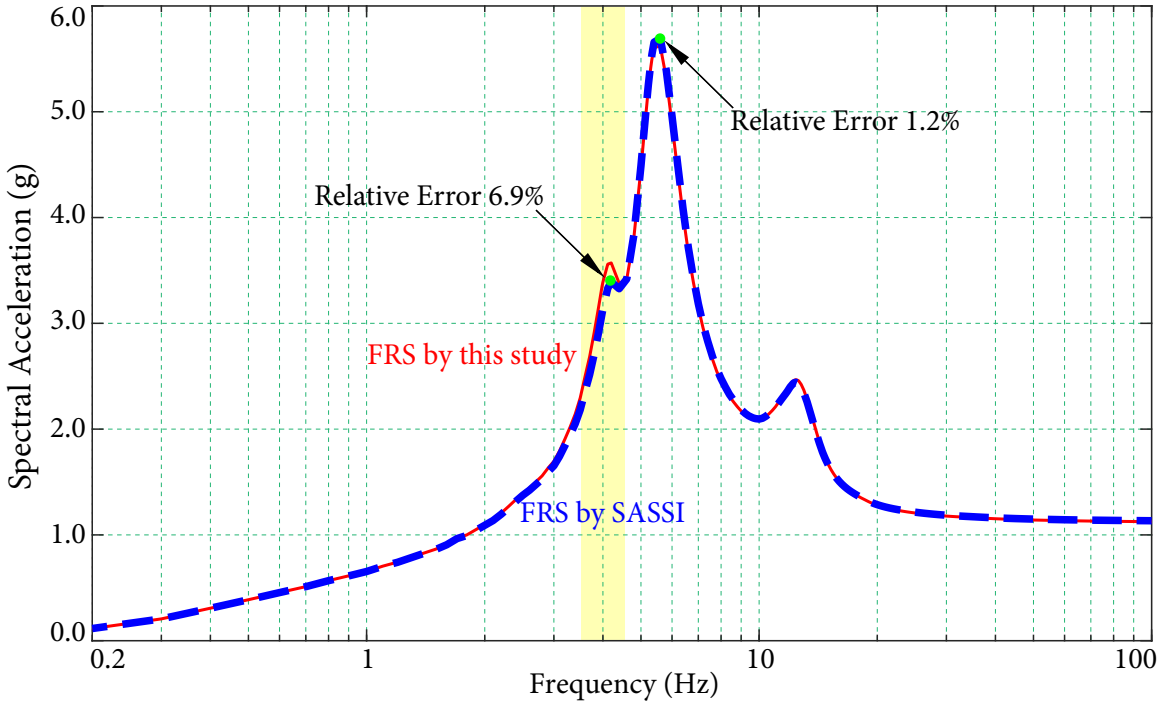

Figure 4.24 Comparison of FRS at Node 5 at reactor building

results. It shows that dynamic soil stiffness varies significantly with changing frequencies, which can not be neglected in the SSI analysis. In the proposed method, the dynamic response of soil base can be addressed accurately.

The generation of FRS is performed with the dynamic soil stiffness given by proposed method and ACS SASSI. The result shows that the proposed method can give accurate dynamic soil stiffness, by which the SSI effect is addressed and the resultant FRS can be generated.

The proposed method has three following features:

- The flexibility function and the Green's influence function are derived rigorously, and then the total dynamic stiffness matrix of foundations is obtained by BEM, which can give an accurate result.
- Each soil layer with any thickness can be treated as one element and the flexibility function is formulated analytically. There is no need to discretize soil layers into sub-layers. As a result, it can quickly generate the flexibility function and Green's influence function.
- The application of BEM enables to calculate the dynamic soil stiffness of rigid or flexible foundations with arbitrary shapes and any number of members.

In summary, the proposed method is accurate and efficient with the analytical formulation of flexibility function and Green's influence function, and the application of BEM. It eliminates the gap between site response analysis and SSI analysis, providing a basis for the analysis of SSI effect with flexible foundations. According to its efficiency, it is convenient to perform the fully probabilistic uncertainty analysis in the generation of FRS.

C H A P T E R 5

Analysis of Uncertainty in the Generation of FRS

In the generation of floor response spectra (FRS), both the earthquake ground motion and the soil properties are not determinant. They are described by probabilistic values, and needs to be considered (USNRS, 1978; ASCE, 1998; EUR, 2002). In this chapter, a fully probabilistic method is proposed to address the uncertainty during the generation of FRS. For a halfspace layered site, characterized by thickness, density (ρ), and shear-wave velocity (V_S), etc. in each layer, and Probabilistic Seismic Hazard Analysis (PSHA) at this site, the uniform hazard FRS is obtained with a specified Return Period (RP).

Based on a given site information, the site profiles and properties are developed by Monte-Carlo simulation to account for soil uncertainties. Different levels of ground motions are taken as the seismic input to capture the uncertainty in earthquake. Through the site response analysis and Soil-Structure Interaction (SSI) analysis, the Foundation Input

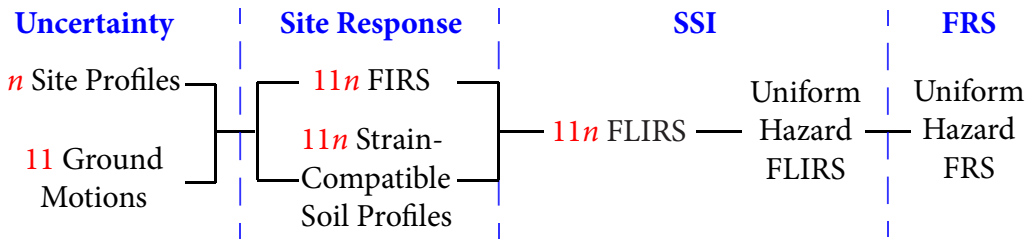

Figure 5.1 Logic Tree of Uncertainty Analysis

Response Spectra (FIRS) and Foundation Level Input Response Spectra (FLIRS) are generated. The FLIRS and input ground motions are compared to calculate the site-structure specific amplification functions which represent both the site response effect and SSI effect. Finally, a set of uniform hazard FLIRS and floor response spectra (FRS) with a specific RP are obtained. The logic tree of the proposed method are shown in Figure 5.1. The uncertainty in the earthquake excitation and soil properties are represented by 11 ground motions and n random geotechnical models, respectively. So there are totally $11 \times n = 11n$ analyses. After site response analysis and SSI analysis, the uncertainty are propagated into the $11n$ FLIRS which is used to develop site and structure specific amplification factors. Finally, a uniform hazard FRS is generated.

5.1 Generation of Fully Probabilistic FRS

5.1.1 Developing Input Ground Motions

The Acceleration Response Spectra (ARS) and Fourier Amplitude Spectra (FAS) of the input ground motion are obtained for given Peak Ground Acceleration (PGA) by the method in Chapter 2. Since the levels of ground motions influence the site response analysis significantly, at least eleven response spectra with PGA ranging from $0.01g$ to $1.5g$ are taken as input ground motions to address variation of earthquakes (EPRI, 2013).

5.1.2 Generating Geotechnical Models

Two kinds of uncertainty, epistemic uncertainty and aleatory uncertainty, are considered in the geotechnical model in current application. Epistemic uncertainty can be addressed by multiple sets of soil properties, and aleatory uncertainty can be accounted by randomizing (at least 30 times) parameters of soil properties. In this study, the uncertainty in layer thickness and depth to bedrock, and dynamic material properties are considered by the traditional approach, while a new combination of V_s in different layers is proposed to treat the uncertainty in V_s.

Uncertainty in Layer Thickness and Depth to Bedrock

Assumptions of the probability distributions (e.g., normal, uniform, or lognormal) of layer thickness and depth to bedrock are based on measured information, such as data in borehole logs. For example, when both properties follow normal distributions, the random values for the ith layer thickness and depth to bedrock can be determined by

$$H_i = \bar{H}_i + \varepsilon_{i,1} \cdot \sigma_{H,i}, \qquad B_i = \bar{B}_i + \varepsilon_{i,2} \cdot \sigma_{B,i},$$

where $\bar{H}_i$ and $\sigma_{H,i}$ are the mean and standard deviation of the ith layer thickness, $\bar{B}_i$ and $\sigma_{B,i}$ are the mean and standard deviation of depth of the ith layer to bedrock, and $\varepsilon_{i,1}$, $\varepsilon_{i,2}$ are random values following the standard normal distribution. The random values should be checked by comparing to measured data. The variation in the depth to bedrock is accommodated by adjusting the thickness of the deepest soil layer.

Uncertainty in Shear-Wave Velocity

Since limited information is available, there is considerable uncertainty in the shear-wave velocity profile. In current application, V_s is assumed to be lognormally distributed. The estimate for epistemic uncertainty in V_s is taken as σ_{LN}^{e} which is taken as 0.35, 0.5 for sparse measurements, and 0.175 for sufficient information. To represent epistemic uncertainty in V_s profiles with a minimum three cases, i.e., 50th-percentile best-estimate (BE), 90th-percentile upper-bound (UB), and 10th-percentile lower-bound (LB), are used, with the weights of 0.4 for BE and 0.3 for LB and UB. In each branch, the V_s in all layers hold the same percentile value. For instance, all V_s are 90th-percentile values in UB case. In other words, V_s in each layer are assumed fully correlated when epistemic uncertainty is considered.

In order to capture aleatory uncertainty, random field models are used to generate V_s profiles (EPRI-1025287). The model assumes that V_s at mid-depth of the layer follows lognormal distribution and correlates between adjacent layers. The empirical standard deviation σ_{LN}^{a} of the natural logarithm of V_s is 0.25 and decreases to 0.15 below 15 m (50 ft). A bound of $2\sigma_{LN}^{a}$ should be imposed throughout the profile, and V_s should be limited to 2830 m/s (9200 ft/s). So V_s actually follows truncated lognormal distribution. The Probability Density Function (PDF) is normalized to let the integration of PDF between

$V_s e^{2\sigma_{LN}^a}$ and $V_s e^{-2\sigma_{LN}^a}$ be equal to 1. Meanwhile, V_s is set to 2830 m/s when the random V_s exceeds this value.

After considering the epistemic uncertainty and aleatory uncertainty in each layer, the random values of $V_{s,i}$ are given by

$$V_{s,i} = V_s \, e^{\sigma_{LN}^e \Phi^{-1}(Q_i) + Z_i \sigma_{LN}^a}, \tag{5.1}$$

where $V_{s,i}$ is the ith random value of V_s.

Q_i is determined by a random value θ_i which follows uniform distribution and ranges from 0 to 1. Q_i is equal to 10% for $0 < \theta_i \leq 0.3$, 50% for $0.3 < \theta_i \leq 0.7$, and 90% for $0.7 < \theta_i \leq 1$.

Z_i is generated from

$$Z_1 = \varepsilon_1; \qquad Z_i = Z_{i-1} \cdot \rho + \varepsilon_i \sqrt{1-\rho^2}, \quad i > 1, \tag{5.2}$$

in which ε_i is a random value following the truncated standard normal distribution between -2 and 2. The PDF of this truncated standard normal distribution is normalized, i.e., let the PDF multiply $1/[\Phi(2) - \Phi(-2)]$.

ρ is the correlation coefficient and is a function of depth d and thickness h of the layer (Toro, 1995):

$$\rho(d,h) = \left[1 - \rho_d(d)\right] \rho_h(h) + \rho_d(d), \tag{5.3}$$

where ρ_h and ρ_d are the thickness-dependent and depth-dependent correlations:

$$\rho_h(h) = \rho_0 \, e^{-\frac{h}{\Delta}}, \qquad \rho_d(d) = \begin{cases} \rho_{200} \left(\dfrac{d + d_0}{200 + d_0} \right)^b, & d < 200 \text{ m}, \\ \rho_{200}, & d \geqslant 200 \text{ m}. \end{cases} \tag{5.4}$$

b and d_0 are parameters given in Geomatrix and V_{s30} classifications. The parameters are listed in Table 5.1 and Geomatrix classification is given in Table 5.2 (Toro, 1995).

In summary, two random numbers θ_i and ε_i are generated for each layer. Then the random value of $V_{s,i}$ is calculated by equation (5.1) to represent the uncertainty in V_s. The probability density function (PDF) are shown in Figure 5.2.

The PDF of current distributions are not continuous as shown in Figure 5.2, and its shape is not realistic. Hence, it is desirable to develop a continuous distribution to represent the

Table 5.1 Parameters for shear-wave velocity correlation coefficient

Parameter	Geomatrix		V_{s30} (m/s)			
	A and B	C and D	<180	180 to 360	360 to 750	$\geqslant 750$
ρ_0	0.96	0.99	0.95	0.97	0.99	0.00
Δ	13.10	8.00	3.40	3.80	3.90	5.00
ρ_{200}	0.96	1.00	0.42	1.00	0.98	0.50
d_0	0.00	0.00	0.00	0.00	0.00	0.00
b	0.095	0.160	0.063	0.293	0.344	0.744

Table 5.2 Geomatrix classification

Description
A. Rock Instrument is found on rock material ($V_s > 600$ m/s) or a very thin veneer (less than 5 m) of soil overlying rock material.
B. Shallow (Stiff) Soil Instrument is founded in/on a soil profile up to 20 m thick overlying rock material, typically a narrow canyon, near a valley edge, or on a hillside.
C. Deep Narrow Soil Instrument is found in/on a soil profile at least 20 m thick overlying rock material in a narrow canyon or valley no more than several kilometers wide.
D. Deep Broad Soil Instrument is found in/on a soil profile at least 20 m thick overlaying rock material in a broad canyon or valley.
E. Soft Deep Soil Instrument is found in/on a deep soil profile that exhibits low average shear-wave velocity ($V_s < 150$ m/s).

uncertainty in soil. $V_{s,i}$ is proposed to be generated by

$$V_{s,i} = V_s \, e^{Z_i \sigma_{LN}}, \tag{5.5}$$

where σ_{LN} is the standard deviation. Z_i is generated from Equation (5.2).

Monte-Carlo simulation are performed for the current distributions. The V_s following 6 distributions are generated for 10^7 times, and the σ_{LN} of each distributions are calculated as

- $\sigma_{LN}=0.4111$ for $\sigma_{LN}^{e}=0.35$ and $\sigma_{LN}^{a}=0.25$,
- $\sigma_{LN}=0.3716$ for $\sigma_{LN}^{e}=0.35$ and $\sigma_{LN}^{a}=0.15$,
- $\sigma_{LN}=0.5428$ for $\sigma_{LN}^{e}=0.5$ and $\sigma_{LN}^{a}=0.25$,

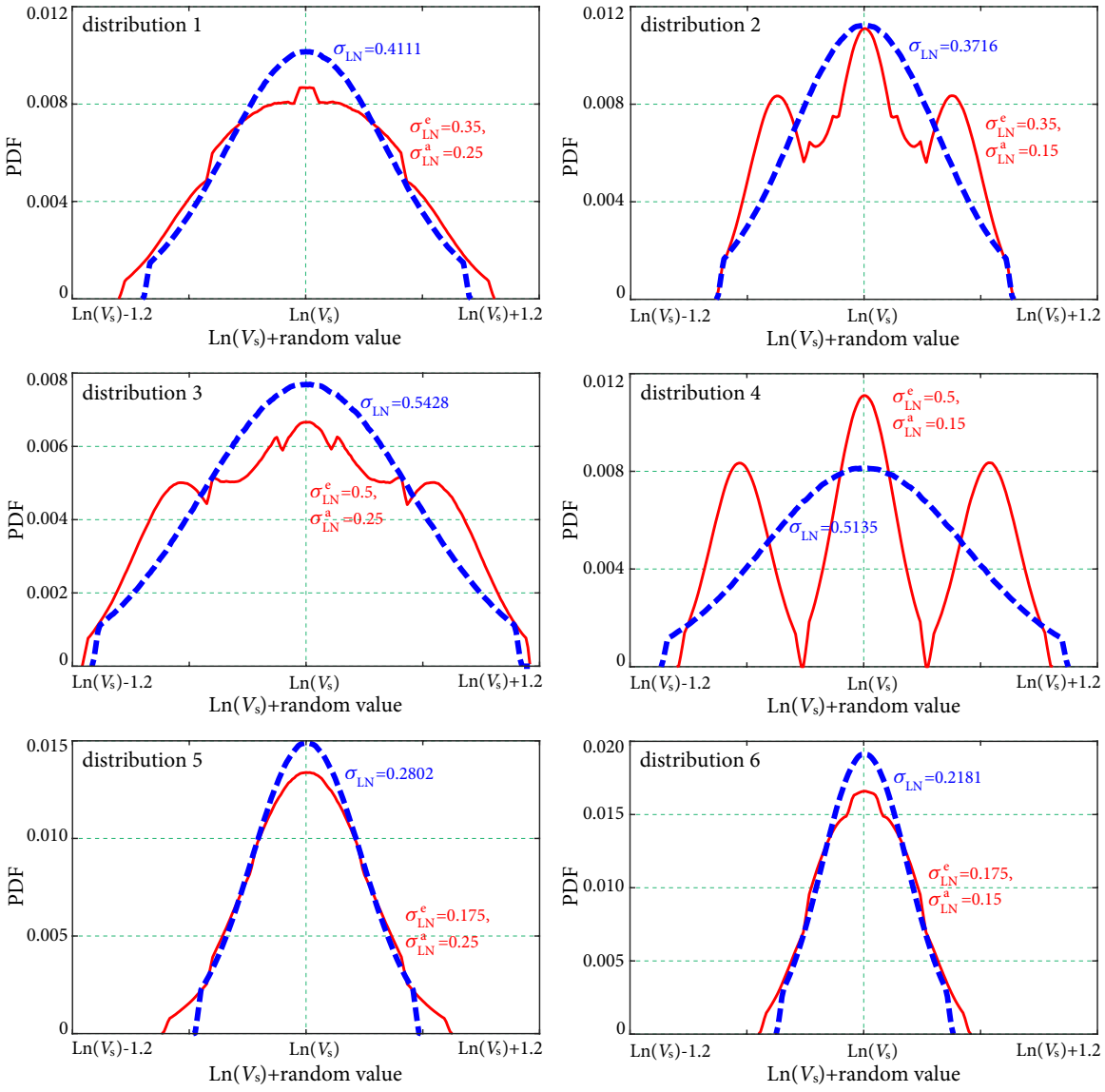

Figure 5.2 Probability density function of V_s distributions

- $\sigma_{LN} = 0.5135$ for $\sigma_{LN}^{e} = 0.5$ and $\sigma_{LN}^{a} = 0.15$,
- $\sigma_{LN} = 0.2802$ for $\sigma_{LN}^{e} = 0.175$ and $\sigma_{LN}^{a} = 0.25$,
- $\sigma_{LN} = 0.2181$ for $\sigma_{LN}^{e} = 0.175$ and $\sigma_{LN}^{a} = 0.15$.

The PDF of proposed distributions are shown in Figure 5.2.

Parametric study is conducted on the proposed distributions and the influence of ρ in Section 5.2.

Uncertainty in Dynamic Material Properties

According to EPRI-1025287, two sets of G/G_{MAX} and hysteretic damping are developed to characterize epistemic uncertainty in material properties for soil (cohesionless soils comprised of sands, gravels, silts, and low plasticity clays) and rock (Cenozoic or Paleozoic sedimentary rocks including shale, sandstones, and siltstone).

For soil conditions, EPRI soil curves in EPRI TR-102293-V2 (EPRI, 1993B), which accommodate with more nonlinear soils (Figure 5.3), and Peninsular Range curves (Silva *et al.*, 1996; Walling *et al.*, 2008), which accommodate with more linear soils, are used. The two sets of soil curves are given equal weights. The Peninsular Range curves reflect a subset of the EPRI soil curves, with the 51 to 120 ft (15 to 37 m) EPRI curve applied to the 0 to 50 ft (0 to 15 m) depth range and the EPRI 501 to 1,000 ft (153 to 305 m) curve applied to the 51 to 500 ft (15 to 152 m) depth range.

For rock conditions, EPRI rock curves in EPRI-1025287 (Figure 5.4) and linear response are used. In the model of linear response, damping remains constant with cyclic shear strain at input loading levels up to and beyond $1.5g$. For all sites where soil and firm rock extended to depth exceeding 150 m (500 ft), linear response can be assumed in the deep portions of profiles.

The two sets of material properties are summarized in Table 5.3.

According to EPRI-1025287, aleatory variability in dynamic material properties is accommodated by randomizing G/G_{max} and hysteretic damping curves. Lognormal distributions are assumed with σ_{LN} of 0.15 and 0.3 for G/G_{max} and hysteretic damping, respectively, at a cyclic shear strain of 0.03%. A bound of $2\sigma_{LN}$ is applied. The random curves are generated by computing the change of G/G_{max} and hysteretic damping at 0.03%

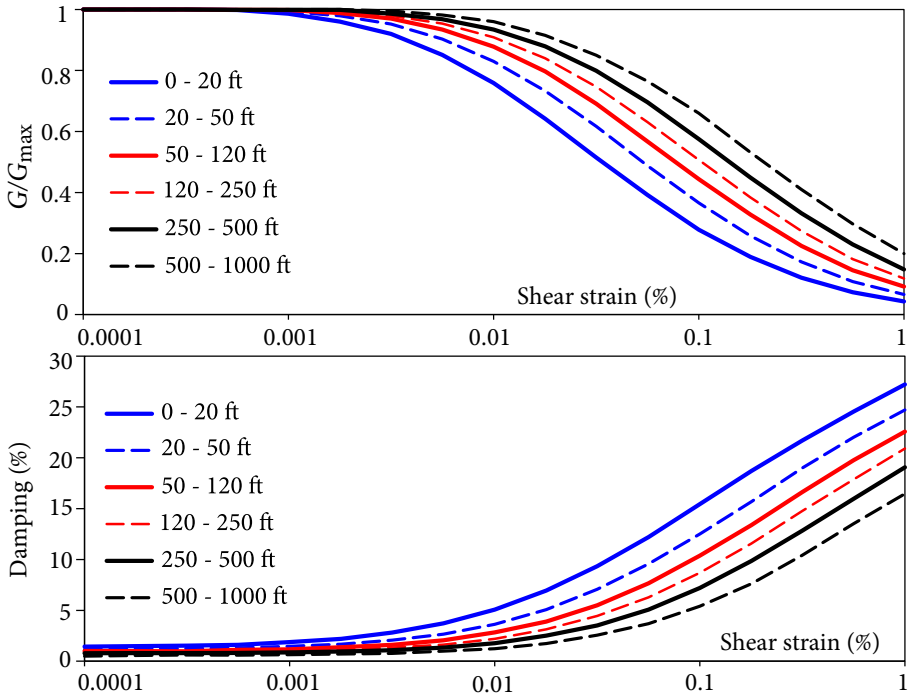

Figure 5.3 Shear modulus and hysteretic damping curves for cohesionless soil

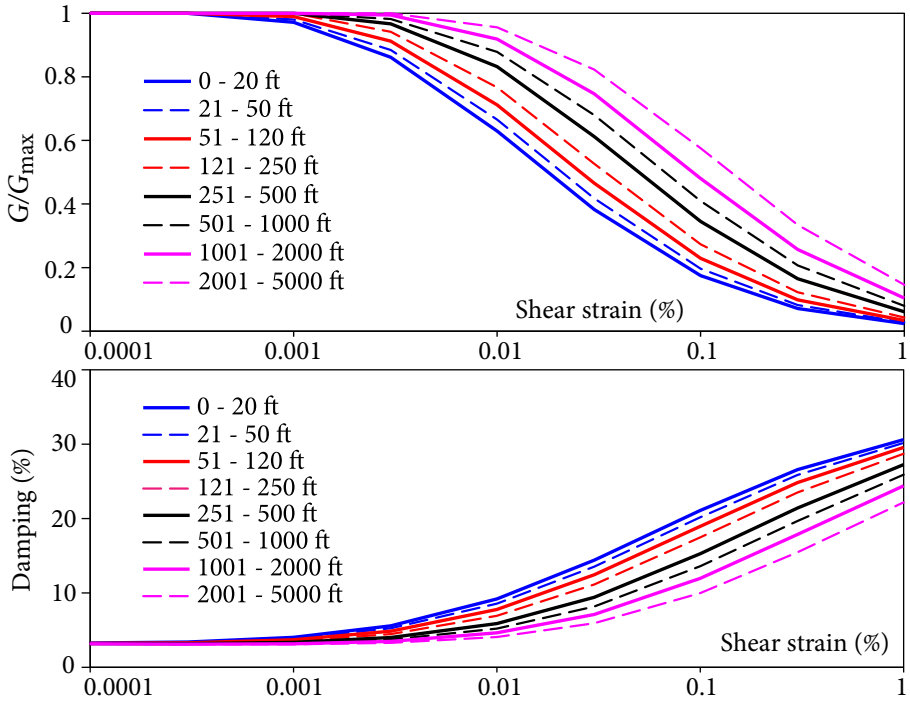

Figure 5.4 Shear modulus and hysteretic damping curves for cohesionless rock

Table 5.3 Dynamic property values

Layers	Curve Set 1	Curve Set 2
Soil	EPRI soil	Peninsular range
Rock in top 150 m (500 ft) depth	EPRI rock	Linear response
Deeper rock	Linear response	Linear response

cyclic shear strain and applying this factor at all strains. The factor should be reduced near the end of the range to preserve the general shape of the base-case curves. Hysteretic damping at 0.03% shear strain should not exceed 15% in applications.

So similar to V_s distribution, G/G_{max} and hysteretic damping also follows truncated lognormal distribution, and the PDF is is normalized to ensure its integration is equal to 1. Meanwhile, hysteretic damping is set to 15% when the random number exceeds this value.

G/G_{max} and hysteretic damping curves can be developed by

$$G/G_{\max,i} = G/G_{\max}\, e^{0.15\varepsilon_{i,1}}, \qquad D_i = D\, e^{0.3\varepsilon_{i,2}}, \tag{5.6}$$

where $G/G_{\max,i}$ and D_i are the ith random modulus reduction and hysteretic damping, respectively, and $\varepsilon_{i,1}$ and $\varepsilon_{i,2}$ are independent standard normal random numbers.

5.1.3 Determining Foundation Level Input Response Spectra

After considering propagation effect, site response analysis, and SSI effect, the site-structure specific amplification functions $\mathcal{A}f$ are calculated. Then seismic hazard curves at reference hard rock and $\mathcal{A}f$ are convolved to compute FLIRS with a specified RP. Based on the direct spectra-to-spectra method, FRS with the RP can be generated.

Amplification Function

The amplification function $\mathcal{A}f$ is defined as the ratio of spectral acceleration $\mathcal{S}_A^S(f|a)$ in FLIRS to $\mathcal{S}_A^{HR}(f|a)$ at reference hard rock, given the amplitude of rock motion a, i.e.,

$$\mathcal{A}f(f|a) = \frac{\mathcal{S}_A^S(f|a)}{\mathcal{S}_A^{HR}(f|a)}. \tag{5.7}$$

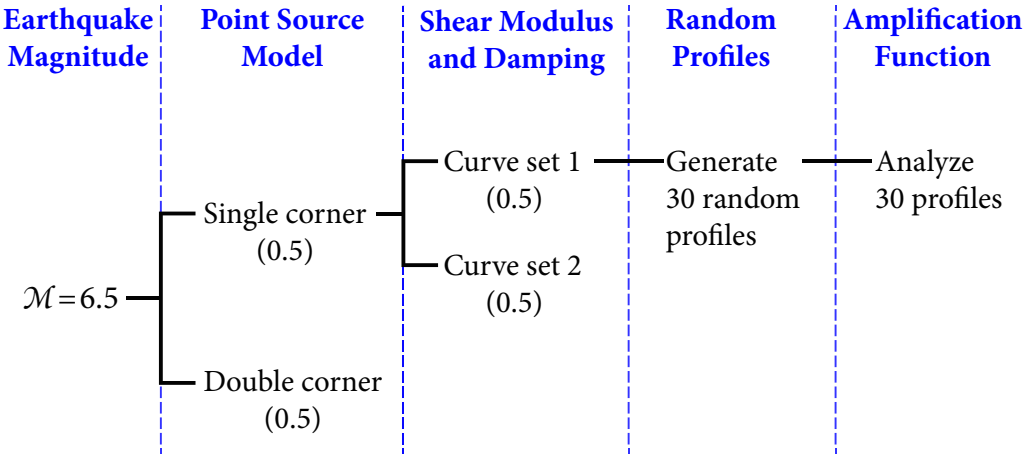

Figure 5.5 Logic tree for the generation of amplification function

Figure 5.5 gives an example logic tree for determining amplification functions $\mathcal{A}$, in which there are 4 branches accounting for epistemic uncertainty in seismic source model and site-specific geotechnical model. For each branch, a minimum of 30 random realizations are generated to capture aleatory randomness in the model. The outputs of analyses are FLIRS by site response analysis and SSI analysis.

The site response analysis is performed at first to give horizontal and vertical FIRS, and the relevant stain-compatible soil properties in each layer. The nonlinearity of G and ζ are considered by an equivalent linear method as described in Section 2.2.2. For example, if the shear strain in the n^{th} soil layer is γ_n, the strain-compatible soil properties are determined from the shear modulus and hysteretic damping curves as $\beta_n G_n$ and ζ_n as shown in Figure 5.6. G_n is the low-strain shear modulus which is determined by density ρ_n and initial shear wave velocity $V_{s,n}$ as $\rho_n {V_{s,n}}^2$. β_n and ζ_n are the shear modulus reduction coefficient, $G/G_{\max}$, and damping ratio with respect to the shear strain γ_n, respectively. Strain-compatible soil properties mean that the ground motion resulting from soil properties $\beta_n G_n$ and ζ_n gives the compatible shear strain γ_n in the n^{th} soil layer.

Then the strain-compatible soil properties are assumed to be constant in the generation of dynamic soil stiffness which can calculated based on Chapter 4. As shown in Figure 5.6, the strain-compatible soil properties $\beta_n G_n$ and ζ_n are used to develop dynamic soil

stiffness. According to the proposed substructure method, FLIRS is generated by each set of FIRS and dynamic soil stiffness.

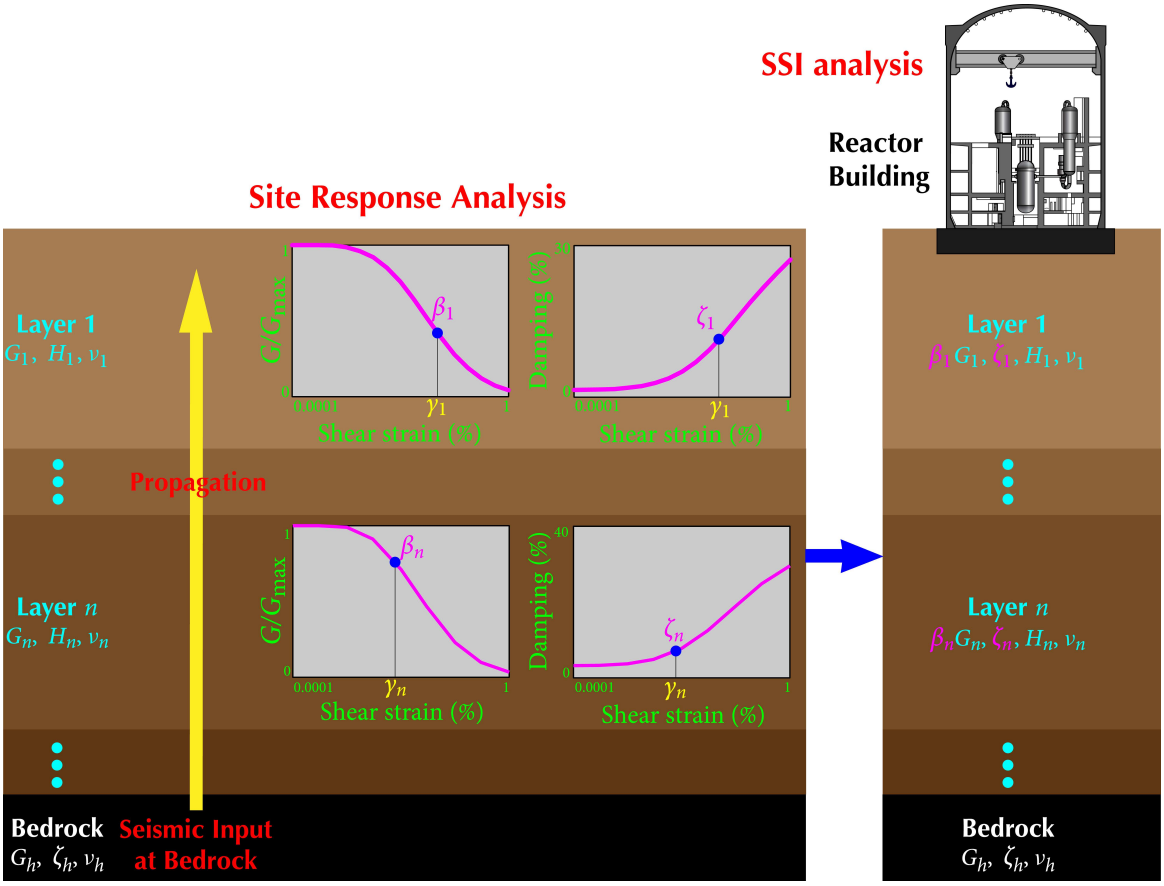

Figure 5.6 Treatment of nonlinear soil properties

$\mathcal{A}f(f|a)$ is assumed to be lognormally distributed given the amplitude of rock motion a. For the ith epistemic branch, the logarithmic mean μ_i and logarithmic standard deviation σ_i of $\mathcal{A}f(f|a)$ can be obtained from the set of at least 30 random profiles. Then the total $\mu_{\ln \mathcal{A}f|a}$ and $\sigma_{\ln \mathcal{A}f|a}$ for each frequency given the amplitude of rock motion a are calculated by

$$\mu_{\ln \mathcal{A}f|a} = \sum_i w_i \cdot \mu_i, \qquad \sigma^2_{\ln \mathcal{A}f|a} = \sum_i w_i \cdot \left[\left(\mu_i - \mu_{\ln \mathcal{A}f|a} \right)^2 + \sigma_i^2 \right], \tag{5.8}$$

where w_i is the weight for the ith epistemic branch.

Foundation Level Input Response Spectra

The seismic hazard on ground surface for a specified structure, uniform hazard FLIRS with RP, is calculated by convolving amplification functions and seismic hazard curves at reference hard rock as

$$\mathcal{H}_Z^{\mathrm{S}}(z) = \int_0^{\infty}\int_r\int_m P\left\{\mathcal{A}\mathrm{f} > \frac{z}{a}\,\middle|\, m, r, a\right\} f_{M,R|A}(m, r\,|\,a)\, h_A^{\mathrm{HR}}(a)\,\mathrm{d}m\,\mathrm{d}r\,\mathrm{d}a, \tag{5.9}$$

where $\mathcal{A}\mathrm{f}$ is the amplification function depending on m, r, and a. a is the amplitude of rock motion, and $f_{M,R|A}(m, r\,|\,a)$ is the joint probability density function of M and R given the amplitude a of rock motion. $h_A^{\mathrm{HR}}(a)$ is the absolute value of the derivative of the seismic hazard at reference hard rock.

As stated in Chapter 2, site amplification is virtually independent of earthquake magnitude $\mathcal{M}$ and source-to-site distance R when frequencies f are greater than initial resonant frequency f_{SC} of soil column, i.e., $f \geqslant f_{\mathrm{SC}}$. When f_{SC} is small enough, equation (5.9) can be simplified as

$$\mathcal{H}_Z^{\mathrm{S}}(z) = \int_0^{\infty} P\left\{\mathcal{A}\mathrm{f} > \frac{z}{a}\,\middle|\, a\right\}\left|\frac{\mathrm{d}\mathcal{H}_A^{\mathrm{HR}}(a)}{\mathrm{d}a}\right|\mathrm{d}a = \int_0^{\infty} P\left\{\mathcal{A}\mathrm{f} > \frac{z}{a}\,\middle|\, a\right\} h_A^{\mathrm{HR}}(a)\,\mathrm{d}a. \tag{5.10}$$

$P\left\{\mathcal{A}\mathrm{f} > \dfrac{z}{a_i}\,\middle|\, a_i\right\}$ can be determined by assuming that $\mathcal{A}\mathrm{f}$ is lognormally distributed given the amplitude a_i of rock motion

$$P\left\{\mathcal{A}\mathrm{f} > \frac{z}{a_i}\,\middle|\, a_i\right\} = 1 - \Phi\left\{\frac{\ln(z/a_i) - \mu_{\ln\mathcal{A}\mathrm{f}|a_i}}{\sigma_{\ln\mathcal{A}\mathrm{f}|a_i}}\right\}, \tag{5.11}$$

where $\mu_{\ln\mathcal{A}\mathrm{f}|a_i}$ and $\sigma_{\ln\mathcal{A}\mathrm{f}|a_i}$ are mean value and standard deviation of $\ln\mathcal{A}\mathrm{f}$ given the amplitude a_i of rock motion, which can be obtained from equation (5.8). Finally FLIRS is taken as the seismic input for primary structures to generate FRS.

The logic tree of the proposed method and the current method are compared as shown in Figure 5.7. Based on 11 ground motions and n random geotechnical models, $11 \times n = 11n$ sets of FIRS and strain-compatible soil properties are obtained from site response analysis. In current application, the FIRS with RP is calculated. Then three site profiles, BE, LB and UB, are used in SSI analysis, which lead to three sets of FLIRS and the resultant FRS. The final FRS is obtained by maximum value method, i.e., three sets of FRS are enveloped at

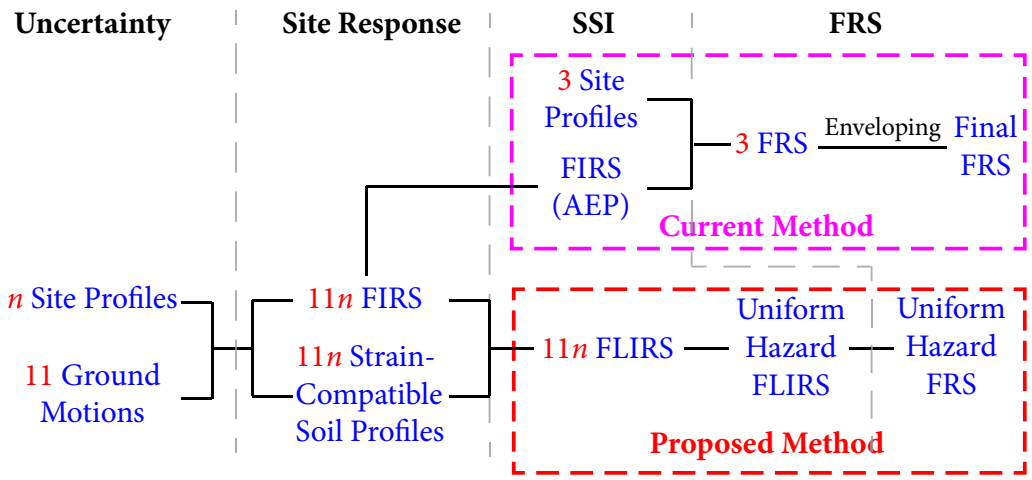

Figure 5.7 Comparison of two methods

each frequency point. Since only three site profiles are considered, the uncertainty in soil properties is not considered from site response and SSI analysis consistently. The risk in the final FRS can not be evaluated. In the proposed method, the uncertainty are propagated into the 11n FLIRS which is used to develop site and structure specific $\mathcal{A}f$. Finally, a uniform hazard FRS is generated after fully considering the uncertainty resulting from both soil and earthquakes.

5.1.4 Procedures of Generating Uniform Hazard FRS

For a structure supported by a horizontally layered soil site, procedures for generating uniform hazard FRS are summarized as follows:

1. The seismic input at bedrock is developed. At least 11 ground motions with different loading levels are needed to represent the uncertainty in earthquakes.
2. The geotechnical models are established including soil parameters of layer thickness, shear-wave velocity, damping ratio, density, and Poisson's ratio. The uncertainty in the layer thickness, depth to bedrock, shear-wave velocity, and soil properties are considered to generate random site profiles based on Monte Carlo simulation.
3. The site response analysis is performed at each random site with every input ground motion to determine the free field motion. The nonlinearity of soil properties is addressed in site response analysis to develop stain-compatible soil properties.

4. The dynamic soil stiffness is generated from the strain-compatible soil properties which are assumed to be constant in this step.
5. Based on the dynamic soil stiffness and structural information, SSI analysis is conducted to generate FLIRS.
6. Comparing FLIRS and input ground motion at bedrock, $\mathcal{A}f$ is determined for each combination of random sites and ground motions. According to the probabilistic description of seismic excitation at bedrock and the distribution of $\mathcal{A}f$, the uniform hazard FLIRS is developed with a desired RP. This uniform hazard FLIRS can be taken as the seismic input for a fixed-base model to generate uniform hazard FRS.

5.2 Application and Parametric Study

The FRS of reactor building shown in Section 3.2 is generated after considering the uncertainty in soil properties and seismic hazard at reference hard rock. The results obtained by the proposed method and the current method are compared.

5.2.1 Site Information and Seismic Input

The uniform hazard spectra representing seismic hazard are shown in Figure 5.8. Two sites, i.e., soil site and rock site, are taken into consideration in this study. The soil properties are listed in Tables 5.4 and 5.5.

According to PSHA results, 11 levels of ground motions are generated with peak acceleration values spanning from $0.01g$ to $1.5g$ to examine the $\mathcal{A}f$ by site response and SSI. The FAS of ground motions are shown in Figure 5.9.

5.2.2 Uncertainty in Geotechnical Model

Shear-Wave Velocity and Thickness Profiles

In this study, the distribution of each layer thickness and the depth to rock are assumed to be normal distribution and coefficient of variation is taken as 0.2.

The V_S follows log-normal distribution. In the three branches, the median values of the V_S in all layers are one of BE, UB, and LB. For instance, V_S in every layer is UB value in

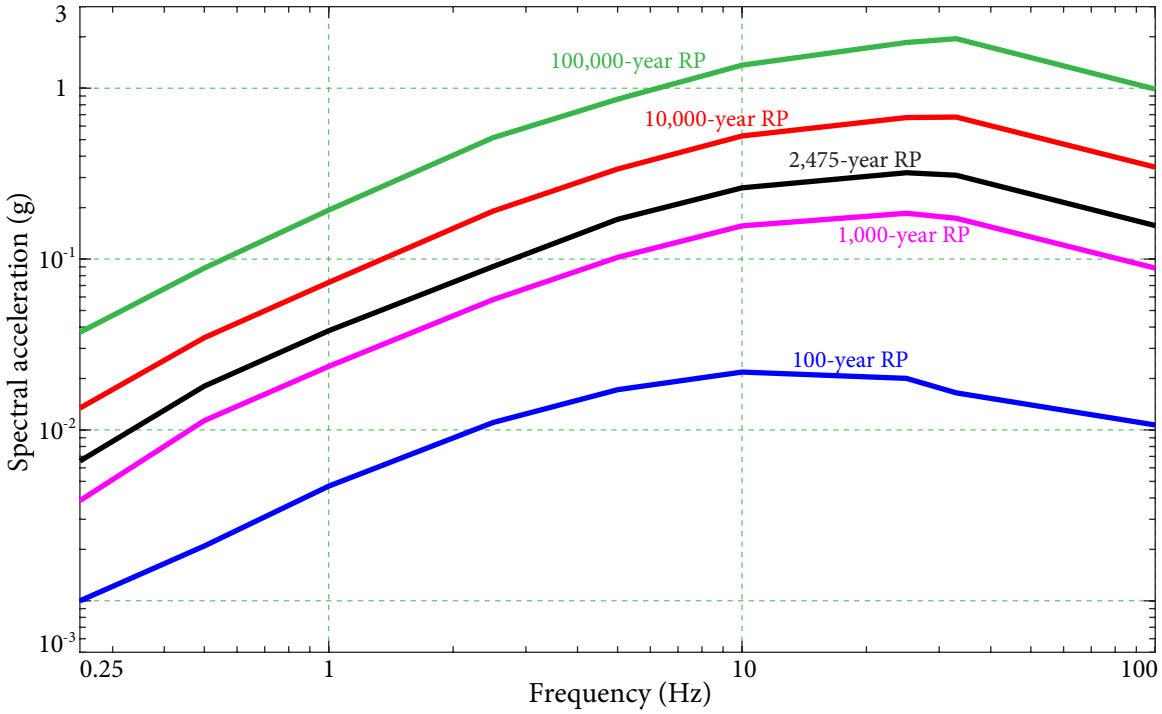

Figure 5.8 UHRS

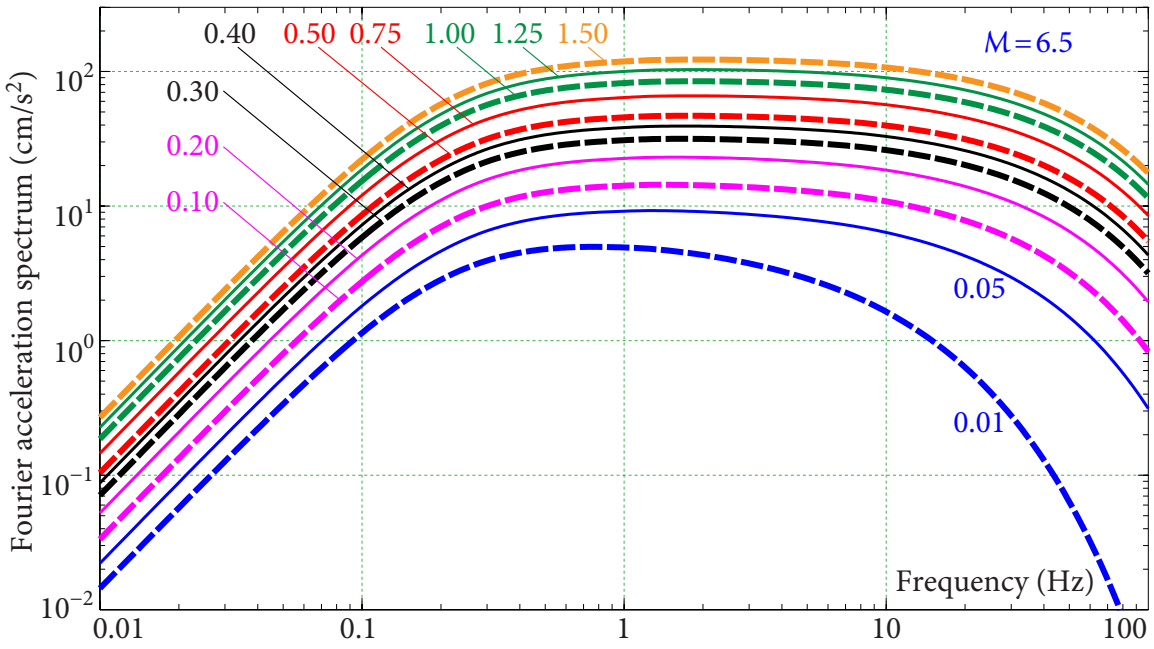

Figure 5.9 FAS for eleven loading levels

UB branch. The weights are 0.4, 0.3, and 0.3 for BE, UB, and LB, respectively. These three V_S profiles are shown in Table 5.6. Then 30 profiles are generated to represent the aleatory uncertainty. The two values of σ_{LN}^{a} are applied in the top 15 m, i.e., 0.25, soil layers and under 15 m, i.e., 0.15. The randomized site profiles are shown in Figure 5.10.

Table 5.4 Soil properties at soil site.

Layer Number	Thickness (m)	Density (g/cm^3)	Shear-Wave Velocity (m/s)	Damping Ratio
1	6	1.9	500	0.05
2	9	2.1	1200	0.03
3	20	2.2	1500	0.03
4	20	2.2	1800	0.03
5	halfspace	2.5	2830	0.01

Table 5.5 Soil properties at rock site.

Layer Number	Thickness (m)	Density (g/cm^3)	Shear-Wave Velocity (m/s)	Damping Ratio
1	15	2.1	1400	0.03
2	20	2.2	1600	0.03
3	20	2.2	1800	0.03
4	halfspace	2.5	2830	0.01

Table 5.6 Shear-wave velocity profiles

Layer Number	Soil Site			Rock Site		
	BE (m/s)	UB (m/s)	LB (m/s)	BE (m/s)	UB (m/s)	LB (m/s)
1	500	783	319	1400	2192	894
2	1200	1879	766	1600	2506	1022
3	1500	2349	958	1800	2819	1149
4	1800	2819	1149	2830	2830	2830
5	2830	2830	2830	N/A	N/A	N/A

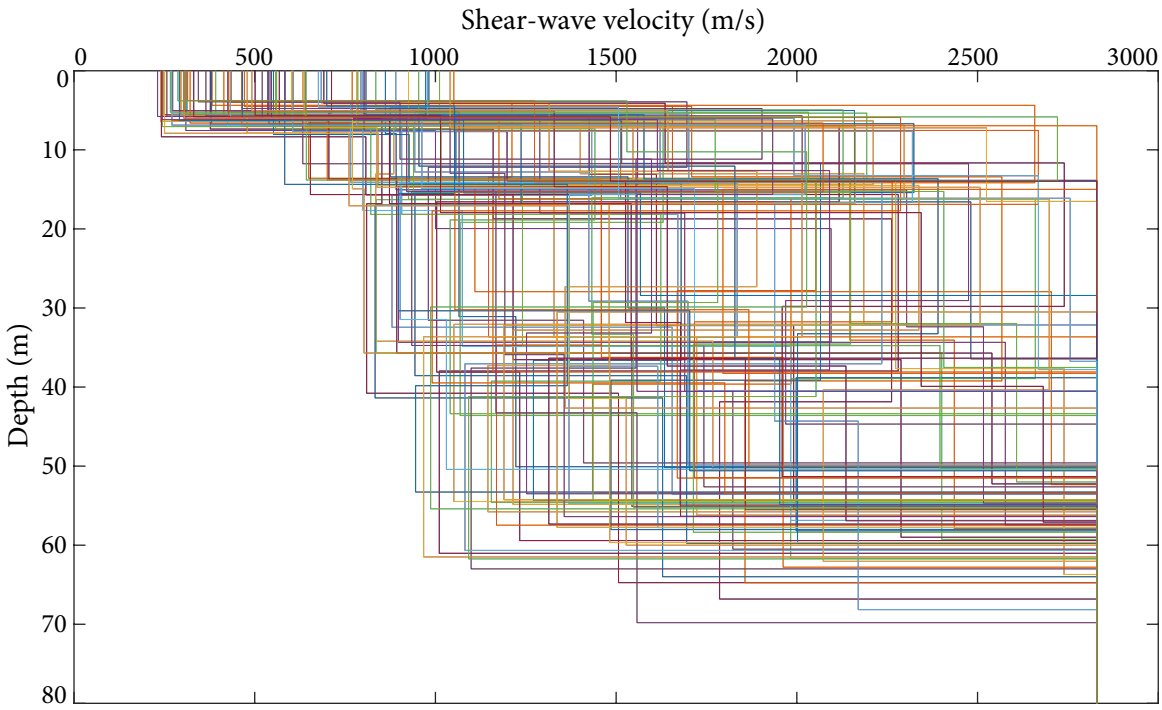

Figure 5.10 Realizations of shear-wave velocity profile in case 1

Dynamic Material Properties Curves

According to Section 5.1.2, 2 sets of G/G_{Max} and damping are used with equal weights. Dynamic properties for the sites are listed in Table 5.7. The random curves of EPRI soil in first layer at the soil site are shown in Figure 5.11 which shows a wide range of random curves used in this study.

Table 5.7 Dynamic property for the sites

Layer Number	Soil Site		Rock Site	
	Curve Set 1	Curve Set 2	Curve Set 1	Curve Set 2
1	EPRI soil	Peninsular range	EPRI rock	Linear 3%
2	EPRI rock	Linear 3%	EPRI rock	Linear 3%
3	EPRI rock	Linear 3%	EPRI rock	Linear 3%
4	EPRI rock	Linear 3%	Linear 1%	Linear 1%
5	Linear 1%	Linear 1%	N/A	N/A

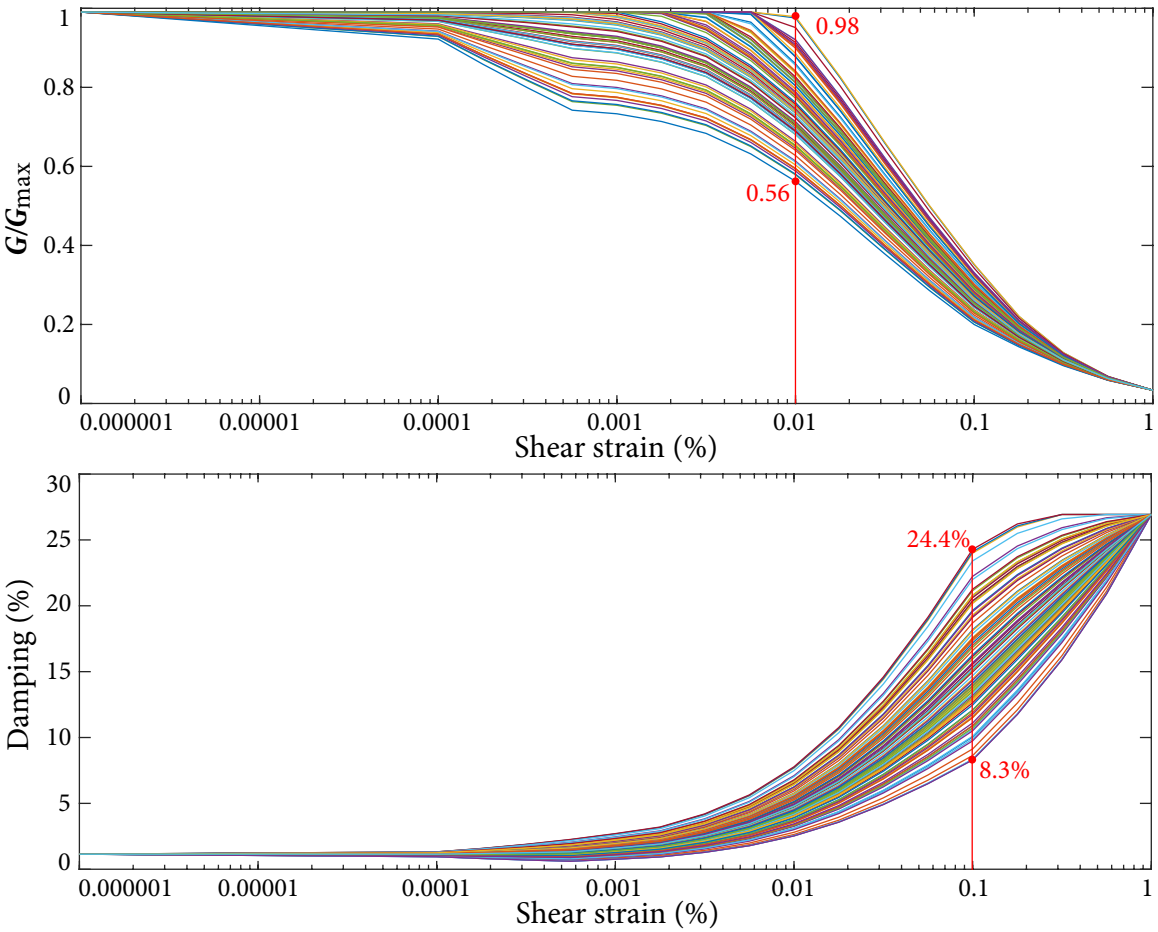

Figure 5.11 Realizations of shear modulus and hysteretic damping curves for 0-6 m soil.

5.2.3 Resultant Foundation Level Input Response Spectra

The logic tree for the generation of FRS in this application is shown in Figure 5.12. There are $2 \times 90 = 180$ geotechnical models generated to capture epistemic uncertainty and aleatory uncertainly. As 11 ground motion levels are considered, a total of $180 \times 11 = 1980$ analyses are performed.

In this example, the site response analysis is conducted in frequency domain. The horizontal FIRS and strain-compatible soil properties for all realizations are obtained. Then the dynamic stiffness is calculated based on the strain-compatible soil properties. The

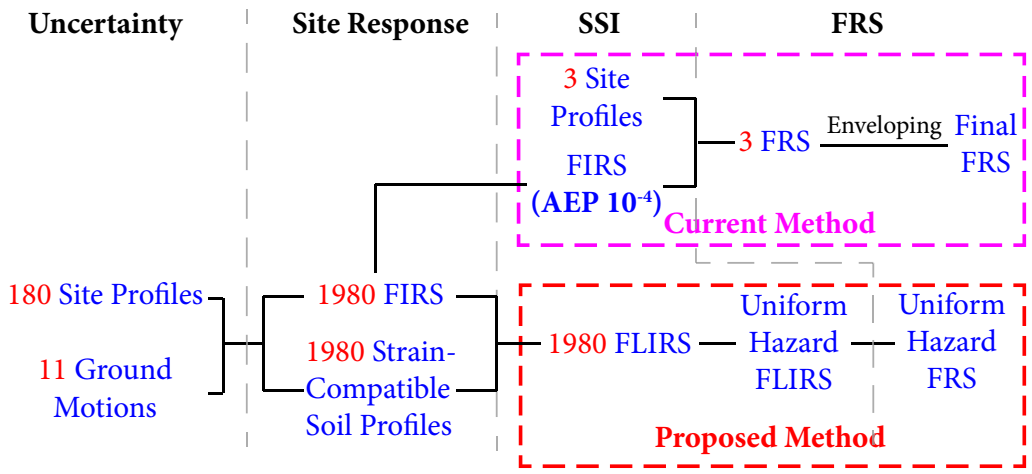

Figure 5.12 Comparison of two methods in the application

strain-compatible dynamic stiffness under the ground motion with PGA of $0.3g$ are shown in Figure 5.13,

V/H ratios from GMPEs in the WUS is applied to calculate the site-specific V/H ratios. Three GMPEs are usually used, e.g., Bozorgnia and Campbell (2004), and Gulerce and Abrahamson (2011). The vertical FIRS is developed from the horizontal FIRS and site-specific V/H ratios and is shown in Figure 5.14.

The horizontal FIRS at the soil site and the rock site are shown in Figures 5.15 and 5.16. The FIRS with RP of 10,000 years is calculated and then used in the SSI analysis by the current method.

According to the proposed substructure method, the FLIRS for each randomization are generated. The horizontal FLIRS are shown in Figures 5.17 and 5.18. It illustrates that FLIRS is amplified at different frequency points for each site. μ_i and σ_i of $\mathcal{A}\!f$ are calculated for each site given the ground motion and frequency. $\mu_{\ln \mathcal{A}\!f|a}$ and $\sigma_{\ln \mathcal{A}\!f|a}$ of $\mathcal{A}\!f$ given eleven loading levels at soil site and rock site are presented in Figures 5.19 to 5.22. Based on $\mathcal{A}\!f$ and seismic hazard curves at reference hard rock, a sets of uniform hazard FLIRS with different RP can be determined according to Equations (5.10) and (5.11) as illustrated in Figures 5.17 and 5.18.

The comparison of FLIRS calculated by proposed method and current method are shown in Figures 5.23 and 5.24. They demonstrate that the peaks of FLIRS at BE, UB, and LB sites

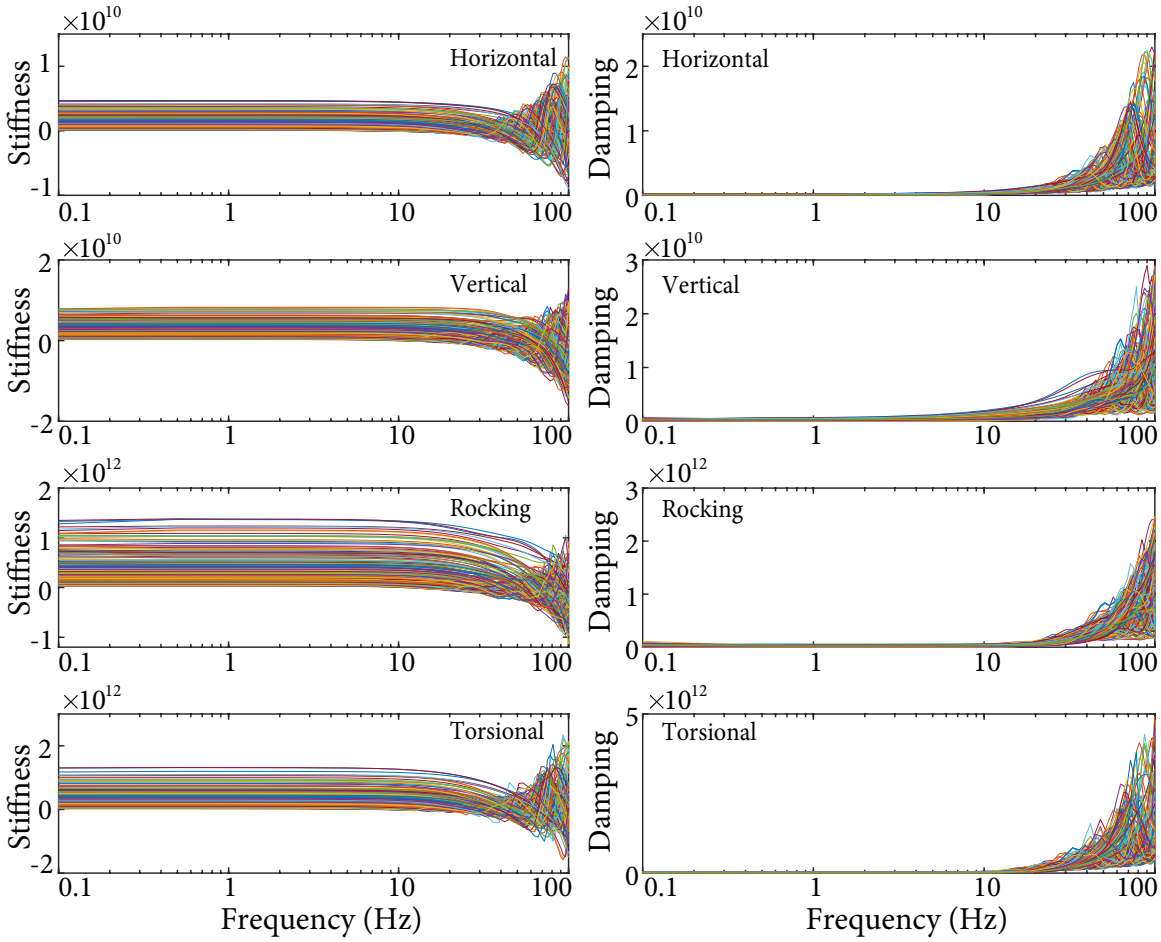

Figure 5.13 Strain-compatible dynamic stiffness

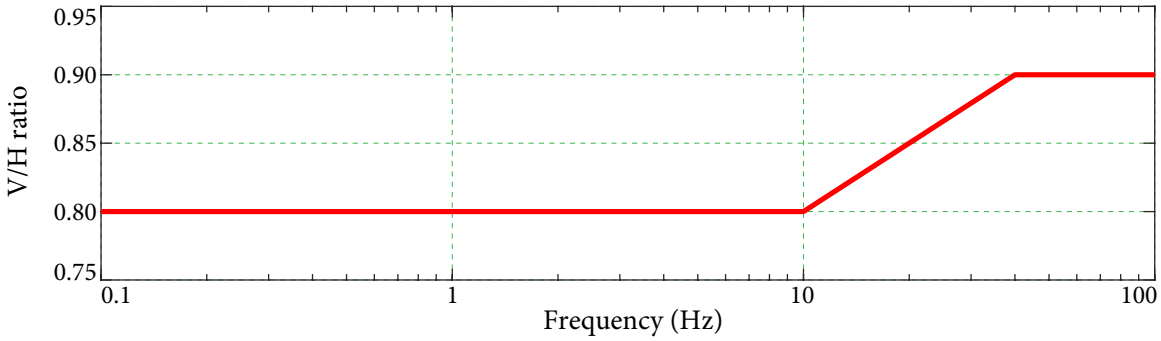

Figure 5.14 V/H ratios for FIRS

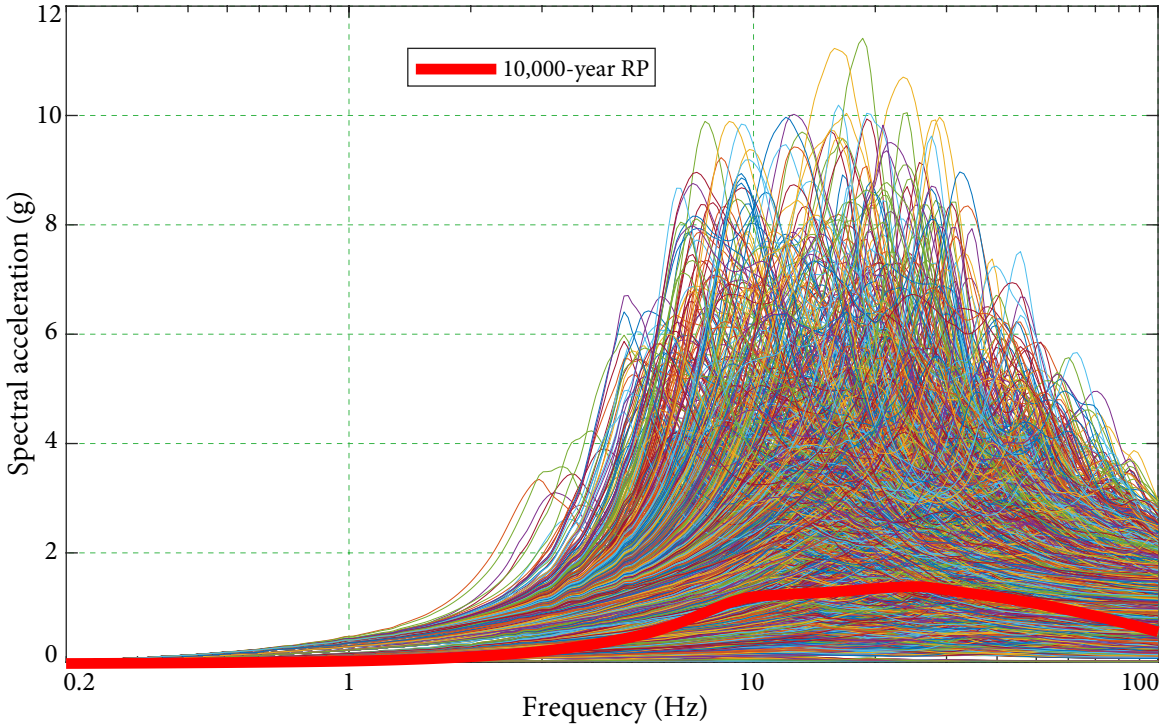

Figure 5.15 Resultant FIRS at soil site

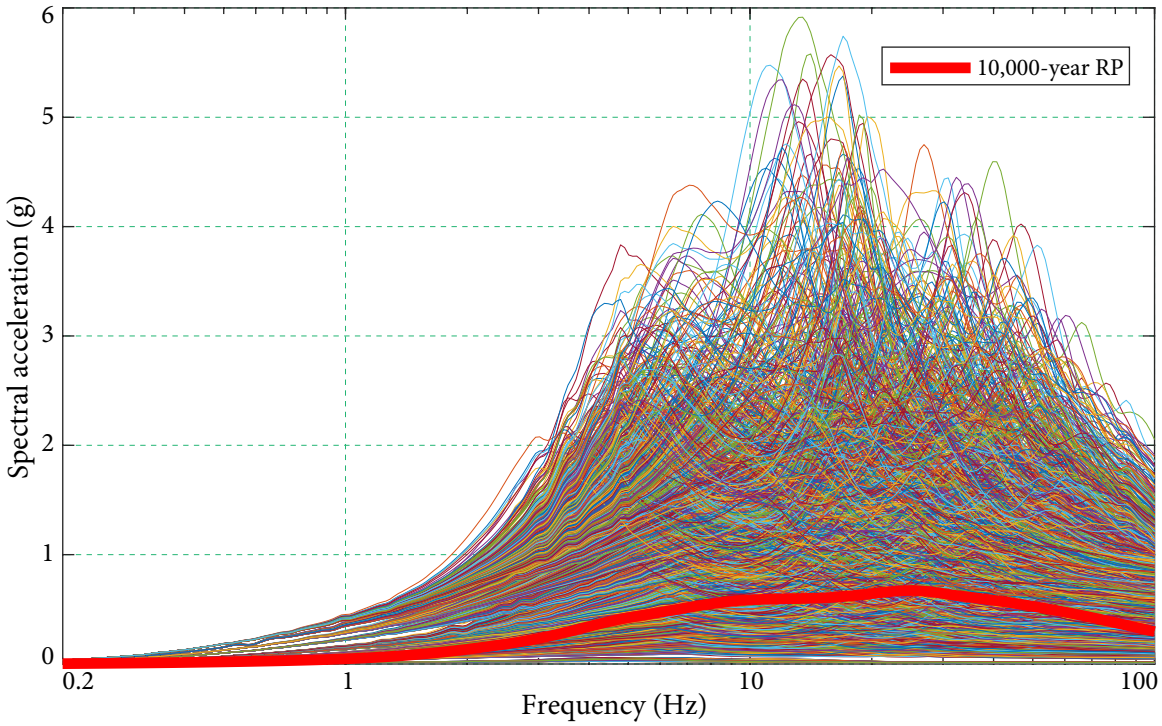

Figure 5.16 Resultant FIRS at rock site

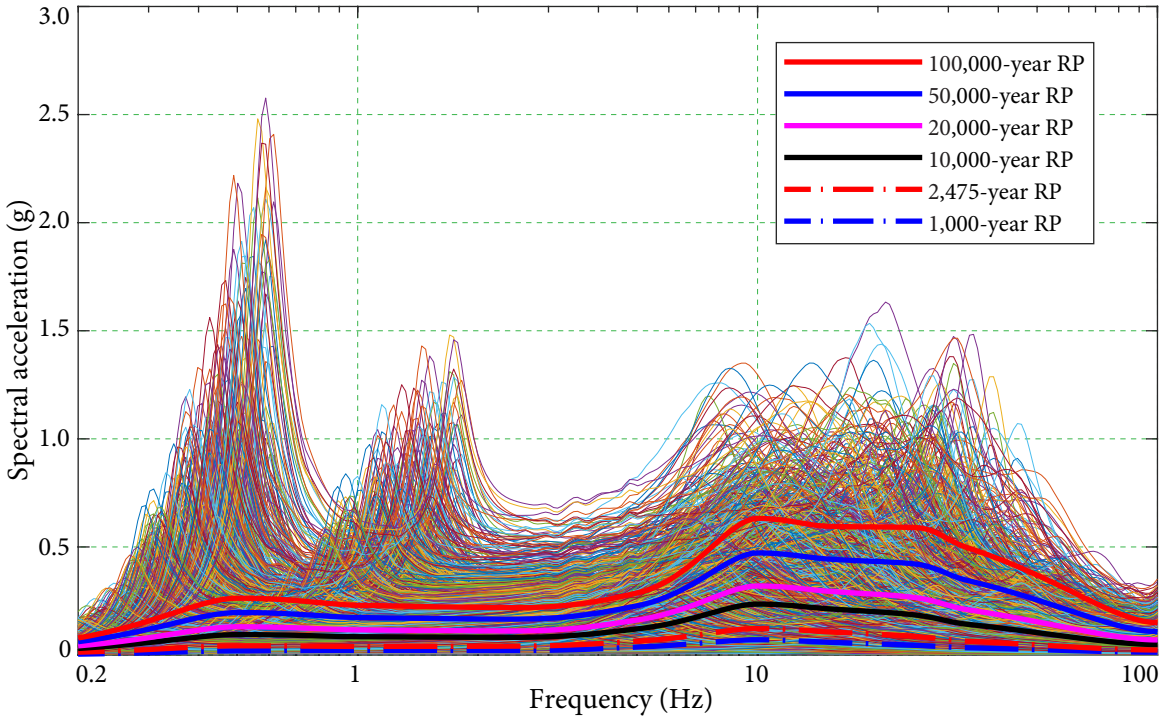

Figure 5.17 Resultant FLIRS at soil site

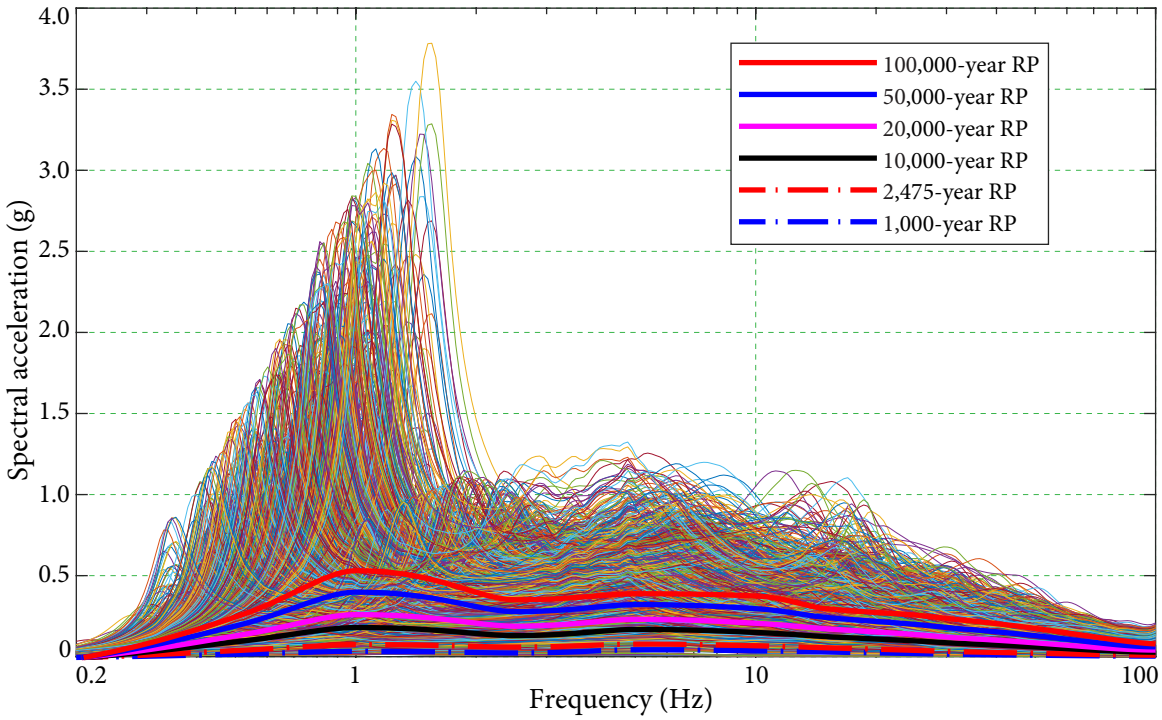

Figure 5.18 Resultant FLIRS at rock site

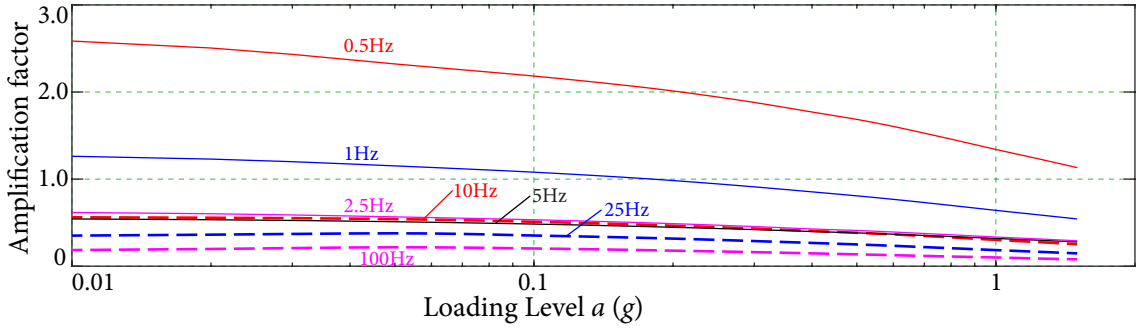

Figure 5.19 Median amplification factors at soil site

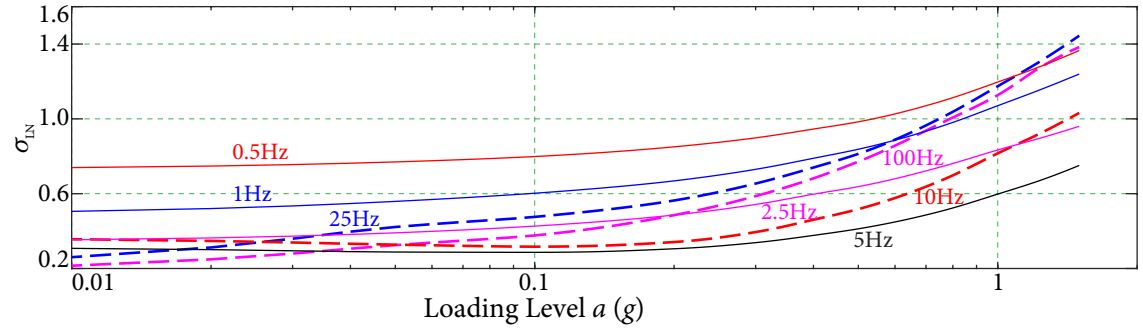

Figure 5.20 Logarithmic standard deviations at soil site

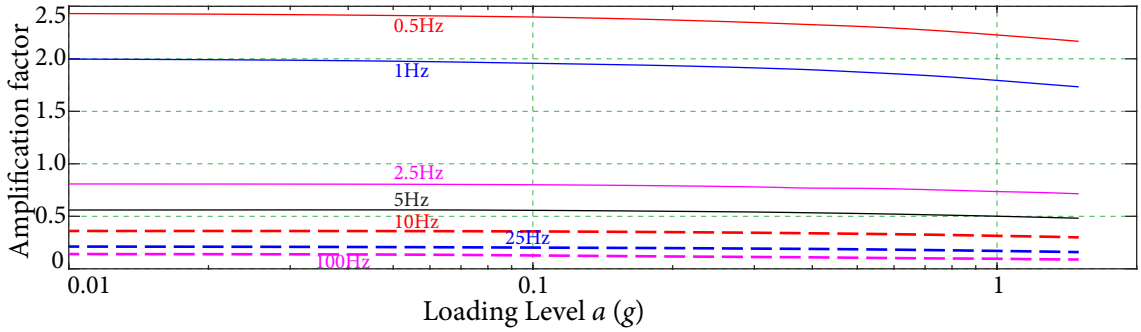

Figure 5.21 Median amplification factors at rock site

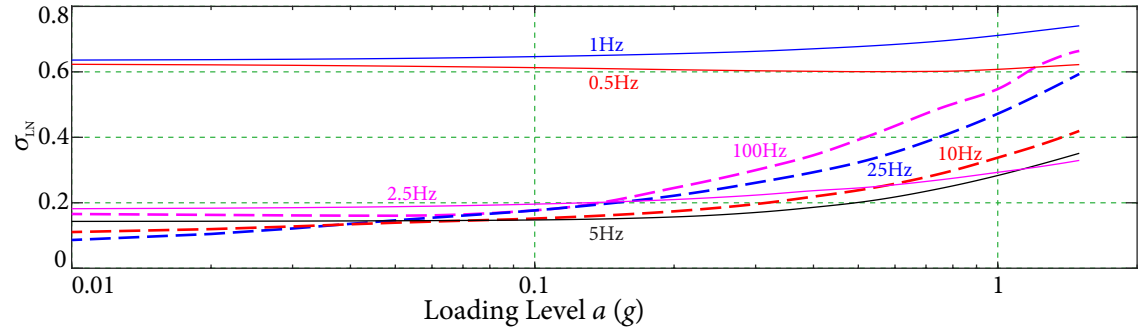

Figure 5.22 Logarithmic standard deviations at rock site

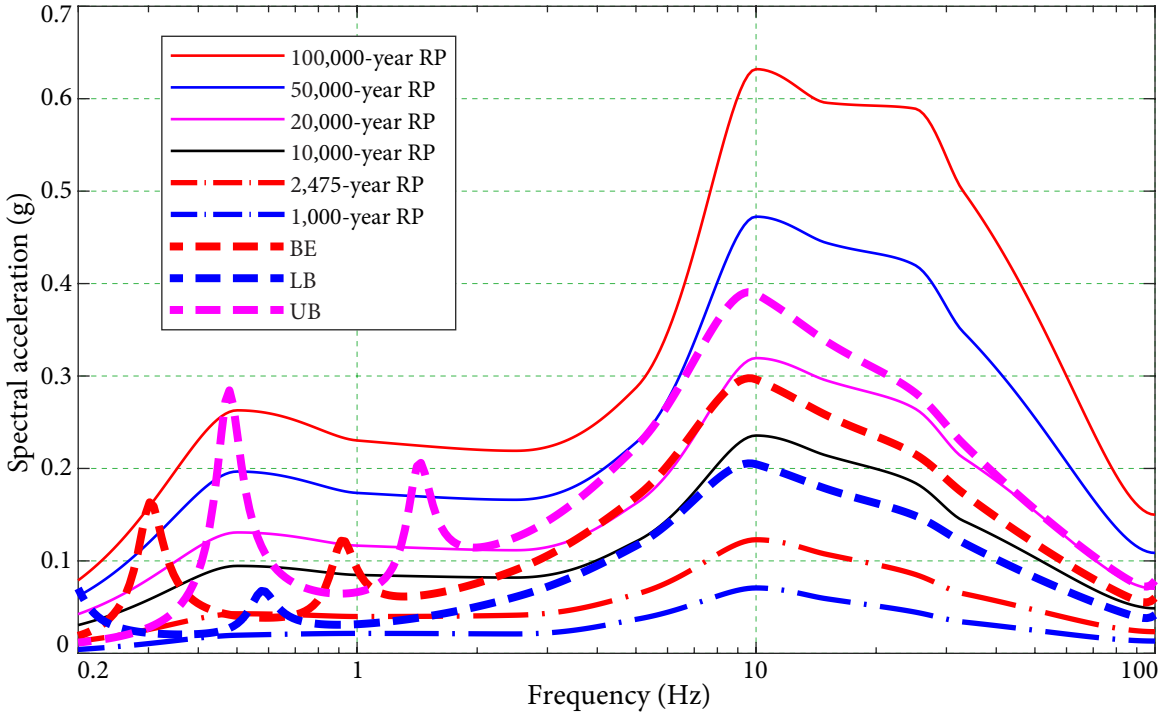

Figure 5.23 FLIRS at soil site

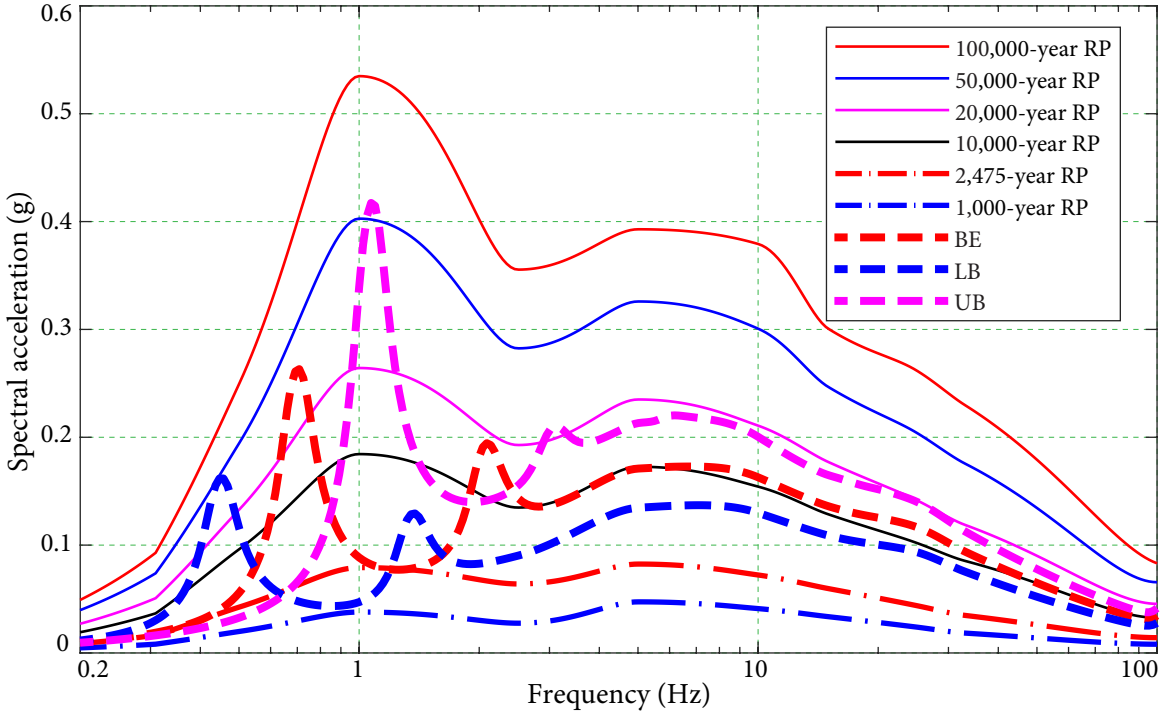

Figure 5.24 FLIRS at rock site

are sharp, while the FLIRS generated by the proposed method is smooth with uniform hazard. In low frequency domain, i.e., 3 Hz and below, the BE, UB, and LB FLIRS vibrate significantly between 1,000-year RP and 100,000-year RP. In the frequency range above 3 Hz, the RP of 3 FLIRS is stable and partly parallel to the uniform hazard FLIRS. The BE FLIRS is between 10,000-year RP and 20,000-year RP, while LB is between 2,475-year RP and 10,000-year RP. However, the RP of UB at soil site changes from 20,000 years to 50,000 years, while this is different in rock case where it ranges from 10,000 years to 20,000 years.

5.2.4 Floor Response Spectra

Depending on the direct spectra-to-spectra method, 3 sets of FRS in the current method, i.e., BE, UB, and LB, are calculated as shown in Figures 5.25 to 5.28. Then the final FRS are obtained by maximum value method, i.e., enveloping the 3 sets of FRS at each frequency point. According to the figures, it is observed that in the frequency range above 1 Hz, the final FRS, the black dashed line, are solely determined from the UB case. That means only one extreme soil case is considered in the the generation of FRS considering SSI after FIRS with RP of 10,000 years is developed. This treatment eventually leads to an extreme FRS which is not a reasonable seismic demand for secondary systems.

Compared to the current method, a set of uniform hazard FRS with different RP are generated by the proposed fully probabilistic method. The comparison of the results are shown in Figures 5.29 to 5.32. In most frequency ranges, i.e., the frequency is above 3 Hz, the RP of FRS is almost equal to 50,000 years at soil site as shown in Figures 5.29 and 5.30, while the RP is close to 20,000 years at rock site as shown in Figures 5.31 and 5.32. It is recognized that the hazard level of the final FRS in the current application is not consistent at different sites. This will result in over estimated FRS at specific sites.

In the frequency range below 3 Hz, the smallest RP of FRS given by the enveloping method is close to 2,475 years at the soil site, but the highest value is larger than 100,000 years. For the rock site, the RP of FRS ranges between 2,475 years to 100,000 years at low frequency domain. This variation also happens between 8 Hz and 20 Hz at the soil site where the RP of FRS at node 5 decreases from 50,000 years significantly. It is demonstrated

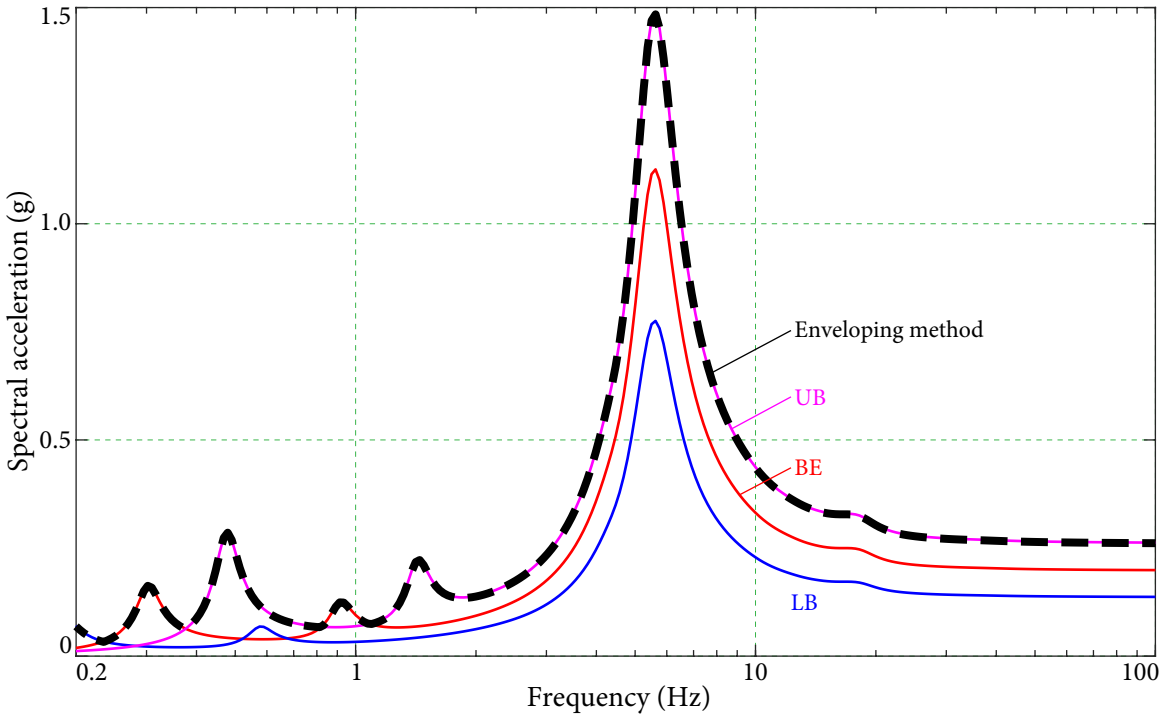

Figure 5.25 FRS by current method at node 4 for soil site

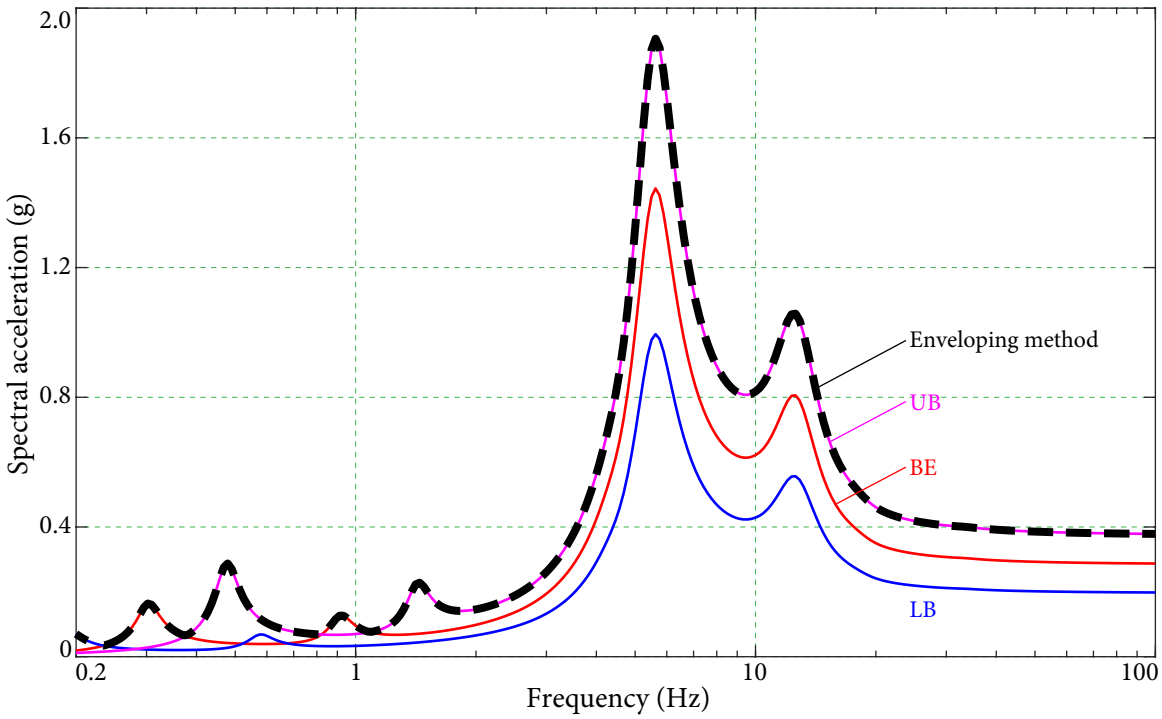

Figure 5.26 FRS by current method at node 5 for soil site

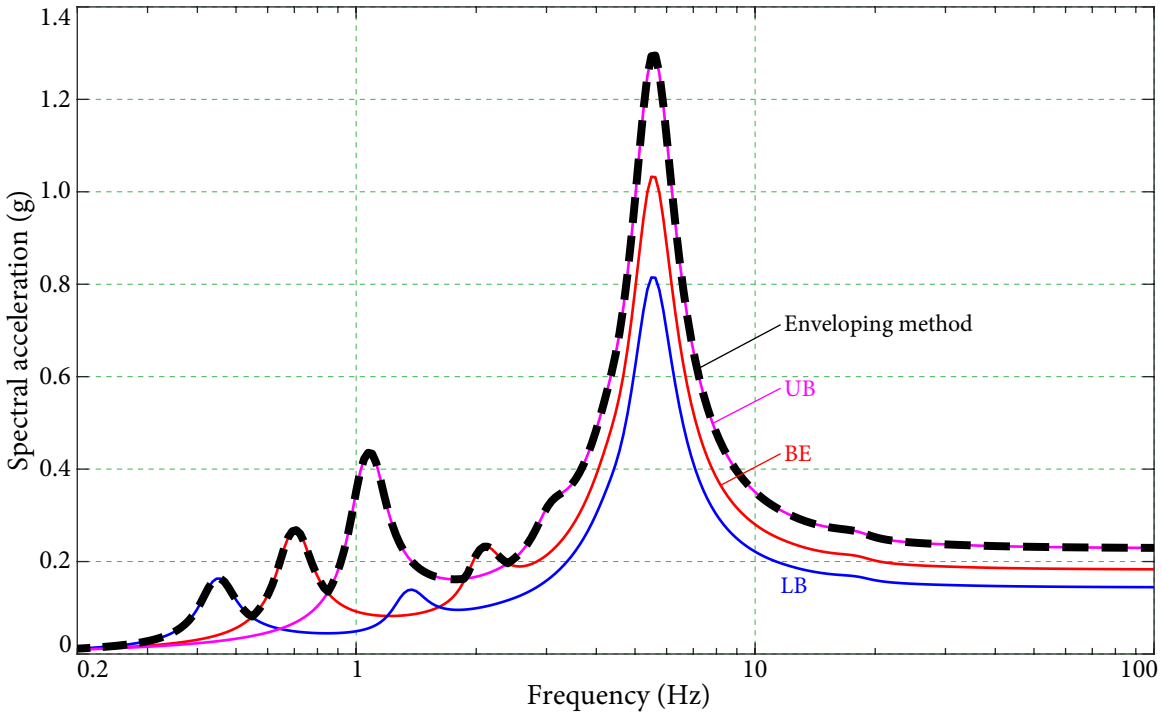

Figure 5.27 FRS by current method at node 4 for rock site

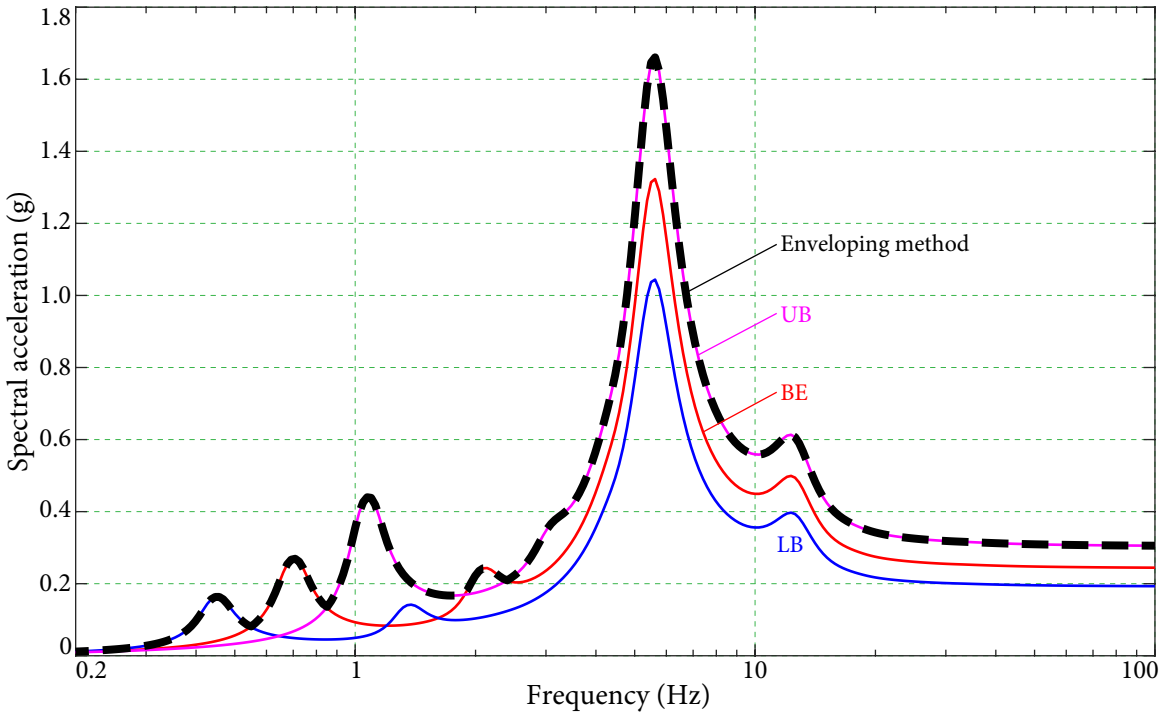

Figure 5.28 FRS by current method at node 5 for rock site

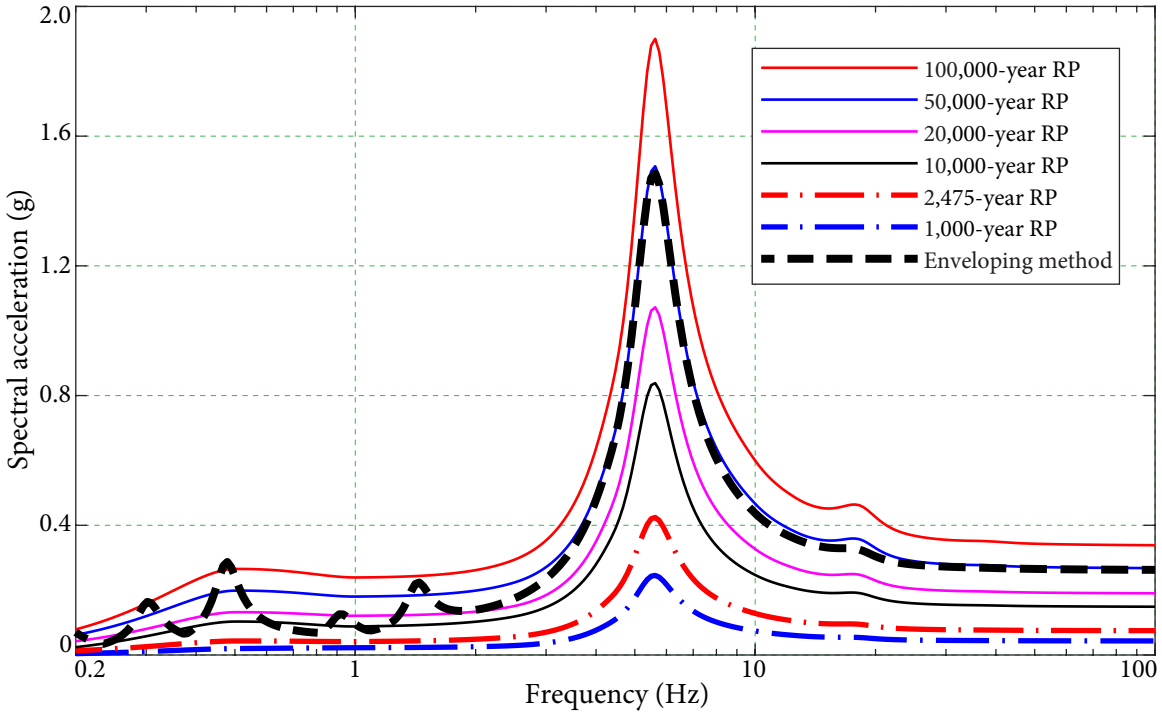

Figure 5.29 Comparison of FRS at node 4 for soil site

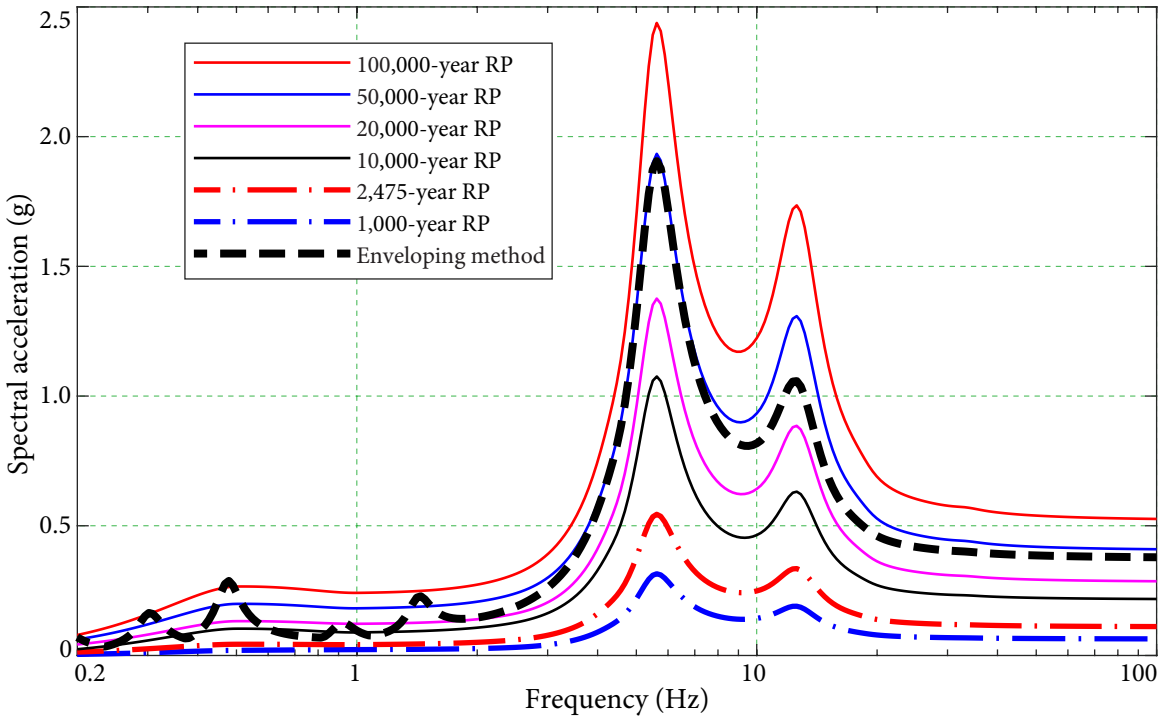

Figure 5.30 Comparison of FRS at node 5 for soil site

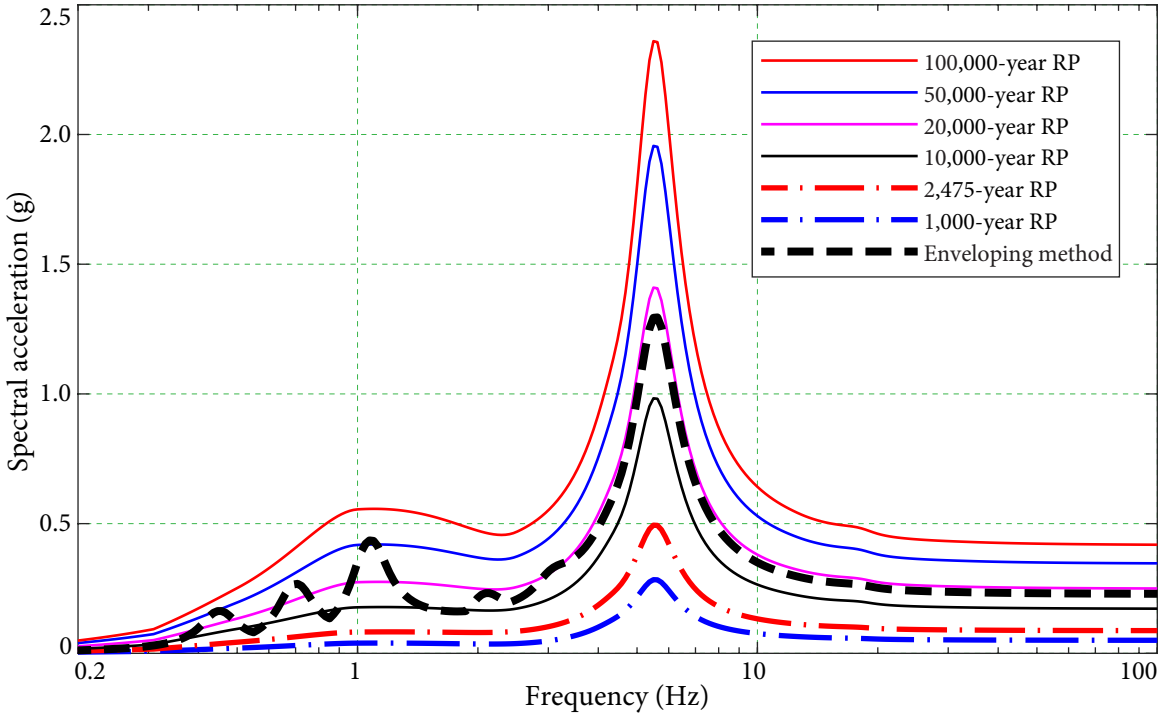

Figure 5.31 Comparison of FRS at node 4 for rock site

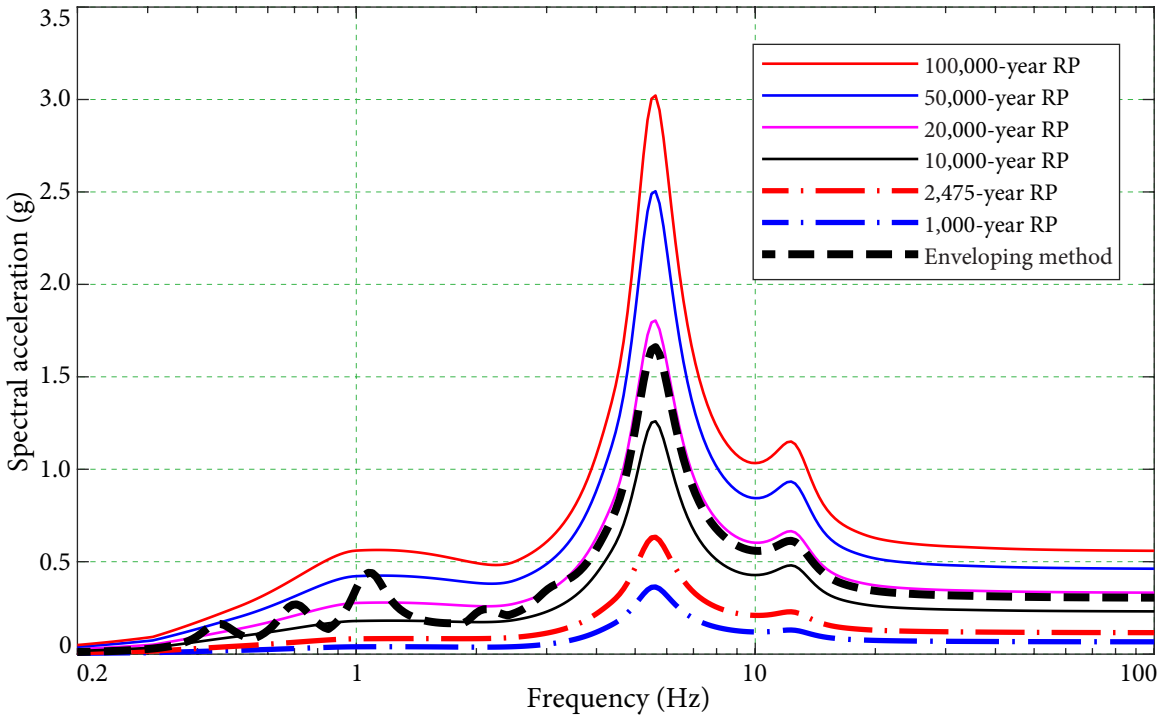

Figure 5.32 Comparison of FRS at node 5 for rock site

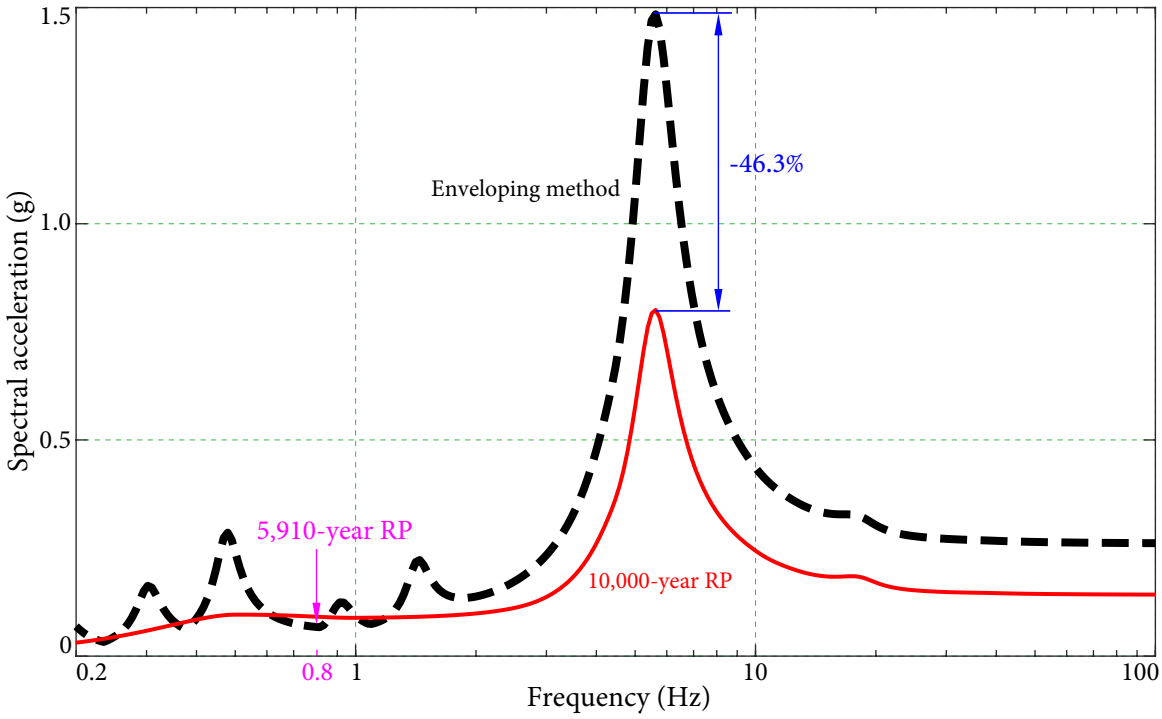

Figure 5.33 Resultant FRS at node 4 for soil site

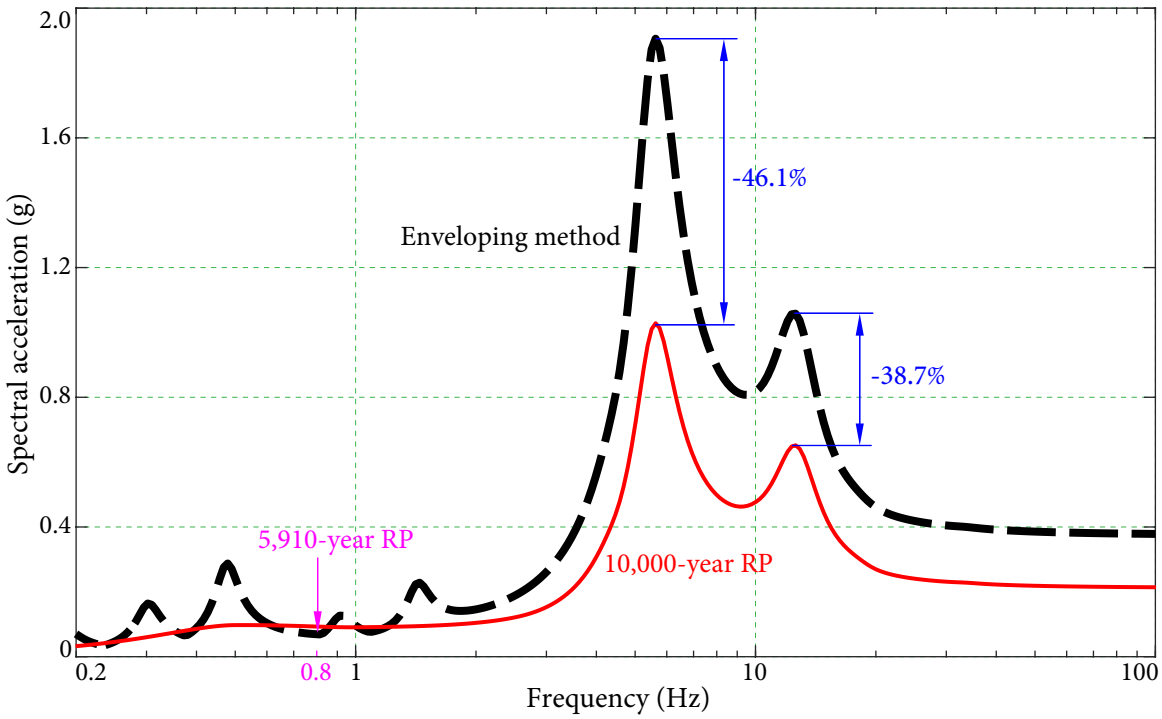

Figure 5.34 Resultant FRS at node 5 for soil site

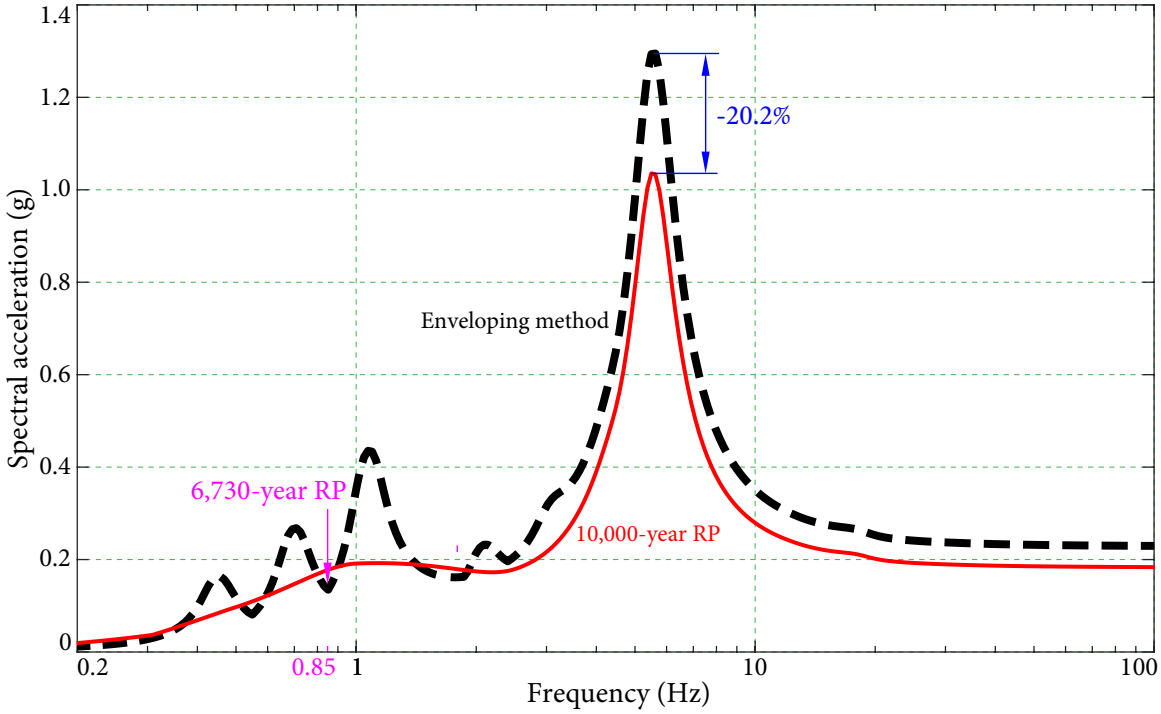

Figure 5.35 Resultant FRS at node 4 for rock site

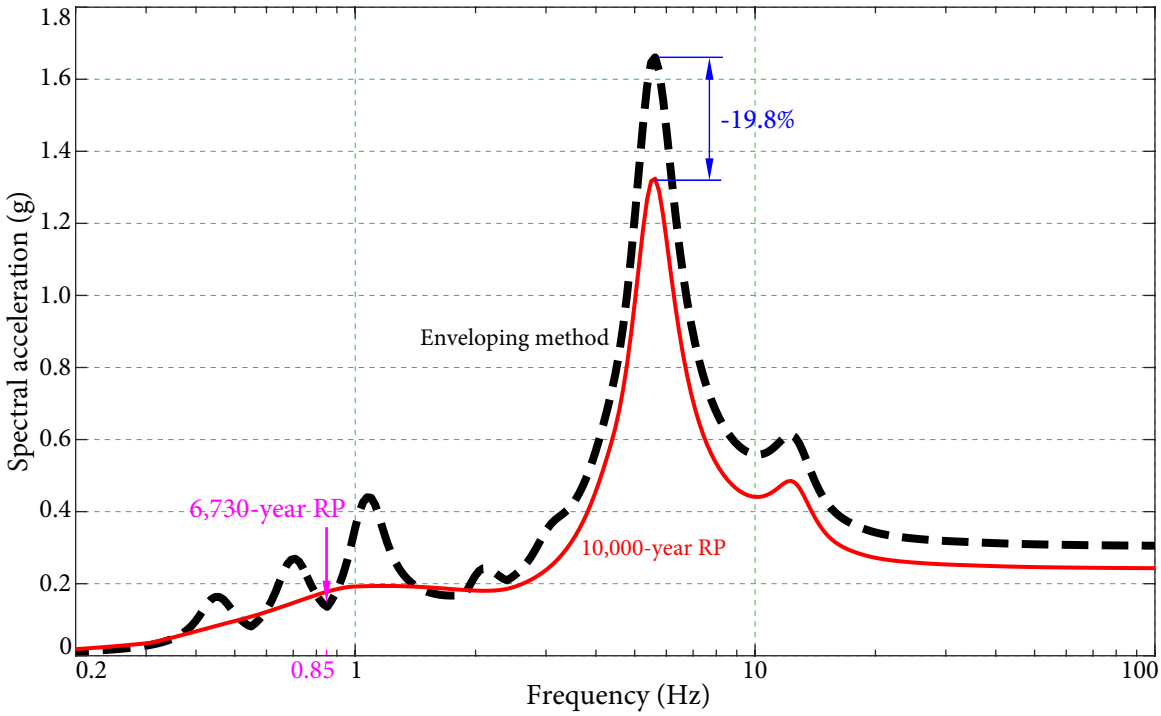

Figure 5.36 Resultant FRS at node 5 for rock site

that the FRS given by enveloping method may be too conservative at some frequency points, while the underestimation also exits.

In nuclear industry, the RP is usually taken as 10,000 years in the seismic design. The comparison of FRS given by the enveloping method and the values with RP of 10,000 years by the proposed method are presented in Figures 5.33 to 5.36. The difference between the enveloping method, the dashed black line, and the proposed method, the solid red line, are noticeable. Based on the proposed method, the peak values of FRS at 5.6 Hz are reduced by 46% and 20% at the soil site and rock site, respectively. For the second peak of node 5 at the soil site, it is reduced by 39%. At the same time, the RP of FRS given by the enveloping method is lower than 10,000 years at some low frequency points, e.g., RP of current application are 5,910 years at 0.8 Hz on soil site and 6,730 years at 0.85 Hz on rock site. In general, the final FRS decreases significantly based on the proposed method which provides a cost-effective solution in the seismic design. Meanwhile, the proposed method also improves the safety in the low frequency domain.

It illustrates that enveloping 3 sets of FRS dose not consider the uncertainty of earthquake excitation and soil properties properly. The resultant FRS by the enveloping method is an extreme case with high seismic demand, and can not represent the variation of the soil properties. The hazard are not addressed reasonably and consistently throughout the frequency range. The proposed method fully captures the uncertainty in the generation of FRS. The uncertainty are convolved into uniform hazard FLIRS, which is the modified free field motion after considering SSI. The uniform hazard FRS is generated by taking the uniform hazard FLIRS as the seismic input in the fixed-base model.

5.2.5 Parametric Study on σ_{LN} and ρ of V_S

In order to address the influence of σ_{LN} and the correlation coefficient ρ of the adjacent layers, 7 cases of both the soil site and rock site are studied. The relevant parameters and the generation of shear-wave velocity profiles are shown in Figure 5.37.

In case 1, current V_S distribution is employed as described in Section 5.2.2, in which the epistemic uncertainty are assumed fully correlated. In case 2, the correlation of epistemic

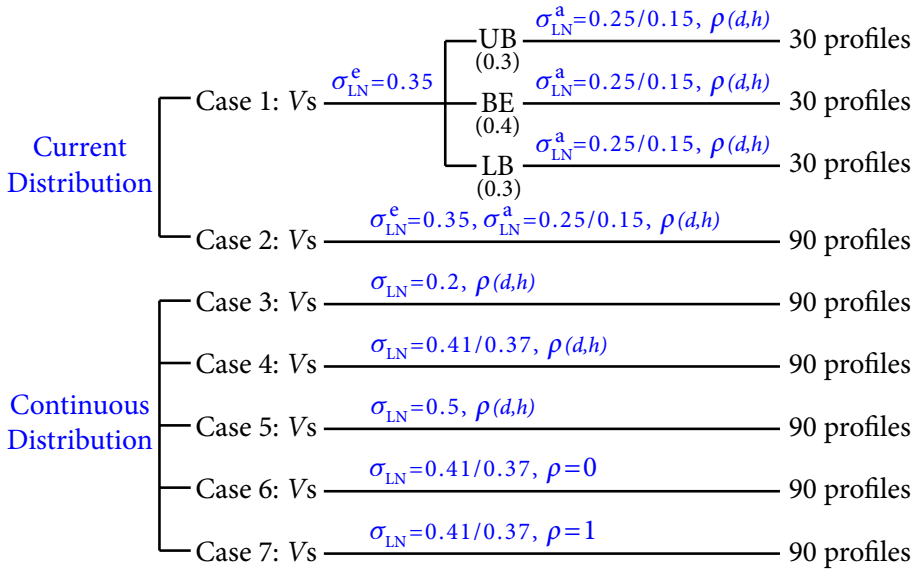

Figure 5.37 Generation of site profiles

uncertainty is treated the same as aleatory uncertainty in each layer. The correlation coefficient is determined as a function of depth and thickness.

In cases 3 to 5, the V_S profiles are generated following Equation (5.5), the continuous log-normal distribution. Different σ_{LN} are used to examine its sensitivity. In case 4, 0.41 used in top 15 m, and 0.37 used in lower layers, are the equivalent σ_{LN} of the current distribution proposed in Section 5.1.2. In cases 6 and 7, different ρ are used to examine the sensitivity about ρ. In order to compare with current application, the same number, 90, of site profiles are generated.

In the comparison of cases 1 and 2 as shown in Figures 5.38 to 5.41, the difference is noticeable, and is up to 5.24% when epistemic uncertainty is treated by different approaches. It

Table 5.8 Relative errors at the peak with different σ_{LN}

Case Number	Soil Site		Rock Site	
	Node 11	Node 12	Node 11	Node 12
3	-1.59%	-1.59%	-0.75%	-0.74%
5	2.21%	2.21%	-1.33%	-1.33%

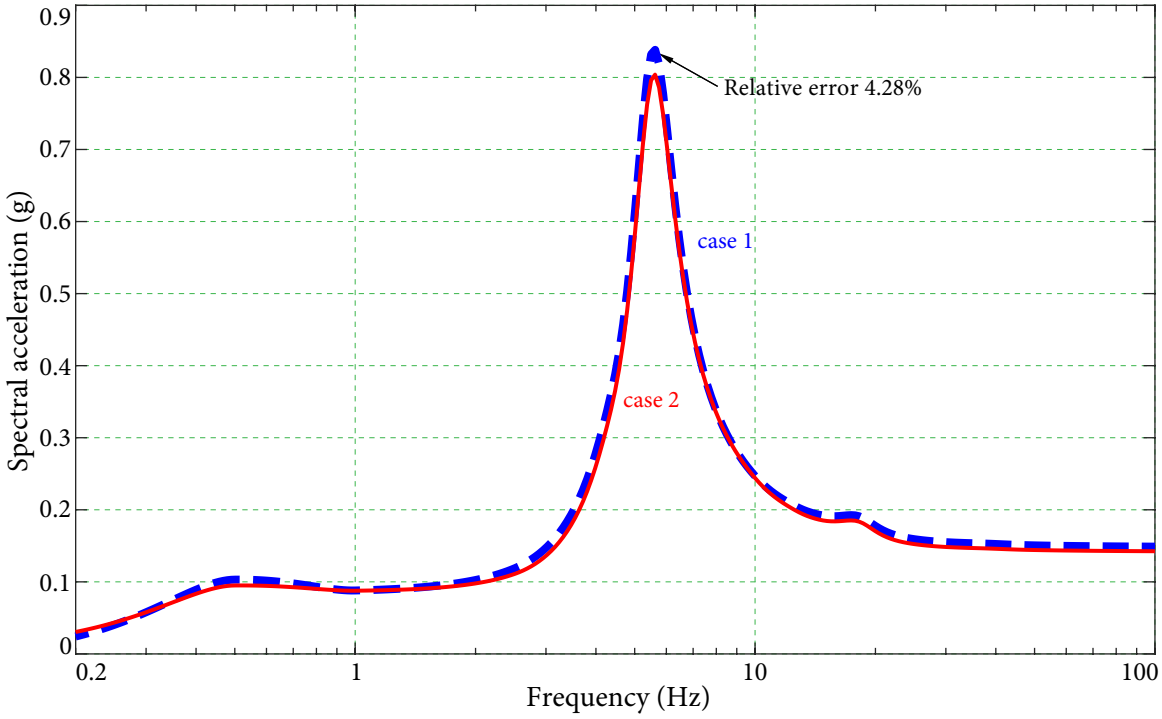

Figure 5.38 FRS at node 4 for different treatment of epistemic at soil site

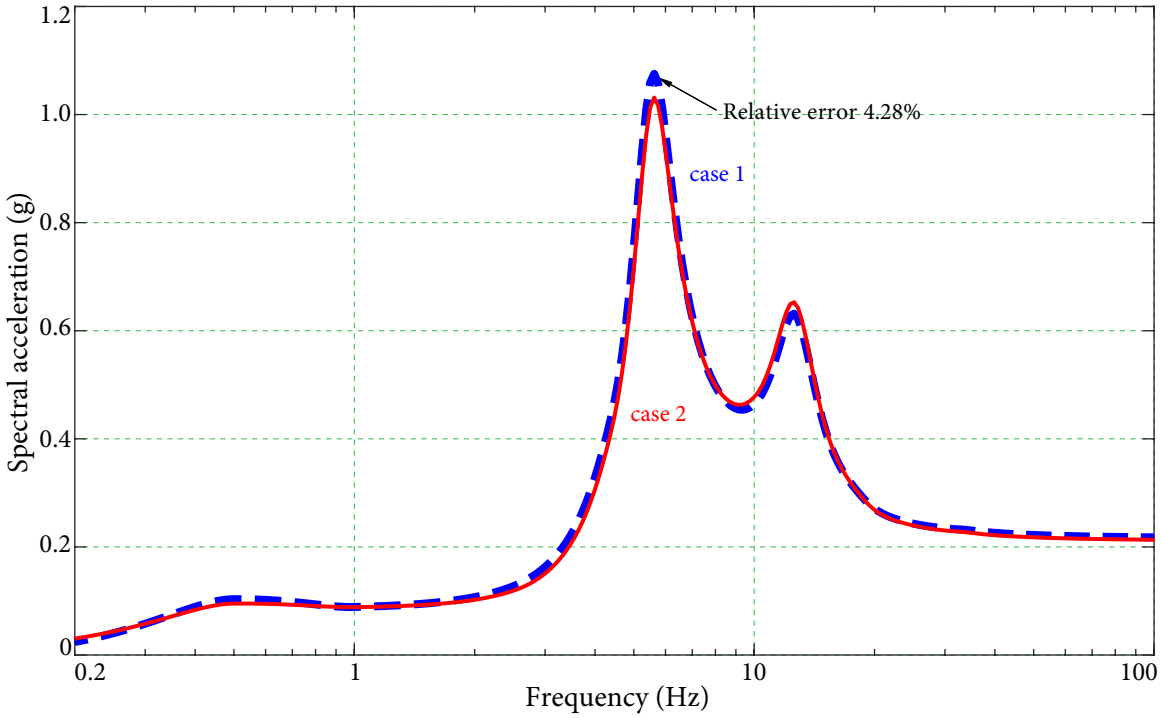

Figure 5.39 FRS at node 5 for different treatment of epistemic at soil site

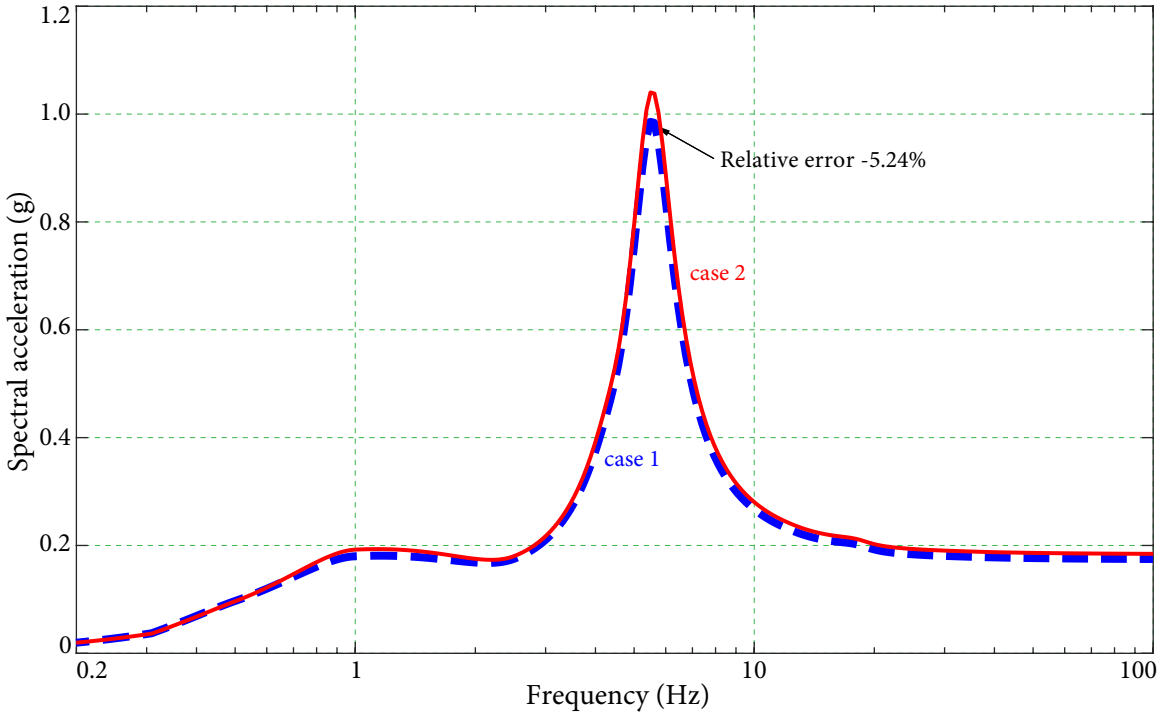

Figure 5.40 FRS at node 4 for different treatment of epistemic at rock site

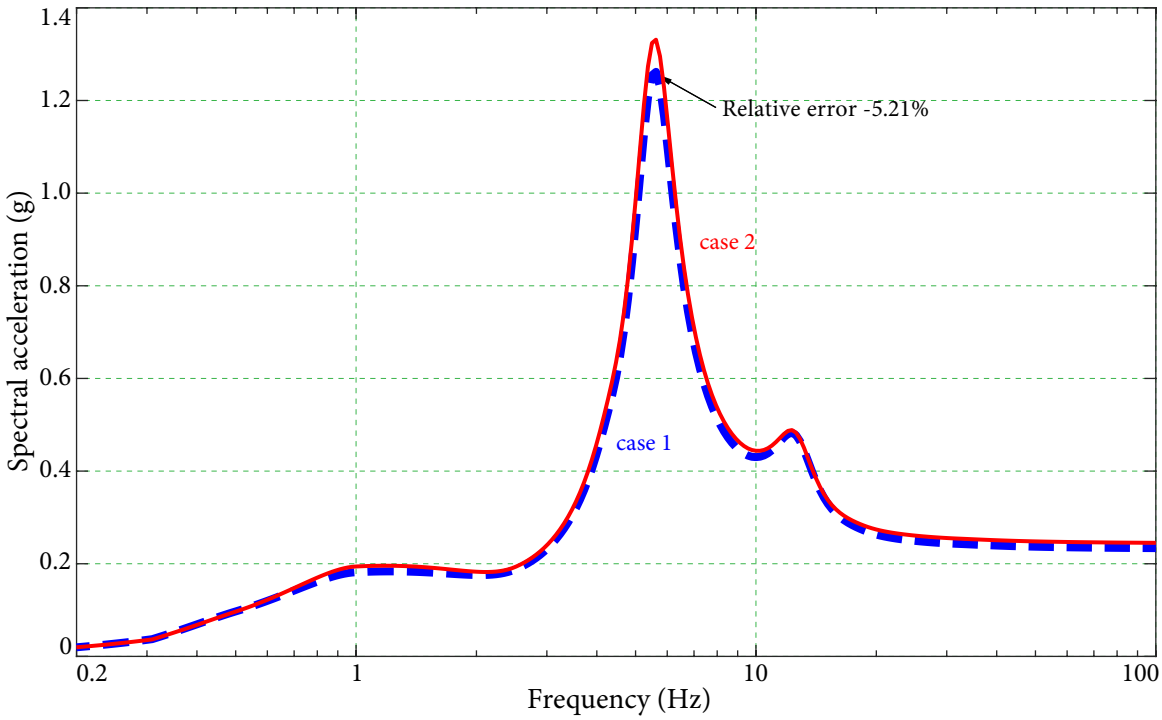

Figure 5.41 FRS at node 5 for different treatment of epistemic at rock site

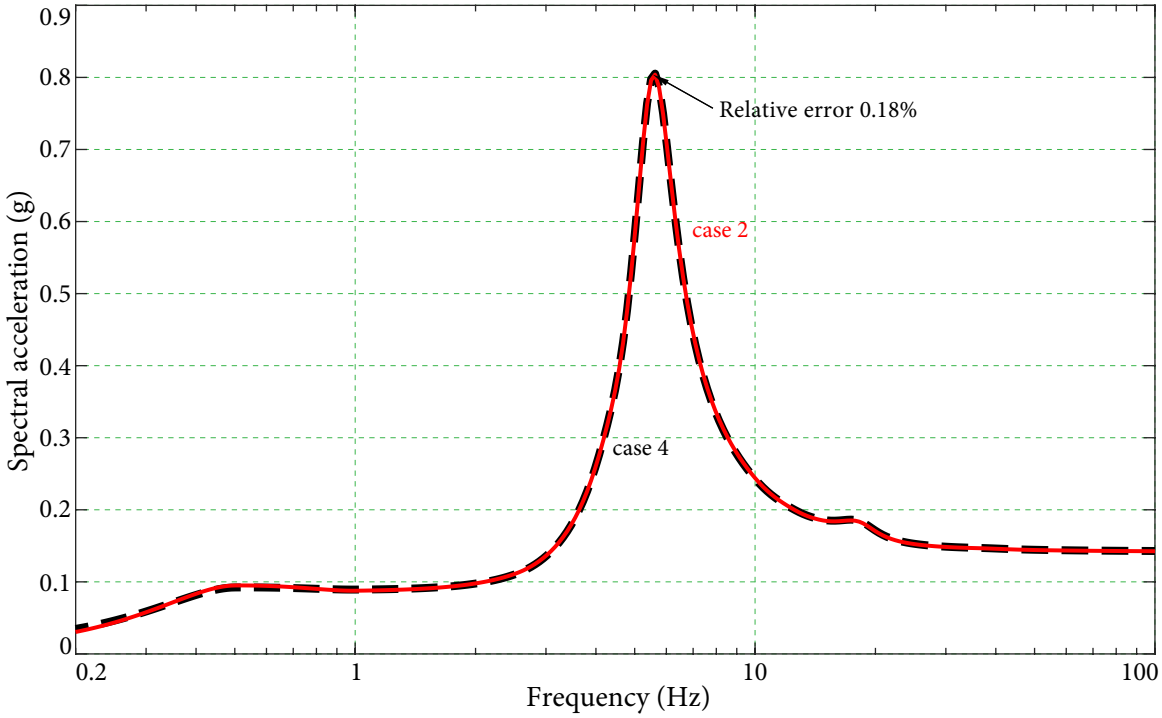

Figure 5.42 FRS at node 4 for proposed V_s distribution at soil site

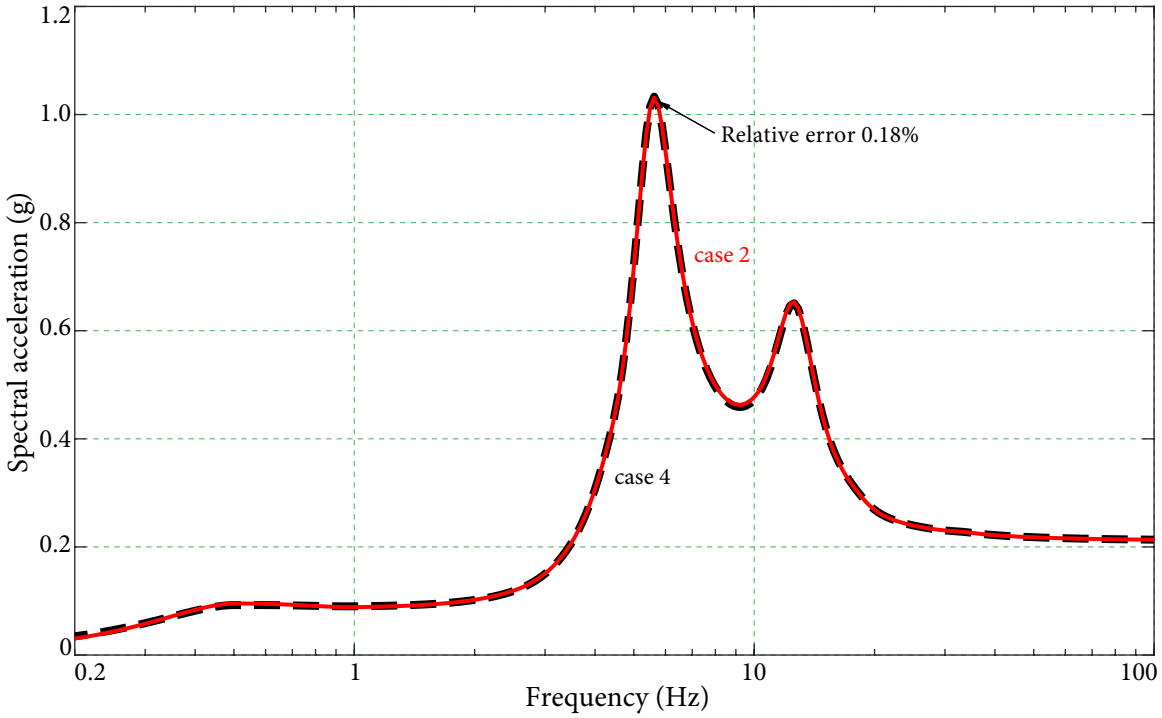

Figure 5.43 FRS at node 5 for proposed V_s distribution at soil site

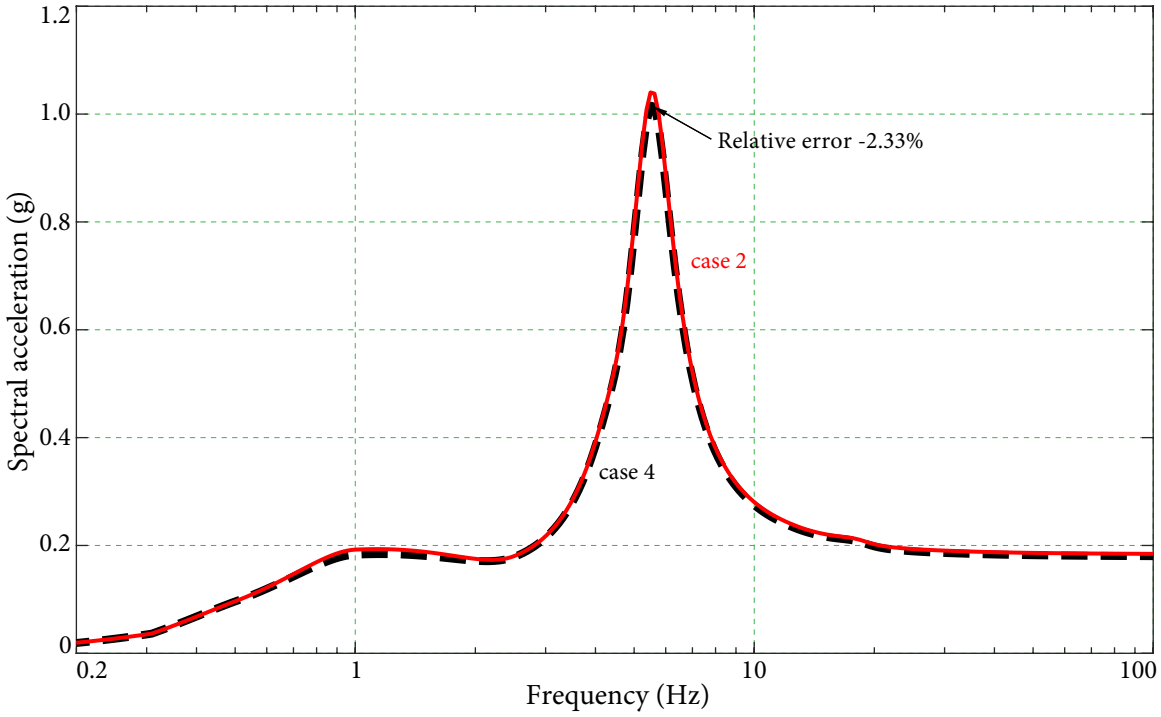

Figure 5.44 FRS at node 4 for proposed V_s distribution at rock site

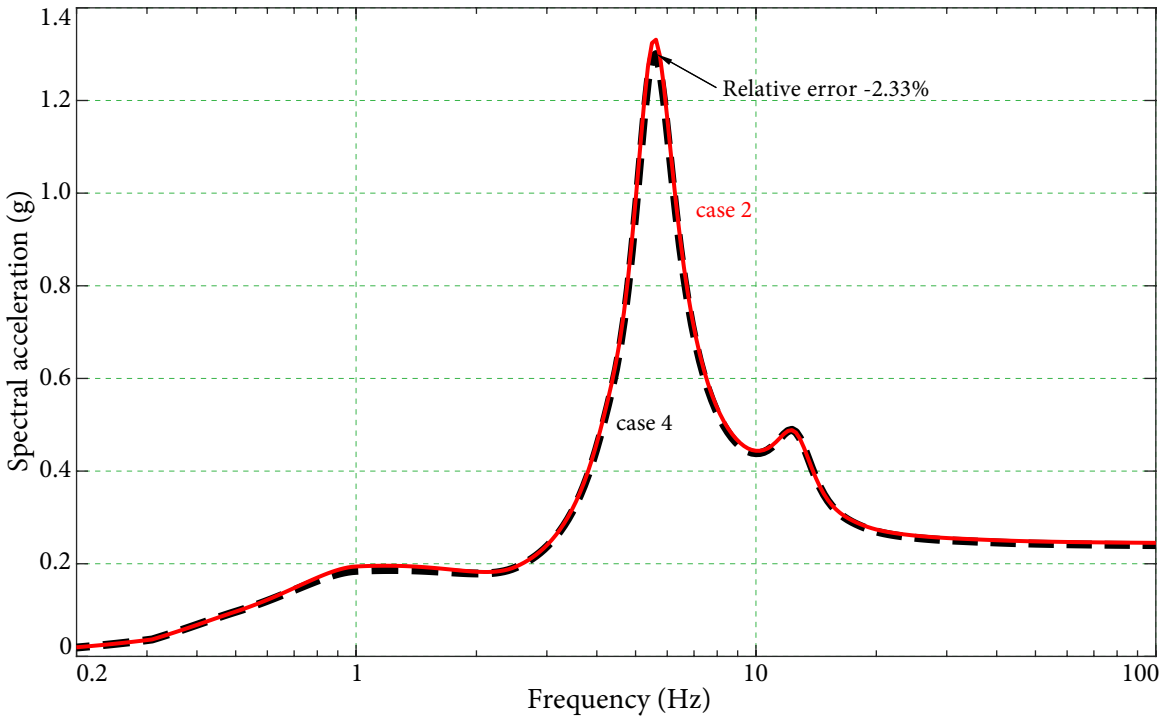

Figure 5.45 FRS at node 5 for proposed V_s distribution at rock site

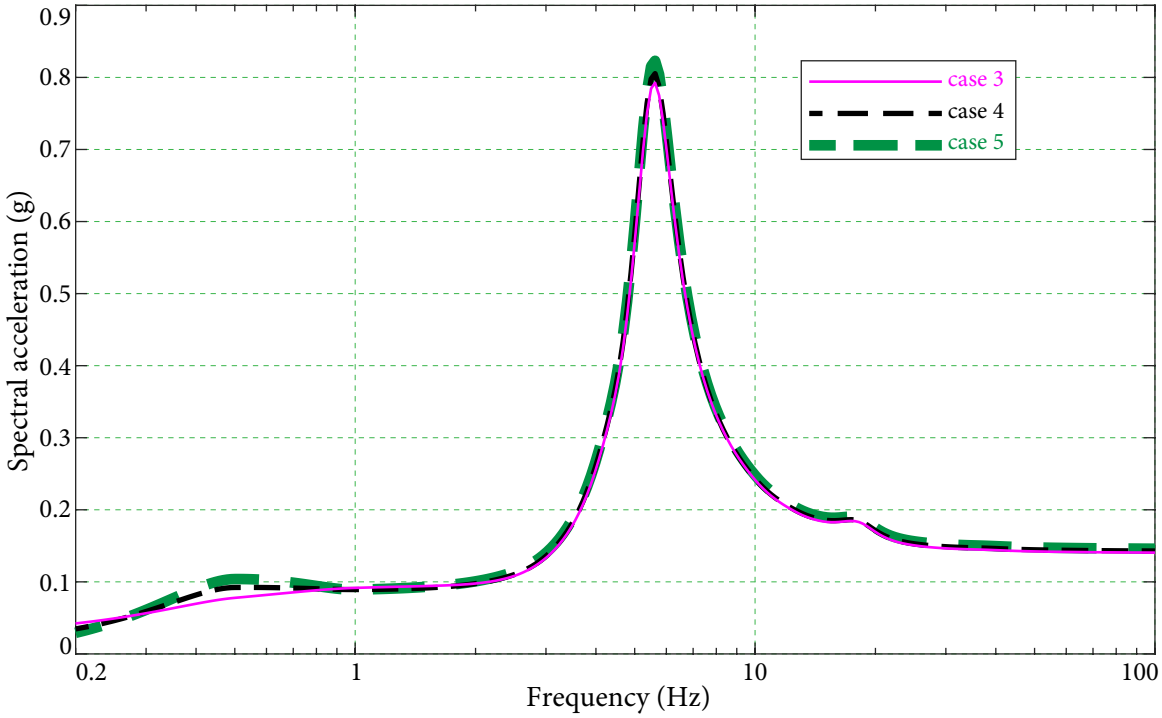

Figure 5.46 FRS at node 4 for different σ_{LN} at soil site

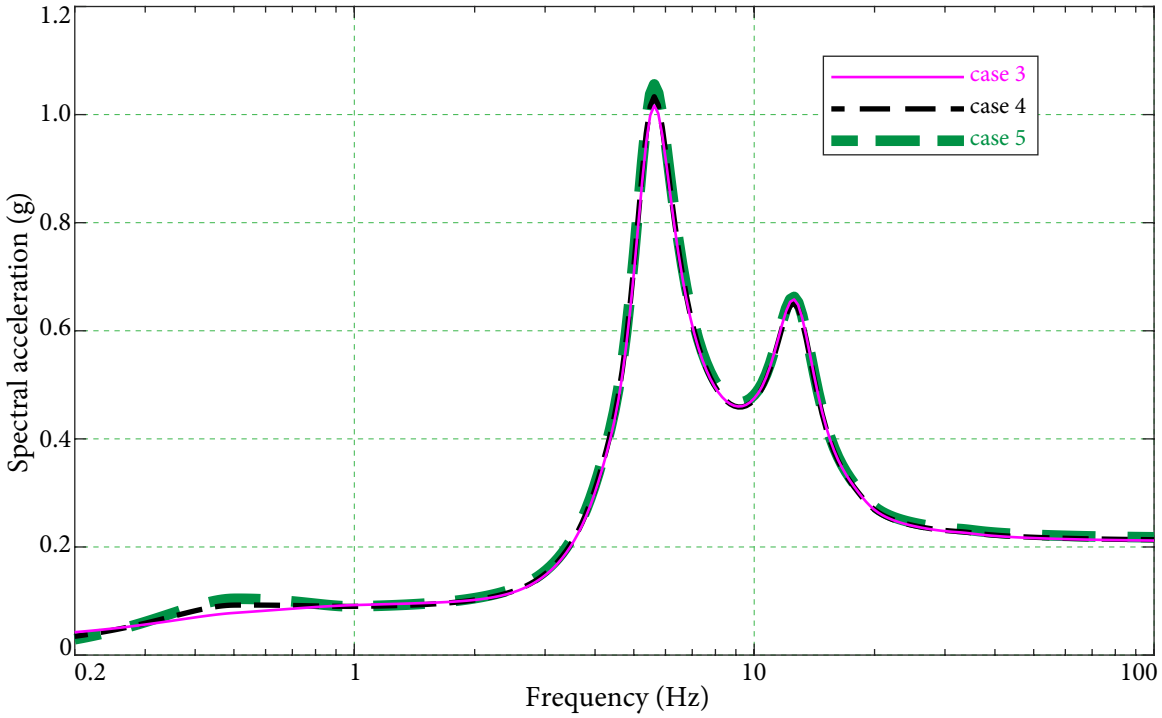

Figure 5.47 FRS at node 5 for different σ_{LN} at soil site

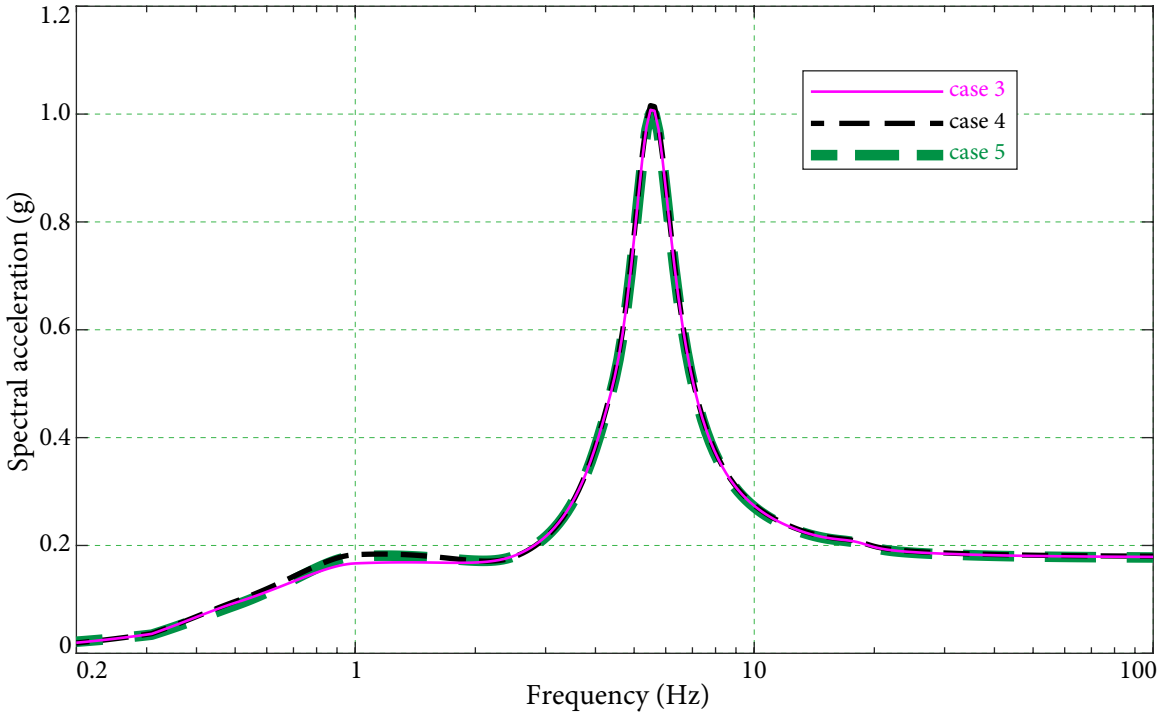

Figure 5.48 FRS at node 4 for different σ_{LN} at rock site

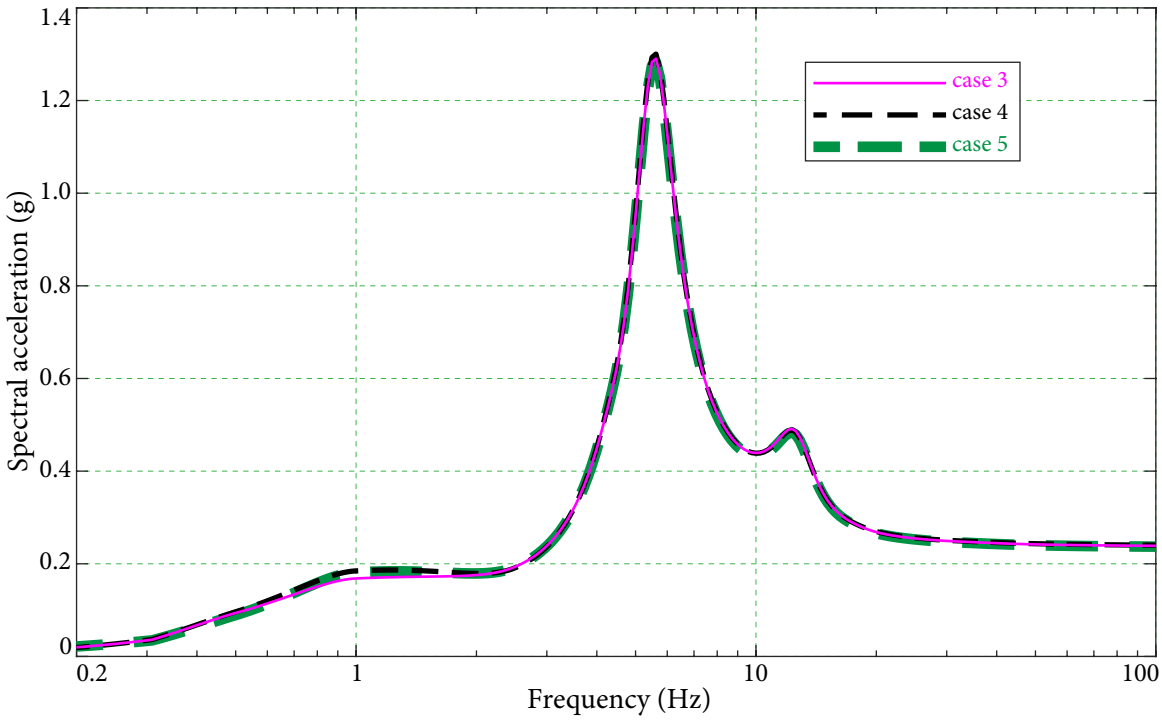

Figure 5.49 FRS at node 5 for different σ_{LN} at rock site

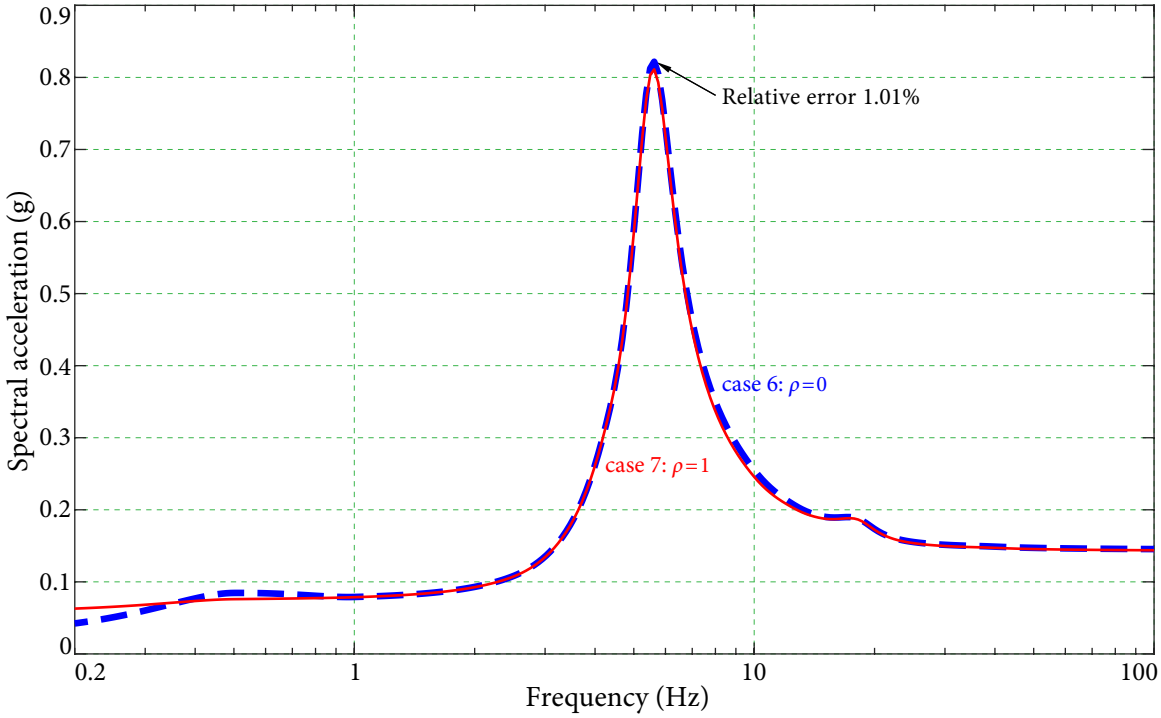

Figure 5.50 FRS at node 4 for different correlation coefficients at soil site

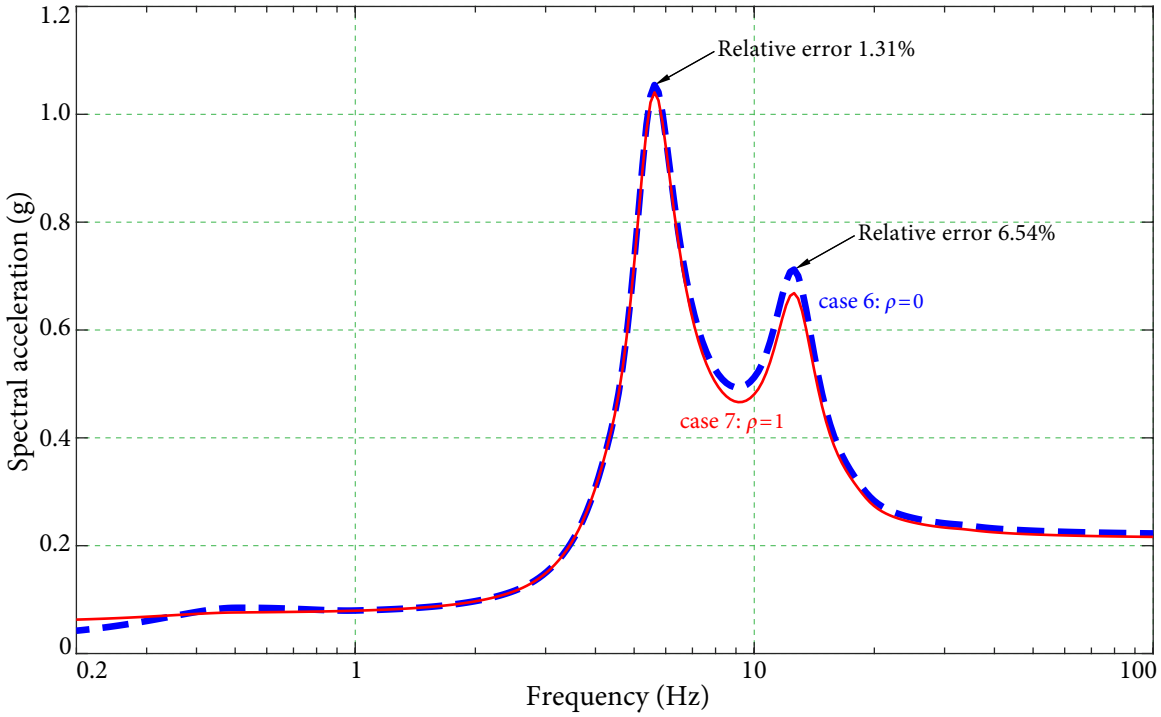

Figure 5.51 FRS at node 5 for different correlation coefficients at soil site

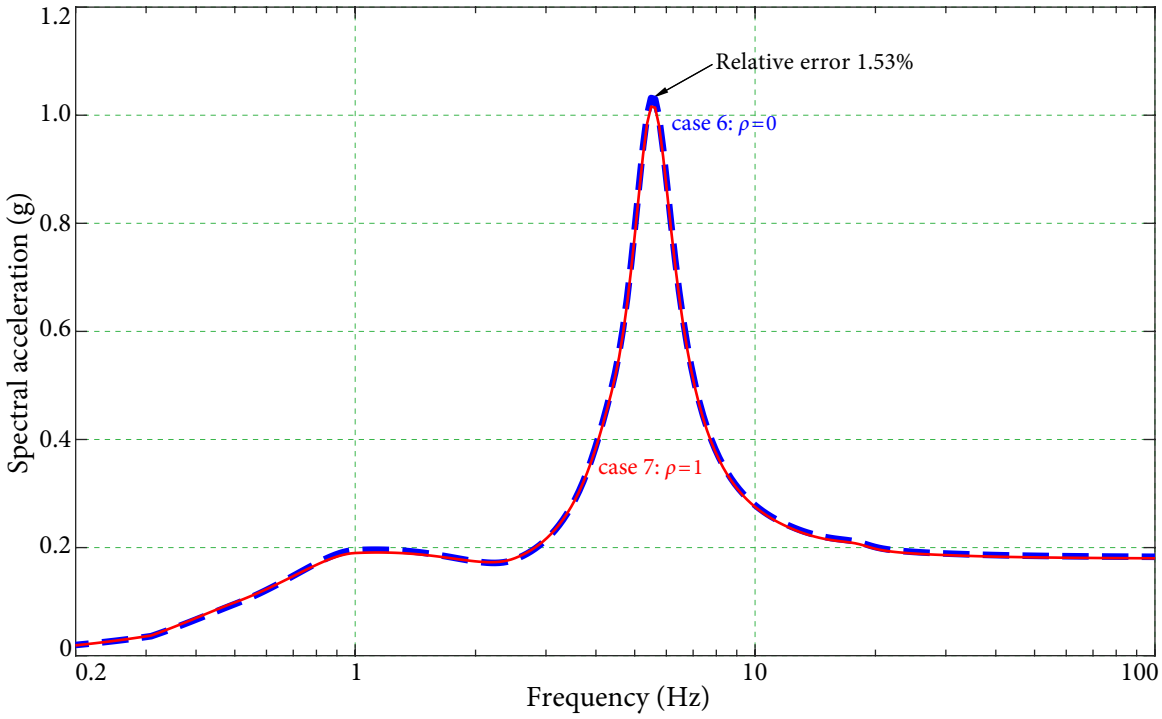

Figure 5.52 FRS at node 4 for different correlation coefficients at rock site

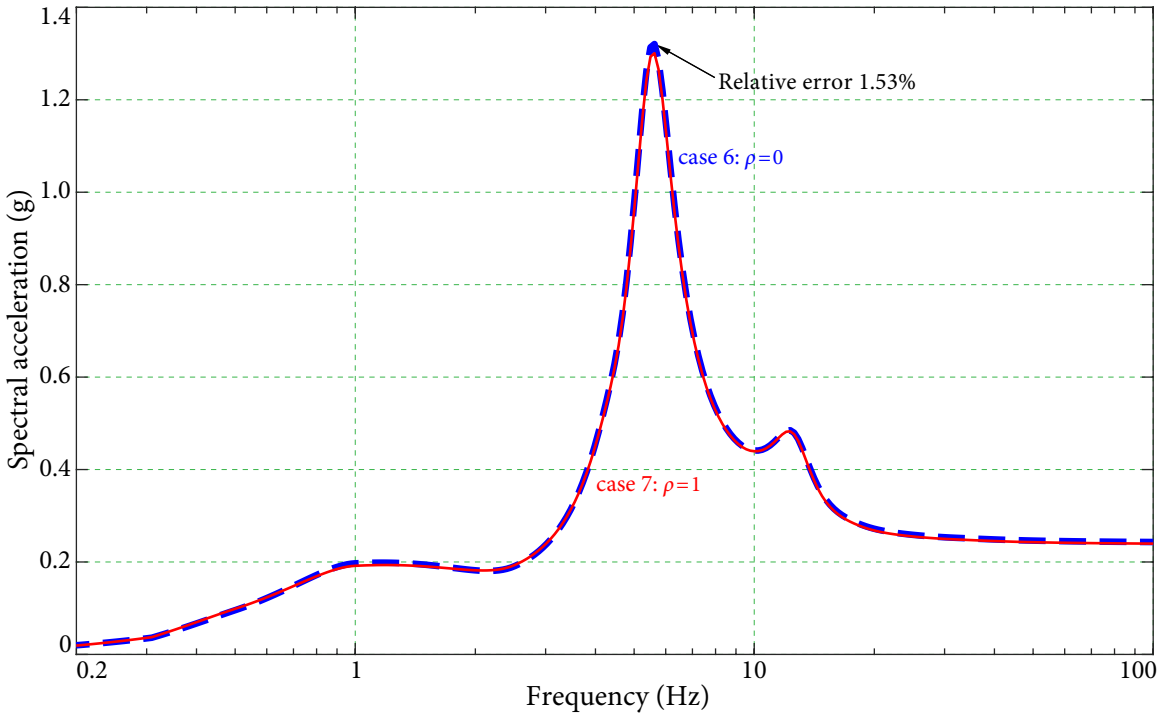

Figure 5.53 FRS at node 5 for different correlation coefficients at rock site

is demonstrated that the influence of correlation coefficient in the consideration of epistemic uncertainty can not be neglected.

According to Figures 5.42 to 5.45, the proposed alternative σ_{LN} in case 4 leads to similar FRS to case 2. The relative error at the peaks are 0.18% in soil case and 2.33% in rock case. It is reasonable to replace the current V_S distribution by the continuous distribution with proposed σ_{LN} as given in Section 5.1.2.

In cases 3 and 5, the FRS given by the different σ_{LN} are close to case 4 as shown in Figures 5.46 to 5.49, and the difference is less than 2.3% given in Table 5.8. It shows that the sensitivity of FRS about σ_{LN} is small. σ_{LN} in this study represents the combination of both the epistemic and aleatory uncertainty. If epistemic uncertainty is neglected, it will result in a smaller σ_{LN}. In this parametric study, the influence of difference σ_{LN} is small, which indicates that epistemic uncertainty will not affect the uniform hazard FRS much.

FRS determined by different ρ of V_S are shown in Figures 5.50 to 5.53. At soil site, the difference are up to 1.31% at 5.6 Hz and 6.54% at 12.6 Hz. At rock site, the 2 sets of FRS is close to each other with the difference of 1.53% at the peak. It is recognized that the influence of ρ is minor in most frequency range, while ρ may influence the resultant FRS in high frequency domain.

5.3 Summary

In this chapter, a fully probabilistic method is developed for addressing the uncertainty in the generation of FRS. Different levels of ground motions are taken to represent the seismic hazard, and the geotechnical models are generated by Monte Carlo simulations to account for the uncertainty in soil properties. The uncertainty is propagated from site response analysis to SSI analysis consistently, and convolved into the uniform hazard FLIRS. Since the fixed-base structure model is determinant without variability, the uniform hazard FLIRS is taken as the seismic input, and FRS are developed with a specific RP. A realistic and continuous V_S distribution is proposed to represent the two kinds of uncertainty, epistemic uncertainty and aleatory randomness.

Numerical examples are conducted to illustrate the proposed method. The FRS are generated by current method and proposed probabilistic method, respectively. Compared to the current method, the proposed method can provide a more reasonable seismic demand. Sensitivity study is performed on the σ_{LN} and ρ of V_{S}. Some conclusions are obtained:

- The FRS generated by the proposed method gives a uniform hazard design spectra. It addresses the uncertainty in earthquake excitation and soil properties in a fully probabilistic approach, which overcomes the underestimation and overestimated results in the current application. The seismic demand for secondary system is reduced significantly. In the numerical examples, the peak values in FRS decrease by 46% and 20% at soil site and rock site, respectively.
- It is unreasonable to assume all layers are fully correlated when treating epistemic uncertainty in current method. The proposed method generates randomization of V_{S} in each layer with a correlation coefficient, which can give a more reasonable FRS.
- The FRS given by the proposed alternative σ_{LN} agrees well with the results led by the current parameters. A continuous and more realistic distribution is applied in Monte Carlo simulation. Sensitivity study shows that final FRS generated by different σ_{LN} do not change noticeably.
- In most frequency ranges, FRS dose not vary significantly with different ρ of V_{S}, especially at rock site. But the peak of FRS in the high frequency domain, e.g., above 10 Hz, may change significantly.

In summary, the proposed method can give a realistic and uniform hazard FRS, which can improve the accuracy and economic in engineering design. The uncertainty is propagated from site response analysis to SSI analysis consistently.

CHAPTER 6

Soil-Structure Interaction Analysis with Flexible Foundation

For reactors placed underground, the earthquake excitation not only comes from the bottom, but also exits at the side walls. The stiffness of external structures of reactors are usually very high, and similar to the values of foundations. Thus the total foundation system, including bottom foundations and external structures, can not be treated as rigid in Soil-Structure Interaction (SSI) analysis. Besides, according to site response analysis, the free field motion at different soil layers are different. In this Chapter, Foundation Level Input Response Spectra (FLIRS) is generated considering the flexibility of foundations and spatially varying ground motions, so that the direct spectra-to-spectra method for generating Floor Response Spectra (FRS) can be applied for structures with flexible foundation under excitations at multiple points.

In the proposed method, the structural response is expressed in terms of the modal information of the structure and the seismic input at multiple points. Then the equilibrium equations are established for each structure and foundation node, as well as the entire structure-foundation system, by which the structural response is obtained from the free field motion. Based on the structural response, a transfer function from the free field motion to fixed-base motion is determined. At last, the modification factor converting Foundation Input Response Spectra (FIRS) to FLIRS is calculated by random vibration theory.

6.1 Substructure Method

6.1.1 Substructure Model for Flexible Foundation

The coupled soil-structure model with flexible foundation is shown in Figure 6.1. Let $\mathbf{U}_s$ and $\mathbf{U}_b$ be amplitudes of the absolute displacement vectors of the superstructure and foundation, respectively, where the subscripts "s" and "b" stand for the degrees-of-freedom of "structure" and "base" (or boundary of soil-structure interface), respectively. The equation of dynamic equilibrium of the structure is given by

$$\begin{bmatrix} \mathbf{S}_{ss}^{s} & \mathbf{S}_{sb}^{s} \\ \mathbf{S}_{bs}^{s} & \mathbf{S}_{bb}^{s} \end{bmatrix} \begin{Bmatrix} \mathbf{U}_s \\ \mathbf{U}_b \end{Bmatrix} = \begin{Bmatrix} \mathbf{P}_s \\ \mathbf{P}_b \end{Bmatrix}, \tag{6.1}$$

where $\mathbf{P}_s$ is the amplitude vector of the load applied on the nodes of the structure, and $\mathbf{P}_b$ is the amplitude vector of the interaction forces between the structure and soil.

Similar to the derivation with rigid foundation as given in Section 3.1, the free-field earthquake excitation at node O is replaced by seismic input at multiple points on the foundation (Figure 6.1). Hence, referring to the case of rigid foundation in Section 3.1.2, one has

$$\mathbf{S}_{OO}^{s} \Longrightarrow \mathbf{S}_{bb}^{s}, \quad \mathbf{S}_{Os}^{s} \Longrightarrow \mathbf{S}_{bs}^{s}, \quad \mathbf{S}_{sO}^{s} \Longrightarrow \mathbf{S}_{sb}^{s}, \quad \mathbf{S}_{OO}^{G} \Longrightarrow \mathbf{S}_{bb}^{G}, \quad \mathbf{S}_{OO}^{F} \Longrightarrow \mathbf{S}_{bb}^{F},$$

$$\mathbf{U}_O \Longrightarrow \mathbf{U}_b, \quad \mathbf{U}_O^{G} \Longrightarrow \mathbf{U}_b^{G}, \quad \mathbf{U}_O^{F} \Longrightarrow \mathbf{U}_b^{F}.$$

Then equation (3.8) becomes

$$\begin{bmatrix} \mathbf{S}_{ss}^{s} & \mathbf{S}_{sb}^{s} \\ \mathbf{S}_{bs}^{s} & \mathbf{S}_{bb}^{s} + \mathbf{S}_{bb}^{G} \end{bmatrix} \begin{Bmatrix} \mathbf{U}_s \\ \mathbf{U}_b \end{Bmatrix} = \begin{Bmatrix} \mathbf{0} \\ \mathbf{S}_{bb}^{F} \mathbf{U}_b^{F} \end{Bmatrix}. \tag{6.2}$$

Equation (6.2) is the equation of motion of the structure supported on *generalized springs* characterized by the dynamic stiffness matrix $\mathbf{S}_{bb}^{F}$ as shown in Figure 6.2. The other ends of the springs are subjected to earthquake excitation $\mathbf{U}_b^{F}$, which is the free-field response of the soil at the foundation level; the acceleration response spectra of $\ddot{\mathbf{u}}_b^{F}$ are the Foundation Input Response Spectra (FIRS), which can be obtained from a site response analysis of the free-field.

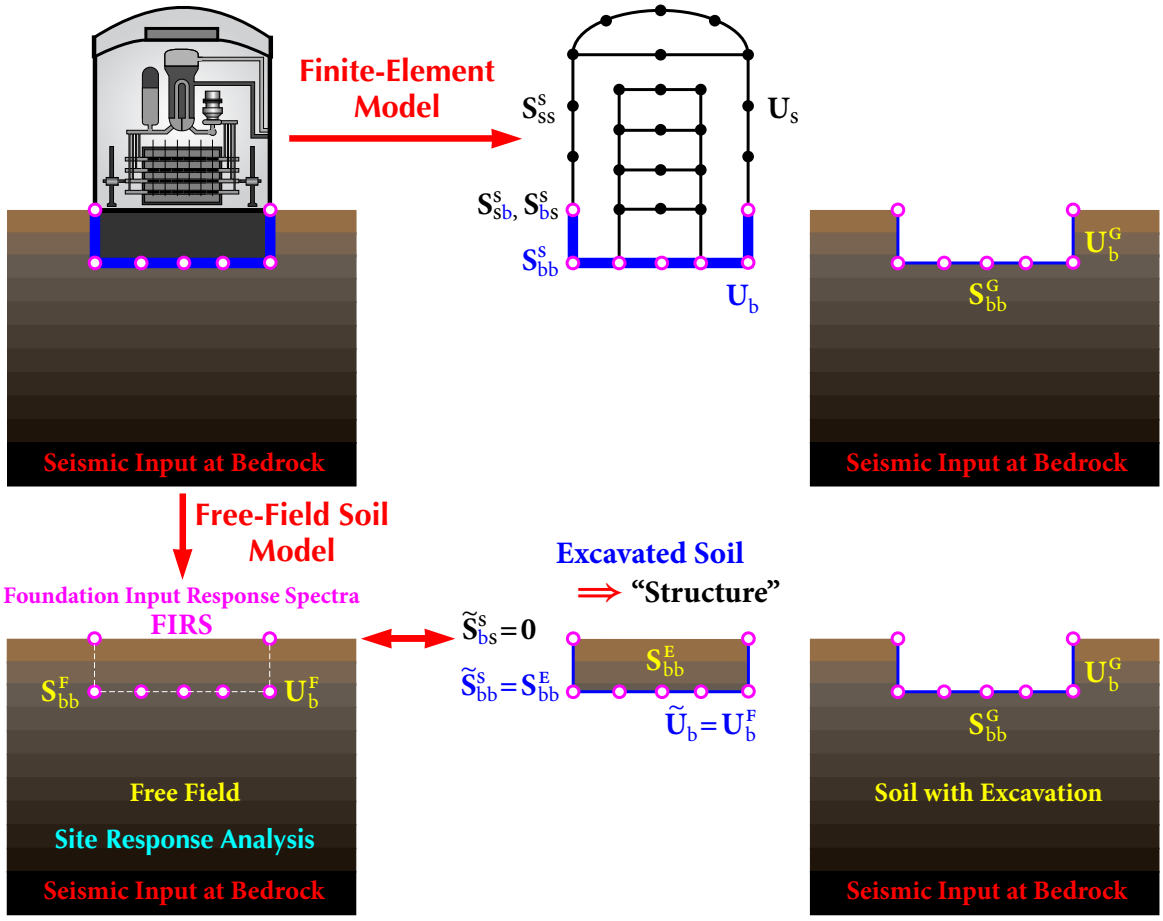

Figure 6.1 Coupled Soil-Structure Model

Considering the excavated soil, equation (6.2) can also be written as

$$\begin{bmatrix} \mathbf{S}^S_{ss} & \mathbf{S}^S_{sb} \\ \mathbf{S}^S_{bs} & (\mathbf{S}^S_{bb}-\mathbf{S}^E_{bb})+\mathbf{S}^F_{bb} \end{bmatrix} \begin{Bmatrix} \mathbf{U}_s \\ \mathbf{U}_b \end{Bmatrix} = \begin{Bmatrix} \mathbf{0} \\ \mathbf{S}^F_{bb}\,\mathbf{U}^F_b \end{Bmatrix}. \tag{6.3}$$

For a structure with N nodes (not including the foundation), each node has 6 DOF (three translational and three rotational). The flexible foundation has M nodes with $6M$ DOF. The dimensions of the vectors $\mathbf{U}_s$, $\mathbf{U}_b$, and $\mathbf{U}^F_b$ are $6N$, $6M$, and $6M$, respectively. The dimensions of the dynamic stiffness sub-matrices of the structure $\mathbf{S}^S_{ss}$, $\mathbf{S}^S_{sb}$, $\mathbf{S}^S_{bs}$, $\mathbf{S}^S_{bb}$ are $6N\times6N$, $6N\times6M$, $6M\times6N$, and $6M\times6M$, respectively. The dimensions of the dynamic stiffness sub-matrices of the soil $\mathbf{S}^F_{bb}$, $\mathbf{S}^G_{bb}$, and $\mathbf{S}^E_{bb}$ are all $6M\times6M$.

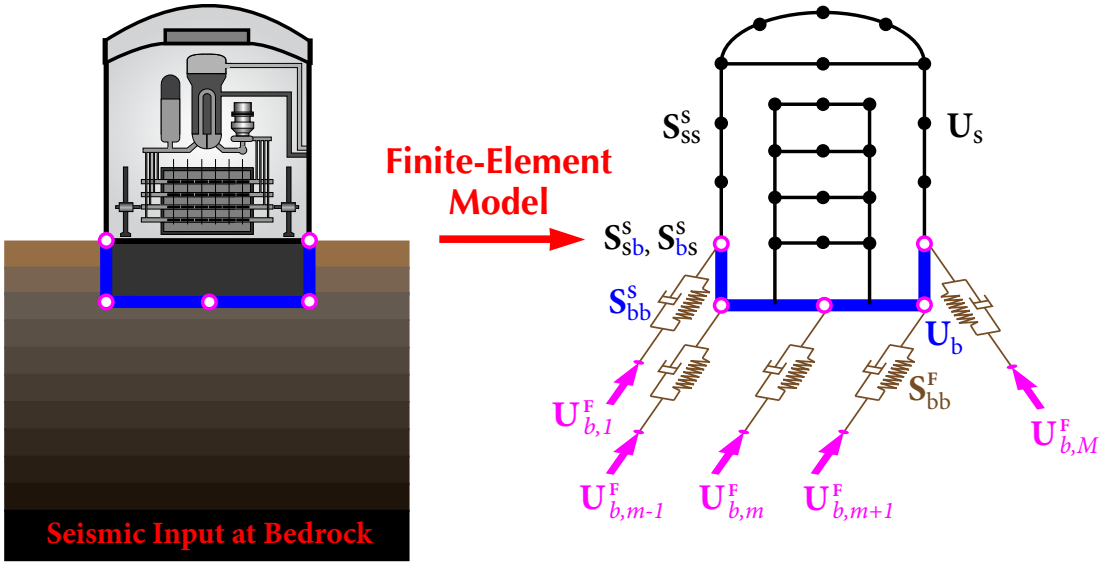

Figure 6.2 Soil-Spring Model of SSI with Flexible Foundation

6.1.2 Fixed-Base Model for Flexible Foundation

For the fixed-base model as shown in Figure 6.3, from the first block-row of equation (6.3), one has

$$\mathbf{S}^{\mathrm{s}}_{\mathrm{ss}}\,\mathbf{U}_{\mathrm{s}} + \mathbf{S}^{\mathrm{s}}_{\mathrm{sb}}\,\mathbf{U}_{\mathrm{b}} = \mathbf{0} \implies \mathbf{U}_{\mathrm{s}} = \mathbf{S}^{\mathrm{FB}}\mathbf{U}_{\mathrm{b}}, \quad \mathbf{S}^{\mathrm{FB}} = -\left(\mathbf{S}^{\mathrm{s}}_{\mathrm{ss}}\right)^{-1}\mathbf{S}^{\mathrm{s}}_{\mathrm{sb}}, \tag{6.4}$$

where $\mathbf{S}^{\mathrm{FB}}$ is the dynamic stiffness matrix for fixed-base analysis with flexible foundation.

When only translational ground motions are considered, Re-organizing vector $\mathbf{U}_{\mathrm{s}}$ and rewriting $\mathbf{U}_{\mathrm{b}}$ as

$$\mathbf{U}_{\mathrm{s}} = \begin{Bmatrix} \mathbf{U}_{\mathrm{s,T}} \\ \mathbf{U}_{\mathrm{s,R}} \end{Bmatrix}_{6N\times 1}, \qquad \mathbf{U}_{\mathrm{b}} = \begin{Bmatrix} \mathbf{U}^{\mathrm{FB}}_{\mathrm{b}} \\ \mathbf{0} \end{Bmatrix}_{6M\times 1}. \tag{6.5}$$

Re-arrange and partition $\mathbf{S}^{\mathrm{FB}}$ accordingly, one has

$$\mathbf{S}^{\mathrm{FB}} = \begin{bmatrix} \mathbf{S}^{\mathrm{FB}}_{\mathrm{TT}} & \mathbf{S}^{\mathrm{FB}}_{\mathrm{TR}} \\ \mathbf{S}^{\mathrm{FB}}_{\mathrm{RT}} & \mathbf{S}^{\mathrm{FB}}_{\mathrm{RR}} \end{bmatrix}_{6N\times 6}, \tag{6.6}$$

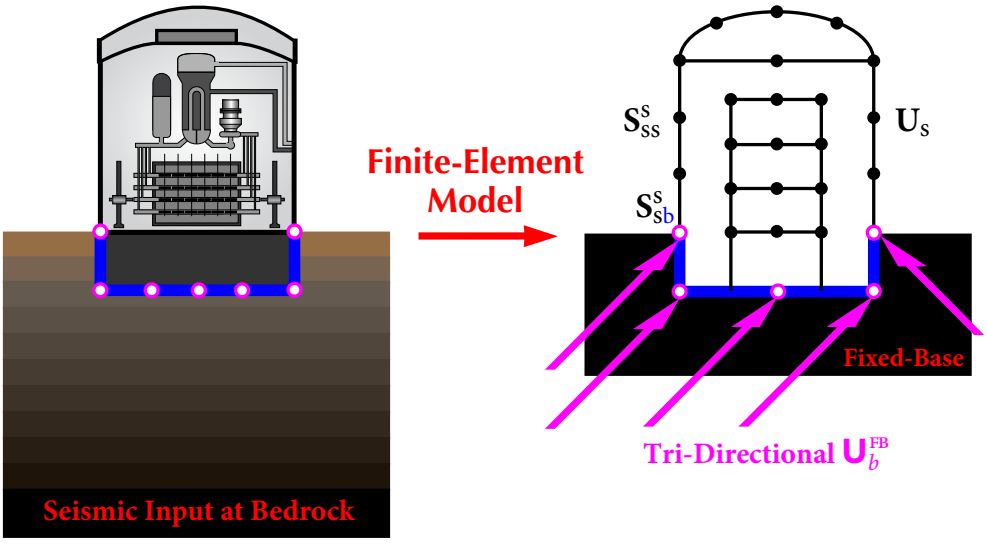

Figure 6.3 Fixed-Base Model with Flexible Foundation

in which each submatrix is of dimension $3N\times3$. Equation (6.4) can be written as

$$\begin{Bmatrix} \mathbf{U}_{s,T} \\ \mathbf{U}_{s,R} \end{Bmatrix} = \begin{bmatrix} \mathbf{S}^{FB}_{TT} & \mathbf{S}^{FB}_{TR} \\ \mathbf{S}^{FB}_{RT} & \mathbf{S}^{FB}_{RR} \end{bmatrix} \begin{Bmatrix} \mathbf{U}^{FB}_{b} \\ \mathbf{0} \end{Bmatrix} = \begin{Bmatrix} \mathbf{S}^{FB}_{TT}\mathbf{U}^{FB}_{b} \\ \mathbf{S}^{FB}_{RT}\mathbf{U}^{FB}_{b} \end{Bmatrix}. \tag{6.7}$$

Multiplying the first block-row of equation (6.7) by $\left(\mathbf{S}^{FB}_{TT,R}\right)^T$ yields

$$\left(\mathbf{S}^{FB}_{TT}\right)^T \mathbf{U}_{s,T} = \left[\left(\mathbf{S}^{FB}_{TT}\right)^T \mathbf{S}^{FB}_{TT}\right] \mathbf{U}^{FB}_{b}. \tag{6.8}$$

The tri-directional (translational) acceleration response spectra $\mathbf{U}^{FB}_{b}$ applied at the flexible foundation of a *fixed-base* structure are the Foundation Level Input Response Spectra (FLIRS), as shown in Figure 6.3.

For a three-dimensional model of a structure with N nodes and a foundation with M nodes, a typical node n has 6 DOF: three translational DOF u_1, u_2, u_3, and three rotational DOF u_4, u_5, u_6. The structure is subjected to tri-directional seismic excitations at one node of the foundation. The displacement vector $\mathbf{u}$ of dimension $6(N+M)$ is governed by

$$\mathbf{M}\ddot{\mathbf{u}}(t) + \mathbf{C}\dot{\mathbf{u}}(t) + \mathbf{K}\mathbf{u}(t) = \mathbf{P}, \tag{6.9}$$

where **M**, **C**, **K** are, respectively, the mass, damping, and stiffness matrices of dimension $(6N+6M)\times(6N+6M)$, given by

$$\mathbf{M}=\begin{bmatrix}\mathbf{M}_{\mathrm{s}} & \mathbf{0}\\ \mathbf{0} & \mathbf{M}_{\mathrm{b}}\end{bmatrix},\qquad \mathbf{C}=\begin{bmatrix}\mathbf{C}_{\mathrm{ss}} & \mathbf{C}_{\mathrm{sb}}\\ \mathbf{C}_{\mathrm{bs}} & \mathbf{C}_{\mathrm{bb}}\end{bmatrix},\qquad \mathbf{K}=\begin{bmatrix}\mathbf{K}_{\mathrm{ss}} & \mathbf{K}_{\mathrm{sb}}\\ \mathbf{K}_{\mathrm{bs}} & \mathbf{K}_{\mathrm{bb}}\end{bmatrix},$$

and **P** is the interaction forces applied on the nodes as

$$\mathbf{P}=\left\{\mathbf{0},\ \mathbf{P}_{\mathrm{b}}\right\}^{T}.$$

u is

$$\mathbf{u}=\left\{\mathbf{u}_{\mathrm{s}},\ \mathbf{u}_{\mathrm{b}}\right\}^{T},$$

where

$$\mathbf{u}_{\mathrm{s}}=\left\{\mathbf{u}_{\mathrm{s}}^{1},\ \mathbf{u}_{\mathrm{s}}^{2},\ \cdots\ \mathbf{u}_{\mathrm{s}}^{N}\right\}^{T},\qquad \mathbf{u}_{\mathrm{s}}^{n}=\left\{u_{\mathrm{s},1}^{n},\ u_{\mathrm{s},2}^{n},\ \cdots,\ u_{\mathrm{s},6}^{n}\right\}^{T},$$
$$\mathbf{u}_{\mathrm{b}}=\left\{\mathbf{u}_{\mathrm{b}}^{1},\ \mathbf{u}_{\mathrm{b}}^{2},\ \cdots\ \mathbf{u}_{\mathrm{b}}^{M}\right\}^{T},\qquad \mathbf{u}_{\mathrm{b}}^{m}=\left\{u_{\mathrm{b},1}^{m},\ u_{\mathrm{b},2}^{m},\ \cdots,\ u_{\mathrm{b},6}^{m}\right\}^{T},$$

Then the displacement of the structure is separated to two parts as a pseudostatic component $\mathbf{u}_{\mathrm{s}}^{\mathrm{s}}$ and a dynamic component **x**

$$\mathbf{u}_{\mathrm{s}}=\mathbf{u}_{\mathrm{s}}^{\mathrm{s}}+\mathbf{x}, \tag{6.10}$$

where $\mathbf{u}_{\mathrm{s}}^{\mathrm{s}}$ is defined as the displacement when the ground motion at time t is applied statically, and meets

$$\begin{bmatrix}\mathbf{K}_{\mathrm{ss}} & \mathbf{K}_{\mathrm{sb}}\\ \mathbf{K}_{\mathrm{bs}} & \mathbf{K}_{\mathrm{bb}}\end{bmatrix}\begin{Bmatrix}\mathbf{u}_{\mathrm{s}}^{\mathrm{s}}\\ \mathbf{u}_{\mathrm{b}}\end{Bmatrix}=\begin{Bmatrix}\mathbf{0}\\ \mathbf{P}_{\mathrm{b}}{}^{\mathrm{s}}\end{Bmatrix}. \tag{6.11}$$

According to the first block row of equation (6.11), one obtains

$$\mathbf{u}_{\mathrm{s}}^{\mathrm{s}}=\mathbf{L}\mathbf{u}_{\mathrm{b}}, \tag{6.12}$$

where

$$\mathbf{L}=-\mathbf{K}_{\mathrm{ss}}^{-1}\mathbf{K}_{\mathrm{sb}}. \tag{6.13}$$

Based on equation (6.10), the first block row of equation (6.9) can be expressed as

$$\mathbf{M}_{\mathrm{s}}\ddot{\mathbf{x}}(t)+\mathbf{C}_{\mathrm{ss}}\dot{\mathbf{x}}(t)+\mathbf{K}_{\mathrm{ss}}\mathbf{x}(t)=-\mathbf{M}_{\mathrm{s}}\ddot{\mathbf{u}}_{\mathrm{s}}^{\mathrm{s}}(t)-\mathbf{C}_{\mathrm{ss}}\dot{\mathbf{u}}_{\mathrm{s}}^{\mathrm{s}}(t)-\mathbf{K}_{\mathrm{ss}}\mathbf{u}_{\mathrm{s}}^{\mathrm{s}}(t)-\mathbf{C}_{\mathrm{sb}}\dot{\mathbf{u}}_{\mathrm{b}}(t)-\mathbf{K}_{\mathrm{sb}}\mathbf{u}_{\mathrm{b}}(t). \tag{6.14}$$

Substituting equation (6.13) into equation (6.14) leads to

$$\mathbf{M}_{\mathrm{s}}\,\ddot{\mathbf{x}}(t)+\mathbf{C}_{\mathrm{ss}}\,\dot{\mathbf{x}}(t)+\mathbf{K}_{\mathrm{ss}}\,\mathbf{x}(t)=-\mathbf{M}_{\mathrm{s}}\mathbf{L}\,\ddot{\mathbf{u}}_{\mathrm{b}}(t)-\mathbf{C}_{\mathrm{ss}}\,\dot{\mathbf{u}}_{\mathrm{s}}^{\mathrm{s}}(t)-\mathbf{C}_{\mathrm{sb}}\,\dot{\mathbf{u}}_{\mathrm{b}}(t). \tag{6.15}$$

In engineering applications, the damping term is usually relatively small compared to the inertia term. Neglecting the damping values in the right side of equation (6.15) gives

$$\mathbf{M}_{\mathrm{s}}\,\ddot{\mathbf{x}}(t)+\mathbf{C}_{\mathrm{ss}}\,\dot{\mathbf{x}}(t)+\mathbf{K}_{\mathrm{ss}}\,\mathbf{x}(t)=-\mathbf{M}_{\mathrm{s}}\mathbf{L}\,\ddot{\mathbf{u}}_{\mathrm{b}}(t). \tag{6.16}$$

Letting $\mathbf{x}(t)=\mathbf{X}\mathrm{e}^{\mathrm{i}\omega t}$ and $\mathbf{u}_{\mathrm{b}}(t)=\mathbf{U}_{\mathrm{b}}\,\mathrm{e}^{\mathrm{i}\omega t}$, equation (6.16) becomes

$$\left(-\omega^2\mathbf{M}_{\mathrm{s}}+\mathrm{i}\omega\,\mathbf{C}_{\mathrm{ss}}+\mathbf{K}_{\mathrm{ss}}\right)\mathbf{X}_{\mathrm{s}}=\omega^2\mathbf{M}_{\mathrm{s}}\mathbf{L}\mathbf{U}_{\mathrm{b}}. \tag{6.17}$$

Applying the modal transformation $\mathbf{X}_{\mathrm{s}}=\boldsymbol{\Phi}_{\mathrm{s}}\mathbf{Q}_{\mathrm{s}}$, where $\boldsymbol{\Phi}_{\mathrm{s}}$ is the modal matrix of the structure obtained by modal analysis without the soil springs when the foundation nodes are constrained, substituting into equation (6.17), and multiplying $\boldsymbol{\Phi}_{\mathrm{s}}^{T}$ from the left yield

$$\left(-\omega^2\boldsymbol{\Phi}_{\mathrm{s}}^{T}\mathbf{M}_{\mathrm{s}}\boldsymbol{\Phi}_{\mathrm{s}}+\mathrm{i}\omega\,\boldsymbol{\Phi}_{\mathrm{s}}^{T}\mathbf{C}_{\mathrm{ss}}\boldsymbol{\Phi}_{\mathrm{s}}+\boldsymbol{\Phi}_{\mathrm{s}}^{T}\mathbf{K}_{\mathrm{ss}}\boldsymbol{\Phi}_{\mathrm{s}}\right)\mathbf{Q}_{\mathrm{s}}=\omega^2\boldsymbol{\Phi}_{\mathrm{s}}^{T}\mathbf{M}_{\mathrm{s}}\mathbf{L}\,\mathbf{U}_{\mathrm{b}}. \tag{6.18}$$

Employing the orthogonality gives

$$\mathrm{diag}\left\{-\omega^2+\mathrm{i}2\zeta_{n,\mathrm{s}}\omega_{n,\mathrm{s}}\omega+\omega_{n,\mathrm{s}}^2\right\}\mathbf{Q}_{\mathrm{s}}=\omega^2\boldsymbol{\Gamma}\,\mathbf{U}_{\mathrm{b}}, \tag{6.19}$$

where $\boldsymbol{\Gamma}$ is a $6N\times 6$ matrix given by

$$\boldsymbol{\Gamma}=\frac{\boldsymbol{\Phi}_{\mathrm{s}}^{T}\mathbf{M}_{\mathrm{s}}\mathbf{L}}{\boldsymbol{\Phi}_{\mathrm{s}}^{T}\mathbf{M}_{\mathrm{s}}\boldsymbol{\Phi}_{\mathrm{s}}}. \tag{6.20}$$

Hence,

$$\mathbf{X}_{\mathrm{s}}=\omega^2\boldsymbol{\Phi}_{\mathrm{s}}\mathbf{H}_{\mathrm{s}}\boldsymbol{\Gamma}\,\mathbf{U}_{O}, \tag{6.21}$$

where $\mathbf{H}_{\mathrm{s}}$ is a diagonal matrix of the complex frequency response functions, i.e.,

$$\mathbf{H}_{\mathrm{s}}=\mathrm{diag}\left\{\frac{1}{\omega_{n,\mathrm{s}}^2-\omega^2+\mathrm{i}2\zeta_{n,\mathrm{s}}\omega_{n,\mathrm{s}}\omega}\right\}. \tag{6.22}$$

Since the dynamic displacement $\mathbf{x}_{\mathrm{s}}=\mathbf{u}_{\mathrm{s}}-\mathbf{u}_{\mathrm{s}}^{\mathrm{s}}$, substituting into equation (6.21) gives

$$\mathbf{U}_{\mathrm{s}}=\left(\omega^2\boldsymbol{\Phi}_{\mathrm{s}}\mathbf{H}_{\mathrm{s}}\boldsymbol{\Gamma}+\mathbf{L}\right)\mathbf{U}_{\mathrm{b}}. \tag{6.23}$$

Comparing equation (6.23) with equation (6.4), one obtains

$$\mathbf{S}^{\mathrm{FB}}=\omega^2\boldsymbol{\Phi}_{\mathrm{s}}\mathbf{H}_{\mathrm{s}}\boldsymbol{\Gamma}+\mathbf{L}. \tag{6.24}$$

6.1.3 Spring-Structure Model under Excitation

The spring-structure system is shown in Figure 6.4. In order to establish the governing equation, the M nodes in the basement is expressed by two parts, i.e., one single node O as origin and $(M-1)$ foundation nodes represented by f. The input earthquake motion becomes

$$\mathbf{U}_{\mathrm{b}}^{\mathrm{F}} = \begin{Bmatrix} \mathbf{U}_{\mathrm{f}}^{\mathrm{F}} \\ \mathbf{U}_{O}^{\mathrm{F}} \end{Bmatrix}. \tag{6.25}$$

Comparing to the displacement at point O, the relative displacement vector $\mathbf{x}$ of dimension $(6N+6M-6)$ is governed by

$$\mathbf{M}\ddot{\mathbf{x}}(t) + \mathbf{C}\dot{\mathbf{x}}(t) + \mathbf{K}\mathbf{x}(t) = -\mathbf{M}\,\boldsymbol{\mathcal{I}}\ddot{\mathbf{u}}_{O}(t) + \mathbf{P}, \tag{6.26}$$

where $\mathbf{M}$, $\mathbf{C}$, $\mathbf{K}$ are, respectively, the mass, damping, and stiffness matrices of dimension $(6N+6M-6)\times(6N+6M-6)$, given as

$$\mathbf{M} = \begin{bmatrix} \mathbf{M}_{\mathrm{s}} & \mathbf{0} \\ \mathbf{0} & \mathbf{M}_{\mathrm{f}} \end{bmatrix}, \qquad \mathbf{C} = \begin{bmatrix} \mathbf{C}_{\mathrm{ss}} & \mathbf{C}_{\mathrm{sf}} \\ \mathbf{C}_{\mathrm{fs}} & \mathbf{C}_{\mathrm{ff}} \end{bmatrix}, \qquad \mathbf{K} = \begin{bmatrix} \mathbf{K}_{\mathrm{ss}} & \mathbf{K}_{\mathrm{sf}} \\ \mathbf{K}_{\mathrm{fs}} & \mathbf{K}_{\mathrm{ff}} \end{bmatrix},$$

and $\mathbf{P}$ is the interaction forces applied on the nodes f as

$$\mathbf{P} = \left\{\mathbf{0},\ \mathbf{P}_{\mathrm{f}}\right\}^{T}.$$

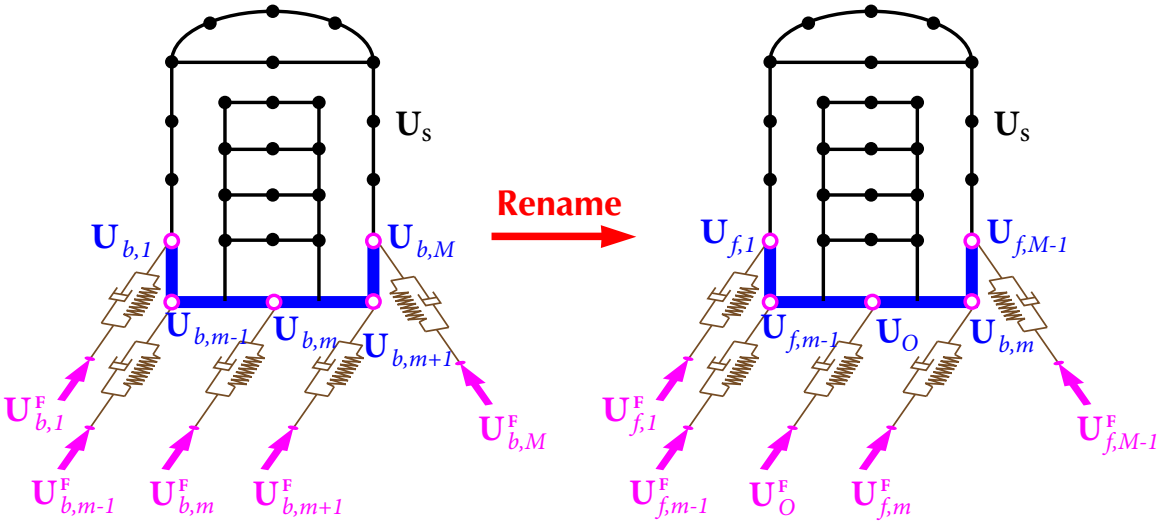

Figure 6.4 Spring-Structure Model with Flexible Foundation under Excitation

$\mathbf{x}$ and $\boldsymbol{\mathcal{I}}$ are

$$\mathbf{x} = \left\{ \mathbf{x}_\mathrm{s},\ \mathbf{x}_\mathrm{f} \right\}^T, \qquad \boldsymbol{\mathcal{I}} = \left\{ \boldsymbol{\mathcal{I}}_\mathrm{s},\ \boldsymbol{\mathcal{I}}_\mathrm{f} \right\}^T,$$

where

$$\mathbf{x}_\mathrm{s} = \left\{ \mathbf{x}_\mathrm{s}^1,\ \mathbf{x}_\mathrm{s}^2,\ \cdots \mathbf{x}_\mathrm{s}^N \right\}^T, \qquad \mathbf{x}_\mathrm{s}^n = \left\{ x_{\mathrm{s},1}^n,\ x_{\mathrm{s},2}^n,\ \cdots,\ x_{\mathrm{s},6}^n \right\}^T,$$

$$\mathbf{x}_\mathrm{f} = \left\{ \mathbf{x}_\mathrm{f}^1,\ \mathbf{x}_\mathrm{f}^2,\ \cdots \mathbf{x}_\mathrm{f}^{M-1} \right\}^T, \qquad \mathbf{x}_\mathrm{f}^m = \left\{ x_{\mathrm{f},1}^m,\ x_{\mathrm{f},2}^m,\ \cdots,\ x_{\mathrm{f},6}^m \right\}^T,$$

$$\boldsymbol{\mathcal{I}}_\mathrm{s} = \left\{ \boldsymbol{\mathcal{I}}_\mathrm{s}^1,\ \boldsymbol{\mathcal{I}}_\mathrm{s}^2,\ \cdots,\ \boldsymbol{\mathcal{I}}_\mathrm{s}^N \right\}^T, \qquad \boldsymbol{\mathcal{I}}_\mathrm{f} = \left\{ \boldsymbol{\mathcal{I}}_\mathrm{f}^1,\ \boldsymbol{\mathcal{I}}_\mathrm{f}^2,\ \cdots,\ \boldsymbol{\mathcal{I}}_\mathrm{f}^{M-1} \right\}^T,$$

$$\boldsymbol{\mathcal{I}}_\mathrm{s}^n = \begin{bmatrix} 1 & 0 & 0 & 0 & z_n - z_o & -(y_n - y_o) \\ 0 & 1 & 0 & -(z_n - z_o) & 0 & x_n - x_o \\ 0 & 0 & 1 & y_n - y_o & -(x_n - x_o) & 0 \\ 0 & 0 & 0 & 1 & 0 & 0 \\ 0 & 0 & 0 & 0 & 1 & 0 \\ 0 & 0 & 0 & 0 & 0 & 1 \end{bmatrix},$$

$$\boldsymbol{\mathcal{I}}_\mathrm{f}^m = \begin{bmatrix} 1 & 0 & 0 & 0 & z_m - z_o & -(y_m - y_o) \\ 0 & 1 & 0 & -(z_m - z_o) & 0 & x_m - x_o \\ 0 & 0 & 1 & y_m - y_o & -(x_m - x_o) & 0 \\ 0 & 0 & 0 & 1 & 0 & 0 \\ 0 & 0 & 0 & 0 & 1 & 0 \\ 0 & 0 & 0 & 0 & 0 & 1 \end{bmatrix}.$$

$\mathbf{x}_\mathrm{s}^n$ and $\mathbf{x}_\mathrm{f}^m$ are the relative displacement vector of structure node n and foundation node m, respectively. $\boldsymbol{\mathcal{I}}_\mathrm{s}$ and $\boldsymbol{\mathcal{I}}_\mathrm{f}$ are the influence matrix of structure nodes and foundation nodes, respectively. x_n, y_n, and z_n are the coordinates of the nth node in a Cartesian coordinate system, and x_o, y_o, and z_o represent the coordinates of the node O.

The first block row of equation (6.26) can be expressed as

$$\mathbf{M}_\mathrm{s}\,\ddot{\mathbf{x}}_\mathrm{s}(t) + \mathbf{C}_\mathrm{ss}\,\dot{\mathbf{x}}_\mathrm{s}(t) + \mathbf{K}_\mathrm{ss}\,\mathbf{x}_\mathrm{s}(t) = -\mathbf{M}_\mathrm{s}\boldsymbol{\mathcal{I}}_\mathrm{s}\,\ddot{\mathbf{u}}_O(t) - \mathbf{C}_\mathrm{sf}\,\dot{\mathbf{x}}_\mathrm{f}(t) - \mathbf{K}_\mathrm{sf}\,\mathbf{x}_\mathrm{f}(t). \tag{6.27}$$

As stated in Section 6.1.2, the damping term $\mathbf{C}_{\mathrm{sf}}\dot{\mathbf{x}}_{\mathrm{f}}(t)$ is usually relatively small. Neglecting the damping term on the right side and introducing $\mathbf{x}(t)=\mathbf{X}\mathrm{e}^{\mathrm{i}\omega t}$ and $\mathbf{u}=\mathbf{U}\mathrm{e}^{\mathrm{i}\omega t}$ lead to

$$(-\omega^2\mathbf{M}_{\mathrm{s}}+\mathrm{i}\omega\mathbf{C}_{\mathrm{ss}}+\mathbf{K}_{\mathrm{ss}})\mathbf{X}_{\mathrm{s}}=\omega^2\mathbf{M}_{\mathrm{s}}\boldsymbol{\mathcal{I}}_{\mathrm{s}}\mathbf{U}_O-\mathbf{K}_{\mathrm{sf}}\mathbf{X}_{\mathrm{f}}. \tag{6.28}$$

Applying the modal transformation $\mathbf{X}_{\mathrm{s}}=\boldsymbol{\Phi}_{\mathrm{s}}\mathbf{Q}_{\mathrm{s}}$, where $\boldsymbol{\Phi}_{\mathrm{s}}$ is the modal matrix obtained by modal analysis without the soil springs when all the foundation nodes are constrained, substituting it into equation (6.28), and multiplying $\boldsymbol{\Phi}_{\mathrm{s}}^T$ from the left yield

$$(-\omega^2\boldsymbol{\Phi}_{\mathrm{s}}^T\mathbf{M}_{\mathrm{s}}\boldsymbol{\Phi}_{\mathrm{s}}+\mathrm{i}\omega\boldsymbol{\Phi}_{\mathrm{s}}^T\mathbf{C}_{\mathrm{ss}}\boldsymbol{\Phi}_{\mathrm{s}}+\boldsymbol{\Phi}_{\mathrm{s}}^T\mathbf{K}_{\mathrm{ss}}\boldsymbol{\Phi}_{\mathrm{s}})\mathbf{Q}_{\mathrm{s}}=\omega^2\boldsymbol{\Phi}_{\mathrm{s}}^T\mathbf{M}_{\mathrm{s}}\boldsymbol{\mathcal{I}}_{\mathrm{s}}\mathbf{U}_O-\boldsymbol{\Phi}_{\mathrm{s}}^T\mathbf{K}_{\mathrm{sf}}\mathbf{X}_{\mathrm{f}}. \tag{6.29}$$

Employing the orthogonality gives

$$\mathrm{diag}\left\{-\omega^2+\mathrm{i}2\zeta_{n,\mathrm{s}}\omega_{n,\mathrm{s}}\omega+\omega_{n,\mathrm{s}}^2\right\}\mathbf{Q}_{\mathrm{s}}=\omega^2\boldsymbol{\Gamma}_{\mathrm{s}}\mathbf{U}_O-\Omega_{\mathrm{s}}\mathbf{X}_{\mathrm{f}}. \tag{6.30}$$

where

$$\boldsymbol{\Gamma}_{\mathrm{s}}=\frac{\boldsymbol{\Phi}_{\mathrm{s}}^T\mathbf{M}_{\mathrm{s}}\boldsymbol{\mathcal{I}}_{\mathrm{s}}}{\boldsymbol{\Phi}_{\mathrm{s}}^T\mathbf{M}_{\mathrm{s}}\boldsymbol{\Phi}_{\mathrm{s}}},\qquad \Omega_{\mathrm{s}}=\frac{\boldsymbol{\Phi}_{\mathrm{s}}^T\mathbf{K}_{\mathrm{sf}}}{\boldsymbol{\Phi}_{\mathrm{s}}^T\mathbf{M}_{\mathrm{s}}\boldsymbol{\Phi}_{\mathrm{s}}}.$$

Hence,

$$\mathbf{X}_{\mathrm{s}}=\omega^2\boldsymbol{\Phi}_{\mathrm{s}}\mathbf{H}_{\mathrm{s}}\boldsymbol{\Gamma}_{\mathrm{s}}\mathbf{U}_O-\boldsymbol{\Phi}_{\mathrm{s}}\mathbf{H}_{\mathrm{s}}\Omega_{\mathrm{s}}\mathbf{X}_{\mathrm{f}}. \tag{6.31}$$

Since the relative displacement $\mathbf{x}=\mathbf{u}-\boldsymbol{\mathcal{I}}\mathbf{u}_O$, $\mathbf{U}_{\mathrm{s}}$ is equal to

$$\mathbf{U}_{\mathrm{s}}=\omega^2\boldsymbol{\Phi}_{\mathrm{s}}\mathbf{H}_{\mathrm{s}}\boldsymbol{\Gamma}_{\mathrm{s}}\mathbf{U}_O-\boldsymbol{\Phi}_{\mathrm{s}}\mathbf{H}_{\mathrm{s}}\Omega_{\mathrm{s}}(\mathbf{U}_{\mathrm{f}}-\boldsymbol{\mathcal{I}}_{\mathrm{f}}\mathbf{U}_O)+\boldsymbol{\mathcal{I}}_{\mathrm{s}}\mathbf{U}_O, \tag{6.32}$$

which can be rewritten as

$$\mathbf{U}_{\mathrm{s}}=\mathbf{a}\mathbf{U}_{\mathrm{f}}+\mathbf{b}\mathbf{U}_O, \tag{6.33}$$

where

$$\mathbf{a}=-\boldsymbol{\Phi}_{\mathrm{s}}\mathbf{H}_{\mathrm{s}}\Omega_{\mathrm{s}},\qquad \mathbf{b}=\omega^2\boldsymbol{\Phi}_{\mathrm{s}}\mathbf{H}_{\mathrm{s}}\boldsymbol{\Gamma}_{\mathrm{s}}+\boldsymbol{\Phi}_{\mathrm{s}}\mathbf{H}_{\mathrm{s}}\Omega_{\mathrm{s}}\boldsymbol{\mathcal{I}}_{\mathrm{f}}+\boldsymbol{\mathcal{I}}_{\mathrm{s}}.$$

The second block row of equation (6.25) is

$$\mathbf{M}_{\mathrm{f}}\ddot{\mathbf{x}}_{\mathrm{f}}(t)+\mathbf{C}_{\mathrm{ff}}\dot{\mathbf{x}}_{\mathrm{f}}(t)+\mathbf{K}_{\mathrm{ff}}\mathbf{x}_{\mathrm{f}}(t)+\mathbf{K}_{\mathrm{fs}}\mathbf{x}_{\mathrm{s}}(t)=-\mathbf{M}_{\mathrm{f}}\boldsymbol{\mathcal{I}}_{\mathrm{f}}\ddot{\mathbf{u}}_O(t)-\mathbf{C}_{\mathrm{fs}}\dot{\mathbf{x}}_{\mathrm{s}}(t)+\mathbf{P}_{\mathrm{f}}. \tag{6.34}$$

Similarly to the first block row, neglecting damping term $\mathbf{C}_{\mathrm{fs}}\dot{\mathbf{x}}_{\mathrm{s}}(t)$, and introducing $\mathbf{x}(t)=\mathbf{X}\mathrm{e}^{\mathrm{i}\omega t}$ and $\mathbf{u}=\mathbf{U}\mathrm{e}^{\mathrm{i}\omega t}$ result in

$$(-\omega^2\mathbf{M}_{\mathrm{f}}+\mathrm{i}\omega\mathbf{C}_{\mathrm{ff}}+\mathbf{K}_{\mathrm{ff}})\mathbf{X}_{\mathrm{f}}+\mathbf{K}_{\mathrm{fs}}\mathbf{X}_{\mathrm{s}}=\omega^2\mathbf{M}_{\mathrm{f}}\boldsymbol{\mathcal{I}}_{\mathrm{f}}\mathbf{U}_O+\mathbf{P}_{\mathrm{f}}. \tag{6.35}$$

According to equation (6.31), $\mathbf{X}_\mathrm{s}$ is replaced in equation (6.35) as

$$(-\omega^2\mathbf{M}_\mathrm{f}+\mathrm{i}\omega\mathbf{C}_\mathrm{ff}+\mathbf{K}_\mathrm{ff}-\mathbf{K}_\mathrm{fs}\boldsymbol{\Phi}_\mathrm{s}\mathbf{H}_\mathrm{s}\Omega_\mathrm{s})\mathbf{X}_\mathrm{f}=\omega^2(\mathbf{M}_\mathrm{f}\boldsymbol{\mathcal{I}}_\mathrm{f}-\mathbf{K}_\mathrm{fs}\boldsymbol{\Phi}_\mathrm{s}\mathbf{H}_\mathrm{s}\boldsymbol{\Gamma}_\mathrm{s})\,\mathbf{U}_O+\mathbf{P}_\mathrm{f}. \tag{6.36}$$

Substituting the modal transformation $\mathbf{X}_\mathrm{f}=\boldsymbol{\Phi}_\mathrm{f}\mathbf{Q}_\mathrm{f}$ into equation (6.36), where $\boldsymbol{\Phi}_\mathrm{f}$ is the modal matrix obtained by modal analysis without the soil springs when all the structure nodes and node O are constrained, and multiplying $\boldsymbol{\Phi}_\mathrm{f}^T$ from the left yield

$$\Delta\mathbf{Q}_\mathrm{f}=\omega^2\boldsymbol{\Phi}_\mathrm{f}^T(\mathbf{M}_\mathrm{f}\boldsymbol{\mathcal{I}}_\mathrm{f}-\mathbf{K}_\mathrm{fs}\boldsymbol{\Phi}_\mathrm{s}\mathbf{H}_\mathrm{s}\boldsymbol{\Gamma}_\mathrm{s})\,\mathbf{U}_O+\boldsymbol{\Phi}_\mathrm{f}^T\mathbf{P}_\mathrm{f}. \tag{6.37}$$

where

$$\Delta=-\omega^2\boldsymbol{\Phi}_\mathrm{f}^T\mathbf{M}_\mathrm{f}\boldsymbol{\Phi}_\mathrm{f}+\mathrm{i}\omega\boldsymbol{\Phi}_\mathrm{f}^T\mathbf{C}_\mathrm{ff}\boldsymbol{\Phi}_\mathrm{f}+\boldsymbol{\Phi}_\mathrm{f}^T\mathbf{K}_\mathrm{ff}\boldsymbol{\Phi}_\mathrm{f}-\boldsymbol{\Phi}_\mathrm{f}^T\mathbf{K}_\mathrm{fs}\boldsymbol{\Phi}_\mathrm{s}\mathbf{H}_\mathrm{s}\Omega_\mathrm{s}\boldsymbol{\Phi}_\mathrm{f}. \tag{6.38}$$

Based on the the orthogonality, Δ can be expressed as

$$\Delta=\boldsymbol{\Phi}_\mathrm{f}^T\mathbf{M}_\mathrm{f}\boldsymbol{\Phi}_\mathrm{f}\mathrm{diag}\{-\omega^2+\mathrm{i}2\zeta_{n,\mathrm{f}}\omega_{n,\mathrm{f}}\omega+\omega_{n,\mathrm{f}}^2\}-\boldsymbol{\Phi}_\mathrm{f}^T\mathbf{K}_\mathrm{fs}\boldsymbol{\Phi}_\mathrm{s}\mathbf{H}_\mathrm{s}\Omega_\mathrm{s}\boldsymbol{\Phi}_\mathrm{f}. \tag{6.39}$$

Then, $\mathbf{X}_\mathrm{f}$ can be obtained as

$$\mathbf{X}_\mathrm{f}=\omega^2\boldsymbol{\Phi}_\mathrm{f}\Delta^{-1}\boldsymbol{\Phi}_\mathrm{f}^T(\mathbf{M}_\mathrm{f}\boldsymbol{\mathcal{I}}_\mathrm{f}-\mathbf{K}_\mathrm{fs}\boldsymbol{\Phi}_\mathrm{s}\mathbf{H}_\mathrm{s}\boldsymbol{\Gamma}_\mathrm{s})\,\mathbf{U}_O+\boldsymbol{\Phi}_\mathrm{f}\Delta^{-1}\boldsymbol{\Phi}_\mathrm{f}^T\mathbf{P}_\mathrm{f}. \tag{6.40}$$

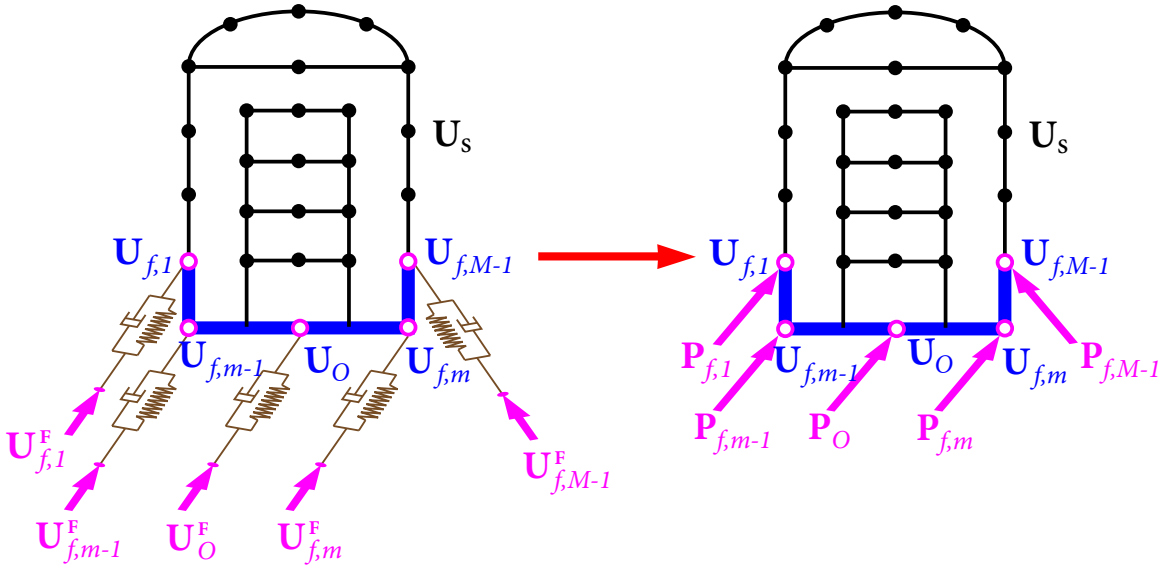

Figure 6.5 Interaction Forces in Spring-Structure Model

The interaction forces applied on the basement $\mathbf{P}_\mathrm{b} = \mathbf{S}^\mathrm{F}_\mathrm{bb}(\mathbf{U}^\mathrm{F}_\mathrm{b} - \mathbf{U}_\mathrm{b})$, as shown in Figure 6.5, can be re-arranged as

$$\begin{Bmatrix} \mathbf{P}_\mathrm{f} \\ \mathbf{P}_O \end{Bmatrix} = \begin{bmatrix} \mathbf{S}^\mathrm{F}_\mathrm{ff} & \mathbf{S}^\mathrm{F}_\mathrm{fO} \\ \mathbf{S}^\mathrm{F}_\mathrm{Of} & \mathbf{S}^\mathrm{F}_\mathrm{OO} \end{bmatrix} \begin{Bmatrix} \mathbf{U}^\mathrm{F}_\mathrm{f} - \mathbf{U}_\mathrm{f} \\ \mathbf{U}^\mathrm{F}_O - \mathbf{U}_O \end{Bmatrix}, \tag{6.41}$$

where $\mathbf{P}_\mathrm{f}$ and $\mathbf{P}_O$ are $(6M-6)\times 1$ and 6×1 vectors, respectively. $\mathbf{S}^\mathrm{F}_\mathrm{ff}$ is a $(6M-6)\times(6M-6)$ matrix, $\mathbf{S}^\mathrm{F}_\mathrm{fO}$ is a $(6M-6)\times 6$ matrix, $\mathbf{S}^\mathrm{F}_\mathrm{Of}$ is a $6\times(6M-6)$ matrix, and $\mathbf{S}^\mathrm{F}_\mathrm{OO}$ is a 6×6 matrix.

Replacing the relative displacement by $\mathbf{x}_\mathrm{f} = \mathbf{u}_\mathrm{f} - \boldsymbol{\mathcal{I}}_\mathrm{f}\mathbf{u}_O$, and substituting the interaction forces into equation (6.40) gives

$$\begin{aligned}\mathbf{U}_\mathrm{f} = \omega^2\boldsymbol{\Phi}_\mathrm{f}\Delta^{-1}\boldsymbol{\Phi}_\mathrm{f}^T(\mathbf{M}_\mathrm{f}\boldsymbol{\mathcal{I}}_\mathrm{f} - \mathbf{K}_\mathrm{fs}\boldsymbol{\Phi}_\mathrm{s}\mathbf{H}_\mathrm{s}\boldsymbol{\Gamma}_\mathrm{s})\,\mathbf{U}_O + \boldsymbol{\mathcal{I}}_\mathrm{f}\mathbf{U}_O + \\ \boldsymbol{\Phi}_\mathrm{f}\Delta^{-1}\boldsymbol{\Phi}_\mathrm{f}^T\left[\mathbf{S}^\mathrm{F}_\mathrm{ff}\left(\mathbf{U}^\mathrm{F}_\mathrm{f} - \mathbf{U}_\mathrm{f}\right) + \mathbf{S}^\mathrm{F}_\mathrm{fO}\left(\mathbf{U}^\mathrm{F}_O - \mathbf{U}_O\right)\right],\end{aligned} \tag{6.42}$$

which can be rewritten as

$$\begin{aligned}&\left(\mathbf{E} + \boldsymbol{\Phi}_\mathrm{f}\Delta^{-1}\boldsymbol{\Phi}_\mathrm{f}^T\mathbf{S}^\mathrm{F}_\mathrm{ff}\right)\mathbf{U}_\mathrm{f} \\ &\quad + \left[-\omega^2\boldsymbol{\Phi}_\mathrm{f}\Delta^{-1}\boldsymbol{\Phi}_\mathrm{f}^T\left(\mathbf{M}_\mathrm{f}\boldsymbol{\mathcal{I}}_\mathrm{f} - \mathbf{K}_\mathrm{fs}\boldsymbol{\Phi}_\mathrm{s}\mathbf{H}_\mathrm{s}\boldsymbol{\Gamma}_\mathrm{s}\right) - \boldsymbol{\mathcal{I}}_\mathrm{f} + \boldsymbol{\Phi}_\mathrm{f}\Delta^{-1}\boldsymbol{\Phi}_\mathrm{f}^T\mathbf{S}^\mathrm{F}_\mathrm{fO}\right]\mathbf{U}_O \\ &\qquad = \boldsymbol{\Phi}_\mathrm{f}\Delta^{-1}\boldsymbol{\Phi}_\mathrm{f}^T\mathbf{S}^\mathrm{F}_\mathrm{ff}\mathbf{U}^\mathrm{F}_\mathrm{f} + \boldsymbol{\Phi}_\mathrm{f}\Delta^{-1}\boldsymbol{\Phi}_\mathrm{f}^T\mathbf{S}^\mathrm{F}_\mathrm{fO}\mathbf{U}^\mathrm{F}_O,\end{aligned} \tag{6.43}$$

where $\mathbf{E}$ is a $(6M-6)\times(6M-6)$ unit matrix.

Based on Newton's second law, the dynamic equilibrium equation of a sub structure-foundation system can be obtained in six directions. It is expressed as

$$-\omega^2\Big(\begin{Bmatrix} \boldsymbol{\mathcal{I}}_\mathrm{s} \\ \boldsymbol{\mathcal{I}}_\mathrm{f} \end{Bmatrix}^T \begin{bmatrix} \mathbf{M}_\mathrm{s} & \mathbf{0} \\ \mathbf{0} & \mathbf{M}_\mathrm{f} \end{bmatrix} \begin{Bmatrix} \mathbf{U}_\mathrm{s} \\ \mathbf{U}_\mathrm{f} \end{Bmatrix} + \mathbf{M}_O\,\mathbf{U}_O\Big) = \mathbf{F}_\mathrm{f} + \mathbf{F}_O, \tag{6.44}$$

where $\mathbf{M}_O$ is the mass matrix of the node O. Then the first term represents the resultant of the foundation (excluding node O) and structure's motion about the origin O, the second term represents the resultant of the node O's motion, $\mathbf{F}_\mathrm{f}$ is the spring force matrix at foundation nodes (excluding node O), and $\mathbf{F}_O$ denotes the force vector acting on the node O. According to equation (6.41), they are equal to

$$\mathbf{F}_\mathrm{f} = \boldsymbol{\mathcal{I}}_\mathrm{f}^\mathrm{T}\mathbf{P}_\mathrm{f} = \boldsymbol{\mathcal{I}}_\mathrm{f}^\mathrm{T}\left[\mathbf{S}^\mathrm{F}_\mathrm{ff}\left(\mathbf{U}^\mathrm{F}_\mathrm{f} - \mathbf{U}_\mathrm{f}\right) + \mathbf{S}^\mathrm{F}_\mathrm{fO}\left(\mathbf{U}^\mathrm{F}_O - \mathbf{U}_O\right)\right],$$

$$\mathbf{F}_O = \mathbf{P}_O = \mathbf{S}^{\mathrm{F}}_{Of}\left(\mathbf{U}^{\mathrm{F}}_{\mathrm{f}} - \mathbf{U}_{\mathrm{f}}\right) + \mathbf{S}^{\mathrm{F}}_{OO}\left(\mathbf{U}^{\mathrm{F}}_{O} - \mathbf{U}_{O}\right).$$

Therefore, equation (6.44) can be rewritten as

$$\begin{aligned}
&\left(-\omega^2 \begin{Bmatrix} \boldsymbol{\mathcal{I}}_{\mathrm{s}} \\ \boldsymbol{\mathcal{I}}_{\mathrm{f}} \end{Bmatrix}^T \begin{bmatrix} \mathbf{M}_{\mathrm{s}} & \mathbf{0} \\ \mathbf{0} & \mathbf{M}_{\mathrm{f}} \end{bmatrix} + \begin{Bmatrix} \mathbf{0} \\ \boldsymbol{\mathcal{I}}_{\mathrm{f}}^T \mathbf{S}^{\mathrm{F}}_{\mathrm{ff}} + \mathbf{S}^{\mathrm{F}}_{Of} \end{Bmatrix}^T\right) \begin{Bmatrix} \mathbf{U}_{\mathrm{s}} \\ \mathbf{U}_{\mathrm{f}} \end{Bmatrix} \\
&+ \left[-\omega^2 \mathbf{M}_O + \left(\boldsymbol{\mathcal{I}}_{\mathrm{f}}^T \mathbf{S}^{\mathrm{F}}_{\mathrm{f}O} + \mathbf{S}^{\mathrm{F}}_{OO}\right)\right] \mathbf{U}_O = \left(\boldsymbol{\mathcal{I}}_{\mathrm{f}}^T \mathbf{S}^{\mathrm{F}}_{\mathrm{ff}} + \mathbf{S}^{\mathrm{F}}_{Of}\right) \mathbf{U}^{\mathrm{F}}_{\mathrm{f}} + \left(\boldsymbol{\mathcal{I}}_{\mathrm{f}}^T \mathbf{S}^{\mathrm{F}}_{\mathrm{f}O} + \mathbf{S}^{\mathrm{F}}_{OO}\right) \mathbf{U}^{\mathrm{F}}_{O}.
\end{aligned} \tag{6.45}$$

Introducing equation (6.33) leads to

$$\begin{aligned}
&\left[-\omega^2 \boldsymbol{\mathcal{I}}_{\mathrm{f}}^T \mathbf{M}_{\mathrm{f}} + \left(\boldsymbol{\mathcal{I}}_{\mathrm{f}}^T \mathbf{S}^{\mathrm{F}}_{\mathrm{ff}} + \mathbf{S}^{\mathrm{F}}_{Of}\right) - \omega^2 \boldsymbol{\mathcal{I}}_{\mathrm{s}}^T \mathbf{M}_{\mathrm{s}} \mathbf{a}\right] \mathbf{U}_{\mathrm{f}} \\
&\qquad + \left[-\omega^2 \mathbf{M}_O + \left(\boldsymbol{\mathcal{I}}_{\mathrm{f}}^T \mathbf{S}^{\mathrm{F}}_{\mathrm{f}O} + \mathbf{S}^{\mathrm{F}}_{OO}\right) - \omega^2 \boldsymbol{\mathcal{I}}_{\mathrm{s}}^T \mathbf{M}_{\mathrm{s}} \mathbf{b}\right] \mathbf{U}_O \\
&\qquad\qquad = \left(\boldsymbol{\mathcal{I}}_{\mathrm{f}}^T \mathbf{S}^{\mathrm{F}}_{\mathrm{ff}} + \mathbf{S}^{\mathrm{F}}_{Of}\right) \mathbf{U}^{\mathrm{F}}_{\mathrm{f}} + \left(\boldsymbol{\mathcal{I}}_{\mathrm{f}}^T \mathbf{S}^{\mathrm{F}}_{\mathrm{f}O} + \mathbf{S}^{\mathrm{F}}_{OO}\right) \mathbf{U}^{\mathrm{F}}_{O}.
\end{aligned} \tag{6.46}$$

Assembling equations (6.25), (6.43) and (6.46) leads to

$$\begin{bmatrix} \mathbf{S}_{\mathrm{ff}} & \mathbf{S}_{\mathrm{f}O} \\ \mathbf{S}_{Of} & \mathbf{S}_{OO} \end{bmatrix} \begin{Bmatrix} \mathbf{U}_{\mathrm{f}} \\ \mathbf{U}_{O} \end{Bmatrix} = \begin{bmatrix} \mathbf{K}^{\mathrm{F}}_{\mathrm{ff}} & \mathbf{K}^{\mathrm{F}}_{\mathrm{f}O} \\ \mathbf{K}^{\mathrm{F}}_{Of} & \mathbf{K}^{\mathrm{F}}_{OO} \end{bmatrix} \begin{Bmatrix} \mathbf{U}^{\mathrm{F}}_{\mathrm{f}} \\ \mathbf{U}^{\mathrm{F}}_{O} \end{Bmatrix} \tag{6.47}$$

where

$$\begin{aligned}
\mathbf{S}_{\mathrm{ff}} &= \mathbf{E} + \boldsymbol{\Phi}_{\mathrm{f}} \Delta^{-1} \boldsymbol{\Phi}_{\mathrm{f}}^T \mathbf{S}^{\mathrm{F}}_{\mathrm{ff}}, \\
\mathbf{S}_{\mathrm{f}O} &= -\omega^2 \boldsymbol{\Phi}_{\mathrm{f}} \Delta^{-1} \boldsymbol{\Phi}_{\mathrm{f}}^T \left(\mathbf{M}_{\mathrm{f}} \boldsymbol{\mathcal{I}}_{\mathrm{f}} - \mathbf{K}_{\mathrm{fs}} \boldsymbol{\Phi}_{\mathrm{s}} \mathbf{H}_{\mathrm{s}} \boldsymbol{\Gamma}_{\mathrm{s}}\right) - \boldsymbol{\mathcal{I}}_{\mathrm{f}} + \boldsymbol{\Phi}_{\mathrm{f}} \Delta^{-1} \boldsymbol{\Phi}_{\mathrm{f}}^T \mathbf{S}^{\mathrm{F}}_{\mathrm{f}O}, \\
\mathbf{S}_{Of} &= -\omega^2 \boldsymbol{\mathcal{I}}_{\mathrm{f}}^T \mathbf{M}_{\mathrm{f}} + \left(\boldsymbol{\mathcal{I}}_{\mathrm{f}}^T \mathbf{S}^{\mathrm{F}}_{\mathrm{ff}} + \mathbf{S}^{\mathrm{F}}_{Of}\right) - \omega^2 \boldsymbol{\mathcal{I}}_{\mathrm{s}}^T \mathbf{M}_{\mathrm{s}} \mathbf{a}, \\
\mathbf{S}_{OO} &= -\omega^2 \mathbf{M}_O + \left(\boldsymbol{\mathcal{I}}_{\mathrm{f}}^T \mathbf{S}^{\mathrm{F}}_{\mathrm{f}O} + \mathbf{S}^{\mathrm{F}}_{OO}\right) - \omega^2 \boldsymbol{\mathcal{I}}_{\mathrm{s}}^T \mathbf{M}_{\mathrm{s}} \mathbf{b}, \\
\mathbf{K}^{\mathrm{F}}_{\mathrm{ff}} &= \boldsymbol{\Phi}_{\mathrm{f}} \Delta^{-1} \boldsymbol{\Phi}_{\mathrm{f}}^T \mathbf{S}^{\mathrm{F}}_{\mathrm{ff}}, \qquad \mathbf{K}^{\mathrm{F}}_{\mathrm{f}O} = \boldsymbol{\Phi}_{\mathrm{f}} \Delta^{-1} \boldsymbol{\Phi}_{\mathrm{f}}^T \mathbf{S}^{\mathrm{F}}_{\mathrm{f}O}, \\
\mathbf{K}^{\mathrm{F}}_{Of} &= \boldsymbol{\mathcal{I}}_{\mathrm{f}}^T \mathbf{S}^{\mathrm{F}}_{\mathrm{ff}} + \mathbf{S}^{\mathrm{F}}_{Of}, \qquad \mathbf{K}^{\mathrm{F}}_{OO} = \boldsymbol{\mathcal{I}}_{\mathrm{f}}^T \mathbf{S}^{\mathrm{F}}_{\mathrm{f}O} + \mathbf{S}^{\mathrm{F}}_{OO}.
\end{aligned}$$

Then one obtains

$$\mathbf{U}_{\mathrm{b}} = \mathbf{T}\, \mathbf{U}^{\mathrm{F}}_{\mathrm{b}}, \tag{6.48}$$

where

$$\mathbf{T} = \mathbf{S}^{-1}\mathbf{K}^{\mathrm{F}}.$$

Special Case 1: Rigid Foundation with Spatially Varying Ground Motions

For a structure with a rigid foundation under multi-support excitations, one has $\mathbf{u}_{\mathrm{f}} = \boldsymbol{\mathcal{I}}_{\mathrm{f}}\mathbf{u}_O$ and $\mathbf{x}_{\mathrm{f}} = 0$. Then equation (6.32) becomes

$$\mathbf{U}_{\mathrm{s}} = \mathbf{S}_{\mathrm{R}}^{\mathrm{FB}}\,\mathbf{U}_O, \tag{6.49}$$

where

$$\mathbf{S}_{\mathrm{R}}^{\mathrm{FB}} = \omega^2\boldsymbol{\Phi}_{\mathrm{s}}\mathbf{H}_{\mathrm{s}}\boldsymbol{\Gamma}_{\mathrm{s}} + \boldsymbol{\mathcal{I}}_{\mathrm{s}}.$$

When the relative displacement of node f is 0, equation (6.35) is simplified as

$$\mathbf{K}_{\mathrm{fs}}\,\mathbf{X}_{\mathrm{s}} = \omega^2\mathbf{M}_{\mathrm{f}}\boldsymbol{\mathcal{I}}_{\mathrm{f}}\,\mathbf{U}_O + \mathbf{P}_{\mathrm{f}}. \tag{6.50}$$

Substituting the interaction forces (6.41) and equation (6.49) lets equation (6.50) become

$$\mathbf{S}_{\mathrm{ff}}^{\mathrm{F}}\mathbf{U}_{\mathrm{f}} + \left[-\omega^2\mathbf{M}_{\mathrm{f}}\boldsymbol{\mathcal{I}}_{\mathrm{f}} + \mathbf{K}_{\mathrm{fs}}\left(\mathbf{S}_{\mathrm{R}}^{\mathrm{FB}} - \boldsymbol{\mathcal{I}}_{\mathrm{s}}\right) + \mathbf{S}_{Of}^{\mathrm{F}}\right]\mathbf{U}_O = \mathbf{S}_{\mathrm{ff}}^{\mathrm{F}}\mathbf{U}_{\mathrm{f}}^{\mathrm{F}} + \mathbf{S}_{Of}^{\mathrm{F}}\mathbf{U}_O^{\mathrm{F}}. \tag{6.51}$$

At the same time, the equilibrium equation (6.46) becomes

$$\begin{aligned}\left[-\omega^2\boldsymbol{\mathcal{I}}_{\mathrm{f}}^T\mathbf{M}_{\mathrm{f}} + \left(\boldsymbol{\mathcal{I}}_{\mathrm{f}}^T\mathbf{S}_{\mathrm{ff}}^{\mathrm{F}} + \mathbf{S}_{Of}^{\mathrm{F}}\right)\right]\mathbf{U}_{\mathrm{f}} + \left[-\omega^2\mathbf{M}_O + \left(\boldsymbol{\mathcal{I}}_{\mathrm{f}}^T\mathbf{S}_{fO}^{\mathrm{F}} + \mathbf{S}_{OO}^{\mathrm{F}}\right) - \omega^2\boldsymbol{\mathcal{I}}_{\mathrm{s}}^T\mathbf{M}_{\mathrm{s}}\mathbf{S}_{\mathrm{R}}^{\mathrm{FB}}\right]\mathbf{U}_O \\ = \left(\boldsymbol{\mathcal{I}}_{\mathrm{f}}^T\mathbf{S}_{\mathrm{ff}}^{\mathrm{F}} + \mathbf{S}_{Of}^{\mathrm{F}}\right)\mathbf{U}_{\mathrm{f}}^{\mathrm{F}} + \left(\boldsymbol{\mathcal{I}}_{\mathrm{f}}^T\mathbf{S}_{fO}^{\mathrm{F}} + \mathbf{S}_{OO}^{\mathrm{F}}\right)\mathbf{U}_O^{\mathrm{F}}.\end{aligned} \tag{6.52}$$

Assemble equations (6.51) and (6.52) gives

$$\begin{bmatrix}\mathbf{S}_{\mathrm{R1,ff}} & \mathbf{S}_{\mathrm{R1},fO}\\ \mathbf{S}_{\mathrm{R1},Of} & \mathbf{S}_{\mathrm{R1},OO}\end{bmatrix}\begin{Bmatrix}\mathbf{U}_{\mathrm{f}}\\ \mathbf{U}_O\end{Bmatrix} = \begin{bmatrix}\mathbf{K}_{\mathrm{R1,ff}}^{\mathrm{F}} & \mathbf{K}_{\mathrm{R1},fO}^{\mathrm{F}}\\ \mathbf{K}_{\mathrm{R1},Of}^{\mathrm{F}} & \mathbf{K}_{\mathrm{R1},OO}^{\mathrm{F}}\end{bmatrix}\begin{Bmatrix}\mathbf{U}_{\mathrm{f}}^{\mathrm{F}}\\ \mathbf{U}_O^{\mathrm{F}}\end{Bmatrix} \tag{6.53}$$

where

$$\begin{aligned}\mathbf{S}_{\mathrm{R1,ff}} &= \mathbf{S}_{\mathrm{ff}}^{\mathrm{F}}, \qquad \mathbf{S}_{\mathrm{R1},fO} = -\omega^2\mathbf{M}_{\mathrm{f}}\boldsymbol{\mathcal{I}}_{\mathrm{f}} + \mathbf{K}_{\mathrm{fs}}\left(\mathbf{S}_{\mathrm{R}}^{\mathrm{FB}} - \boldsymbol{\mathcal{I}}_{\mathrm{s}}\right) + \mathbf{S}_{Of}^{\mathrm{F}},\\ \mathbf{S}_{\mathrm{R1},Of} &= -\omega^2\boldsymbol{\mathcal{I}}_{\mathrm{f}}^T\mathbf{M}_{\mathrm{f}} + \left(\boldsymbol{\mathcal{I}}_{\mathrm{f}}^T\mathbf{S}_{\mathrm{ff}}^{\mathrm{F}} + \mathbf{S}_{Of}^{\mathrm{F}}\right),\\ \mathbf{S}_{\mathrm{R1},OO} &= -\omega^2\mathbf{M}_O + \left(\boldsymbol{\mathcal{I}}_{\mathrm{f}}^T\mathbf{S}_{fO}^{\mathrm{F}} + \mathbf{S}_{OO}^{\mathrm{F}}\right) - \omega^2\boldsymbol{\mathcal{I}}_{\mathrm{s}}^T\mathbf{M}_{\mathrm{s}}\mathbf{S}_{\mathrm{R}}^{\mathrm{FB}},\end{aligned}$$

$$\mathbf{K}^{\mathrm{F}}_{\mathrm{R1,ff}} = \mathbf{S}^{\mathrm{F}}_{\mathrm{ff}}, \qquad \mathbf{K}^{\mathrm{F}}_{\mathrm{R1},fO} = \mathbf{S}^{\mathrm{F}}_{\mathrm{f}O},$$

$$\mathbf{K}^{\mathrm{F}}_{\mathrm{R1},Of} = \boldsymbol{\mathcal{I}}^{T}_{\mathrm{f}}\mathbf{S}^{\mathrm{F}}_{\mathrm{ff}} + \mathbf{S}^{\mathrm{F}}_{Of}, \qquad \mathbf{K}^{\mathrm{F}}_{\mathrm{R1},OO} = \boldsymbol{\mathcal{I}}^{T}_{\mathrm{f}}\mathbf{S}^{\mathrm{F}}_{\mathrm{f}O} + \mathbf{S}^{\mathrm{F}}_{OO}.$$

Then one obtains

$$\mathbf{U}_{\mathrm{b}} = \mathbf{T}_{\mathrm{R1}}\,\mathbf{U}^{\mathrm{F}}_{\mathrm{b}}, \tag{6.54}$$

where

$$\mathbf{T}_{\mathrm{R1}} = \mathbf{S}^{-1}_{\mathrm{R1}}\mathbf{K}^{\mathrm{F}}_{\mathrm{R1}}.$$

Special Case 2: Rigid Foundation with Uniform Seismic Input

For a structure with a rigid foundation under uniform seismic input, both the $\mathbf{U}^{\mathrm{F}}_{\mathrm{b}}$ and $\mathbf{U}_{\mathrm{b}}$ are the same at each point, and can be represented by the motion at a single point, i.e., $\mathbf{U}^{\mathrm{F}}_{O}$ and $\mathbf{U}_{O}$. In this case, only the second block row of equation (6.53) is needed. It can be expressed as

$$\mathbf{S}_{\mathrm{R2}}\mathbf{U}_{O} = \mathbf{K}^{\mathrm{F}}_{\mathrm{R2}}\mathbf{U}^{\mathrm{F}}_{O}, \tag{6.55}$$

where

$$\mathbf{S}_{\mathrm{R2}} = \left(-\omega^2\boldsymbol{\mathcal{I}}^{T}_{\mathrm{f}}\mathbf{M}_{\mathrm{f}} - \omega^2\mathbf{M}_{O} - \omega^2\boldsymbol{\mathcal{I}}^{T}_{\mathrm{s}}\mathbf{M}_{\mathrm{s}}\mathbf{S}^{\mathrm{FB}}_{\mathrm{R}}\right) + \left(\boldsymbol{\mathcal{I}}^{T}_{\mathrm{f}}\mathbf{S}^{\mathrm{F}}_{\mathrm{ff}}\boldsymbol{\mathcal{I}}_{\mathrm{f}} + \mathbf{S}^{\mathrm{F}}_{Of}\boldsymbol{\mathcal{I}}_{\mathrm{f}} + \boldsymbol{\mathcal{I}}^{T}_{\mathrm{f}}\mathbf{S}^{\mathrm{F}}_{\mathrm{f}O} + \mathbf{S}^{\mathrm{F}}_{OO}\right),$$

$$\mathbf{K}^{\mathrm{F}}_{\mathrm{R2}} = \boldsymbol{\mathcal{I}}^{T}_{\mathrm{f}}\mathbf{S}^{\mathrm{F}}_{\mathrm{ff}}\boldsymbol{\mathcal{I}}_{\mathrm{f}} + \mathbf{S}^{\mathrm{F}}_{Of}\boldsymbol{\mathcal{I}}_{\mathrm{f}} + \boldsymbol{\mathcal{I}}^{T}_{\mathrm{f}}\mathbf{S}^{\mathrm{F}}_{\mathrm{f}O} + \mathbf{S}^{\mathrm{F}}_{OO}.$$

Both $\mathbf{S}_{\mathrm{R2}}$ and $\mathbf{K}^{\mathrm{F}}_{\mathrm{R2}}$ are 6×6 matrices. In $\mathbf{S}_{\mathrm{R2}}$, the first term is the total inertia forces of the foundation-structure system, while the second term and $\mathbf{K}^{\mathrm{F}}_{\mathrm{R2}}$ represent the dynamic soil stiffness under the entire foundation.

Then one obtains

$$\mathbf{U}_{O} = \mathbf{T}_{\mathrm{R2}}\,\mathbf{U}^{\mathrm{F}}_{O}, \tag{6.56}$$

where

$$\mathbf{T}_{\mathrm{R2}} = \mathbf{S}^{-1}_{\mathrm{R2}}\mathbf{K}^{\mathrm{F}}_{\mathrm{R2}}.$$

6.2 Foundation Level Input Response Spectra (FLIRS)

FLIRS for the structure with flexible foundation is needed to be taken as the seismic input in a fixed-base analysis instead of considering a coupled soil-structure analysis using FIRS as the seismic input.

As demonstrated in Section 3.1.4, the seismic input in the fixed-base model and the free field motion can be bridged by the translational responses. Hence, one obtains the FLIRS with a flexible foundation as

$$\mathbf{U}_{\mathrm{b}}^{\mathrm{FB}} = \boldsymbol{\mathcal{T}}\,\mathbf{U}_{\mathrm{b,T}}^{\mathrm{F}}, \tag{6.57}$$

where $\boldsymbol{\mathcal{T}}$ is a complex transfer matrix from FIRS (generated by $\mathbf{U}_{\mathrm{b,T}}^{\mathrm{F}}$) to FLIRS (generated by $\mathbf{U}_{\mathrm{b}}^{\mathrm{FB}}$), given as

$$\boldsymbol{\mathcal{T}} = \mathbf{T}_{\mathrm{TT}} + \left[\left(\mathbf{S}_{\mathrm{TT}}^{\mathrm{FB}}\right)^{T}\mathbf{S}_{\mathrm{TT}}^{\mathrm{FB}}\right]^{-1}\left(\mathbf{S}_{\mathrm{TT}}^{\mathrm{FB}}\right)^{T}\mathbf{S}_{\mathrm{TR}}^{\mathrm{FB}}\,\mathbf{T}_{\mathrm{RT}}, \tag{6.58}$$

where $\boldsymbol{\mathcal{T}}$ and $\mathbf{T}_{\mathrm{TT}}$ are $3M\times 3M$, $\mathbf{T}_{\mathrm{RT}}$ is $3N\times 3M$, and $\mathbf{S}_{\mathrm{TT}}^{\mathrm{FB}}$ is $3N\times 3M$.

For the rigid foundation, the transfer function $\boldsymbol{\mathcal{T}}_{\mathrm{R}}$ is

$$\boldsymbol{\mathcal{T}}_{\mathrm{R}} = \mathbf{T}_{\mathrm{TT,R2}} + \left[\left(\mathbf{S}_{\mathrm{TT,R}}^{\mathrm{FB}}\right)^{T}\mathbf{S}_{\mathrm{TT,R}}^{\mathrm{FB}}\right]^{-1}\left(\mathbf{S}_{\mathrm{TT,R}}^{\mathrm{FB}}\right)^{T}\mathbf{S}_{\mathrm{TR,R}}^{\mathrm{FB}}\,\mathbf{T}_{\mathrm{RT,R2}}, \tag{6.59}$$

where $\boldsymbol{\mathcal{T}}_{\mathrm{R}}$ and $\mathbf{T}_{\mathrm{TT,R2}}$ are 3×3, $\mathbf{T}_{\mathrm{RT,R2}}$ is $3N\times 3$, and $\mathbf{S}_{\mathrm{TT\,R}}^{\mathrm{FB}}$ is $3N\times 3$.

Based on the transformation from response spectra $\boldsymbol{\mathcal{S}}_{\mathrm{A}}$ to fourier amplitude spectra as stated in Section 2.1, the fourier amplitude spectra of free field motion $\mathbf{U}_{\mathrm{b,T}}^{\mathrm{F}}$ can be obtained from $\boldsymbol{\mathcal{S}}_{\mathrm{A}}^{\mathrm{F}}$. Then one obtains

$$\mathbf{U}_{\mathrm{b,T}}^{\mathrm{F}} = \boldsymbol{\mathcal{T}}^{\mathrm{F}}\mathbf{U}_{\mathrm{m}}^{\mathrm{F}}, \tag{6.60}$$

where $\mathbf{U}_{\mathrm{m}}^{\mathrm{F}}$ can be any element of $\mathbf{U}_{\mathrm{b,T}}^{\mathrm{F}}$, e.g., the free field motion at node O in the first horizontal direction, and $\boldsymbol{\mathcal{T}}^{\mathrm{F}}$ is given by

$$\boldsymbol{\mathcal{T}}^{\mathrm{F}} = \frac{\mathbf{U}_{\mathrm{b,T}}^{\mathrm{F}}}{\mathbf{U}_{\mathrm{m}}^{\mathrm{F}}}. \tag{6.61}$$

Finally, FLIRS with a flexible foundation under multi-support excitations is obtained as

$$\mathbf{U}_{\mathrm{b}}^{\mathrm{FB}} = \boldsymbol{\mathcal{T}}_{\mathrm{m}}\,\mathbf{U}_{\mathrm{m}}^{\mathrm{F}}, \tag{6.62}$$

where $\boldsymbol{\mathcal{T}}_{\mathrm{m}}$ is the transformed complex transfer matrix from FIRS to FLIRS, given as

$$\boldsymbol{\mathcal{T}}_{\mathrm{m}} = \boldsymbol{\mathcal{T}}\boldsymbol{\mathcal{I}}^{\mathrm{F}}, \tag{6.63}$$

where $\boldsymbol{\mathcal{T}}_{\mathrm{m}}$ is $3M\times 1$.

The fixed-base analysis of the structure under the excitation of FLIRS $\mathbf{U}_{\mathrm{b}}^{\mathrm{FB}}$ given by equation (6.62) can give exactly the same FRS as a full coupled soil-structure analysis under the excitation of FIRS $\mathbf{U}_{\mathrm{b,T}}^{\mathrm{F}}$.

Based on the theory of random vibration, Equations 3.41 and 3.42, the ratios between the mean-square responses of a SDOF oscillator under base excitation $\mathbf{U}_{\mathrm{b}}^{\mathrm{FB}}$ and those under base excitation $\mathbf{U}_{\mathrm{b},\mathrm{T}}^{\mathrm{F}}$ can be calculated by

$$\begin{aligned}\boldsymbol{\mathcal{R}}^2(\omega_0,\zeta_0) &= \frac{\displaystyle\int_{-\infty}^{\infty} \left|\omega_0^2 H_0(\omega)\right|^2 \left[\left|\boldsymbol{\mathcal{T}}_{\mathrm{m}}(\omega)\right|^2\right] \mathbf{S}_{\ddot{U}\ddot{U}}^{\mathrm{F}}(\omega)\,\mathrm{d}\omega}{\displaystyle\int_{-\infty}^{\infty} \left|\omega_0^2 H_0(\omega)\right|^2 \mathbf{S}_{\ddot{U}\ddot{U}}^{\mathrm{F}}(\omega)\,\mathrm{d}\omega} \\ &= \frac{\displaystyle\int_{-\infty}^{\infty} \left|H_0(\omega)\right|^2 \left[\left|\boldsymbol{\mathcal{T}}_{\mathrm{m}}(\omega)\right|^2\right] \mathrm{d}\omega}{\displaystyle\int_{-\infty}^{\infty} \left|H_0(\omega)\right|^2 \mathrm{d}\omega}.\end{aligned} \tag{6.64}$$

According to Equations 3.44 and 3.45, neglecting the difference of of peak factors leads to FLIRS as

$$\boldsymbol{S}_{\mathrm{A}}^{\mathrm{FB}}(\omega_0,\zeta_0) = \boldsymbol{\mathcal{R}}(\omega_0,\zeta_0)\ \cdot \boldsymbol{S}_{\mathrm{A}}^{\mathrm{F}}(\omega_0,\zeta_0), \tag{6.65}$$

in which $\boldsymbol{\mathcal{R}}(\omega_0,\zeta_0)$ are the modification factors from FIRS to FLIRS.

6.2.1 Generating FRS Considering SSI

For a structure in a nuclear power plant with its foundation embedded in layered soil, a procedure for generating FRS considering SSI is illustrated in Figure 6.6 and is summarized as follows:

1. Consider the layered soil as a free-field. With seismic input applied at the bedrock, a site response analysis is performed to obtain the Foundation Input Response Spectra (FIRS) $\mathbf{U}_{\mathrm{b}}^{\mathrm{F}}$ or $\mathbf{U}_{\mathrm{b,T}}^{\mathrm{F}}$ at the elevation of the foundation.

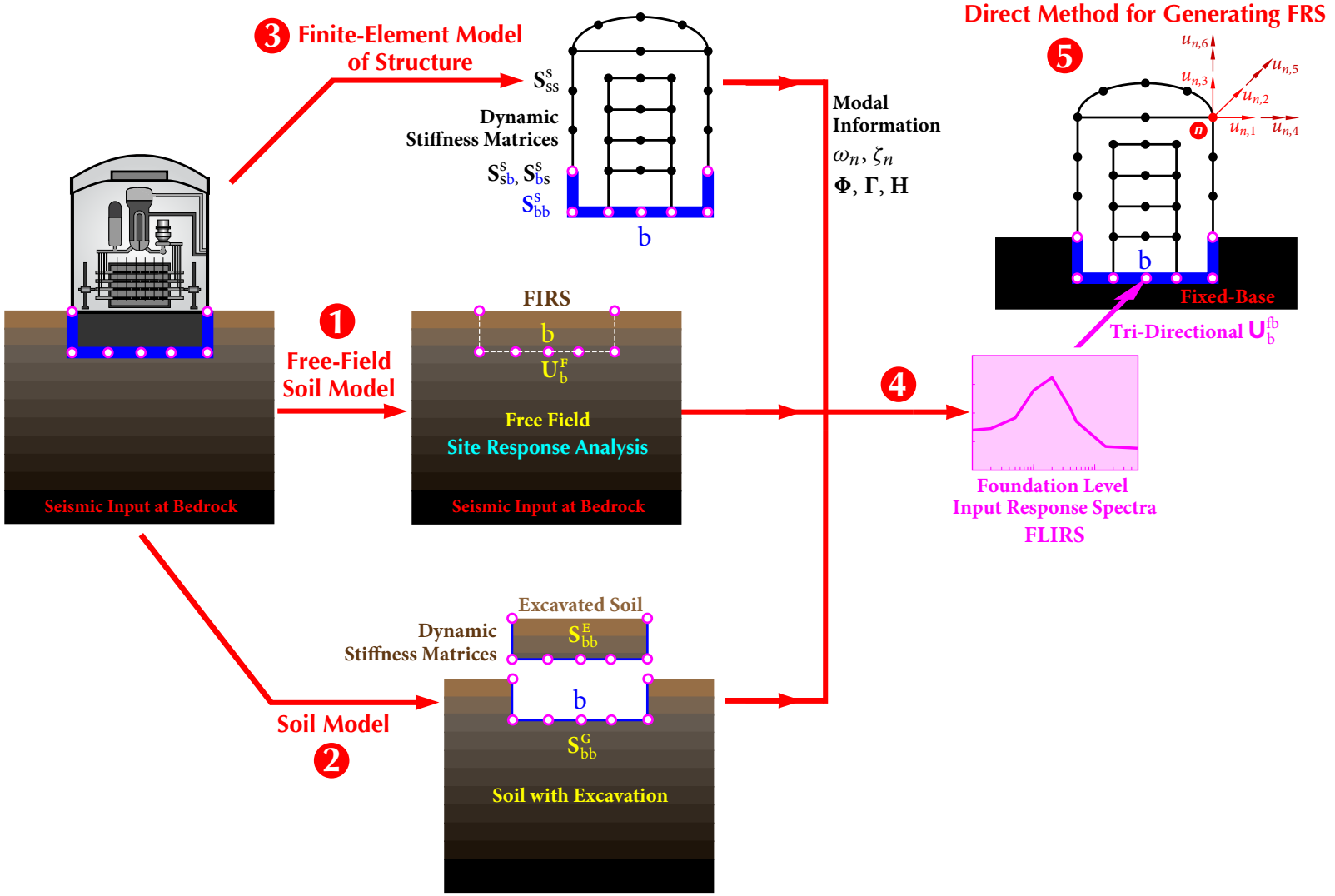

Figure 6.6 Procedure for generating FRS considering SSI

2. Establish a model of the layered soil. Determined the dynamic stiffness matrices of the free-field is $\mathbf{S}_{\mathrm{bb}}^{\mathrm{F}}$.
3. Set up a finite element model of the structure and the foundation. Perform a modal analysis to obtain the modal frequencies ω_n, modal damping coefficients ζ_n, modal matrix $\mathbf{\Phi}$, and matrix of modal contribution factors $\mathbf{\Gamma}$, and get the stiffness matrix $\mathbf{K}_{\mathrm{ss}}$ and $\mathbf{K}_{\mathrm{sb}}$.
4. Determine the Foundation Level Input Response Spectra (FLIRS):
   - $\mathbf{S}^{\mathrm{FB}} = \omega^2 \mathbf{\Phi}_{\mathrm{s}} \mathbf{H}_{\mathrm{s}} \mathbf{\Gamma} + \mathbf{L} = \begin{bmatrix} \mathbf{S}_{\mathrm{TT}}^{\mathrm{FB}} & \mathbf{S}_{\mathrm{TR}}^{\mathrm{FB}} \\ \mathbf{S}_{\mathrm{RT}}^{\mathrm{FB}} & \mathbf{S}_{\mathrm{RR}}^{\mathrm{FB}} \end{bmatrix}_{6N \times 6M}$
   - $\mathbf{S} = \begin{bmatrix} \mathbf{S}_{\mathrm{ff}} & \mathbf{S}_{\mathrm{f}O} \\ \mathbf{S}_{O\mathrm{f}} & \mathbf{S}_{OO} \end{bmatrix}_{6M \times 6M}$
   - $\mathbf{K} = \begin{bmatrix} \mathbf{K}_{\mathrm{ff}}^{\mathrm{F}} & \mathbf{K}_{\mathrm{f}O}^{\mathrm{F}} \\ \mathbf{K}_{O\mathrm{f}}^{\mathrm{F}} & \mathbf{K}_{OO}^{\mathrm{F}} \end{bmatrix}_{6M \times 6M}$
   - $\begin{bmatrix} \mathbf{T}_{\mathrm{TT}} & \mathbf{T}_{\mathrm{TR}} \\ \mathbf{T}_{\mathrm{RT}} & \mathbf{T}_{\mathrm{RR}} \end{bmatrix}_{6M \times 6M} = \mathbf{S}^{-1} \mathbf{K}^{\mathrm{F}}$
   - Transfer matrix: $\boldsymbol{\mathcal{T}} = \mathbf{T}_{\mathrm{TT}} + \left[\left(\mathbf{S}_{\mathrm{TT}}^{\mathrm{FB}} \right)^T \mathbf{S}_{\mathrm{TT}}^{\mathrm{FB}} \right]^{-1} \left(\mathbf{S}_{\mathrm{TT}}^{\mathrm{FB}} \right)^T \mathbf{S}_{\mathrm{TR}}^{\mathrm{FB}} \mathbf{T}_{\mathrm{RT}}$
   - FLIRS modification factor: $\boldsymbol{\mathcal{R}}^2(\omega_0, \zeta_0) = \dfrac{\displaystyle\int_{-\infty}^{\infty} \left| H_0(\omega) \right|^2 \left[\left| \boldsymbol{\mathcal{T}}_{\mathrm{m}}(\omega) \right|^2 \right] \mathbf{1} \, \mathrm{d}\omega}{\displaystyle\int_{-\infty}^{\infty} \left| H_0(\omega) \right|^2 \, \mathrm{d}\omega}$
   - FLIRS: $\boldsymbol{\mathcal{S}}_{\mathrm{A}}^{\mathrm{fb}}(\omega_0, \zeta_0) = \boldsymbol{\mathcal{R}}(\omega_0, \zeta_0) \, \boldsymbol{\mathcal{S}}_{\mathrm{A}}^{\mathrm{f}}(\omega_0, \zeta_0)$
5. The FLIRS $\boldsymbol{\mathcal{S}}_{\mathrm{A}}^{\mathrm{fb}}(\omega_0, \zeta_0)$ are input to the fixed-base model of the structure to generate the required FRS by the direct spectra-to-spectra method.

6.3 Application and Parametric Study on Foundation Flexibility

The SSI effect is determined by both the the structure properties and dynamic soil stiffness. In this section, the SSI analysis with flexible foundation is performed, and parametric study is conducted to illustrate the influence of foundation flexibility in the determination of FLIRS. A rigid foundation and six flexible foundations are considered in this study to show the impact of foundation flexibility.

The same reactor building employed in Section 3.2 is utilized in this study.

Foundation input response spectra

The R.G. 1.60 response spectra (USNRC, 1973) are assumed as free field motions at foundation level, i.e., FIRS. The peak ground accelerations are anchored to $0.3g$ and $0.2g$ for the horizontal and vertical directions, respectively. The seismic input is assumed to be uniform under the foundation in this study, i.e., FIRS at each foundation point are the same.

Foundation Information

The base slab is discretized into massless shell elements, and the base of the superstructure connects to the center of the circular foundation. There are 112 plate elements for the foundation, and the lumped masses are assigned at 9 points in the foundation, i.e., points *O* and F1∼F8, as shown in Figure 6.7 and Table 6.1. The flexible foundations are assigned

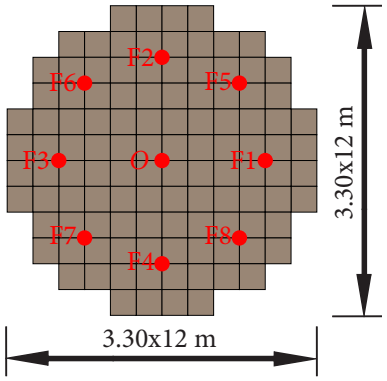

Figure 6.7 Mass distribution of flexible foundation

different modulus of elasticity, given in Table 6.2, to present the influence of varying foundation flexibility on SSI effect. The value in foundation 1 is the concrete modulus of elasticity.

Table 6.1 Flexible foundation information of reactor building model

Node	Mass ($\times 10^6$ kg)	Moment of inertia ($\times 10^6 \text{kg}\cdot\text{m}^2$)	
		$I_{xx} = I_{yy}$	I_{zz}
O, F1∼F4	1.2	16.6	33.3
F5∼F8	0.6	4.16	8.32

Table 6.2 Modulus of elasticity of foundations

Foundation Number	1	2	3	4	5	6
Elasticity Modulus (Pa)	4×10^{10}	4×10^{11}	4×10^{12}	4×10^{13}	4×10^{14}	4×10^{15}

Soil Property

The underlying site consists of 2 infinite soil layers resting on a homogeneous half-space. The unit weight, Poisson's ratio, damping ratio, thickness of the top layers, and V_s are shown in Figure 6.8.

Developing Foundation Level Input Response Spectra

A modal analysis is performed for the fixed-base model by ANSYS, which provides the structure information, including natural frequencies, mode shapes of all the modes, mass matrix, and influence matrix. The damping ratio of the structure is taken as 5%.

The transfer matrix $\boldsymbol{\mathcal{T}}$ is defined by equation (6.58), in which the first term $\mathbf{T}_{\mathrm{TT},11}$ indicates the translational component and the second term accounts for the rotational component. The modulus of entire transfer function in horizontal direction $\boldsymbol{\mathcal{T}}_{11}$ and its translational component are shown in Figure 6.9 for the rigid foundation and Figure 6.10 for foundation 1. Compared to the translational component, the $\boldsymbol{\mathcal{T}}_{11}$ varies significantly because of the rotation component due to SSI effect. It is demonstrated that their difference

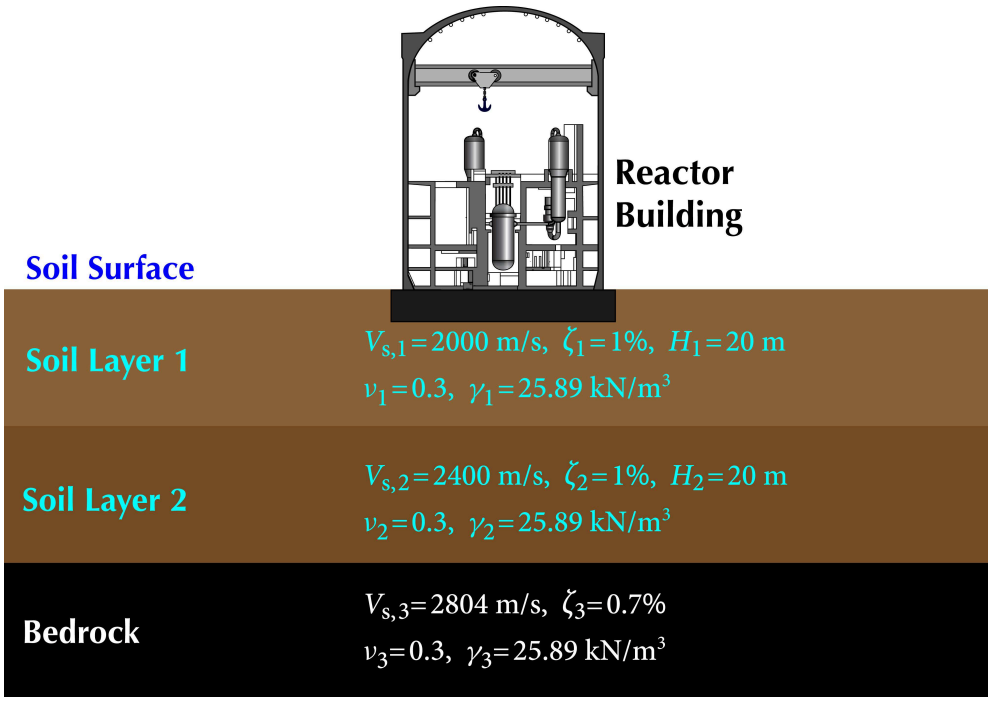

Figure 6.8 The soil layers and properties

is pronounced in the frequency range of 1 Hz to 10 Hz, which covers the frequencies of the dominant structural modes. Therefore, the rotational movement of foundation during the ground motion cannot be neglected.

The frequencies corresponding to the peaks in Figures 6.9 and 6.10 can be interpreted as the natural frequencies ω_{sf} of the entire soil-structure system (or the equivalent synthesized mass-spring-damper system). For instance, the first peak of the soil-structure system, is located at 2.24 Hz for foundation 1, and 4.07 Hz for the rigid foundation, which can be explained as a result of the frequency shifting of the fixed-base model from 4.44 Hz caused by the SSI effect.

$\boldsymbol{\mathcal{T}}_{11}$ for the 6 foundations are shown in Figure 6.11. The main difference appears during 1 Hz to 5 Hz resulting from different foundation flexibility.

FLIRS are generated for the structures with different foundations as shown in Figure 6.12. Comparing to the fixed-base motion FIRS, FLIRS changes significantly. Especially from 1 Hz to 5 Hz, a new peak is observed. When the foundation becomes more flexible, the corresponding frequency point of the peak decreases, and the peak value becomes larger.

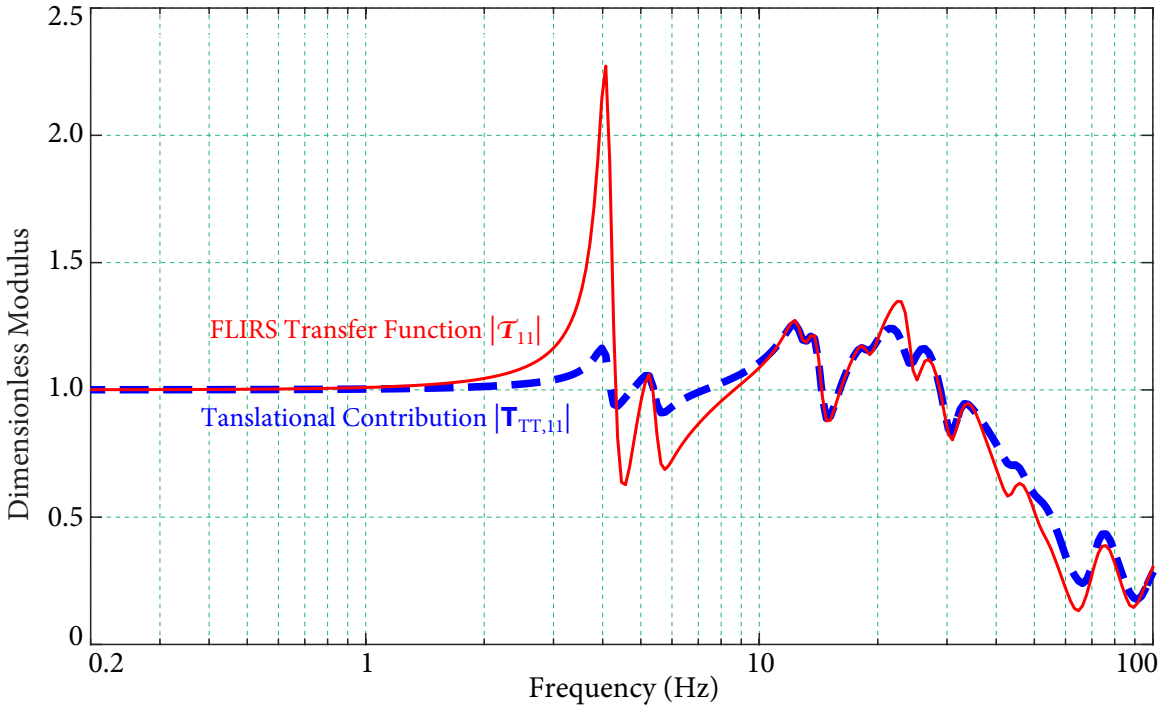

Figure 6.9 Modulus of transfer matrix at node *O* for rigid foundation

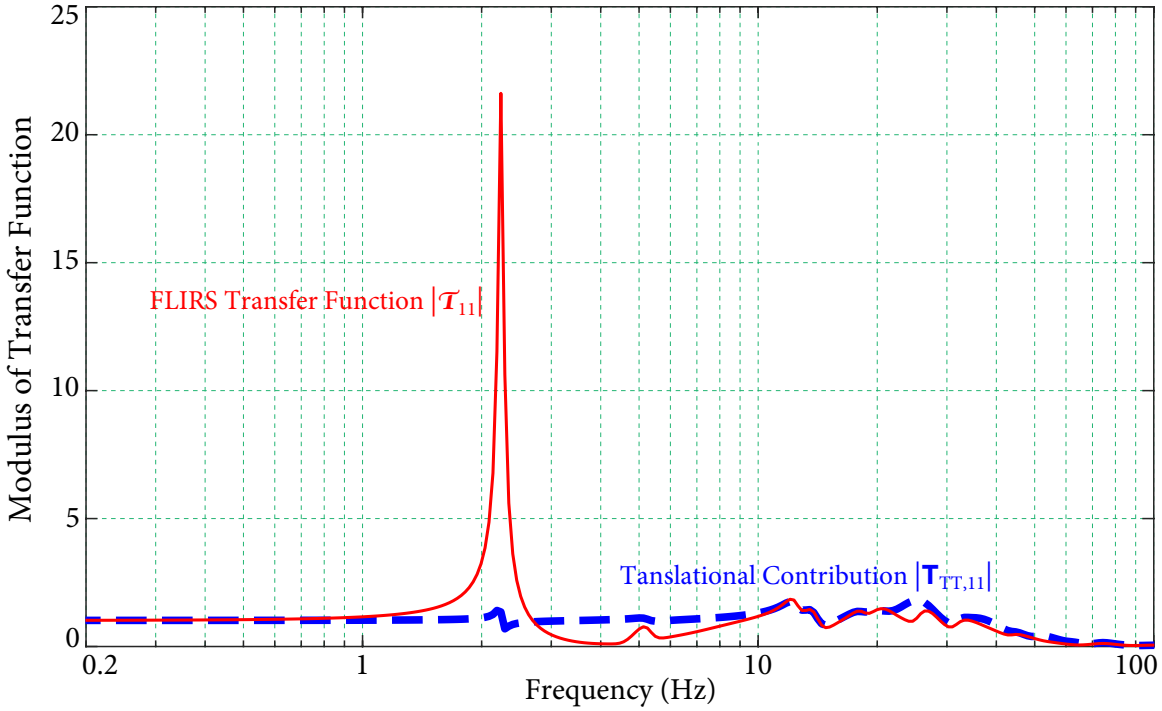

Figure 6.10 Modulus of transfer matrix at node *O* for foundation 1

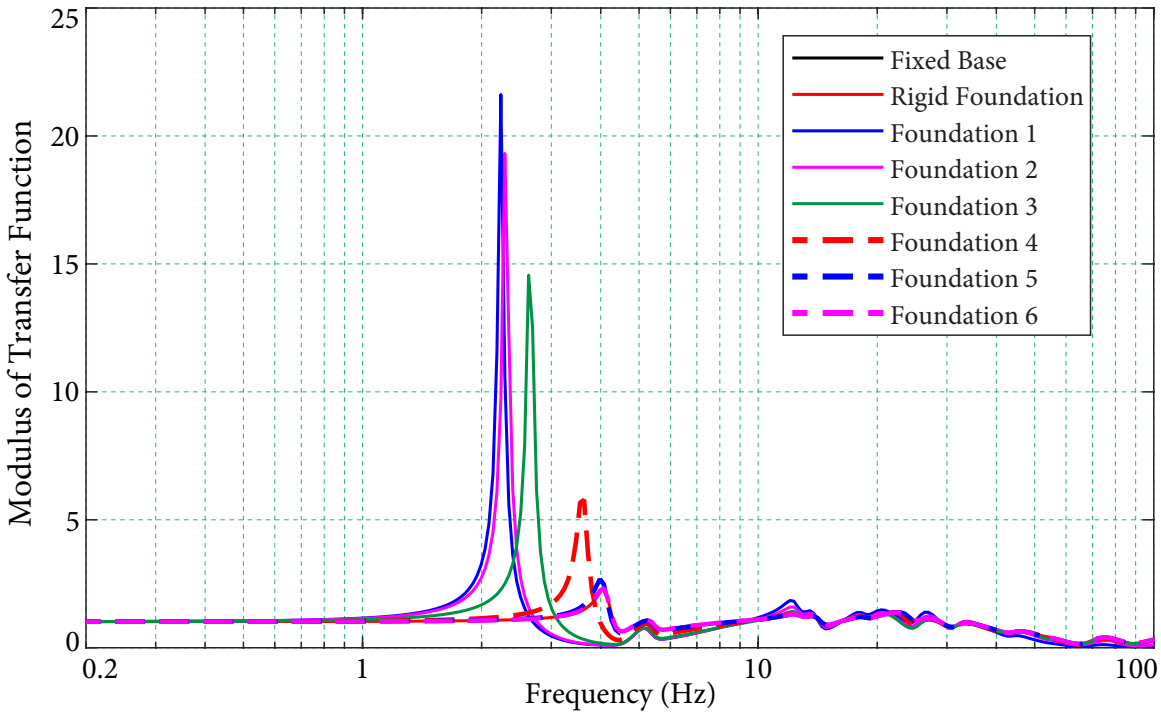

Figure 6.11 Comparison of modulus of transfer matrix horizontal component

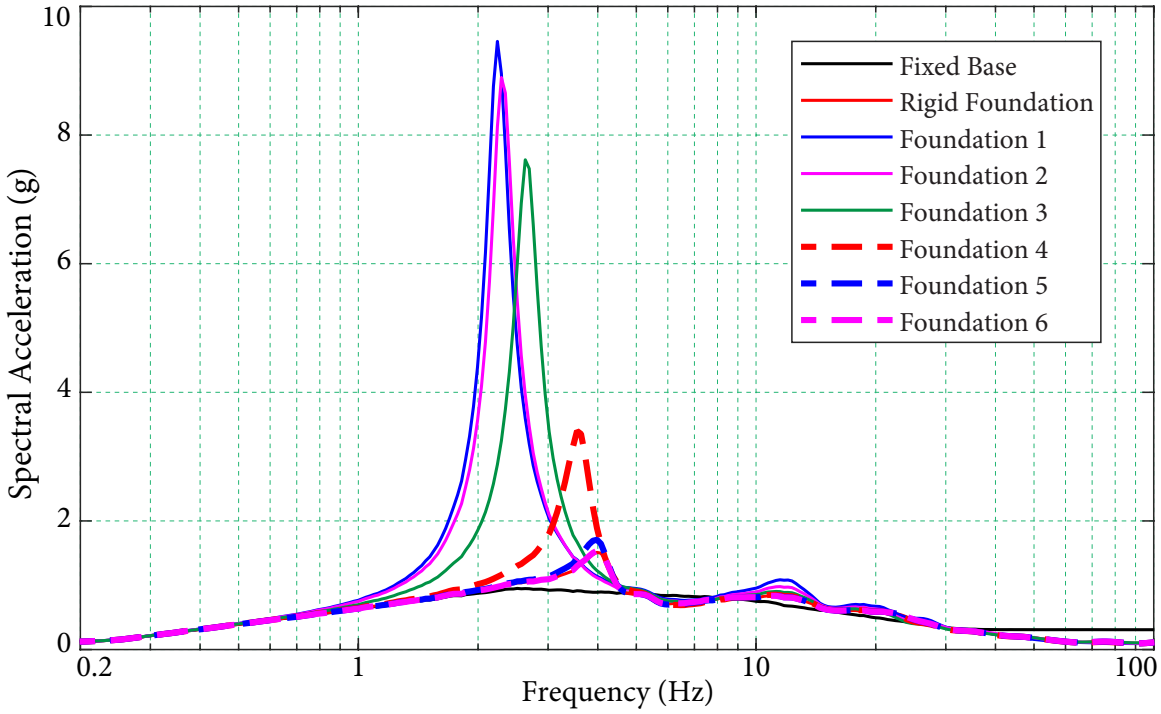

Figure 6.12 FLIRS by different foundation flexibility

The FLIRS with foundation 6 is almost the same as FLIRS with rigid foundation. As long as the foundation is not perfectly rigid, the resulting FLIRS is different from rigid foundation as shown in Figure 6.12 and Table 6.3.

Table 6.3 Peak of FLIRS for all foundations

Foundation Number	1	2	3	4	5	6	rigid
FLIRS peak value (g)	9.46	8.90	7.62	3.40	1.70	1.53	1.50
FLIRS peak frequency location (Hz)	2.24	2.29	2.63	3.55	3.98	3.98	3.98

The foundation and the supporting soil springs can be defined as an interface system between structures and sites. So at the same site, a softer foundation leads to a more flexible interface system and soil spring-foundation-structure system. Thus, the structure rotation is more severe as a result of SSI effect. Hence, ω_{sf} decreases and the peak value increases as shown in Figure 6.12. It is observed that the flexible foundation leads to a higher peak, but it also undergoes lower values in specific frequency domain. For instance, the values between 3.5 Hz to 4.5 Hz of FLIRS with foundation 1 is smaller than FLIRS with a rigid foundation.

Generating Floor Response Spectra

FRS at nodes 4 and 5 are generated by the direct method as shown in Figures 6.13 and 6.14. FRS changes significantly when flexible foundation is considered. Compared to the fixed-base case, the peak between 5 Hz and 6 Hz of FRS considering SSI is smaller. This is caused by the smaller values in FLIRS between 5 Hz and 6 Hz. Besides that, an extra peak appears at ω_{sf} between 2 Hz and 4 Hz due to SSI effect.

It shows that a flexible foundation will not lead to a conservative FRS than a rigid foundation, since the FRS with a flexible foundation is smaller than rigid foundation in some frequency points, e.g., between 3.5 Hz to 4.5 Hz for foundation 1.

6.4 Summary

In this chapter, a substructure method is developed to conduct the SSI analysis considering the flexible foundation under the excitation of spatially varying ground motions.

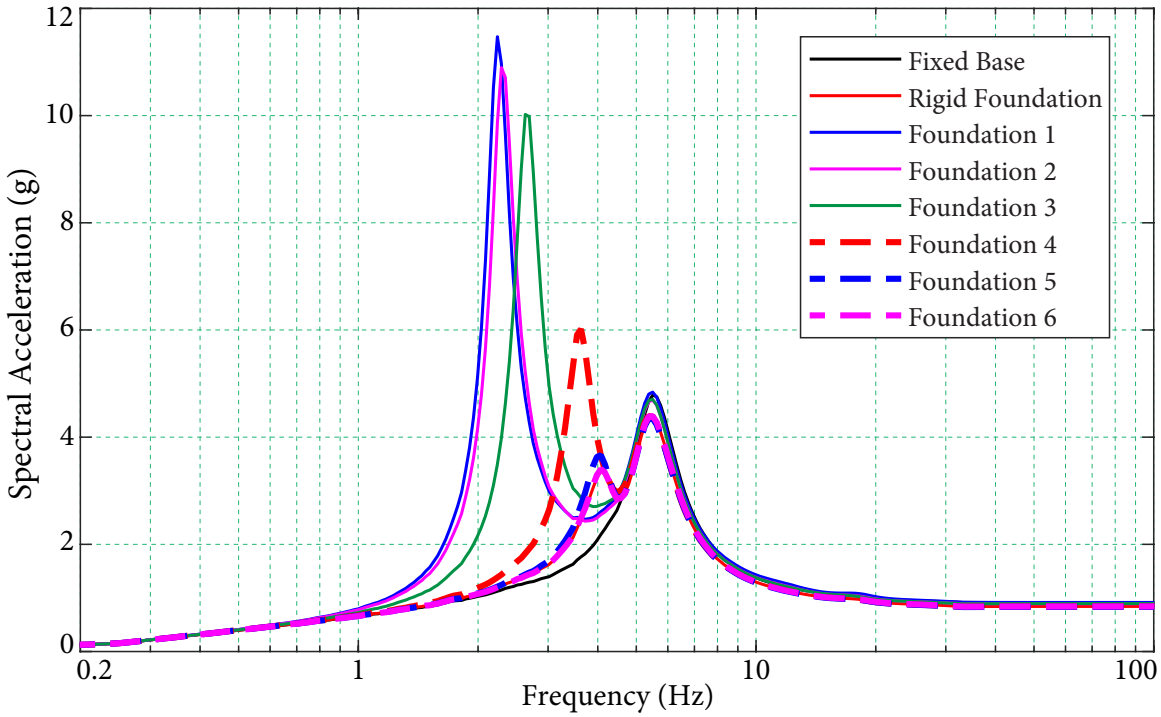

Figure 6.13 Comparison of FRS at Node 4

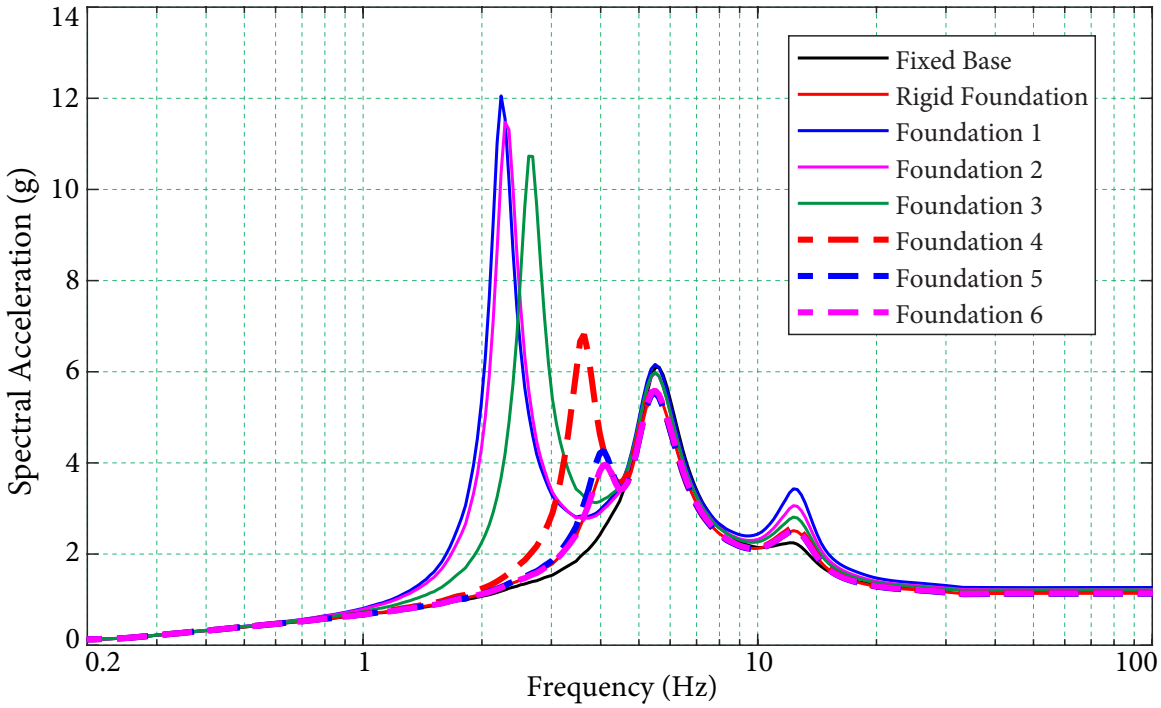

Figure 6.14 Comparison of FRS at Node 5

Depending on the properties of structure and soil, the tri-directional response spectra are determined by modifying the free-field ground motion. The modified response spectra, FLIRS, is considered as the seismic input, which is integrated with SSI effect, to the fixed-base structure for generating.

Numerical examples are performed to illustrate the proposed method and study the influence of foundation flexibility in SSI analysis. FLIRS is generated for different foundations, i.e., a rigid foundation and foundations with a couple of elasticity modulus. It is recognized that FLIRS varies dramatically with changing elasticity modulus of foundations. Some conclusions are obtained:

- The ground motion is modified noticeably because of SSI effect. The numerical example illustrates that the spectral acceleration is scaled significantly at certain frequencies, and the natural frequency of the soil-structure system shifts to a smaller value compared with the fixed-base structure due to SSI effect.
- When the foundation and site interface system become more flexible, e.g., the foundation is softer, the amplitude of the peak resulting from SSI is larger, and the natural frequency of the soil-structure system is smaller.
- Since FLIRS is amplified and de-amplified in certain frequency domain for a specific foundation and soil site, it is necessary to establish the exactly realistic structure-foundation model. Otherwise, the resultant FLIRS will be underestimated at some frequency points.

In summary, the flexible foundation and the excitation of spatially varying ground motions are considered in SSI analysis by the proposed analytical method. Based on dynamic soil stiffness and the modal information of structures and foundations, FLIRS can be obtained conveniently to compute the FRS, which shows the seismic demand for the equipment in the supporting structure.

CHAPTER 7

Conclusions and Future Research

Soil-Structure Interaction (SSI) analysis is essential for the generation of Floor Response Spectra (FRS), which represent the demand for seismic design of secondary systems in nuclear power facilities. The objective of this study is to develop an approach to address SSI effect with flexible foundations and seismic input at multiple points in the generation of Floor Response Spectra (FRS). FRS is developed after considering SSI effect accurately and efficiently in this study. The uncertainty in soil properties and earthquakes are addressed to generate a hazard consistent FRS with a specific Return Period (RP). Some contributions made in this study are summarized as follows.

7.1 Generation of Dynamic Soil Stiffness

A semi-analytical method is developed for accurately and efficiently generating dynamic soil stiffness of rigid foundations and flexible foundations. Given the soil properties, the Green's influence function is formulated analytically from wave propagation functions. Based on Boundary Element Method (BEM), the dynamic stiffness of foundations with arbitrary shapes is generated. Some features and conclusions are summarized as follows:

- As a semi-analytical method, the Green's influence function is derived analytically, and the soil-foundation interface is treated by numerical method BEM, which models the unbounded soil properly. The dynamic soil stiffness can be generated accurately. It bridges the site response analysis and SSI analysis, i.e., it links these two steps by

calculating the dynamic soil stiffness for SSI analysis from the strain-compatible soil properties given by site response analysis.

- The Green's influence function is formulated rigorously based on wave propagation function. Once the soil properties are known, it is convenient to calculate the Green's influence function. Each soil layer is treated as a single element in the formulation of Green's influence function, and only the soil-foundation interface is discretized by BEM. Thus only a limited number of elements are involved in the proposed method, which guarantees the efficiency of the proposed method.
- The application of BEM adapts the proposed method to foundations with arbitrary shapes or multiple components. Thus, it can provide the $6M \times 6M$ dynamic soil stiffness matrix for SSI analysis with flexible foundations.
- The influence of dynamic soil stiffness on the generation of FRS is examined. It affects the resultant FRS noticeably.

7.2 Developing Framework to Construct Uniform Hazard FLIRS

This study proposes a fully probabilistic method for addressing the uncertainty of seismic input and soil properties in the generation of FRS. The uncertainty is propagated from site response analysis to SSI analysis consistently, and a uniform hazard FLIRS is developed. Some remarkable features and advantages of the proposed method are summarized as follows:

- The uniform hazard FLIRS and FRS with specific annual exceedance probability are generated. Compared to the current approach, The seismic demand for secondary system is reduced significantly. The uniform hazard FRS provide a safer and more economical demand for seismic design. Meanwhile, the FRS may be underestimated by the current method at some frequency range, which is overcame by the proposed method.
- A realistic and continuous shear wave velocity (V_S) distribution is proposed to replace the current treatment of uncertainty which is not continuous and assumes the V_S in

all layers are fully correlated. The difference of FRS generated by the proposed parameters is small and negligible. The uncertainty in soil properties can be accounted reasonably.

- Sensitivity study is performed on the correlation coefficient and the standard derivation of V_S. The results show that their influence on FRS is minor. The FRS generated by different standard derivation are almost the same as each other. There is only a little difference around the peak. For correlation coefficients equal to 0 or 1, the change of FRS is not significant. Hence, the correlation coefficient and the standard derivation of V_S are not important parameters in uncertainty analysis.

7.3 SSI Analysis Considering Foundation Flexibility and Inputs at Multiple Points

For nuclear power plants, the stiffness of foundations may be close to the values of the external and internal structures. Thus the foundation flexibility can not be neglected. Besides, the seismic excitation may be different at side walls and foundations for fully or partly embedment reactors. A substructure method is proposed to perform SSI analysis considering the flexible foundation under the excitation of spatially varying ground motions. Depending on the properties of structure and soil, the three dimensional response spectra are determined by modifying the free-field ground motion. Some remarkable features and advantages of the proposed scaling method are summarized as follows:

- The SSI effect is integrated into Foundation Input Response Spectra (FIRS), which is free field motion and obtained from site response analysis. The modified ground motion is called Foundation Level Input Response Spectra (FLIRS), which can be used as the seismic input for fixed model to generate FRS by the direct spectra-to-spectra method. Thus, the SSI effect is addressed in the resultant FRS.
- The foundation flexibility is considered in the proposed method, by which the SSI analysis is more realistic. It is observed that, as long as the foundation is not perfectly rigid, the foundation flexibility can not be neglected. Meanwhile, seismic excitation is

imposed at the representative points of flexible foundations. This enables the analysis with spatially varying ground motions.

- Parametric study is performed to illustrate the influence of foundation flexibility on SSI effect. FLIRS is generated for different foundations, i.e., a rigid foundation and foundations with a couple of elasticity modulus. It is recognized that FLIRS varies dramatically with changing elasticity modulus of foundations. When the foundation becomes more flexible, the amplitude of the peak resulting from SSI is larger, and the natural frequency of the soil-structure system is smaller. It is demonstrated that the exactly realistic model of structures, and foundations is necessary for SSI analysis.
- The influence of SSI effect on FRS is studied. FRS is amplified at the natural frequency of the soil-structure system, and the seismic demand of secondary system increases. Meanwhile, FRS will decrease at specific frequency points.
- The proposed substructure method is analytically formulated, so that it is convenient to implement by a programming language, e.g., MATLAB or Python. Once the dynamic soil stiffness and structure modal information are provided, FLIRS can be generated efficiently. Besides, the soil and structure are analyzed separately, which means the change of system only leads to repeated work of relevant part. The reanalysis of the entire system is avoided.

7.4 Future Research

In the seismic analysis of secondary systems, FRS can be obtained by the direct spectra-to-spectra method efficiently and accurately without variability. The fixed model considered in the current direct spectra-to-spectra method assumes that the foundation is rigid and the three dimensional seismic input is the same at any location of the foundation. For foundations with fully or partly embedment, seismic input not only comes from the bottom foundation, but also from the side walls, which leads to multiple points excitation. In future research, the direct spectra-to-spectra method needs to be extended to generate FRS under multiple seismic input.

In the proposed substructure method, the surrounding soil, can be called interface elements, is assumed to have the same properties as the site. Actually, the ground motion at the foundation side of interface elements is the FLIRS which is generated by modifying FIRS due to SSI effect, while the excitation at the other side is the free field motion FIRS. Since FLIRS is amplified from FIRS in certain frequency domain, the properties of interface elements will be different from the free field. This will influence the dynamic soil stiffness and SSI effect. Thus, further studies needs to consider how the interface elements is influenced by SSI effect, and how to integrate this influence into SSI analysis.

Bibliography

Abascal, R. and Dominguez, J., 1986. Vibrations of footings on zoned viscoelastic soils. *Journal of Engineering Mechanics*, **112**, 433–447.

Apsel, R. J. and Luco, J. E., 1983. On the green's functions for a layered half-space. part ii. *Bulletin of the Seismological Society of America*, **73**(4), 931–951.

ASCE, 1978. *Development of Floor Design Response Spectra for Seismic Design of Floor-supported Equipment or Components*, **Standard R.G. 1.122**. U.S. Atomic Energy Commission, Washington D.C.

ASCE, 1998. *Seismic Analysis of Safety-Related Nuclear Structures and Commentary*, **asce 4-98**. American Society of Civil Engineers (ASCE).

ASCE, 2000. *Seismic Analysis of Safety-related Nuclear Structures and Commentary, Standard* ASCE 4-98. American Society of Civil Engineers, Reston, Virginia.

Astley, R. J., 1983. Wave envelope and infinite elements for acoustical radiation. *International Journal for Numerical Methods in Fluids*, **3**(5), 507–526.

Atkinson, G. M. and Boore, D. M., 1995. Ground motion relations for eastern north america. *Bulletin of Seismological Society of America*, **85**, 15–35.

Atkinson, G. M. and Boore, D. M., 2006. Earthquake ground-motion prediction equations for eastern north america. *Bulletin of the Seismological Society of America*, **96**(6), 2181–2205.

Baffet, D., Bielak, J., and Givoli, D., 2012. Long-time stable high-order absorbing boundary conditions for elastodynamics. *Computational Methods in Applied Mechanics and Engineering*, **241**(244), 20–37.

Basu, U. and Chopra, A. K., 2003. Perfectly matched layers for time-harmonic elastodynamics of unbounded domains: theory and finite-element implementation. *Computer*

Methods in Applied Mechanics and Engineering, **192**(11–12), 1337–1375.

Bazzurro, P. and Cornell, C. A., 2004. Nonlinear soil-site effects in probabilistic seismic-hazard analysis. *Bulletin of the Seismological Society of America*, **94**(6), 2110–2123.

Berenger, J. P., 1994. A perfectly matched layer for the absorption of electromagnetic waves. *Journal of Computational Physics*, **114**, 185–200.

Bettess, P., 1977. Infinite elements. *International Journal for Numerical Methods in Engineering*, **11**(1), 53–64.

Bielak, J. and Christiano, P., 1984. On the effective seismic input for non-linear soil-structure interaction systems. *Earthquake Engineering and Structural Dynamics*, **12**, 107–119.

Birk, C. and Behnke, R., 2012. A modified scaled boundary finite element method for three-dimensional dynamic soil–structure interaction in layered soil. *International Journal for Numerical Methods in Engineering*, **89**(3), 371–402.

Boore, D. M. and Joyner, W. B., 1984. A note on the use of random vibration theory to predict peak amplitudes of transient signals. *Bulletin of the Seismological Society of America*, **74**(5), 2035–2039.

Boore, D. M., 1983. Stochastic simulation of high-frequency ground motions based on seismological models of the radiated spectra. *Bulletin of the Seismological Society of America*, **73**(6), 1865–1894.

Boore, D. M., 2003. Simulation of ground motion using the stochastic method. *Pure and Applied Geophysics*, **160**, 635–676.

Bozorgnia, Y. and Bertero, V. V., 2004. *Earthquake Engineering: from Engineering Seismology to Performance-based Engineering*. CRC press, Boca Raton, Florida.

Bozorgnia, Y. and Campbell, K. W., 2004. The vertical to horizontal response spectral ratio and tentative procedures for developing simplified v/h and vertical design spectra. *Journal of Earthquake Engineering*, **8**(2), 175–207.

Campbell, K.W., 2003. Prediction of strong ground motion using the hybrid empirical method and its use in the development of ground-motion (attenuation) relations in eastern north america. *Bulletin of Seismological Society of America*, **93**(3), 1012–1033.

Cartwright, D. E. and Longuet-Higgins, M. S., 1956. The statistical distribution of the maxima of a random function. *Mathematical and Physical*, **237**(1209), 212–232.

Chen, Y. and Soong, T.T., 1988. Seismic response of secondary systems. *Engineering Structures*, **10**(4), 218–228.

Clayton, R. and Engquist, B., 1977. Absorbing boundary conditions for acoustic and elastic wave equations. *Bulletin of the Seismological Sociaty of America*, **67**(6), 1529–1540.

Collino, F., 1993. High order absorbing boundary conditions for wave propagation models. straight line boundaries and corner cases. *Proceedings of the Second International Conferenceon Mathematical and Numerical Aspects of Wave Propagation*, p. 161–171.

Dasgupta, G., 1982. A finite element formulation for unbounded homogeneous continua. *Journal of Applied Mechanics*, **49**(1), 136–140.

Elleithy, W. M. and Tanaka, M., 2003. Interface relaxation algorithms for bem-fem coupling and fem-bem coupling. *Coumputational Methods Applied to Mechanical Engineering*, **192**(26-27), 2977–2992.

EPRI, 1993A. *Guidelines for Determining Design Basis Ground Motions-Volume 1: Method and Guidelines for Estimating Earthquake Ground Motion in Eastern North America*. Electric Power Research Institute, Palo Alto, California.

EPRI, 1993B. *Guidelines for Determining Design Basis Ground Motions-Volume 2: Appendices for Ground Motion Estimation*. Electric Power Research Institute, Palo Alto, California.

EPRI, 2013. *Seismic Evaluation Guidance: Screening, Prioritization and Implementation Details (SPID) for the Resolution of Fukushima Near-Term Task Force Recommendation 2.1: Seismic*. Electric Power Research Institute, Palo Alto, California.

Estorff, O. V. and Kausel, E., 1989. Coupling of boundary and finite elements for soil-structure interaction problems. *Earthquake Engineering and Structural Dynamics*, **18**(7), 1065–1075.

Estorff, O. V. and Prabucki, M. J., 1990. Dynamic response in the time domain by coupled boundary and finite elements. *Coumputational Mechanics*, **6**(1), 35–46.

EUR, 2002. *European Utility Requirements for LWR Nuclear Power Plants*. European Utility Requirements Organisation.

Gasparini, D. A. and Vanmarcke, E. H., 1976. *Simulated earthquake motions compatible with prescribed response spectra*. Massachusetts Institute of Technology, Cambridge, Massachusetts.

Gazetas, G. and Rosset, J. M., 1976. Forced vibrations of strip footings on layered soils. *Method of Structural Analysis*, **1**, 115–131.

Givoli, D., 2004. High-order local non-reflecting boundary conditions: a review. *Wave Motion*, **39**, 319–326.

Gulerce, Z. and Abrahamson, N. A., 2011. Site-specific design spectra for vertical ground motion. *Earthquake Spectra*, **27**, 1023–1047.

Gutierrez, J.A. and Chopra, A.K., 1978. A substructure method for earthquake analysis of structures including structure-soil interaction. *Earthquake Engineering and Structural Dynamics*, **6**(1), 51–69.

Hashash, Y. M. A. and Park, D., 2002. Viscous damping formulation and high frequency motion propagation in nonlinear site response analysis. *Soil Dynamics and Earthquake Engineering*, **22**(7), 611–624.

Higdon, R. L., 1978. Boundry conditions for the numerical solution of wave propagation problems. *Geophysics*, **43**(6), 1099–1110.

Higdon, R. L., 1990. Radiation boundary conditions for the scalar wave equation. *SIAM Journal on Numerical Analysis*, **27**(4), 831–870.

Higdon, R. L., 1991. Absorbing boundary conditions for elastic waves. *Geophysics*, **56**(2), 231–241.

Idriss, I. M. and Sun, J. I., 1992. *"A Computer Program for Conducting Equivalent Linear Seismic Response Analysis of Horizontally Layered Soil Deposits" in Users' Manual for SHAKE91*. University of California at Davis, Davis, California.

Jiang, W., Li, B., Xie, W-C, and Pandey, M. D., 2015. Generate floor response spectra: Part 1. direct spectra-to-spectramethod. *Nuclear Engineering and Design*, **293**, 525–546.

Jiang, W., 2016. *Direct Method of Generating Floor Response Spectra*. PhD thesis, University of Waterloo.

Karabalis, D. L. and Mohammadi, M., 1991. *Foundation-Soil-Foundation Dynamics Using a 3-D Frequency Domain BEM*, **Boundary Elements XIII**. Springer, Dordrecht.

Kausel, E., Roesset, J. M., and Waas, G., 1975. Dynamic analysis of footings on layered media. *Journal of Engineering Mechanics*, **101**, 679–693.

Kausel, E., 1984. Early history of soil-structure interaction. *Soil Dynamics and Earthquake Engineering*, **30**, 1743–1761.

Kottke, A. R., Wang, X., and Rathje, E. M., 2013. *Technical Manual for Strata*. University of Texas, Austin, USA.

Liu, L. and Pezeshk, S., 1999. An improvement on the estimation of pseudoresponse spectral velocity using rvt method. *Bulletin of the Seismological Society of America*, **89**(5), 1384–1389.

Li, B., Jiang, W., Xie, W-C, and Pandey, M. D., 2015. Generate floor response spectra: Part 2 response spectra for equipment-structure resonance. *Nuclear Engineering and Design*, **293**, 547–560.

Li, B., 2015. *Response Spectra for Seismic Analysis and Design*. PhD thesis, University of Waterloo.

Li, Z.-X., LI, Z.-C., and Shen, W.-X., 2005. Sensitivity analysis for floor response spectra of nuclear reactor buildings. *Nuclear Power Engineering*, **26**(1), 44–50.

Luco, J. E. and Apsel, R. J., 1983. On the green's functions for a layered half-space. part i. *Bulletin of the Seismological Society of America*, **73**(4), 909–929.

Luco, J. E. and Westmann, R. A., 1972. Dynamic response of rigid footing bonded to an elastic half-space. *Journal of Applied Mechanics*, **39**(2), 527–534.

Luco, J. E., 1971. Westmann ra. dynamic response of circular footing. *Journal of the Engineering Mechanics Division*, **97**(5), 1381–1395.

Luco, J. E., 1974. Impedance functions for a rigid foundation on a layered medium. *Nuclear Engineering and Design*, **31**(2), 204–217.

Luco, J. E., 1976. Vibrations of a rigid disk on a layered viscoelastic medium. *Nuclear Engineering and Design*, **36**, 325–340.

Lysmer, J. and Kuhlemeyer, R. L., 1969. Finite dynamic model for infinite media. *Journal of Engineering Mechanics Division*, **95**(4), 859–878.

Lysmer, J. and Waas, G., 1972. Shear waves in plane infinite structures. *Journal of the Engineering Mechanics Division*, **98**, 85–105.

Matasovic, N. and Vucetic, M., 1993. Cyclic characterization of liquefiable sands. *Journal of Geotechnical Engineering*, **119**, 1805–1822.

Matasovic, N. and Vucetic, M., 1995. Seismic response of soil deposits composed of fully saturated clay and sand layers. In *Proceedings of Is-Tokyo'95, The First International Conference on Earthquake Geotechnical Engineering*, Netherlands.

McGuire, R. K., Becker, A. M., and Donovan, N. C., 1984. Spectral estimates of seismic shear waves. *Bulletin of Seismological Society of America*, **74**(4), 1427–1440.

Mesquita, E. and Pavanello, R., 2005. Numerical methods for the dynamics of unbounded domains. *Computational and Applied Mathematics*, **1**(24), 1–26.

Ni, S-H., Xie, W-C., and Pandey, M. D., 2011. Tri-directional spectrum-compatible earthquake time-histories for nuclear energy facilities. *Nuclear Engineering and Design*, **241**(8), 2732–2743.

Ni, S-H., Xie, W-C., and Pandey, M. D., 2013. Generation of spectrum-compatible earthquake ground motions considering intrinsic spectral variability using Hilbert-Huang transform. *Structural Safety*, **42**, 45–53.

Pak, R. Y. S. and Guzina, B. B., 1999. Seismic soil-structure interaction analysis by direct boundary element methods. *International Journal of Solids and Structures*, **36**(31-32), 4743–4766.

Rabinovich, D., Givoli, D., and Becache, E., 2010. Comparison of high-order absorbing boundary conditions and perfectly matched layers in the frequency domain. *International Journal for Numerical Methods in Biomedical Engineering*, **26**, 1351–1369.

Rathje, E. M. and Kottke, A. R., 2008. *Procedures for Random Vibration Theory Based Seismic Site Response Analyses: A White Paper Prepared for the Nuclear Regulatory Commission*. University of Texas at Austin, Austin, TX.

Rizzo, F. J., 1967. An integral equation approach to boundary value problems of classical elastostatics. *Quarterly of Applied Mathematics*, **25**(1), 83–95.

Schnabel, P. B., Lysmer, J., and Seed, H. B., 1972. *SHAKE: A computer program for earthquake response analysis of horizontally-layered*. Earthquake Engineering Research Center, Berkeley, California.

Seed, H. B. and Idress, I. M., 1969. Influence of soil conditions on ground motions during earthquakes. *Journal of the Soil Mechanics and Foundations Division*, **95**, 99–138.

Shah, S. G., Solanki, C.H., and Desai, J. A., 2011. Soil structure interaction analysis methods - state of art - review. *International Journal of Civil and Structural Engineering*, **2**(1), 176–204.

Silva, W., Abrahamson, N., Toro, G., and Costantino, C., 1996. *Description and Validation of the Stochastic Ground Motion Model*. Pacific Engineering and Analysis, El Cerrito, USA.

Singh, M.P., 1988. Seismic design of secondary systems. *Probabilistic Engineering Mechanics*, **3**(3), 151–158.

Song, C. and Wolf, J. P., 1995b. Consistent infinitesimal finite-element-cell method: out of-plane motion. *Journal of Engineering Mechanics*, **121**(5), 613–619.

Song, C. and Wolf, J. P., 1996b. Consistent infinitesimal finite-element cell method: three-dimensional vector wave equation. *International Journal For Numerical Methods in Engineering*, **39**(13), 2189–2208.

Song, C. and Wolf, J. P., 1997. The scaled boundary finite-element method ¨calias consistent infinitesimal finite-element cell method¨c for elastodynamics. *Coumputer Methods in Applied Mechanics and Engineering*, **147**(3-4), 329–355.

Toro, G. R., 1995. *Probabilistic Models of Site Velocity Profiles for Generic and Site-Specific Ground-Motion Amplification Studies*. Brookhaven National Laboratory, Upton, New York.

Ungless, R. F., 1973. *An infinite finite element*. PhD thesis, University of British Columbia.

USNRC, 1973. *Design Response Spectra for Seismic Design of Nuclear Power Plants*, **R.G. 1.60**. U.S. Atomic Energy Commission.

USNRS, 1978. *Development of Floor Design Response Spectra for Seismic Design of Floor-Supported Equipment or Components. Revision 1*, **Regulatory Guide 1.122**. U.S. Nuclear Regulatory Commission.

Veletsos, A. S. and Verbic, B., 1973. Vibration of viscoelastic foundations. *Earthquake Engineering and Structural Dynamic*, **2**, 87–102.

Veletsos, A. S. and Verbic, B., 1987. Impedance functions for foundations embedded in a layered medium: an integral equation approach. *Earthquake Engineering and Structural Dynamic*, **15**, 213–231.

Veletsos, A. S. and Wei, Y. T., 1971. Lateral and rocking vibration of footings. *Journal of the Soil Mechanics and Foundation Division, ASCE*, **97**, 1227–1248.

Villaverde, R., 1997. Seismic design of secondary structures: state of the art. *Journal of Structural Engineering*, **123**(8), 1011–1019.

Villaverde, R., 2009. *Fundamental Concepts of Earthquake Engineering*. CRC Press, Baton Raton, Florida.

Waas, G., 1972. *Linear two-dimensional analysis of soil dynamics problems in semi-infinite layered media*. PhD thesis, The University of California, Berkeley.

Walling, M., Silva, W., and Abrahamson, N., 2008. Nonlinear site amplification factors for constraining the nga models. *Earthquake Spectra*, **24**(1), 243–255.

Wolf, J. P. and Darbre, G. R., 1984. Dynamic-stiffness matrix of soil by the boundary-element method: Embedded foundation. *Earthquake Engineering and Structural Dynamics*, **12**(3), 401–416.

Wolf, J. P. and Song, C., 1995a. Consistent infinitesimal finite-element cell method: inplane motion. *Computer Methods in Applied Mechanics and Engineering*, **123**(1-4), 355–370.

Wolf, J. P. and Song, C., 1996a. Finite-element modelling of unbounded media. In *Eleventh World Conference on Earthquake Engineering*, Mexico.

Wolf, J. P., 1985. *Dynamic Soil-Structure Interaction*. Prentice-Hall, New Jersey, USA.

Wong, H. L. and Luco, J. E., 1985. Tables of impedance functions for square foundations on layered media. *Soil Dynamics and Earthquake Engineering*, **4**(2), 64–81.